Oliver Roser

Heat Conduction in Filled Polymers

Experimental and Simulative Investigations on Microscopic Heat Transport and Particle-Level Phenomena

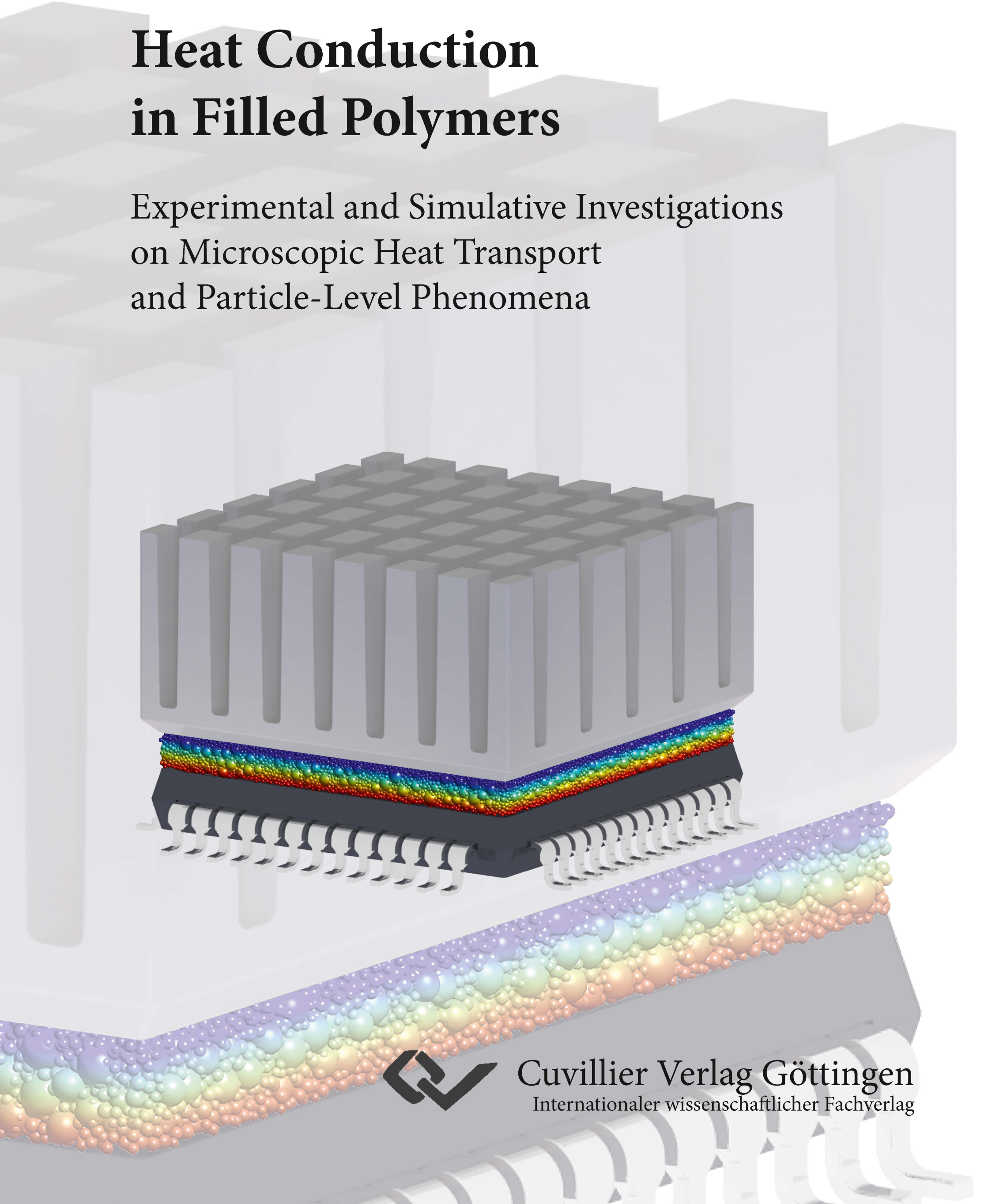

Cuvillier Verlag Göttingen
Internationaler wissenschaftlicher Fachverlag

Heat Conduction in Filled Polymers
Experimental and Simulative Investigations
on Microscopic Heat Transport and Particle-Level Phenomena

Heat Conduction in Filled Polymers

Experimental and Simulative Investigations on Microscopic Heat Transport and Particle-Level Phenomena

Dissertation zur Erlangung
des Doktorgrades Dr. rer. nat.
der Fakultät für Naturwissenschaften
der Universität Ulm

vorgelegt von

Oliver Roser
geboren in Freiburg i. Br.

2025
Universität Ulm
Institut für Experimentelle Physik

Impressum

Titel des Werkes: Heat Conduction in Filled Polymers. Experimental and Simulative Investigations on Microscopic Heat Transport and Particle-Level Phenomena
Autor: Oliver Roser
Cuvillier Verlag GmbH Nonnenstieg 8 37075 Göttingen
Telefon: 0049-551-547240
Webseite: www.cuvillier.de **E-Mail:** info@cuvillier.de

Bibliografische Informationen der Deutschen Nationalbibliothek Die Deutsche Nationalbibliothek verzeichnet diese Publikation in der Deutschen Nationalbibliografie; detaillierte bibliografische Daten sind im Internet über http://dnb.dnb.de abrufbar.

1. **Auflage,** Göttingen. 2025
Zugl.: Ulm, Universität, Dissertation, 2025

1. Gutachter: Sen.-Prof. Dr. sc. nat. / ETH Zürich Othmar Marti
2. Gutachter: Prof. Dr. Ulrich Herr
Amtierender Dekan: Prof. Dr. Kay-E. Gottschalk
Tag der mündlichen Prüfung: 03.11.2025

Diese Publikation wurde durch Mittel aus dem Publikationsfonds NiedersachsenOPEN unterstützt, der von zukunft.niedersachsen finanziert wird.

Gedruckt auf umweltfreundlichem, säurefreiem Papier aus nachhaltiger Forstwirtschaft.

ISBN 978-3-68952-389-3
eISBN 978-3-68952-390-9
Orcid 0009-0001-5931-5483
ISNI 0000000528894955

PREFACE

With the progression of miniaturization and the rise in performance requirements, thermal management in electronic systems is becoming increasingly important. Thermal interface materials and other filled polymers play a major role. While working on numerous industrial projects at the Centre for Heat Management (ZFW) in Stuttgart, I was able to gain valuable insights into the recent developments of materials and their application. It has become clear that the development and optimization of materials is always associated with extensive experimental investigations and trial-and-error processes. Important knowledge about the impact of the microscopic material structure is still scarce. Against this backdrop, the present work was carried out with the aim of investigating heat conduction in filled polymers at the microscopic level and making a decisive contribution to understanding the interaction between filler packing, polymers, and substrate surfaces.

My grateful thanks go to Professor Othmar Marti from Ulm University for supervising this project and reviewing my work. It was a privilege to have him as my mentor. The hours of technical discussions with numerous helpful suggestions and creative ideas made a significant contribution to the overall success of the project. I would also like to thank Professor Andreas Griesinger, head of ZFW, for making the project possible and for providing the ideal working environment. His enduring willingness to engage in profitable and in-depth technical discussions needs to be acknowledged. To Professor Ulrich Herr, for the interesting and stimulating discussions, for his valuable advice on scientific writing, and for preparing the second review I would like to offer my sincere thanks. Furthermore, I acknowledge the support of all my colleagues and friends at ZFW and the Institute for Experimental Physics at Ulm University. Regardless of whether it was technical discussions, active help with the experiments, travelling together to conferences, proofreading support, or their continuous encouragement. Without their help, the realization of this project would not have been possible. I am grateful to the Institute for Microtechnology and Photonics at the Eastern Switzerland University of Applied Sciences for carrying out the particle size analyses. Sibelco - Ankerpoort NV, The Netherlands and Eckart GmbH, Germany have been helpful in providing fillers for the experimental investigations. Last but not least, my deepest thanks go to my beloved wife Simone who, from the very outset, has supported me in many different ways and made the project possible. She has always given me the help and encouragement I needed and shown a total devotion to our little family.

Bad Urach, July 2025

Oliver Roser

ABSTRACT

Thermally conductive filled polymers are widely used in micro and power electronics as well as in electromobility. They have a highly complex and heterogeneous microstructure. The present work describes the development and application of experimental and simulative methods to investigate the microscopic heat transport through filled polymers and across filled polymer to substrate transitions. The aim is to develop a comprehensive understanding of the effects of various polymer, filler, and substrate properties on the effective thermal conductivity and on thermal contact resistance between filled polymers and solid surfaces. Experimental studies are carried out using the steady-state cylinder method and a newly developed technique based on micro thermography. This enables microscopic resolution of the thermal contact resistances, providing insight into the mechanisms in filled polymer to substrate transitions that were previously unattainable. In addition, microstructure simulation models assist the investigation into the processes inside the materials that cannot be resolved experimentally. The simulative investigations also allow an isolated analysis of individual influencing variables, which is only possible to a limited extent experimentally due to the versatile property profiles of available fillers. The geometrically detailed microstructure models can be constructed based on measurable material properties such as particle shape plus size distribution or surface structure of a substrate and thus reconstruct the structure of real sample materials.

Generally, the effect of the microscopic packing structure is more significant than that of the thermal properties of polymer, filler, and substrate. Particle morphology, size distribution, packing compaction and phenomena such as agglomeration and sedimentation define how well thermally conductive paths are formed in the material and which filler volume fractions are necessary to achieve the desired effective thermal conductivity. With multiscale filler blends, it is the combination of particle sizes, maximum packing densities and thermal conductivities in the individual fractions that largely affects the achievable effective thermal conductivity.

Investigations on filled polymer to substrate transitions show that it is primarily the local disturbance of the particle packing structure by the adjacent substrate that leads to increased thermal contact resistance. Narrow particle size distributions and very smooth substrate surfaces favor the formation of a micro-order and intensify the effect, while very rough substrate surfaces and wide particle size distributions will increase the boundary layer thickness but reduce the thermal contact resistances. In conclusion, a comprehensive overview of heat conduction in filled polymers is formulated, deriving valuable knowledge for future material developments.

CONTENTS

NOMENCLATURE AND ABBREVIATIONS

Latin letters

Qty	Unit	Description
A	m^{2}	Area
a	$\mathrm{m}^{2}\ \mathrm{s}^{-1}$	Thermal diffusivity
$A1$	–	Dimensionless ITZ thickness
$A2$	–	Ratio of filler volume fractions
$A3$	–	Ratio of thermal conductivities
C	m^{4}	Roughness power spectrum
c	$\mathrm{J\ kg^{-1}\ K^{-1}}$	Specific heat capacity
C_{V}	$\mathrm{J\ m^{-3}\ K^{-1}}$	Heat capacity per unit volume
D	µm	Particle size (diameter)
D_{C}	m^{2}	Determinant of coefficients
d	mm	Thickness
E	MPa	Young’s modulus
E_{F}	J	Fermi Energy
f_{ACF}	–	Autocorrelation function
h	$\mathrm{W\ m^{-2}\ K^{-1}}$	Thermal conductance
I	–	Iteration
L	µm	(Particle) length
l	m	Mean free path
m	kg	Mass
N	–	Number of possible particle positions
n	–	Number of (…)
$\dot{Q}$	W	Heat flow (magn.)
q	$\mathrm{W\ m^{-2}}$	Heat flux (magn.)
q_{w}	m^{-1}	Wave vector (magn.)
Q_{3}	%	Vol. cumulative particle size distribution
R	$\mathrm{K\ W^{-1}}$	Thermal resistance
R_{p}	–	Roundness
r	$\mathrm{m^{2}\ K\ W^{-1}}$	Specific thermal resistance
r_{p}	µm	Particle size (radius)
R'	–	Rotation matrix
S	–	Sphericity
s	µm	Distance
S_{a}	µm	Arithmetical mean height
S_{al}	µm	Autocorrelation length
S_{q}	µm	Root mean square roughness
S_{sk}	–	Skewness
S_{V}	$\mathrm{\mu m^{-1}}$	Specific surface
S_{z}	µm	Maximum height
T	K	Temperature
t_{x}, t_{y}	µm	Displacement
U	J	Inner energy
u	$\mathrm{m\ s^{-1}}$	Velocity
V	m^{3}	Volume
v	–	Coefficient of variation
$\vec{v}$	–	Orientation vector
x	µm	Coordinate
y	µm	Coordinate
z	µm	Coordinate
z_{th}	µm	Equiv. thermal height

Greek letters

Qty	Unit	Description
α	rad	Rotation angle
α_I	–	Dimensionless thermal interfacial resistance
α_0	$\mathrm{m^2\ K\ W^{-1}}$	Linear fit $r(d)$ - axis intercept
α_1	$\mathrm{m\ K\ W^{-1}}$	Linear fit $r(d)$ - slope
β	rad	Rotation angle
β_sed	–	Level of sedimentation
γ_a	–	Adiabatic index
γ	rad	Rotation angle
δ	–	Particle shift parameter
ε	–	Emissivity
η	Pa s	Viscosity
Θ_D	K	Debye temperature

Qty	Unit	Description
κ	–	Th. cond. (TC) ratio
Λ	–	Thermal conductivity magnification
ν	–	Wetting density
ρ	$\mathrm{g\ cm^{-3}}$	Density
σ_el	$\mathrm{S\ m^{-1}}$	Electrical conductivity
σ_S	µm	RMS surface roughness
σ	var.	Standard deviation
τ_r	s	Relaxation time
τ	–	Level of alignment
ϕ	–	(Filler) volume fraction
Φ	–	Filler loading level
ψ	–	Level of agglomeration
ω	$\mathrm{rad\ s^{-1}}$	Angular frequency

All variables, parameters and indices used within this work are listed. Excluded are special parameters from the referenced literature in chapter 2 and the models in appendix A, which are explained in the respective literature review.

Important indices

app	Apparent
A	Agglomerate
bulk	Bulk material
C	Continuous phase
C	Contact
c	Cold
calib	Calibration
D	Disperse phase
eff	Effective
el	Electron
fit	Fitted
geo	Geometrical
G	Gas
h	Hot
I	Interfacial
ITZ	Interfacial transition zone
K	Kapitza
L	Lower

l	Larger (fractions)
max	Maximum
min	Minimum
p	Particle
ph	Phonon
R	Residual
r	Relative
ref	Reference
RND	Random (uncertainty)
shrink	(Particle) shrinkage
S	Substrate
SYS	Systematic (uncertainty)
TIM	Thermal interface material
tot	Total
th	Thermal
U	Upper

Abbreviations

AMM	Acoustic Mismatch Model
CCP	Cubic Close Packing
DMM	Diffuse Mismatch Model
EMA	Effective Medium Approach
FEM	Finite Element Method
FPS	Filled Polymer to Substrate
FVM	Finite Volume Method
GPU	Graphics Processing Unit
HCP	Hexagonal Close Packing
IMS	Insulated Metal Substrate
IR	Infrared

ITZ	Interfacial Transition Zone
LED	Light Emitting Diode
PPD	Particle-Particle Distance
PSD	Particle-Substrate Distance
RCP	Random Close Packing
RLP	Random Loose Packing
RMP	Random Medium Dense Packing
RNM	Random Network Model
RVE	Representative Volume Element
SCP	Simple Cubic Packing
TIM	Thermal Interface Material

1 INTRODUCTION

1.1 BACKGROUND AND APPLICATIONS

Polymer materials are suitable for numerous applications in a variety of fields due to their good processability, high durability, low price, and low weight. They are among the most adaptable materials and are utilized for diverse tasks. However, there are limits to polymer applications due to their crucial weak point: thermal conductivity.

With $\lambda = (0.1 \ldots 0.5)\ \mathrm{W\ m^{-1}\ K^{-1}}$ [1–4], this is far below that of metallic and ceramic materials. In micro and power electronic systems, heat loss often needs to be transferred to cooling systems or the environment across very small areas and with minimal temperature drops. By using highly thermally conductive materials in the heat path, the system temperature can be sustainably reduced and the service life of the system increased. To employ polymer materials in these applications, they must be modified with highly thermally conductive, granular fillers. Recent review articles report numerous use cases and requirements for thermally conductive filled polymers in electronic applications [2,4–6]. **Figure 1.1** illustrates typical applications of thermally conductive filled polymers in electronics and shows exemplary cross-sections through the material structure.

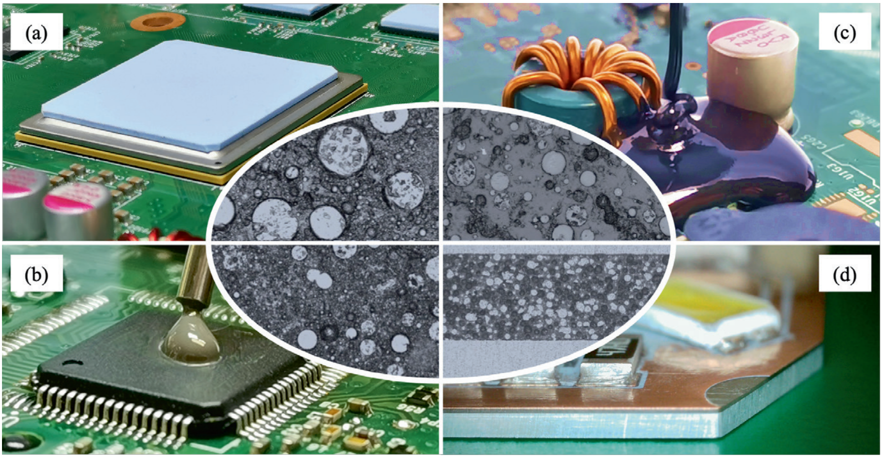

Figure 1.1. Thermally conductive filled polymer applications in electronics.
Thermal interface materials: Thermal pad (a) and thermal grease (b), potting compound (c), and insulated metal substrate (d). The inner illustrations show cross-sections of typical material compositions in the corresponding applications.

Thermal interface materials (TIMs), such as thermal pads (a) or thermal grease (b), are used to optimize thermal transfer between two solids in a heat path. For example, between a chip and a heat sink or, in the automotive sector, a battery module and a cooling unit. Surface roughness and manufacturing tolerances of the two contact partners lead to poor thermal contact and air inclusions. Soft and elastic thermal interface materials can displace this air and thus optimize thermal transfer. A review of materials, established technologies, applications, and recent advances is given in [5,7–11]. In part (c) of **Figure 1.1** a potting or encapsulant is shown. The main purpose of these materials is to protect the electronic assembly from environmental impact, while guaranteeing good heat dissipation. Shen and Feng [12] published an extensive review on the recent advances in encapsulants for light emitting diodes (LEDs) in 2023.

As a last example, an insulated metal substrate (IMS) is presented in part (d) of **Figure 1.1**. Electronic components with large power densities, such as LEDs, require a circuit board with good heat spreading characteristics. An IMS is a layered structure consisting of an aluminum or copper base plate, a thin dielectric intermediate layer, and a thin copper layer into which the circuit paths can be inserted. While copper and aluminum provide outstanding thermal conductivities, the dielectric layer in between is always the bottleneck for heat dissipation. The basis is usually an epoxy polymer, modified with ceramic filler particles. The layers are kept very thin, often less than $100\ \mu\mathrm{m}$, to ensure that the thermal resistance is as low as possible. The structure, requirements, applications, and current advances in IMS are described in [13–15].

Thermally conductive fillers are not only used for polymers in the applications shown. Other examples are injection-molded casings or heat sinks [16–18], or thermally conductive adhesives [19].

The use of thermally conductive polymers in all those applications has been established for decades. Recent market research reports a large increase in market volume of thermally conductive filled polymers and predicts further significant growth until the beginning of the 2030s. This is primarily due to the increasing digitalization and simultaneous miniaturization of electronic systems [6]. For thermal interface materials a compound annual growth rate of $10.49\ \% - 21\ \%$ is predicted [20–23]. The market growth for pottings and IMS is assumed at an annual rate of $3.9\ \% - 6.15\ \%$ [24–27]. For thermally conductive compounds, an annual growth of $12.8\ \%$ is predicted [28].

1.2 OBJECTIVE AND METHODS

The targeted and efficient development of advanced, high-performance polymer composites requires a profound understanding of the heat transport processes in the materials. From afar, it seems to be obvious and is well known that thermal conductivity increases with the concentration of highly thermally conductive fillers and that in principle, more thermally conductive base materials enable higher effective thermal conductivities [29]. It follows that it is crucial how effectively the filler particles can form a thermally conductive network in the polymer matrix. This ability probably depends on many factors, such as particle shape, size distribution and dispersion. The exemplary cross-sections in **Figure 1.1** show the complexity and versatility of the material structures. For thermal interface materials, shown in part (a) and part (b), multi-scale filler blends with grain sizes in different orders of magnitude are used to achieve the highest possible filler volume fractions. The result is a highly complex microstructure with filler concentrations close to the maximum packing density. Pottings (c) require good flowability for processing, i.e., a low viscosity, thus the possible filler volume fraction is very limited. In these loose filler packings, agglomeration and sedimentation phenomena are favored. With IMS, the complexity of the microstructure increases because of the two contact surfaces of the metal layers above and below the dielectric layer. Often only a few particle layers are between the contact surfaces. This influences the overall packing structure.

Numerous recent review articles conclude that there are still many open questions and unexplored relationships, especially with regard to the microscopic filler packing structure [2,4,5,19,29,30]. The most concise conclusions were formulated by Burger et al. in 2016 [29],

> *"Nevertheless, it will be crucial to focus in future work on the structural and geometrical aspects of the materials, which are essential parameters to increase thermal conductivity."*

and Xu et al. in 2021 [5],

> *"For the critical thermal percolation [...], existing knowledge is still very limited and a universal picture about the threshold of the thermal percolation is still lacking. Open questions remain on how to form a more effective heat conduction network with less thermal resistances between fillers."*

There remain questions regarding whether there are pronounced percolation effects in thermally conductive filled polymers and how the formation of thermally conductive paths in the material can be favored [3,5,30]. Furthermore, Yang et al. [6] see a need to improve and expand existing approaches for calculation and simulation, as these have so far neglected many important parameters. In principle, however, detailed simulation and calculation approaches promise important insights into the microscopic heat transport processes and can help answer the open questions. With this as a basis, the present work is intended to make a decisive contribution to the development of a detailed and comprehensive understanding of microscopic heat transport processes in filled polymers. The aim is a detailed investigation and quantification of the effects of filler properties, geometric packing structure, and interactions of different fillers in mixtures. The focus is on the effective thermal conductivity of the particle-filled polymer and filled polymer to substrate (FPS) transitions, which are of exceptional importance in IMS, for example. Both phenomena are investigated experimentally and using newly developed simulation methods.

Experimental techniques are mainly used to access macroscopic material properties. Since the spatial resolution of simulative approaches is unlimited in principle, these techniques allow analyses at the microscopic level which may then help explain macroscopic observations. Local heat transport processes inside the materials can be analyzed that are not experimentally accessible. Experimental, and simulative investigations combine to allow derivation of empirical theories on the impact of the geometric microstructure of filled polymers on their heat transport properties. This is a common strategy used also in particle physics, as the numerical reconstruction of processes can reach spatial and time scales for which there are no experimental techniques yet available.

Chapter 2 begins with a discussion of the physical principles of heat conduction in solids and composites. Thermal interfacial and thermal contact resistances are introduced and discussed regarding their significance for filled polymers. A comprehensive summary of the current knowledge and state of the art of thermally conductive filled polymer composites are presented. Chapter 3 provides an overview of the polymers and fillers used in the experimental investigations. Additionally presented is an overview of the two main measurement methods: the steady-state cylinder method and the newly developed micro thermography method. Chapter 4 includes numerical and experimental studies on the impact of filler properties and packing structures on the effective thermal conductivity of single scale filled polymers. The newly developed microscale modeling method used for these investigations is introduced at the beginning. Chapter 5 deals with the analysis of multiscale filled polymers with an emphasis on the interaction of different fillers at different scales. Once again, both experimental and numerical studies are presented. Chapter 6 focuses on FPS transitions and the contact resistances that occur using new experimental and simulative methods. Chapter 7 summarizes the findings and completes the comprehensive picture of heat conduction in particle-filled polymers.

2 PHYSICAL BASICS OF HEAT CONDUCTION

This introductory chapter provides an overview of the physical mechanism of heat conduction, first in solids and later in composites. In addition, it explains the phenomenon of thermal contact resistance and the resulting need for thermal interface materials. Thermal interface materials are a major area of application for the investigations and findings of this thesis. The chapter finishes with a brief overview of the current advances in the development of thermally conductive polymer composites.

2.1 HEAT CONDUCTION IN SOLIDS

In physics, there are various mechanisms of heat transport including: heat conduction through matter, heat transport through mass transport, and heat radiation. The basics of heat conduction in matter, and particularly in solids, are discussed below. Heat conduction is the transport of thermal energy through matter, mainly by diffusion of internal energy when a driving temperature gradient is imposed. In 1822, Fourier formulated the proportionality known today as Fourier's law [31]

$$\boldsymbol{q} = -\lambda\ \boldsymbol{\nabla} T \tag{2.1}$$

between the conducted heat flux $\boldsymbol{q}$ (vector) and the applied temperature gradient $\boldsymbol{\nabla} T$. According to the second law of thermodynamics, heat will always flow against the temperature gradient. The proportionality constant between heat flux and temperature gradient in Fourier's law is known as thermal conductivity. Thermal conductivity λ (second-order tensor in **Eq. (2.1)**) is an intrinsic thermophysical property of the heat conducting matter, nowadays specified with

$$[\lambda] = \mathrm{W\ m^{-1}\ K^{-1}}\ . \tag{2.2}$$

In general, it is a temperature dependent quantity [32,33], and can also depend on applied pressures, particularly for compressible matter [33]. The temperature dependence is often ignored when small temperature differences are applied [32]. Furthermore, thermal conductivity can be an anisotropic material property.

The theory of heat conduction in solids has been worked out in detail and is widely accepted. It is part of the basic repertoire of modern solid-state physics and is described in detail in numerous textbooks [34–37]. As the theory is very complex and multifaceted, there is additional specialized literature focusing solely on thermal conductivity [38–40]. Given here is a rough and simplified introduction to the topic for the purpose of assessing the differences in thermal conductivities of the polymer matrices and the metallic and non-metallic fillers and evaluating the heat transfer across the interface from matrix to particle. Heat transfer through solids cannot be depicted using generally applicable models [41] and there is no possibility for an exact prediction of thermal conductivity [40]. Nevertheless, a general impression and comprehension of the relationships can be acquired by discussing different basic approaches and models. To begin, a short introduction is given using the simple example of an ideal gas, before continuing with heat conduction in solids. A very helpful derivation can be performed, based on the theory of ideal gas molecular motion, following e.g., [33,35,41].

All particles of the gas are handled as point masses, perform a disordered thermal motion, and collide perfectly elastic with each other. The precondition for the validity of the following consideration is the existence of a sufficient number of individual particles for the thermodynamic equilibrium. The average time between two collisions of a particle is τ_r and the average absolute velocity of all particles is u. τ_r is sometimes referred to as relaxation time. The mean free path, the average distance a particle can travel freely, is [41]

$$l = u\tau_\mathrm{r} \ . \tag{2.3}$$

To induce one-dimensional heat conduction in the x direction, a temperature difference $\Delta T = T_2 - T_1$ with $T_1 > T_2$ is applied at the distance $\Delta x = x_2 - x_1$. On average, $1/3$ of all particles move in x direction and contribute to the heat conduction. The position $x_1 < x < x_2$ is considered. Particles that reach this position with positive velocity had their last collision at position $x - u\tau_\mathrm{r}$, and particles that reach this position with negative velocity had their last collision at position $x + u\tau_\mathrm{r}$. Let $U(T)$ be the temperature-dependent internal energy per particle. Then the particle with positive velocity brings the higher energy $U(T(x - u\tau_\mathrm{r}))$ and the particle with negative velocity brings the lower energy $U(T(x + u\tau_\mathrm{r}))$ to position x. To calculate the net heat flux q_x at the position x, the energies transferred by individual particles must be added together and multiplied by the mean particle velocity u and the number of particles n per Volume V.

$$q_x = -\frac{1}{6}\frac{n}{V}u\left[U\big(T(x + u\tau_\mathrm{r})\big) - U\big(T(x - u\tau_\mathrm{r})\big)\right] \ . \tag{2.4}$$

The sign determines the direction of the heat flow and the pre-factor $1/6$ considers that on average $1/3$ of all particles move in the x direction. $1/2$ each in the positive and negative x direction. If τ_r and thus l are small, q_x can be written as in [35]

$$q_x = -\frac{1}{6}\frac{n}{V}u\frac{\mathrm{d}U}{\mathrm{d}T}\frac{\mathrm{d}T}{\mathrm{d}x}2u\tau_\mathrm{r} \ . \tag{2.5}$$

$\frac{n}{V}\frac{dU}{dT} = C_\mathrm{V}$ is the heat capacity per unit volume and $\mathrm{d}T/\mathrm{d}x$ the local temperature gradient in x direction. After substitution and rearrangement, the equation becomes

$$q_x = -\frac{1}{3}C_\mathrm{V}u^2\tau_\mathrm{r}\frac{\mathrm{d}T}{\mathrm{d}x} \ . \tag{2.6}$$

A comparison with Fourier's law in one-dimensional notation

$$q_x = -\lambda \frac{\mathrm{d}T}{\mathrm{d}x} \; , \tag{2.7}$$

results in a thermal conductivity [33,35,41]

$$\lambda = \frac{1}{3} C_\mathrm{V} u^2 \tau_\mathrm{r} \; . \tag{2.8}$$

Finally, $u\tau_\mathrm{r}$ can be replaced with **Eq. (2.3)**, resulting in

$$\lambda = \frac{1}{3} C_\mathrm{V} u l \; , \tag{2.9}$$

as a general model for the thermal conductivity of an ideal gas, when considering the free gas molecules as the carriers of heat.

In solids, different carriers contribute to heat conduction. The main carriers are lattice waves and electrons. Less dominant carriers are magnetic excitations, spin waves, and radiation [40,42,43]. In non-metallic solids without any free electrons, the lattice waves dominate and are often the only noticed carriers [33,38,40,42,44]. In metallic solids, the electron contribution to heat conduction can predominate [33,40,42,44]. The total thermal conductivity can be generally expressed as the sum

$$\lambda = \frac{1}{3} \sum_i C_{\mathrm{V},i} u_i l_i \tag{2.10}$$

of all contributions, adapted from **Eq. (2.9)**. The subscript i stands for the respective carrier (electrons, lattice waves, $\ldots$). $C_{\mathrm{V},i}$ is the heat capacity per unit volume due to the carrier i, u_i is the velocity of the carrier, and l_i its mean free path. At least velocity and mean free path for the different carriers are not as clearly defined as for gases. Models must be found to approximate them. In the following section, the thermal conductivity of non-metallic solids, metallic solids, and the special case of polymers are discussed.

2.1.1 NON-METALLIC SOLIDS

In contrast to the atoms of a gas, the atoms of a solid do not move freely but have a fixed equilibrium position. Many solids have a crystalline structure with a regular lattice [36]. The atoms perform thermal oscillations around their equilibrium position. As the temperature rises, the internal energy and thus the vibrational energy of the solid increases. Since the atoms are closely coupled, a temperature increase on one side of the solid and thus an increase in vibrational energy is transported further in the body by lattice waves. Lattice waves are primarily structure-borne sound waves that propagate through the solid body. In 1932, Frenkel introduced the term "phonons" for the energy quanta transported by these waves [45]. To simplify, the phonons can be imagined as free gas particles. They move through the lattice, transporting a certain thermal energy at a specific velocity and over a certain mean path. This idea supports the use of the **Eq. (2.9)** or **(2.10)** to describe the lattice contribution λ_{ph} to the overall thermal conductivity. The objective quantities of the following discussion are therefore the heat capacity of the lattice waves, their propagation velocity, and their mean free path. Comprehensive descriptions of the theoretical foundations and models developed over the decades can be found in [38–41,43,46]. Brief summaries of the key aspects are presented in [42,44,47]. Such a description is also provided here for introductory purposes.

The lattice waves occur in a broad frequency spectrum. The wavelength of the occurring vibration modes starts at atomic dimensions and extends to long waves comparable to the external dimensions [42]. Of particular interest are the propagating modes. To consider the specific contribution of the individual angular frequencies ω, the basic **Eqs. (2.9)** or **(2.10)** can be generalized to [42]

$$\lambda_{\mathrm{ph}} = \frac{1}{3}\int_0^{\omega_{\mathrm{D}}} C_{\mathrm{V,ph}}(\omega) u_{\mathrm{ph}} l_{\mathrm{ph}}(\omega)\,\mathrm{d}\omega \tag{2.11}$$

using the Debye theory [48] in good approximation. Strictly taken, a differentiation of the polarization should also be taken into account [46]. For a general discussion of the relationships, however, **Eq. (2.11)** will suffice. Frequencies up to a cutoff value ω_{D}, called Debye frequency, are considered [37,41,42,46]. It is selected to include $3N$ modes, with N being the number of atoms per unit volume. In the simplest form, u_{ph} is the velocity of sound averaged over the transverse and longitudinal velocities [41]. $C_{\mathrm{V,ph}}(\omega)\ \mathrm{d}\omega$ is the specific heat contribution of the corresponding frequency interval with [42,49]

$$C_{\mathrm{V,ph}}(\omega)\ \mathrm{d}\omega = 9Nk_{\mathrm{B}}\left(\frac{T}{\Theta_{\mathrm{D}}}\right)^3 \frac{x^4 e^x}{(e^x-1)^2}\ \mathrm{d}\omega\ , \tag{2.12}$$

where k_{B} is the Boltzmann constant, T the absolute temperature, Θ_{D} the Debye temperature of the solid, and $x = \hbar\omega/k_{\mathrm{B}}T$, with $\hbar$ being the Planck constant divided by 2π. The Debye temperature is [37]

$$\Theta_{\mathrm{D}} = \frac{\hbar\omega_{\mathrm{D}}}{k_{\mathrm{B}}} = \frac{\hbar u_{\mathrm{ph}}}{k_{\mathrm{B}}}\sqrt[3]{\frac{6\pi^2 N}{V}} \tag{2.13}$$

for a crystal with N oscillators (atoms) in the volume V. Even though the Debye model for specific heat only provides a rough approximation, it is regularly used, as the influence of the uncertainties in the determination of the mean free path is much greater [42,46]. If there were infinite ideal crystals, with perfectly regular structures and harmonic interatomic forces, the mean free path and thus the thermal conductivity would be infinite [46]. In real solids, there are barriers that limit the mean free path and thus limit heat transport. There is scattering caused by the collisions of phonons with impurities, crystal defects, grain boundaries, and external boundaries [41]. The phonons are scattered from one mode into another [46]. Anharmonicity in real crystal lattices additionally causes phonon-phonon collisions. However phonon-phonon collisions do not necessarily contribute to limiting the mean free path [36]. If a normal process (N-process) occurs, neither momentum nor energy flow is affected. In 1929, Peierls [50] showed that, in addition to N-processes, there are also Umklapp-processes (U-processes) that lead to an intrinsic resistance, since the direction of the energy flow changes after the phonon-phonon collision (German: umklappen, English: to flip over). The lattice absorbs momentum [36]. As given in **Eq. (2.11)**, the limited mean free path is a function of the frequency and generally also of the temperature $l_{\mathrm{ph}}(\omega, T)$ [36,38,40,46]. Thus, the specific heat $C_{\mathrm{V,ph}}$ and the mean free path l_{ph} are temperature-dependent, resulting in a strongly temperature-dependent lattice component of thermal conductivity $\lambda_{\mathrm{ph}}(T)$.

The influence of temperature on the specific heat is particularly evident at very low temperatures $(T < \Theta_{\mathrm{D}}/3)$ in a T^3 dependency. At high temperatures $(T > \Theta_{\mathrm{D}})$, the heat capacity is approximately constant. At low temperatures, the influence of boundary collisions increases as the low frequencies become more dominant [44]. The mean free path can be limited by the dimensions of the sample [36,42]. As the effects of low temperatures are strongly pronounced, this range is in focus of certain specialized work [51,52]. In general, the thermal conductivity in this range increases with temperature. The thermal conductivity then reaches its maximum in the intermediate temperature range before decreasing again due to the growing influence of defect and impurity scattering [38,41,43]. The mean free path decreases stronger than the heat capacity increases. Further increasing temperatures increase the probability of phonon-phonon collisions and cause the thermal conductivity to drop further, approximately proportional to T^{-1} in the high temperature range [41,42].

The discussion thus far has been limited to crystalline solids with long-range order in structure. However, glasses and many polymers do not have long-range order. Section 2.1.3 is explicitly dedicated to polymers. For the sake of completeness, however, a few general connections will be made here.

Amorphous structures tend to have lower thermal conductivities than crystals [39,41]. Theories for predicting the thermal conductivity of amorphous solids emerged long after the fundamental theories for crystalline solids [33,42]. However, it was established early that the assumption of a constant, temperature-independent mean free path is sufficiently good, at least in the range of ordinary (e.g., room temperature) and high temperatures [41,42]. The mean free path in amorphous solids is closely linked to the structural length units of the solids [38,41]. In polymers, these are the building blocks of the polymer chains.

2.1.2 METALLIC SOLIDS

In metallic solids, heat can also be transported via lattice waves as in the non-metallic solids mentioned previously, however the contribution from free electrons as carriers of heat is just as important. In the case of pure metals, the contribution of the electrons λ_{el} can significantly exceed the contribution of the lattice waves λ_{ph}. Alloy thermal conductivity always depends on which elements are added and in what quantities, as well as the conductivity of the parent material. At ordinary and high temperatures, the contribution of the lattice becomes more important the worse the parent material conducts electricity [53].

We can model free electrons in metals as a free electron gas [36]. Again, we can adapt the general formulation from **Eq. (2.10)** [33,36,38,41,53]

$$\lambda_{\mathrm{el}} = \frac{1}{3} C_{\mathrm{V,el}} u_{\mathrm{el}} l_{\mathrm{el}} \ , \tag{2.14}$$

and consider the specific heat of the gas particles $C_{\mathrm{V,el}}$, their velocity u_{el}, and the mean free path l_{el} they can travel between two collisions. While the electrons are much faster than the phonons $u_{\mathrm{el}} \gg u_{\mathrm{ph}}$, typically two or three orders of magnitude faster, the electron specific heat is smaller than the lattice contribution to specific heat [41]. Considering a Fermi gas, the specific heat of the electrons is [38,41]

$$C_{\mathrm{V,el}} = \frac{\pi^2}{2} \frac{k_{\mathrm{B}}^2 T}{E_{\mathrm{F}}} n_{\mathrm{el}} \ , \tag{2.15}$$

where n_{el} is the electron density and E_{F} is the Fermi energy. If

$$u_{\mathrm{el}} = \sqrt{\frac{2E_{\mathrm{F}}}{m_{\mathrm{el}}}} \tag{2.16}$$

with m_{el} being the electron mass, is then set for the velocity of the electrons in a Fermi gas [38,41], the only unknown is again the mean free path l_{el}. The same factors must be considered as with phonons. Collisions between electrons or collisions with phonons, as well as scattering at grain boundaries, imperfections, and defects limit the mean free path [43,53]. The contribution of the electrons to the thermal conductivity also depends on the temperature. Zhang et al. [33] describe a linear increase with temperature in the low temperature range, a constant contribution in the intermediate range and a slight decrease with temperature at high absolute temperatures. If first **Eq. (2.3)** and then **Eqs. (2.15)** and **(2.16)** are put into **Eq. (2.14)**, the thermal conductivity of an electron gas is obtained as a function of the relaxation time $\tau_{\mathrm{r,el}}$ [41]

$$\lambda_{\mathrm{el}} = \frac{\pi^2}{3} \frac{k_{\mathrm{B}}^2}{m_{\mathrm{el}}} n_{\mathrm{el}} T \tau_{\mathrm{r,el}} \ . \tag{2.17}$$

Since the carriers are the same, the theory of the mean free path and thus of the relaxation time is the same as for electrical conductivity. This can be expressed as [38,41]

$$\sigma_{\mathrm{el}} = \frac{n_{\mathrm{el}}}{m_{\mathrm{el}}} e^2 \ \tau_{\mathrm{r,el}} \ , \tag{2.18}$$

where e is the elementary charge. If the thermal (**Eq. (2.17)**) and electrical conductivity (**Eq. (2.18)**) are set in relation, one obtains with [38,41]

$$\frac{\lambda_{\mathrm{el}}}{\sigma_{\mathrm{el}}} = \frac{\pi^2}{3} \left(\frac{k_{\mathrm{B}}}{e} \right)^2 T = L \ T \tag{2.19}$$

the proportionality between thermal and electric conductivity of metals. This relationship that Wiedemann and Franz have already found empirically is known as the Wiedemann-Franz law. $\lambda_{\mathrm{el}}/(\sigma_{\mathrm{el}} T)$ is a constant, only depending on two natural constants and is called the Lorentz number with [53]

$$L = 2.443 \times 10^{-8} \ \mathrm{V}^2 \ \mathrm{K}^{-2}. \tag{2.20}$$

For $T > \Theta_{\mathrm{D}}$, good agreement with experimental values is reported [37,41].

2.1.3 POLYMERS

Polymers have a comparatively low thermal conductivity. The aim of this section is to assess the reasons for their low thermal conductivity and to identify opportunities for optimization besides the use of thermally conductive fillers. There are numerous applications for which elevated thermal conductivity of polymers is interesting, independent of the use of fillers [54]. However, the potential is highly limited due to polymers' fundamental structure. The different types and structures of polymer materials make it highly challenging to apply universal theories, given the close structure-property relationships. To a certain extent however, we can refer back on the phonon theory presented in section 2.1.1 and discuss expected influences. Heat transport in polymers mainly happens along polymer chains [55]. These individual chains can even have an outstanding thermal conductivity of several hundred W m^{-1} K^{-1}, exceeding that of many metals [54,56,57]. In polymer bulk materials though, the thermal conductivity drops significantly. Wei et al. [54] therefore discuss the thermal conductivity of bulk materials separate to that of thin fibers with aligned chains in their recent review.

Many polymers have amorphous or semi-crystalline structures and therefore no regular lattice that could effectively contribute to thermal transfer. Lattice waves in the actual sense thus occur only in crystalline subregions. Nevertheless, the concept of phonons is also used for polymers, even though it is only to be understood symbolically. The fact that the individual polymer chain itself has a very high thermal conductivity shows that it cannot be the specific heat or the propagation speed limiting the thermal conductivity to this extent.

Both cannot significantly change from single chain to bulk material [2]. Once again, it must be the mean free path that determines the thermal conductivity of the bulk material. As already discussed in section 2.1.1, there are numerous internal and external influences and defects that lead to the scattering of phonons and thus limit the mean free path. In crystalline polymers, these are still impurities, defects, dislocations, boundaries, and domain interfaces [2,5,54]. In amorphous polymers, the chains are randomly oriented and entangled, only bound by weak van der Waals forces. This limits the mean free path to a length smaller than a single polymer chain [2]. Branched polymer chains also lead to increased phonon scattering compared to straight chains [56]. In amorphous domains, the heat cannot be transported through the grid in a straight line, but rather takes random, diffuse paths [6]. If the structure is crystalline, or at least partially crystalline, it is generally reflected in higher thermal conductivities [2]. The high thermal conductivity of the individual chains is mainly due to strong covalent bonds in the polymer backbone. Crosslinking several polymer chains with covalent bonds to an effective conducting polymer network increases the overall thermal conductivity [3]. There are possible approaches being pursued to align individual domains or the entire polymer [3,54,57]. Nanoscale templating or electrospinning are options [3]. However, great success has also been achieved by mechanical methods like stretching the polymer. The result is a strongly anisotropic structure with outstanding thermal conductivity in the stretch direction [3]. In addition to structural modifications of a polymer to increase its thermal conductivity, the use of micro and nano fillers has been established. This method is the subject of the present work.

2.1.4 EFFECT OF POROSITY

After the purely molecular considerations in the previous chapters, this concluding section will provide some reflections on macroscopic porosity. The filler particles used and filled polymers can be porous to a certain extent, which has a considerable effect on thermal conductivity. If the pores in the solid are filled with a poorly conducting gas, there will always be a reduction in thermal conductivity [33]. The effect of porosity on the thermal conductivity of a solid was comprehensively investigated experimentally [58–61], theoretically [62–64], and with numerical simulations [65]. A very thorough study and summary of these effects was published by Smith et al. in 2013 [66].

When heat is conducted through a porous material, heat paths are created in parallel through the remaining solid and through the gaseous phase. With closed pores, there are only local parallel paths through the gas in the pores. The gas generally has a lower thermal conductivity, which can be additionally reduced by the Knudsen effect in the case of very small pores. With open-pored materials, there are continuous gas paths. Heat can be conducted in the pores, transported via radiation, or transported via convection, when the pore sizes are sufficiently large [66]. When the pores are very small, they reduce the mean free path of the bulk material therefore reducing its thermal conductivity [64].

2.2 THERMAL TRANSFER ACROSS INTERFACES

If heat is conducted via the interface between two dissimilar materials, a temperature drop occurs not only in the two bulk materials due to their finite thermal conductivity. A temperature drop ΔT_I is also observed at the interface. The interface forms a specific thermal interfacial resistance

$$r_\mathrm{I} = \frac{\Delta T_\mathrm{I}}{q} = h_\mathrm{I}^{-1} \tag{2.21}$$

to the heat flux q. A specific thermal resistance r, also referred to as thermal insulance or thermal impedance, is specified by the units $\mathrm{m}^2\ \mathrm{K}\ \mathrm{W}^{-1}$. With division by the effective heat-transferring area A, the absolute thermal resistance

$$R = r\ A^{-1} \tag{2.22}$$

with the units $\mathrm{K}\ \mathrm{W}^{-1}$ is obtained. A thermal interfacial resistance r_I, sometimes also specified by a thermal interfacial conductance h_I, occurs not only with poor surface contact due to macroscopically perceptible roughness and surface mismatch, but also with two solids that lie perfectly on top of each other at the atomic level [47]. This effect is particularly interesting for this work because heat in filled polymers must always cross the interface between filler particles and the surrounding polymer several times.

The effect was first described by Kapitza in 1941 (reprint 1971 [67]). Kapitza investigated heat transport in liquid helium II at low temperatures and found a thermal interfacial resistance towards copper. Thermal interfacial resistance, or Kapitza resistance, has since been the subject of numerous research projects and demonstrated for various material combinations. A comprehensive overview of the current state of knowledge, experimental findings, and calculation techniques was published by Giri and Hopkins in 2020 [68]. According to Giri and Hopkins [68], typical specific thermal interfacial resistances are in the range of $3 \cdot 10^{-9}\ \mathrm{m}^2\ \mathrm{K}\ \mathrm{W}^{-1}$ up to $5 \cdot 10^{-8}\ \mathrm{m}^2\ \mathrm{K}\ \mathrm{W}^{-1}$ for crystalline solids with phonon-dominated heat conduction. Giri and Hopkins further highlight a work by Swartz and Pohl from 1989 [69], which presents numerous experimental studies conducted up to that time as well as a comprehensive theoretical discussion of the phenomenon. They reported on methods for predicting interfacial resistances.

The first model, introduced by Khalitnikov in 1952 [70] and extended for solid-solid interfaces in 1959 by Little [71], is the acoustic mismatch model (AMM). The AMM is the most fundamental model, the validity of which is often only shown for low temperatures. However, Khvesyuk et al. [72] point out that nanoscale analyses are also valid at higher temperatures. In the AMM, both solids are considered as a perfect continuum and only the interface is considered as an imperfection. The phonons are abstracted as plane waves whose transmission probability at a planar interface can be calculated based on the acoustic properties of the solids. Phonons hitting the surface can be specular reflected, reflected and mode converted, refracted, or refracted and mode converted. The transmission probability is the fraction of the transmitted energy of all these cases [69]. An example of the calculation guidelines is given in [68,69]. The more similar the acoustic impedance of the materials, the higher the probability of transmission. If the materials have significantly different impedances, the model assumes a low transmission probability.

Another model, the diffuse mismatch model (DMM), was proposed by Swartz and Pohl [69,73]. This model considers diffuse scattering of phonons at an interface. The model is therefore generally more suitable for estimating the interfacial resistance at rough surfaces and at elevated temperatures [74]. Both models assume that at least one contact partner is electrically insulating, as they both account for elastic phonon transport. However, there are variations of the DMM that can be used for electron-dominated heat conduction at interfaces [68]. Over the years, further models and extensions have been developed, and first-principle methods, as well as atomistic simulations have been applied, e.g., [68,72,75,76]. In filled polymers, thermal interfacial resistances occur between filler particles and the polymeric matrix. Their impact on the effective thermal conductivity is discussed in section 2.4.2.

2.3 THERMAL CONTACT RESISTANCE

After the thermal resistance at a perfect surface contact of two dissimilar solids was discussed in the previous chapter, this chapter deals with thermal resistance at imperfect surface contacts. First, solid-solid contacts are discussed, followed by an introduction to the state of the art in thermal interface materials (TIMs). These are used to optimize the heat transfer between two solid surfaces. This results in the need to discuss thermal contact resistances of solid-liquid contacts.

2.3.1 SOLID-SOLID CONTACT RESISTANCE

Technical surfaces are not ideally smooth and even. This means that when two surfaces touch, only a fraction of the nominal surface is realistically in contact. In [74,77], a proportion of $1\ \% - 2\ \%$ of the surface is given as a general guide. Between the non-contacting surface areas there is a filling gas, most commonly air. The gas is a poor conductor of heat, resulting in a clearly perceptible thermal contact resistance between the surfaces [5,74,77,78]. A brief review of the literature is enough to recognize that this contact resistance is of a completely different order of magnitude than pure interfacial resistance. The phenomenon takes place on a totally different length scale. The specific contact resistances in [78] are in the range of $10^{-5}\ \mathrm{m^2\ K\ W^{-1}}$ up to $10^{-2}\ \mathrm{m^2\ K\ W^{-1}}$ and thus 3 to 7 orders of magnitude higher than the thermal interfacial resistances in [68]. **Figure 2.1** illustrates the heat transfer between two solids and the temperature differences occurring at the contact if only interfacial resistance occurs and alternatively if microscopic roughness causes a thermal contact resistance. The comparatively small temperature drop ΔT_{I} occurring at the interface between to dissimilar solids, but with perfect surface contact (a) has already been discussed in chapter 2.2. In part (b) of **Figure 2.1**, the significantly higher temperature drop ΔT_{C} at an imperfect contact between two rough surfaces is illustrated. It is the result of a specific thermal contact resistance r_{C}. Equivalent to equation **(2.21)** this can be expressed as

$$r_{\mathrm{C}} = \frac{\Delta T_{\mathrm{C}}}{q} = h_{\mathrm{C}}^{-1} \ , \tag{2.23}$$

where q is the one-dimensional steady-state heat flux crossing the contact and ΔT_{C} is the occurring temperature drop occurring at the specific thermal contact resistance r_{C}. The reciprocal value of the specific contact resistance is referred to as thermal contact conductance h_{C}. Part (c) of **Figure 2.1** illustrates the microscopic reason for the occurring thermal resistance. In the illustrated section, there are only three contact points between the two surfaces. The heat flow (indicated by qualitative heat flow lines) is concentrated at these contact points. This results in constriction and reduction of the heat-transferring area. Even though the phenomenon is now considered to be well understood, it is difficult to study quantitatively due to the many parameters involved (contact partners, surface structure, contamination, filling gas, temperature, surface pressure), and high randomness [79]. According to [80,81], the experimental determination of thermal contact resistances is associated with high uncertainties. Shojaefard and Goudarzi 2008 [82] state that the many different measurement methods used often lead to significantly different results.

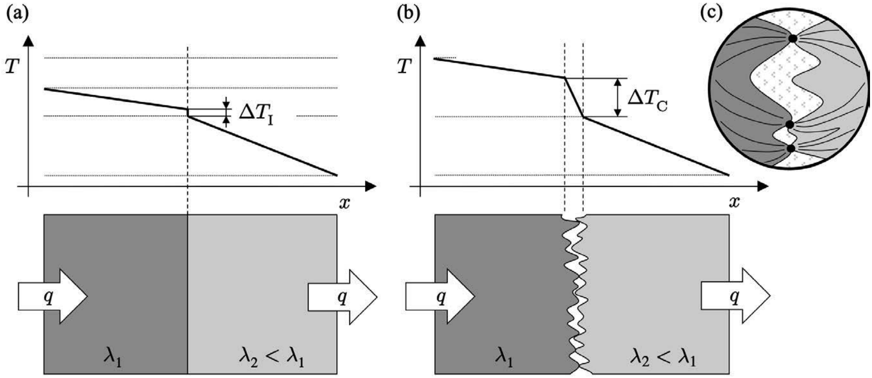

Figure 2.1. Comparison of thermal interfacial resistance and thermal contact resistance.

Temperature profile along the heat flow direction when two ideally smooth solids come into contact (a), and temperature profile along the heat flow direction when two microscopically rough solids come into contact (b). Schematic representation of the heat flux concentration at the contact points (c).

Different boundary conditions during the measurement, such as temperatures and temperature gradients, time-dependent effects, surface pressure, sample size and the resulting surface contact vary and limit the comparability. From today's point of view, the most pioneering work in predicting thermal contact resistances was done by Yovanovich and coworkers as well as Madhusudana, summarized in [74,77,78]. In addition, there have been several theoretical [83,84], experimental [79,82,85–98], and numerical [85,87,99–105] studies on the subject over the past decades. All have contributed to the general understanding of the phenomenon and the broad database available today. A general summary shows that thermal contact resistances between two solids decrease with contact pressure and temperature [79,82,85–88,90–93,96,97,102–105]. In addition, a drop in thermal contact resistance with increasing thermal conductivity of the solids was reported [87,100].

It is obvious that thermal contact resistance is not a purely thermal phenomenon. Contact mechanics and surface geometry also have a decisive influence. Yovanovich [78] refers to it as the triad of thermal contact conductance. It is important to know the exact surface geometry and how the asperities of the surfaces deform when the solids are joined. This is the only way to estimate the actual contact area. Experimental studies have shown that multiple, cyclical joining of the solids can lead to a reduction in contact resistance [78,85,89]. The asperities of the surfaces deform more and more, and the two surfaces adapt better to each other in a stepwise fashion. Thus, larger contact areas are established and the mean gap width decreases. However, this effect cannot be used continuously. After a few cycles, saturation occurs.

An increase in thermal contact resistance with surface roughness has been reported several times [98,99,103], but could not be proven in e.g., [90]. Numerical studies usually deal with the phenomenon on several scales [99,102], and sometimes also combine different simulation methods on the different scales [102]. A good way to achieve realistic results is to model the rough surfaces on the basis of microscopic images or topography data [87,99].

In most theoretical models, two or more parallel heat paths across the contact surface are taken into account: Solid heat conduction across the contacting asperities, gas heat transfer in the gaps, and sometimes also a radiative contribution. Commonly, the total specific thermal contact resistance r_C is expressed as the reciprocal sum of all contributing thermal resistances r_i. Equivalently, the total thermal contact conductance h_C can be specified as the sum of the individual conductances h_i. It can be written as

$$r_\mathrm{C}^{-1} = r_\mathrm{S}^{-1} + r_\mathrm{G}^{-1} = h_\mathrm{C} = h_\mathrm{S} + h_\mathrm{G} \ , \qquad \textbf{(2.24)}$$

where the index S indicates the solid heat path, i.e., heat conduction via the contacting asperities, and the index G indicates the gas path, i.e., heat transfer via the gas inclusions. An additional radiation path is usually neglected at ordinary temperatures [77,78]. Appendix A.1 provides the Cooper-Mikic-Yovanovich (CMY) model [78,106], a very popular model for determining the solid contribution to contact conductance h_S. In addition, appendix A.2 provides a statistical model, developed by Yovanovich et al. [107], for calculating the gap conductance h_G between two conforming rough surfaces. These two models give an impression of the origin of thermal contact resistance and the parameters that influence it.

2.3.2 USE OF THERMAL INTERFACE MATERIALS

The phenomenon of contact resistance has been known for a long time and is a serious problem in many technical applications. In electronic applications, they considerably increase the thermal resistance of heat dissipation paths and thus lead to higher operating temperatures [108]. Thermal interface materials (TIMs) have therefore been established, particularly in the field of micro and power electronics, but also in several other applications, such as electric vehicles, aircrafts, satellites, and radar systems [5]. There are several different types of TIMs, all serving the same purpose: Replacing the air in the cavities of a solid-solid-contact and thus optimizing thermal transfer between the surfaces, see **Figure 2.2**. The higher the thermal conductivity and the thinner the TIM layer, the lower the thermal resistance of the junction and the lower ΔT_TIM. Most of the TIMs are based on polymeric matrices and modified with highly thermally conductive fillers to enhance their thermal conductivity. Soft, elastic, and easy-to-process polymer matrices are the best solution to fill the micro cavities between the surfaces in the best possible way and to withstand vibrations and thermal expansion during operation.

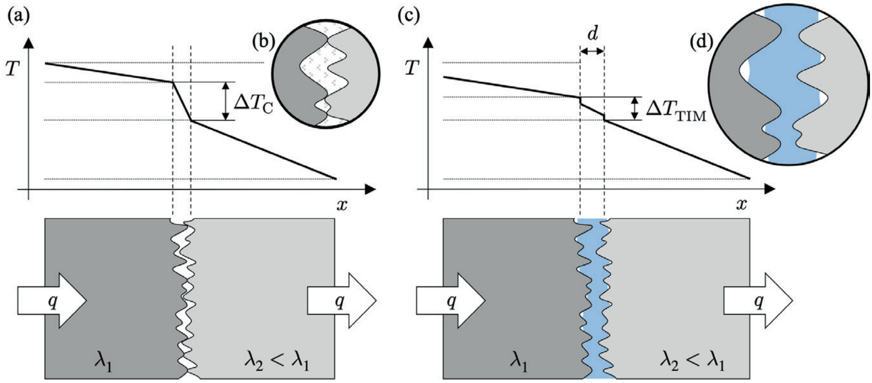

Figure 2.2. Optimizing thermal transfer across solid-solid interfaces by using TIMs.
Temperature profile along the heat flow direction when two microscopically rough solids come into contact and the gaps are filled with a poorly conductive gas (a). Temperature profile along the heat flow direction when the solid-solid contact is optimized with a thermal interface material (e.g., thermal grease) and the gas is almost fully replaced (c). (b) and (d) show a schematic close-up of the contact zone with and without TIM.

Other types of TIMs that will not be discussed further are e.g., thin and soft graphite or metal sheets, and liquid metals [5,8,9]. The current state of the art in thermal interface materials is well summarized in [5,7–11]. The overall specific thermal resistance of a TIM junction can be expressed as

$$r = r_{\mathrm{TIM}} + r_{\mathrm{C},1} + r_{\mathrm{C},2} \ , \tag{2.25}$$

where $r_{\mathrm{TIM}} = d/\lambda$ is the specific thermal resistance of the TIM layer with thickness d and thermal conductivity λ. $r_{\mathrm{C},1}$ and $r_{\mathrm{C},2}$ are the specific contact resistances that occur at the FPS transitions between the TIM and the adjacent solid surfaces. If TIMs are applied in thick layers and rough surface structures can be neglected, the thickness d can be defined and determined easily. However, it is noticeably difficult to define and determine d, if it is on the order of magnitude of the surface roughness. All three resistance contributions according to **Eq. (2.25)** cause a fractional temperature drop, see **Figure 2.2**, part (c). As most TIMs are filled polymers with a highly complex microstructure, it is difficult to quantify the three resistance components individually, see **Figure 2.3**, part (a). Alternatively, the overall specific thermal resistance r can be expressed as

$$r = \frac{d}{\lambda_{\mathrm{app}}} \ , \tag{2.26}$$

where λ_{app} denotes the apparent thermal conductivity of the TIM and already includes the influences of the contact zone. For the following analyses, however, the individual resistances are analyzed separately. The target quantities are the thermal conductivity of the filled polymer λ, unaffected by the contact zones, as well as the specific thermal contact resistances $r_{\mathrm{C}} = h_{\mathrm{C}}^{-1}$.

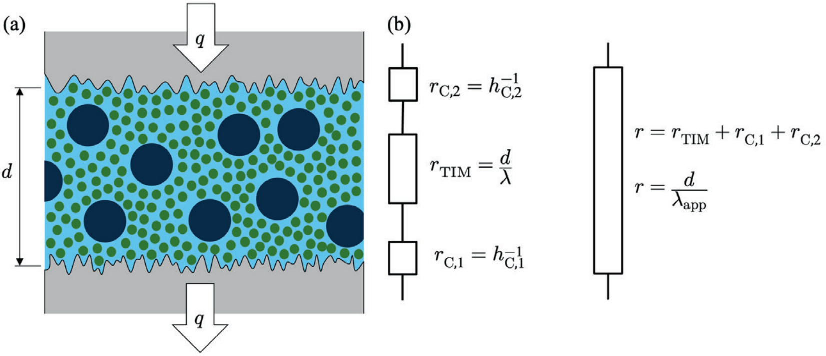

Figure 2.3. Schematic illustration of a TIM junction and a simplified thermal resistance chain. Schematic cross-section through a TIM layer of thickness d between two rough solid surfaces (a). Illustration of the absolute thermal resistances of the TIM junction based on **Eq. (2.25)** (b). Based on [0].

As described in the introduction, there has been considerable research into how the effective thermal conductivity of a filled polymer is achieved [2,29], however there are still many unanswered questions that are addressed in this thesis. An overview of the previous findings on the effective thermal conductivity of filled polymers is given in the following chapter 2.4. Complete understanding about the thermal contact resistance between particle-filled polymers and rough solid surfaces is still lacking. If this topic has been dealt with, it has been from a purely macroscopic point of view, neglecting the microstructure. A brief introduction to these approaches is given in section 2.3.3.

2.3.3 SOLID-LIQUID CONTACT RESISTANCE

By disregarding the microstructure of a TIM and considering it to be at least macroscopically homogeneous, the contact resistances occurring between the TIM and adjacent solid surfaces can be handled as pure solid-liquid contact resistances. Many TIMs are applied in liquid state. However, the following considerations can be transferred to cured TIMs, as the curing process just freezes the geometrical situation. The surface wetting and the capability of a TIM to fill the surface cavities mainly depends on the liquid state properties. Among others, the thermal contact resistance at solid-liquid interfaces was studied in [109–113]. Fujiwara and Shibahara [109] dealt with the topic of solid-liquid interfaces from a molecular dynamics perspective. In [110,111,113] predictive models for thermal contact resistance at solid-liquid interfaces were developed. Li et al. [110] and Yuan et al. [111] refer explicitly to TIMs in their work. Li et al. consider a phase change material (PCM). PCMs are a special type of TIM that must be melted for joining and can easily fill the surface cavities in the liquid state. All studies assume that when a liquid contacts a solid, a certain amount of gas (air) is trapped in the surface valleys of the solid, see **Figure 2.2**, page 17. This trapped air and the constriction resistance in the solid asperities are considered to contribute to thermal contact resistance. The depth to which the liquid can penetrate into the cavities depends on when a state of equilibrium is reached between the external pressure, gas pressure in the cavity, and the capillary pressure, based on the surface energy of the liquid [111]. As an example, appendix A.3 provides a concise summary of the model developed by Li et al. [110]. It is based on the fractal theory of surface characteristics. In their study, Li et al. used the presented model to predict the thermal contact resistance as an input for melting simulations of their PCM. They found good agreement with their experimental findings. The reported specific thermal contact resistances between the PCM and an aluminum solid were on the order of $10^{-5}\ \mathrm{m^2\ K\ W^{-1}}$ to $10^{-4}\ \mathrm{m^2\ K\ W^{-1}}$.

2.4 HEAT CONDUCTION IN FILLED POLYMERS

When two or more different materials are joined together to combine their advantageous properties, a composite material is created. The effective properties of the composite depend on the properties of the base materials, the composition ratio, the geometric arrangement, and probably some material interactions. The focus of this work is on the heat transport properties of filled polymer composites. They consist of a continuous phase, the polymeric matrix and one or more disperse phases formed by the filler particles. For several applications there is interest into the effective thermal conductivity of the composite and the thermal transfer from a filled polymer into an adjacent solid surface, or vice versa. This chapter introduces the general concept of deriving an effective thermal conductivity of a composite and summarizes the current understanding of heat transport in filled polymers. Typical base materials, their properties, and several models and equations for predicting the effective thermal conductivity are presented.

2.4.1 A GENERAL INTRODUCTION TO EFFECTIVE THERMAL CONDUCTIVITY OF COMPOSITES

The effective thermal conductivity of a composite is not a material property but describes the apparent thermal conductivity of the entire composite structure. Composite materials can have material structures of different complexity. In the simplest case, there is a laminated composite panel consisting of two or more parallel layers, where it is normally easy to analyze the effective material properties. Simple theoretical models can be used for predicting the effective thermal conductivity. If the material structure becomes more complex, the determination of the effective thermal conductivity also becomes more complicated. **Figure 2.4** schematically illustrates different levels of complexity of the material structure. Cross-sections of volumetric materials are shown. For introductory purposes, the descriptions are limited to binary composites consisting of two base materials with thermal conductivities λ_1 and λ_2.

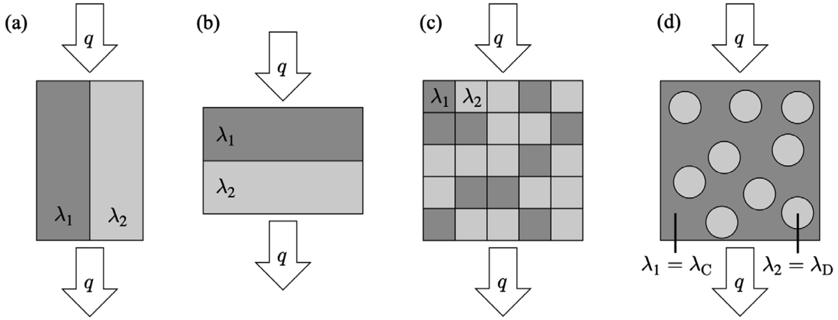

Figure 2.4. Heat conduction through composite material structures.
Parallel heat conduction model for a composite with two or more material layers parallel to the heat flow direction (a). Serial heat conduction model for a composite with two or more material layers perpendicular to the heat flow direction (b). Geometric mean model for a composite with geometrically arbitrarily arranged materials (c). Heat conduction model for a composite with a continuous phase (matrix) and a disperse phase (filler), e.g., filled polymer (d).

In parts (a) and (b) a laminated composite panel is shown, which conducts heat parallel to the material layers (a) or perpendicular to the material layers (b). In part (c), a geometrically arbitrary arrangement of materials is shown. Part (d) illustrates a composite structure with clearly differentiated continuous and disperse phases. The volume fractions of the base materials are given by

$$\phi_i = \frac{V_i}{V} \,, \tag{2.27}$$

where V_i is the volume of base material i and V is the total volume of the composite. In case (a), assuming ideal one-dimensional heat conduction, the effective thermal conductivities for the parallel connection of thermal resistors can be expressed as [114,115]

$$\lambda_{\text{eff}} = \phi_1\lambda_1 + \phi_2\lambda_2 = \phi_1\lambda_1 + (1-\phi_1)\lambda_2. \tag{2.28}$$

For the series connection of thermal resistors in (b), the result is [114,115]

$$\lambda_{\text{eff}} = \left[\frac{\phi_1}{\lambda_1} + \frac{\phi_2}{\lambda_2}\right]^{-1} . \tag{2.29}$$

While it is possible to find consistent theoretical solutions for ideal parallel or serial arrangements, the determination of the effective thermal conductivity for the cases in part (c) and (d) is much more difficult. This is primarily attributable to the fact that the local heat transport within the composite is not one-dimensional. It results in many arbitrary parallel heat paths which can no longer be modeled in simple equivalent resistance models. To calculate the effective permittivity of arbitrarily arranged material components in a globally uniform and isotropic structure, Lichtenecker proposed a logarithmic mixing formula in 1924 [116]. Applied to the calculation of the effective thermal conductivity, we obtain

$$\ln(\lambda_{\text{eff}}) = \ln\left(\lambda_1^{\phi_1}\right) + \ln\left(\lambda_2^{\phi_2}\right) . \tag{2.30}$$

Eq. (2.30) can be simplified to

$$\lambda_{\text{eff}} = \lambda_1^{\phi_1}\lambda_2^{\phi_2} . \tag{2.31}$$

It is nowadays called Lichtenecker model, or more generally, the geometric mean model [114]. **Eq. (2.30)** weights both material proportions equally. No distinction is made between continuous and disperse phases, as they appear in filled polymers, see part (d) of **Figure 2.4**. As can be easily demonstrated, the geometric mean model already provides a good approximation of the effective thermal conductivity of filled polymers when the thermal conductivities of the polymer and filler are similar. If the two thermal conductivities are significantly different, the geometric mean model notably overestimates the effective thermal conductivity. For this reason, special models are used to predict the effective thermal conductivity of filled polymers. These account for the fact that the polymer forms a continuous phase, and the filler forms a disperse phase. Such models are presented in the next section.

2.4.2 EFFECTIVE THERMAL CONDUCTIVITY OF FILLED POLYMERS

To properly handle filled polymers, there must be a clear distinction between the continuous phase, and the disperse phase. As shown in part (d) of **Figure 2.4**, λ_C denotes the thermal conductivity of the polymer and λ_D the thermal conductivity of the filler (provided that only one type of filler is present). In addition, the filler volume fraction ϕ is defined as

$$\phi = \frac{V_\mathrm{D}}{V} = \frac{V_\mathrm{D}}{V_\mathrm{C} + V_\mathrm{D}} , \qquad \textbf{(2.32)}$$

where V_D is the volume of the disperse phase and V_C the volume of the continuous phase. **Figure 2.5** and **Table 2.1** give an overview of typical ranges of thermal conductivities of polymers, fillers, and filled polymers. All ranges are intended as a rough guide and are not exhaustive.

For the polymers, polystyrene (PS), silicone rubber (SR), epoxy (EP), and high-density polyethylene (HDPE) are listed as examples in ascending order of thermal conductivity. Filled polymers' effective thermal conductivities are given in the rough range of $(0.3 \ldots 30)\ \mathrm{W\ m^{-1}\ K^{-1}}$, with a majority of the values in the range of few $\mathrm{W\ m^{-1}\ K^{-1}}$, see **Figure 2.5**. For a better overview, the fillers are grouped into three classes. Filler class I contains materials with a thermal conductivity up to $20\ \mathrm{W\ m^{-1}\ K^{-1}}$, class II contains materials in the intermediate range up to $100\ \mathrm{W\ m^{-1}\ K^{-1}}$, and all highly thermally conductive fillers with $\lambda_\mathrm{D} > 100\ \mathrm{W\ m^{-1}\ K^{-1}}$ are summarized in class III. Class I contains minerals and ceramics, in class II mainly oxide ceramics and in class III nitrides, metals, and diamond are present.

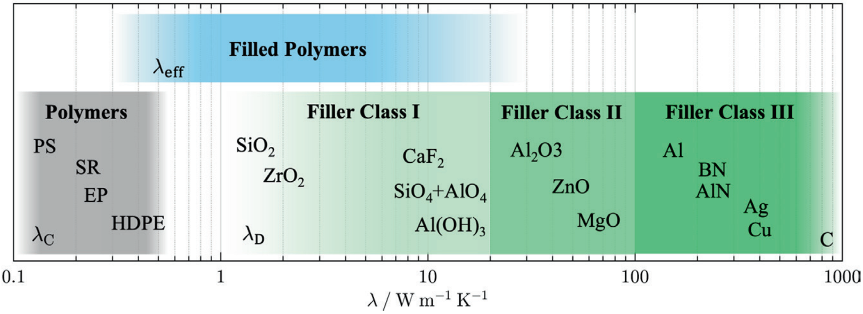

Figure 2.5. Overview of typical thermal conductivity ranges for polymers, fillers, and filled polymers. For the individual values, see **Table 2.1**.

Table 2.1. Tabular overview of typical thermal conductivity ranges for polymers and fillers. All values taken at 300 K. * No general material data available.

Group	Material	Thermal conductivity λ / W m^{-1} K^{-1}	Ref.
Polymers	Polystyrene (PS)	0.10 … 0.20	[2,4,117]
	Silicone rubber (SR)	0.15 … 0.30	[118–122]
	Epoxy (EP)	0.17 … 0.36	[4,117,123,124]
	High-density polyethylene (HDPE)	0.33 … 0.58	[2,4,117,123]
Filler Class I	Silica (SiO_2)	1.3 … 1.5	[10,44,119,125]
	Zirconia (ZrO_2)	2	[42,125]
	Calcium fluoride (CaF_2)	10	[125]
	Aluminosilicate (SiO_4 + AlO_4)	14	[126]
	Aluminum hydroxide ATH ($Al(OH)_3$)	10 … 20	[127,128]*
Filler Class II	Alumina (Al_2O_3)	30 … 40	[42,119,125,129]
	Zinc oxide (ZnO)	54	[119]
	Magnesia (MgO)	60 … 70	[44]
Filler Class III	Aluminum incl. alloys (Al)	110 … 237	[44,53,125]
	Boron nitride (BN)	185 … 300	[2,119,123]
	Aluminum nitride (AlN)	100 … 300	[2]
	Copper (Cu)	401	[53,125]
	Silver (Ag)	428 … 429	[53,125]
	Diamond (C)	1000	[2,42,125]

Since the prediction of the effective thermal conductivity of granular filled composites, even beyond polymers, has been of great interest for a long time, numerous theories and models have been developed for this purpose. The physical principles and current understanding of heat conduction in filled polymers are summarized in [2,3,54,56,57]. Especially well studied is the range of low filler volume fractions with isolated, non-interacting particles and a moderate increase in effective thermal conductivity. The findings come from experimental studies, e.g., [119,122,130–133], as well as from the application of theoretical and empirical models, e.g., [114,134], and less often from numerical calculations, e.g., [135,136]. Theoretical, empirical, and semi-empirical models, so-called effective medium approaches (EMA), are a good way of analyzing qualitative relationships quickly and efficiently. However, the validity of the results depends strongly on the simplifications made in the model and the quality of the input parameters.

Most EMAs consider dilute dispersions of particles and neglect particle-particle interactions. They are therefore particularly suitable for low filler volume fractions [56]. Percolation models, such as those proposed in [137,138], are more suitable for higher filler concentrations. These account for the probability of the particles forming closed paths and thus significantly increasing the effective thermal conductivity. A comprehensive summary and evaluation of the models was published in 1976 by Progelhof et al. [114] and in 2015 by Pietrak and Wiśniewski [134]. Comprehensive overviews of the various models can also be found in e.g., [6,9,139]. While initial, simple approaches only consider filler volume fraction and the two thermal conductivities of polymer and filler, later work also includes other parameters such as particle shape, particle size, thermal interfacial resistances between filler particles and polymer, or maximum packing density. Many of the later approaches are based on the original and early models of Maxwell in 1873 [140], Rayleigh in 1892 [141], or Bruggeman in 1935 [142]. Not all these models have been developed primarily for estimating effective thermal conductivity. They were developed, or are at least additionally suitable for many effective properties, such as thermal diffusivity, magnetic permeability or electric permittivity [134]. Both Maxwell and Rayleigh derived theoretically exact solutions but simplified the system strongly. Maxwell considered spherical particles in low concentrations, without any interactions. In Rayleigh's assumption, the particles form a simple cubic array, and may interact, i.e., form well conducting paths, when the filler concentrations increase. In both models, the polymer and the particles are in perfect thermal contact and no thermal interfacial resistances occur. As an example, the Maxwell model is shown here, with the effective thermal conductivity expressed by [140]

$$\lambda_{\text{eff}} = \frac{2\lambda_{\text{C}} + \lambda_{\text{D}} + 2\phi(\lambda_{\text{D}} - \lambda_{\text{C}})}{2\lambda_{\text{C}} + \lambda_{\text{D}} - \phi(\lambda_{\text{D}} - \lambda_{\text{C}})} \lambda_{\text{C}} \;, \tag{2.33}$$

as a function of the polymer's thermal conductivity λ_{C}, the filler's thermal conductivity λ_{D}, and the filler volume fraction ϕ. The derivation of this model, as well as those that follow, can be found in the referenced literature. Bruggeman took a slightly different approach in his model. He considered the individual particles as successively added to the matrix or composite. The result is a differential effective medium approach, which is expressed using the implicit formulation [142]

$$1 - \phi = \frac{\lambda_{\text{D}} - \lambda_{\text{eff}}}{\lambda_{\text{D}} - \lambda_{\text{C}}} \left(\frac{\lambda_{\text{C}}}{\lambda_{\text{eff}}} \right)^{\frac{1}{3}}. \tag{2.34}$$

It is generally reported that the Bruggeman model provides more accurate solutions at higher filler volume fractions [134]. Bruggeman's model is based on the same input parameters as Maxwell's or Rayleigh's model.

Over the last decades, numerous other models have been created, based on new considerations or as extensions to the three basic models mentioned. The aim was to consider further parameters or to optimize the model quality, especially for higher filler volume fractions. Today, many purely theoretical, empirical, and semi-empirical models are available. The next example presented is a theoretical model published in 1969 by Cheng and Vachon [143]. They started with a probabilistic model, previously suggested by Tsao [144]. They derived a consistent solution from it, with the assumption that the discontinuous phase is present in a parabolic distribution of volume fractions. The effective thermal conductivity can then be derived as

$$\lambda_{\text{eff}} = \left[\frac{1-B_1}{\lambda_\text{C}} + \frac{1}{\sqrt{C_1\Delta\lambda(\lambda_\text{C}+B_1\Delta\lambda)}}\ \ln\left(\frac{\sqrt{\lambda_\text{C}+B_1\Delta\lambda}+\frac{B_1}{2}\sqrt{C_1\Delta\lambda}}{\sqrt{\lambda_\text{C}+B_1\Delta\lambda}-\frac{B_1}{2}\sqrt{C_1\Delta\lambda}}\right)\right]^{-1}, \qquad \textbf{(2.35)}$$

with the thermal conductivity difference

$$\Delta\lambda = \lambda_\text{D} - \lambda_\text{C}\ , \qquad \textbf{(2.36)}$$

as well as the parameters

$$B_1 = \sqrt{\frac{3\phi}{2}}\ , \qquad \textbf{(2.37)}$$

and

$$C_1 = 4\sqrt{\frac{2}{3\phi}}\ . \qquad \textbf{(2.38)}$$

Cheng and Vachon [143] compared the results of their model with experimental data and found better agreement than with other existing models. The model published only a short time later by Lewis and Nielsen in 1970 [145–148] is semi-empirical and is one of the first to include parameters such as the particle shape and the maximum packing density of the filler. It is still very popular today [134], since the addition of the two parameters in the model generally leads to better results compared to the basic models of e.g., Maxwell and Bruggeman. It can be easily adapted to experimental data by adjusting those parameters. In the Lewis and Nielsen model the, effective thermal conductivity is expressed as [145–148]

$$\lambda_{\text{eff}} = \lambda_\text{C}\frac{1+AB_2\phi}{1-B_2C_2\phi}\ , \qquad \textbf{(2.39)}$$

where A is a factor, describing the particles' shape,

$$B_2 = \frac{\lambda_D/\lambda_C - 1}{\lambda_D/\lambda_C + A}\,, \tag{2.40}$$

and

$$C_2 = 1 + \phi\frac{(1-\phi_{max})}{\phi_{max}^2}\,. \tag{2.41}$$

ϕ_{max} denotes the maximum packing density of the filler to be considered. Values for A and ϕ_{max} are given in tables, e.g., in [114,134,148]. For spherical filler particles and a random dense packing structure, $A = 1.5$ and $\phi_{max} = 0.637$ must be set. The introduced models given in the **Eqs. (2.33)**, **(2.34)**, **(2.35)**, and **(2.39)** are well suited for a first basic analysis of the effects and their magnitudes. They were used to calculate the effective thermal conductivity as a function of filler volume fraction for a reference mixture of epoxy and alumina, see **Figure 2.6**. The thermal conductivities of the base materials were set to $\lambda_C = 0.25$ W m^{-1} K^{-1}, representing epoxy, and $\lambda_D = 35$ W m^{-1} K^{-1}, representing alumina. Additionally, **Figure 2.6** shows the results of calculations with the basic **Eqs. (2.28)**, **(2.29)**, and **(2.30)** for the parallel, serial, and geometric mean models introduced in section 2.4.1. Except for the parallel connection model, all models predict a superlinear increase in the effective thermal conductivity with the filler volume fraction.

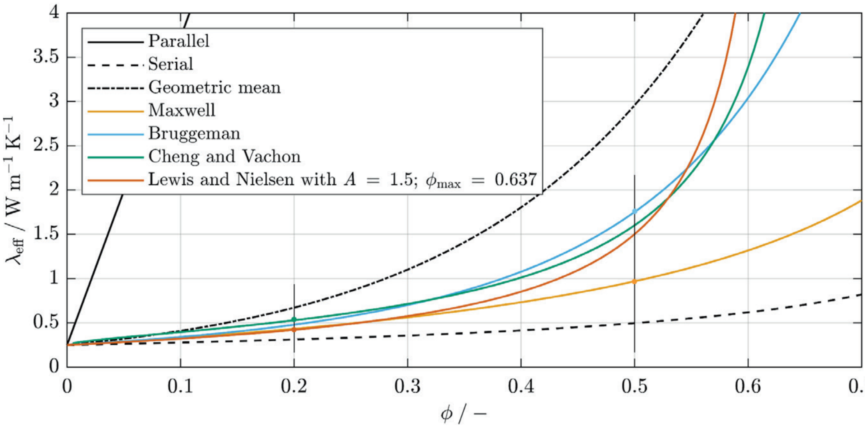

Figure 2.6. Effective thermal conductivity of a filled polymer as a function of filler volume fraction. Reference calculations based on the **Eqs. (2.28)**, **(2.29)**, and **(2.30)** with $\phi = \phi_2$, and with thermal conductivities $\lambda_1 = 0.25$ W m^{-1} K^{-1} and $\lambda_2 = 35$ W m^{-1} K^{-1}. Further calculations based on the **Eqs. (2.33)**, **(2.34)**, **(2.35)**, and **(2.39)** with a thermal conductivity of the continuous phase $\lambda_C = 0.25$ W m^{-1} K^{-1} and a thermal conductivity of the disperse phase $\lambda_D = 35$ W m^{-1} K^{-1}. For the Lewis and Nielson model, $A = 1.5$ and $\phi_{max} = 0.637$ are specified additionally.

The pure parallel connection model (**Figure 2.4** (a)) provides a linear increase and far too high effective thermal conductivity, as it assumes a continuous filler path. The lower limit is given by the series connection model, see **Figure 2.4** (b). The entire polymer volume is abstracted as a continuous poorly thermally conductive layer. The geometric mean approach gives values in between, at least in the same order of magnitude as the EMAs from **Eqs. (2.33)**, **(2.34)**, **(2.35)**, and **(2.39)**. The colored curves, representing the results of those EMAs are located between the geometric mean and the series connection model.

For $\phi = 0.2$, the span of predictions ranges from $\lambda_{\text{eff}} = 0.42\ \text{W m}^{-1}\ \text{K}^{-1}$ to $\lambda_{\text{eff}} = 0.53\ \text{W m}^{-1}\ \text{K}^{-1}$ and for $\phi = 0.5$ from $\lambda_{\text{eff}} = 0.97\ \text{W m}^{-1}\ \text{K}^{-1}$ to $\lambda_{\text{eff}} = 1.75\ \text{W m}^{-1}\ \text{K}^{-1}$. This corresponds to a relative span of $\pm 11.5\ \%$ and $\pm 45.3\ \%$ based on the average value. The Maxwell model provides the lowest values by far, especially for $\phi > 0.3$, as it generally excludes particle-particle interactions and thus the formation of good thermally conductive paths in the material.

In contrast to the electrical conductivity of filled polymers, the effective thermal conductivity increases only moderately and does not show a pronounced percolation threshold above which the conductivity increases abruptly, see e.g., [149]. This is presumably because the thermal conductivities of the base materials are of a similar order of magnitude, whereas the typical specific electrical conductivities of polymers and conductive fillers differ by several orders of magnitude. The two additional parameters of the Lewis and Nielsen model appear to increase suitability of the model for general investigation on basic parameters, affecting the effective thermal conductivity. The results of a parametric study on the effects of the thermal conductivities of filler and polymer, the shape factor A, and the maximum packing density ϕ_{max} are shown in **Figure 2.7**. The calculations are based on the same initial parameter set, as used for the calculations shown in **Figure 2.6**, representing spherical alumina fillers in an epoxy matrix. Part (a) of **Figure 2.7** presents the results of a variation of the polymer's thermal conductivity λ_{C} between $0.15\ \text{W m}^{-1}\ \text{K}^{-1}$ and $0.35\ \text{W m}^{-1}\ \text{K}^{-1}$. The thermal conductivity of the polymer has a decisive influence on the effective thermal conductivity. The effective thermal conductivity in the parameter range investigated scales, at least approximately, with the polymer's thermal conductivity, see **Eq. (2.39)**. With double the polymer thermal conductivity, almost double the effective thermal conductivity is achieved. Only the change in the thermal conductivity ratio $\lambda_{\text{D}}/\lambda_{\text{C}}$ in **Eq. (2.40)** leads to a slightly lower effective thermal conductivity.

Presented in part (b) of **Figure 2.7** are the results of a variation of the filler's thermal conductivity λ_{D} between $1\ \text{W m}^{-1}\ \text{K}^{-1}$ and $100\ \text{W m}^{-1}\ \text{K}^{-1}$. In line with assumptions, the effective thermal conductivity increases with the thermal conductivity of the filler. However, the sensitivity appears to decrease with increasing absolute values, with minimal differences between $35\ \text{W m}^{-1}\ \text{K}^{-1}$ and $100\ \text{W m}^{-1}\ \text{K}^{-1}$.

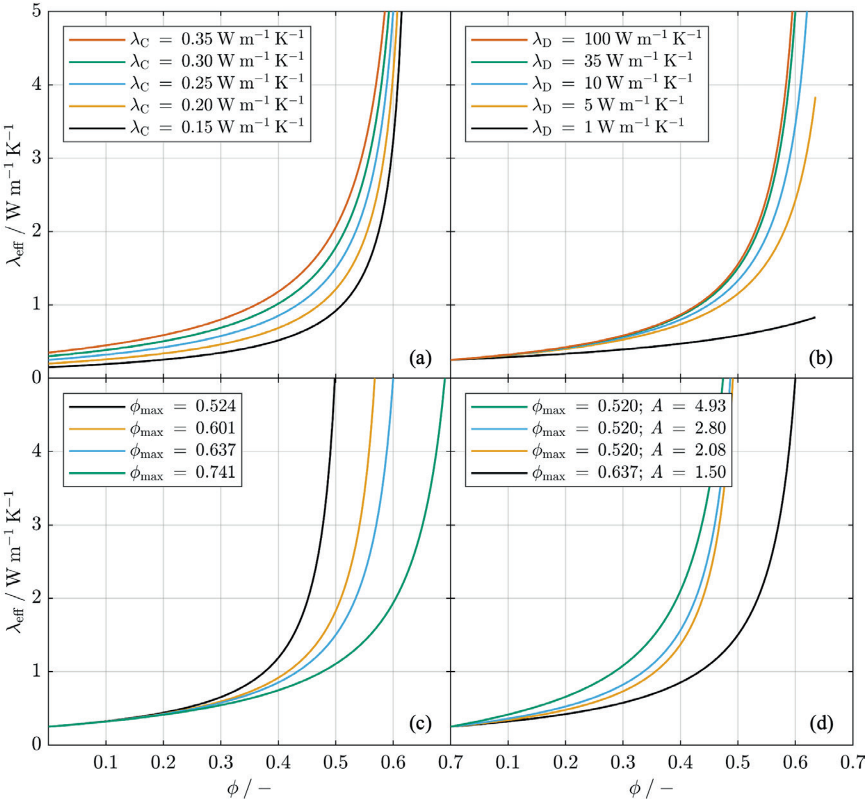

Figure 2.7. Parametric study on effective thermal conductivity of a filled polymer, based on the semi-empirical Lewis and Nielsen model.

Calculations based on the **Eq. (2.39)** with the general parameter set: $\lambda_C = 0.25$ W m^{-1} K^{-1}, $\lambda_D = 35$ W m^{-1} K^{-1}, $\phi_{max} = 0.637$, $A = 1.5$, representing alumina spheres with a random close packing, dispersed in epoxy. Variation of the polymer's thermal conductivity λ_C in (a). Variation of the filler's thermal conductivity λ_D in (b). Variation of the maximum packing density with $\phi_{max} = 0.524$ for a simple cubic packing, $\phi_{max} = 0.601$ for a random loose packing, $\phi_{max} = 0.637$ for a random close packing, and $\phi_{max} = 0.741$ for a face centered cubic packing in (c). Variation of the particle shape and corresponding maximum packing density with $A = 4.93$ for randomly oriented rods of aspect ratio 10, $A = 2.80$ for randomly oriented rods of aspect ratio 6, $A = 2.08$ for randomly oriented rods of aspect ratio 4, and $A = 1.5$ for spheres in (d). Values for ϕ_{max} and A are taken from [148].

Furthermore, the Lewis and Nielsen model allows for the discussion of the basic effects of particle shape and maximum packing density. Parts (c) and (d) of **Figure 2.7** present the calculation results with variation of particle shape and related maximum packing density. Only the values and combinations, proposed by Nielsen et al. in [148] were used. Part (c) shows the results of an isolated variation of the maximum packing density for a spherical filler. The variation of $\phi_{\max}$ leads to a horizontal stretching in the thermal conductivity curve. If the filler can be packed more densely, higher filler volume fractions are necessary to achieve the desired effective thermal conductivity.

Part (d) shows the comparison of the increase of effective thermal conductivity between differently sized rods and spherical particles. The maximum packing densities were adjusted accordingly, following [148]. This study leads to the conclusion that increasing aspect ratio (from 4 to 10) in the rods leads to an earlier and more significant increase in effective thermal conductivity, even at low filler volume fractions. In the Lewis and Nielsen model, the simultaneous adjustment of shape factor A and maximum packing density $\phi_{\max}$ leads to a superimposed effect and similar shifts, see parts (c) and (d) of **Figure 2.7**.

The two studies shown in part (c) and part (d) allow a first basic discussion of the microstructure effects in filled polymers, qualitatively and with little specificity. It must be assumed that the maximum packing density parameter, which is only used here as a rough orientation value from generally valid tables, depends on numerous filler properties such as particle shape, size, size distribution, agglomeration, and particle-polymer interactions. The situation is similar with the shape factor. It is questionable whether a single parameter can describe all the effects of different shape and size distribution combinations. It is also important to note at this point that the parameters in the Lewis and Nielsen model and in many other models might not be directly measurable for real materials. As a result, predicting the effect of a real filler based solely on its measured properties is highly challenging. It is always possible to adjust the parameters empirically based on experimental findings, however, this means that the models lose their predictive power.

What is still missing from the first summary of the current state of knowledge are the effects of thermal interfacial resistances between polymer and filler particles. Following Kapitza's discovery of the phenomenon [67], numerous theoretical and experimental studies were carried out. The effects of thermal interfacial resistances in particulate composites were first reported by Anderson and Rauch in 1970 [150]. They carried out experiments below 1 K, and found that thermal interfacial resistances between copper particles and a grease matrix reduce the effective thermal conductivity of the composite. The impact of the effect increased with decreasing temperature. With a reduction in temperature from 1 K to 0.1 K, the effective thermal conductivity drops by approximately 82 %. In 1974, Garrett and Rosenberg [151] reported similar results in their analysis of the effects on an epoxy resin filled with glass spheres, quartz, corundum, and diamond at temperatures between 2 and 300 K. They also found that the effect increases with decreasing temperature, while it is negligible at higher temperatures. Schmidt additionally reported on the effects of thermal interfacial resistances on a copper-filled epoxy resin in 1975 [152], and did not attribute any significance to the effect at higher temperatures. Furthermore, the work of

Devpura et al. from 2001 [153] must be mentioned. They also investigated the effects of thermal interfacial resistances between filler particles and matrix for common particle sizes in the lower micrometer range. For the combination of a polyethylene matrix and alumina fillers, they concluded that the effects are negligible at room temperature. In their general review on thermal interfacial resistances published 2020, Giri and Hopkins [68] report that these are of negligible magnitude in amorphous materials, such as many polymers. They justify their statement with the very low thermal conductivity of the amorphous structure which superimposes the effect.

Despite these findings, there is still a debate as to whether thermal interfacial resistances play a crucial role in filled polymers [2–4,56,57], or rather from which particle sizes and in which temperature ranges they are relevant. In general, it is very difficult to determine thermal interfacial resistances for realistic material combinations from the first principles. Measurements on particle surfaces are limited and what remains, is an observation from a macroscopic point of view. With decreasing particle size the interfacial area per unit volume increases. Thus, the influence of thermal interfacial resistances, i.e., the reduction of effective thermal conductivity, must increase [54]. If two fillers with different grain sizes and otherwise identical properties are compared and the finer-grained material shows a lower effective thermal conductivity, this is an indication of the effect of thermal interfacial resistance. This is of course difficult to demonstrate experimentally, as it is highly challenging to find two otherwise identical fillers, differing only in grain sizes. In general, the distribution of the particle size or the particle shape change at the same time. This means that a perceptible size effect may or may not be an indication of thermal interfacial resistances, as it may be superimposed by other effects [2].

There will always be a particle size below which the thermal interfacial resistances are of considerable magnitude. The question is whether this limit is already reached with typical particle sizes in the lower micrometer range or whether the phenomenon is only important with nano composites. In recent review articles [2–4,56,57], the effect is always considered and discussed, however a clear statement on its magnitude is missing. While some report on studies in which a clear reduction in effective thermal conductivity with decreasing particle size was observed, other groups also report contradictory effects [2,4]. Therefore, neither a conclusive assessment of the effect nor its extent seems possible.

It will be necessary to investigate the effects for the materials and combinations used in this work as well. In general, it can be expected that the effect increases with decreasing temperature and increasing thermal conductivity of the polymer [54,151,152]. To describe the general effects of thermal interface resistance on the effective thermal conductivity of particulate composites, not only for filled polymers, a further theoretical model for calculating the effective thermal conductivity of filled polymers is introduced [154]. It is a comparatively modern theoretical approach which is based on the Bruggeman model, but additionally includes the effect of particle shape and size as well as thermal interfacial resistances. In 2004 Jiajun and Xiao-Su [154] suggested an expression for the effective thermal conductivity of a filled polymer in the following form:

$$(1-\phi)^{n_\mathrm{P}} = \left(\frac{\lambda_\mathrm{eff}-\lambda_\mathrm{D}(1-\alpha_\mathrm{I})}{\lambda_\mathrm{C}-\lambda_\mathrm{D}(1-\alpha_\mathrm{I})}\right)^{\frac{n_\mathrm{p}}{1-\alpha_\mathrm{I}}} \left(\frac{\lambda_\mathrm{C}}{\lambda_\mathrm{eff}}\right)^{\frac{1+n_\mathrm{p}\alpha_\mathrm{I}-\alpha_\mathrm{I}}{1-\alpha_\mathrm{I}}}\ , \tag{2.42}$$

where n_p is a dimensionless particle shape factor, based on the particles' sphericity S, with [154]

$$n_\mathrm{p} = \frac{3}{S}\ . \tag{2.43}$$

The sphericity is the ratio of the surface area of a sphere of the same volume to the surface area of the particle of interest. α_I represents the thermal interfacial resistances, also dimensionless, with [154]

$$\alpha_\mathrm{I} = \frac{r_\mathrm{p,K}}{r_\mathrm{p}}\ , \tag{2.44}$$

where r_p is the radius of the equally sized particles, without further shape-dependent specification, and $r_\mathrm{p,K}$ denotes the Kapitza radius. The Kapitza radius is the threshold, below which the further insertion of filler particles leads to a reduction in effective thermal conductivity instead of an increase due to the additional interfacial area. It can be derived from the thermal interfacial resistance r_I and the thermal conductivity of the continuous phase λ_C [154]

$$r_\mathrm{p,K} = r_\mathrm{I}\ \lambda_\mathrm{C}. \tag{2.45}$$

As the thermal interfacial resistance r_I, the Kapitza radius $r_\mathrm{p,K}$ decreases with increasing temperature. For spherical particles ($n_\mathrm{p} = 3$) and zero interfacial resistances ($\alpha = 0$), **Eq. (2.42)** is identical to the basic Bruggeman model in **Eq. (2.34)**.

An additional parametric study is presented to analyze both the effects of shape factor and thermal interfacial resistances on the effective thermal conductivity, see **Figure 2.8**. The same initial parameter set with $\lambda_\mathrm{C} = 0.25$ W m^{-1} K^{-1}, representing epoxy, and $\lambda_\mathrm{D} = 35$ W m^{-1} K^{-1}, representing alumina is used as in the previous discussion with the Lewis and Nielsen model, see **Figure 2.7**. Part (a) of **Figure 2.8**. shows the increase of effective thermal conductivity with filler volume fraction, without considering interfacial resistances, but with variable shape factor. The higher the shape factor, i.e., the lower the sphericity, the lower the necessary filler volume fraction for a desired effective thermal conductivity. A similar effect has already been shown in **Figure 2.7**, based on the Lewis and Nielsen model.

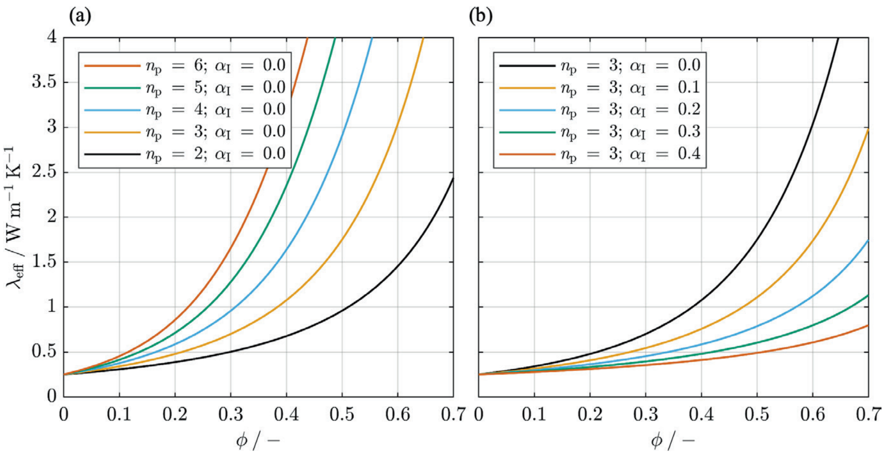

Figure 2.8. Effects of particle shape and thermal interfacial resistance on effective thermal conductivity of a filled polymer as a function of filler volume fraction.

Calculations based on **Eq. (2.42)** with a thermal conductivity of the continuous phase $\lambda_C = 0.25$ W m^{-1} K^{-1}, and a thermal conductivity of the disperse phase $\lambda_D = 35$ W m^{-1} K^{-1}.

Part (b) of **Figure 2.8** shows the increase of effective thermal conductivity with filler volume fraction, with a constant shape factor ($n_p = 3$, spheres), but with varying thermal interfacial resistances up to $\alpha_I = 0.4$. A significant drop in effective thermal conductivity is observed with increasing thermal interfacial resistances. The effect is similar to that of reducing the filler thermal conductivity, see **Figure 2.7**. Alternative models that take thermal interfacial resistances into account have been proposed in e.g., [153,155,156]. For further models that take into account, e.g., particle size distribution [157] or percolation paths and particle aggregates [158], the reader is referred to the respective literature.

After the presentation of numerous calculation models for the effective thermal conductivity of filled polymers and several parametric studies on individual parameters, the following can be summarized: The effective thermal conductivity of particulate composites depends not only on the thermal conductivity of the base materials but also on the geometric situation in the material microstructure. This determines the success of the formation of highly thermally conductive paths. It is known that particles with large aspect ratios ensure an increase in effective thermal conductivity already with lower filler volume fractions, and that different maximum packing densities of a filler can stretch the thermal conductivity curve horizontally. Thermal interfacial resistances, on the other hand, affect the growth rate of the effective thermal conductivity with increasing filler volume fraction, but may only have a noticeable effect at very low temperatures.

From a phenomenological point of view, it is evident that the formation of continuous heat-conducting paths in the microstructure must have a decisive influence. Unfortunately, this phenomenon cannot be quantified to any extent using the models presented. They each represent only a small selection of the possible parameters and are therefore only suitable for isolated, qualitative analyses of these factors. Numerous contributing parameters and complex interactions must be suspected, necessitating detailed modeling of the microstructure to answer open questions and provide quantitative predictions. Particularly in the last few decades, numerical simulation methods have also emerged. These offer the possibility of resolving and analyzing a packing structure, down to the scale of individual particles, if necessary. The numerical simulation methods used so far still lack a comprehensive representation of the phenomena, so that no calculation approach can be directly adopted for this work. Nevertheless, these approaches provide a good basis for the work described in this thesis. An introduction to numerical calculation methods is provided in section 4.1.1.

2.4.3 THERMAL CONTACT RESISTANCE BETWEEN FILLED POLYMERS AND SOLIDS

As previously emphasized in the introduction, thermal contact resistances between filled polymers and solid surfaces play a major role in TIM and IMS applications [5,8–10,159–161], but have thus far been very rarely studied. As will be shown in chapter 3.3, experimental access is currently only possible using macroscopic methods. These do not provide any insight into microstructural relationships. The surface wetting of the continuous phase on the rough solid surface can also have an effect, as in unfilled systems [109,112,113]. In addition, there are most likely effects of the filler-surface interaction and the local packing structure. Li et al. [110] and Yuan et al. [111] considered TIMs in their previously introduced (section 2.3.3) studies on contact resistances, but treated the TIM as a continuum and neglected the microstructural effects.

2.5 ADVANCES IN DEVELOPMENT OF HIGHLY CONDUCTIVE FILLED POLYMERS

Over the years, new filled polymer composites have been developed for heat transport applications. New boundary conditions, different applications, and increased performance requirements are constantly forcing researchers and developers to come up with new approaches, strategies, and material combinations. This chapter is intended to provide an overview of development progress at the microstructure level, and thus giving the reader a comprehensive picture of possible material combinations and achievable performance. For further discussion and comparison, the materials are divided into three categories, see **Figure 2.9**, with differentiation relating to the characteristics of the filler packing. In part (a), a single-scale filler packing is shown, where only one type of filler with particles of similar size is used. The particles naturally have a certain size distribution, but with monomodal characteristics.

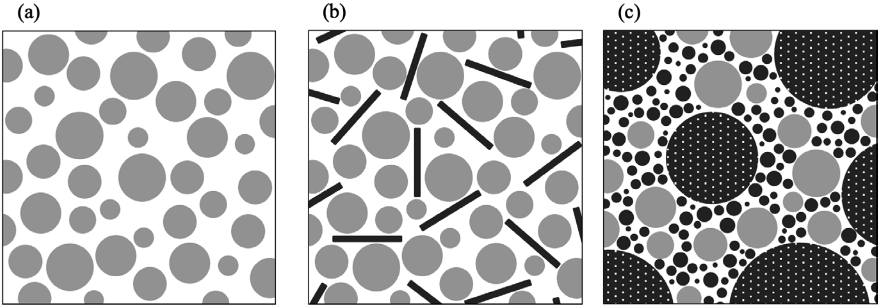

Figure 2.9. Three categories of filler packings.
Single-scale filler packing (a), hybrid filler packing (b), and multi-scale filler packing (c).

Single-scale filler packings are the most basic system and have been the subject of the descriptions in chapter 2.4. For some applications, it may be necessary to combine different types of fillers, while the size of the different filler particles remains similar. These filler packings are called hybrid filler packings and are illustrated in part (b) of **Figure 2.9**. A hybrid filler packing is shown, containing a spherical and a fibrous filler. Such a combination can be beneficial from a thermal point of view, as the fibers can efficiently bridge gaps between spherical particles and generate highly conductive heat paths. The different filler particles in hybrid packings might have a different particle shape or different chemistry.

Possible filler volume fraction in single-scale and hybrid filler packings is restricted by a sharp increase in viscosity as the filler volume fraction increases, thereby limiting the achievable thermal conductivity. To overcome this processing limitation, it is common practice to use multi-scale filler packings, which allow for higher total filler volume fractions with lower viscosities. The background and details of this effect are explained in section 5.1.1. Part (c) of **Figure 2.9** shows a multi-scale filler packing based on a ternary filler blend. The complexity of material development increases as it shifts from single-scale to hybrid to multi-scale filler packings. Beyond thermal aspects, a variety of target properties must be considered including density, effective viscosity, effective permittivity, etc. For example, [162] and [163] describe two recent material developments in which the filler packing is selected from not only a thermal point of view but also considering the mechanical and rheological properties of the composite.

Recent material developments for the three introduced categories of filler packings are reviewed in sections 2.5.1 - 2.5.3. Additionally, there are a few further studies with unusual approaches or special applications. Skrabala and Bonten [164] introduced a new extrusion technique in 2014 that can be used to influence the particle orientation of fibers or platelets in polymer composites and thus tailor the anisotropic thermal conductivity. Zhu et al. [165] reported on the effective thermal conductivity of immiscible low-density polyethylene (LDPE) / epoxy blends with hybrid filler systems in 2017. They investigated the influence of the LDPE to epoxy mixing ratio on the microstructure and the formation of good heat-conducting paths. Tian et al. [166] developed a foam-template method and fabricated a thermal interface material with boron nitride fillers in 2018. This novel technique enabled the generation of continuous heat-conducting paths along the particles, even at low filler volume fractions.

2.5.1 POLYMERS WITH SINGLE-SCALE FILLER PACKING

The most frequently used fillers up to now are alumina and boron nitride [119,122,132,167–172]. Other commonly used fillers are aluminum nitride, silica, or zinc oxide [120,130,168–170,173]. For the polymeric matrix, a silicone rubber has been used most often [119–122,132,167,169], followed by epoxy [168,171,173].

In 1999, Wong and Bollampally [173] studied the effects of several ceramic fillers, such as silica, alumina, and aluminum nitride, on the effective thermal conductivity of epoxy resins. The best result of roughly $2\ \mathrm{W\ m^{-1}\ K^{-1}}$ was obtained with a filler volume fraction of $\phi = 0.5$ and silica-coated aluminum nitride. Weidenfeller et al. [174] reported on a study with fillers made of magnetite, barite, talcum, copper, strontium ferrite, and glass fibers. This study showed the highest thermal conductivity of $2.5\ \mathrm{W\ m^{-1}\ K^{-1}}$, achieved with $\phi = 0.3$ of talcum in the polypropylene matrix under investigation. Sim et al. [169] investigated the effects of low filler concentrations of zinc oxide in a silicone rubber attaining roughly $0.25\ \mathrm{W\ m^{-1}\ K^{-1}}$ with $\phi = 0.1$.

A high density polyethylene was modified by Lee et al. in 2006 [170] with several fillers including aluminum nitride, wollastonite, silicon carbide, and boron nitride. A maximum thermal conductivity was attained for boron nitride at $\phi = 0.5$ of $3.66\ \mathrm{W\ m^{-1}\ K^{-1}}$, and for aluminum nitride at $\phi = 0.6$ of $2.42\ \mathrm{W\ m^{-1}\ K^{-1}}$.

Copper fillers with different particle shapes were used by Tekce et al. in 2007 [131] and added to a matrix of polyamide. With $\phi = 0.6$ of spherical particles they achieved $3.66\ \mathrm{W\ m^{-1}\ K^{-1}}$; however, they increased that to $11.57\ \mathrm{W\ m^{-1}\ K^{-1}}$ with $\phi = 0.6$ of platelets and to $8.71\ \mathrm{W\ m^{-1}\ K^{-1}}$ with $\phi = 0.3$ of fibers. Another study on zinc oxide filled silicone rubber was published in 2007 by Mu et al. [120]. The effective thermal conductivity was just under $0.5\ \mathrm{W\ m^{-1}\ K^{-1}}$ at $\phi = 0.35$. They investigated the size effect by using different sized filler particles, however no clear tendency was observed.

A study on alumina-filled silicone rubber was reported by Zhou et al. in 2007 [167], where they were able to observe an interesting size effect. The use of different micrometer sized fillers only led to $(0.8 \ldots 0.9)\ \mathrm{W\ m^{-1}\ K^{-1}}$, however the use of nano scale filler at $\phi = 0.64$ permitted an effective thermal conductivity of $1.38\ \mathrm{W\ m^{-1}\ K^{-1}}$. Within the microscale fillers, a clear effect of size with the highest effective thermal conductivities achieved via the largest particles was only observed for $\phi < 0.5$. The same group performed similar studies with boron nitride in which the potential influence of thermal interfacial resistances was clearly recognizable in the decreasing thermal conductivities of smaller particles [132]. The highest effective thermal conductivity obtained of $1.2\ \mathrm{W\ m^{-1}\ K^{-1}}$ was reached at $\phi = 0.6$ in a silicone rubber. In 2008, a clear size effect was seen in a study with silicon nitride in a silicone rubber matrix [121] with the highest achievable thermal conductivity of $1.4\ \mathrm{W\ m^{-1}\ K^{-1}}$ at $\phi = 0.6$.

In 2010 Kochetov et al. [168] compared the thermal performance of alumina and silica fillers in an epoxy polymer. At an equal filler weight fraction of $60\ \%$ they reached $0.675\ \mathrm{W\ m^{-1}\ K^{-1}}$ with alumina and $0.735\ \mathrm{W\ m^{-1}\ K^{-1}}$ with silica. A 2011 study, reported by Kong et al. [119] compared the effects of different nano fillers (boron nitride, silicon nitride, and diamond) on the effective thermal conductivity of silicone rubber. A maximum filler volume fraction of $2\ \%$ was used, and they found a thermal conductivity enhancement of roughly 40 % compared with the pure silicone rubber. Harada et al. [171] studied the effects of boron nitride on the effective thermal conductivity of a liquid crystalline epoxy resin, achieving up to $2.5\ \mathrm{W\ m^{-1}\ K^{-1}}$ with $\phi = 0.35$.

In a polypropylene matrix, Muratov et al. [172] attained $0.469\ \mathrm{W\ m^{-1}\ K^{-1}}$ with a weight fraction of $33.7\ \%$ hexagonal boron nitride. In 2015 Gao et al. [122] studied the effects of different sized alumina particles in a silicone rubber managing well above $2\ \mathrm{W\ m^{-1}\ K^{-1}}$ with $\phi \approx 0.63$ using the largest filler particles. They found a reduction in effective thermal conductivity with decreasing particle size.

In a recent study, Liu und Li [130] evaluated the effects of aluminum, zinc oxide, silicon carbide, graphite, and aluminum nitride in a silicone oil based thermal grease. The highest thermal conductivity achieved was $1.55\ \mathrm{W\ m^{-1}\ K^{-1}}$ with aluminum in a filler weight fraction of $80\ \%$.

2.5.2 POLYMERS WITH HYBRID FILLER PACKINGS

Most studies of hybrid filler packings report on binary filler blends, where particle shape and chemistry differ among the filler components [121,130,170,175,176]. In 2006, Lee et al. [170] fabricated high density polyethylene composites, using not only single-scale filler packings but also several binary blends. The fibrous secondary fillers were expected to fill the gaps between the spherical aluminum nitride particles and generate more highly conductive thermal paths. They observed a clear enhancement in effective thermal conductivity when adding wollastonite and silicon carbide whisker to the aluminum nitride filler packing up to a total $\phi = 0.5$. The highest enhancement with almost $50\ \%$ increase was achieved at $\phi = 0.1$.

Zhou et al. [121] also did not limit their investigations to single-scale filler packings, but combined the silicon carbide particles with silicon carbide whiskers. In a silicone rubber matrix, they were able to achieve $1.57\ \mathrm{W\ m^{-1}\ K^{-1}}$ with $\phi = 0.5$ in total. An enhancement in thermal conductivity was observed for the entire investigated range of filler volume fractions. While a $10\ \%$ increase was achieved at a higher filler concentration ($\phi = 0.5$), an increase of over $40\ \%$ was attained at a lower concentration ($\phi = 0.3$).

In 2012 Pak et al. [176] studied the performance of a binary filler blend consisting of boron nitride particles and multi-wall carbon nanotubes in a polyphenylene sulfide matrix. With filler weight fractions of $50\ \%$ boron nitride and $1\ \%$ multi-wall carbon nanotubes, they achieved an effective thermal conductivity of $1.74\ \mathrm{W\ m^{-1}\ K^{-1}}$.

Akhtar et al. [175] studied the effects of an alumina graphene blend on the effective in-plane thermal conductivity of an anisotropically structured epoxy composite in 2017. $1.68\ \mathrm{W\ m^{-1}\ K^{-1}}$ were achieved with $\phi = 0.5$ of alumina and additionally one weight percent of graphene.

Finally, we return to the study by Liu and Li [130], as they investigated not only single-scale filler packings, but also multi-scale and hybrid filler packings. A combination of similar sized spherical aluminum and irregular shaped aluminum nitride particles with weight fractions of $75\ \%$ and $10\ \%$ led to the achievement of $1.982\ \mathrm{W\ m^{-1}\ K^{-1}}$ in silicone oil.

2.5.3 POLYMERS WITH MULTI-SCALE FILLER PACKINGS

There are numerous options for creating multi-scale filler packings. However, it is noticeable that numerous studies report on pure alumina filler packings with three size classes [167,177,178].

In addition to studying the effects of zinc oxide in single-scale filler packings, Mu et al. [120] also combined the fillers in binary blends and attained up to $0.56\ \mathrm{W\ m^{-1}\ K^{-1}}$ with $\phi \approx 0.32$. Yung and Liem [179] presented castable epoxy resins filled with fine grained hexagonal boron nitride and coarse-grained cubic boron nitride fillers in 2007. Their impressive result of $19\ \mathrm{W\ m^{-1}\ K^{-1}}$ was achieved with only $\phi = 0.265$. In their earlier introduced study, Zhou et al. [167] combined the alumina fillers of four different size classes in binary, ternary, and quaternary blends. The highest thermal conductivity achieved was $1.45\ \mathrm{W\ m^{-1}\ K^{-1}}$ at $\phi = 0.64$.

The study by Zhou et al. [121] from 2008 has already been presented in section 2.5.1 for single-scale filler packings and in section 2.5.2 for hybrid filler packings. In addition, Zhou et al. tested a binary combination of fine and coarse-grained silicon nitride. They achieved $1.48\ \mathrm{W\ m^{-1}\ K^{-1}}$ with $\phi = 0.5$ in an optimal weight ratio of $40{:}\ 60$ for the coarse to fine-grained filler fractions.

Using a very high filler volume fraction of $\phi = 0.8$, Hong et al. [180] fabricated an epoxy composite with an effective thermal conductivity of $8\ \mathrm{W\ m^{-1}\ K^{-1}}$. They have combined aluminum nitride and boron nitride fillers in binary blend of volumetric ratio $1{:}\ 1$.

In 2013, Choi and Kim also reported on a variation of binary filler blends consisting of alumina and aluminum nitride [181]. The higher performance of $3.40\ \mathrm{W\ m^{-1}\ K^{-1}}$ was attained with aluminum nitride in the larger size class and alumina in the smaller size class, using in total $\phi = 0.584$ in a ratio of $7{:}\,3$ for the coarse to fine-grained filler fractions.

Mao et al. [182] focused on creating a composite with low viscosity in the liquid state and therefore combined three size classes of spherical aluminum in 2018. With $\phi = 0.5$, $1.381\ \mathrm{W\ m^{-1}\ K^{-1}}$ was achieved in a silicone rubber.

In 2021, Su et al. [183] carried out a similar work using a polydimethylsiloxane as the matrix. They could only achieve $0.71\ \mathrm{W\ m^{-1}\ K^{-1}}$ with a filler volume fraction of $\phi = 0.6$. They also used three size classes of spherical aluminum. Further material developments with high effective thermal conductivities were published in 2021 by Li and Zheng [177] and in 2022 by Feng et al. [178]. In both studies, a ternary mixture of alumina was optimized using epoxy as a matrix. Li and Zheng [177] achieved an effective thermal conductivity of $6.7\ \mathrm{W\ m^{-1}\ K^{-1}}$ with $\phi = 0.79$ and Feng et al. [178] achieved $2.707\ \mathrm{W\ m^{-1}\ K^{-1}}$ with $\phi = 0.5$.

3 EXPERIMENTAL METHODS AND MATERIALS

In this chapter, the materials used in the experimental studies of this work are presented. Furthermore, this chapter introduces the two main experimental techniques applied. The steady-state cylinder method according to ASTM D5470-17 [184] was applied for thermal conductivity measurements. For thermal contact resistance measurements, a novel micro thermography technique was developed as part of this work [0]. This method will be introduced and discussed in chapter 3.3.

3.1 RAW MATERIALS AND THEIR CHARACTERISTICS

Different polymers, fillers, and substrates were used in the experimental studies of this work. The following sections provide tabular overviews of the materials and their basic properties.

3.1.1 POLYMERS

Four polymers were selected for the experimental studies, which are particularly suitable due to their processability as well as their thermal and mechanical properties. The assortment is comprised of an epoxy resin and three silicone rubbers, see **Table 3.1**. All materials are two-component systems that cure at room temperature. The aim was not to select polymers for possible applications, but to use neutral model systems. This limits the transferability of the results to explicit applications regarding the chemical interactions between polymers and fillers but is not a limitation for a systematic investigation of the predominantly geometric, microstructural effects of filler packings. In **Table 3.1**, the measured densities and thermal conductivities are listed for the cured state. The values provided were determined experimentally. Disc-shaped samples were prepared and analyzed using the buoyancy method[1] and the steady-state cylinder method (see chapter 3.2 for more information). In addition, **Table 3.1** lists the Shore hardness[2] of the cured polymers and the viscosity of the polymer mixtures according to the referenced data sheets. Epoxy E01 was chosen because it has a very low viscosity of $\eta = 500\ \mathrm{mPa\ s}$ at $298\ \mathrm{K}$ and high hardness in the cured state. The low viscosity enables higher filler concentrations, and the high hardness allows for grinding and thus the creation of micrographs. Also, no compression effects of the filled materials need to be considered if measurements are performed at an elevated surface pressure.

---

[1] Density measurements were performed using a Sartorius Semi-Micro - ME235S Balance with a YDK 01 density determination kit.

[2] Shore hardness describes the resistance of a material to indentation.

Table 3.1. Overview of polymers and their technical data.
All measurements were performed on samples after curing for seven days at room temperature. Densities were measured with the buoyancy method. Thermal conductivities were measured using the steady-state cylinder method, see chapter 3.2. Viscosity and hardness values were taken from the data sheet, see references.

ID	Name	Density ρ / g cm^{-3}	Thermal conductivity λ / W m^{-1} K^{-1}	Viscosity of mixture η / mPa s	Hardness Shore	Ref.
E01	Epoxy Resin SikaBiresin® TD150 – TD165	1.124 ± 0.001	0.25 ± 0.04	500	D80	[185]
S01	Silicone Rubber ELASTOSIL® RT 604 A/B	0.970 ± 0.001	0.22 ± 0.04	800	A25	[186]
S02	Silicone Rubber ELASTOSIL® RT 620 A/B	1.070 ± 0.001	0.25 ± 0.04	6000	A17	[187]
S03	Silicone Rubber ELASTOSIL® RT 625 A/B	1.095 ± 0.001	0.28 ± 0.05	12000	A25	[188]

The three silicone rubbers (S01-S03) were selected to determine the effect of polymer thermal conductivity in experimental studies. The thermal conductivities of the unfilled silicone rubbers are $\lambda = (0.22 \ldots 0.28)$ W m^{-1} K^{-1}. The given viscosities refer to the mixture of A and B components as specified in the data sheets at a temperature of 296 K. While the silicone rubbers were processed unmodified, two additives were used for epoxy E01. Up to 3 wt% fumed silica powder[3] was added to prevent the sedimentation phenomena that otherwise occur at lower filler concentrations. Fumed silica powder gives the polymer thixotropic properties. Impacts on the thermal conductivity could only be resolved in measurements with > 5 wt%. For samples with high filler concentrations, close to the maximum packing density, the wetting and dispersing agent BYK-W 996[4], a solution of a copolymer with acidic groups, was added with up to 1.5 % of the filler mass. In a preliminary study, no measurable effect on thermal conductivity was observed, so the function and impact of the dispersing agent are not further considered. However, dispersing agents

---

[3] HP-PK22 from HP-Textiles GmbH [189]

[4] BYK-W 996 from BYK-Chemie GmbH, Germany [190]

and other surfactants generally influence the particle-polymer interface by lowering surface tension, potentially reducing agglomeration, and thereby changing the composite structure. Consequently, certain material combinations may have a thermal conductivity that depends on the type and use of the surfactant.

3.1.2 FILLERS

The central objective of this work is to investigate the effects of the microscopic packing structure of filled polymers on their effective thermal conductivity. Therefore, fillers with significantly different property profiles are investigated in the experimental studies. **Table 3.2** lists the fillers and their basic properties.

Table 3.2. Overview of fillers and their technical data.
Particle size data was measured using a laser particle sizer Fritsch Analysette 22 NanoTec. Particle densities were measured using a liquid pycnometer. Thermal conductivity data is based on the general material data from **Figure 2.5**, page 22.

			Particle size D_{10} D_{50} / µm D_{90}	**Thermal conductivity**	**Particle density**
ID	**Name**	**Morphology**	S_{V} / µm^{-1}	λ / W m^{-1} K^{-1}	ρ / g cm^{-3}
Alox-S-01	Alumina Bestry BAK-1	spherical	0.3 1.1 2.7 2.22	35	3.457 ± 0.006
Alox-S-08	Alumina Sibelco Boratherm™ SA0050	spherical	2.7 7.9 18.0 0.39	35	3.851 ± 0.047
Alox-S-22	Alumina Sibelco Boratherm™ SA0200N	spherical	7.7 22.2 43.8 0.15	35	3.772 ± 0.021
Alox-S-40	Alumina Sibelco Boratherm™ SA0380	spherical	12.8 40.1 74.1 0.09	35	3.858 ± 0.027
Alox-S-63	Alumina Sibelco Boratherm™ SA0700	spherical	24.1 63.4 106.9 0.07	35	3.790 ± 0.010

ID	**Name**	**Morphology**	**Particle size** D_{10} D_{50} / μm D_{90} S_{V} / μm^{-1}	**Thermal conductivity** λ / W m^{-1} K^{-1}	**Particle density** ρ / g cm^{-3}
ATH-I-75	Aluminum hydroxide Sibelco Portaflame™ SG200E	irregular	31.5 74.6 120.8 0.06	10	2.454 ± 0.040
Siox-S-03	Silica Sibelco Megasil® SS-0030	spherical	1.2 3.3 10.3 0.06	1.4	2.084 ± 0.070
Al-S-06	Aluminum Eckart CoolSpheric S5	spherical	3.2 6.2 10.7 0.57	150	2.842 ± 0.025
Al-S-22	Aluminum Eckart CoolSpheric S20	approx. spherical	12.5 21.5 34.8 0.20	150	2.786 ± 0.050
Al-S-45	Aluminum n.n. lab sample	spherical	27.6 44.6 68.4 0.11	150	2.864 ± 0.003
Al-I-88	Aluminum Eckart CoolSpheric N100	irregular	48.6 87.7 140.5 0.04	150	2.875 ± 0.073
Al-I-103	Aluminum n.n. lab sample	irregular	50.9 103.1 202.9 0.03	150	2.640 ± 0.015

For simplicity, each filler is assigned a unique ID containing information on the material (Alox - Alumina, ATH - Aluminum hydroxide, Siox - Silica, Al - Aluminum), the particle shape (S -Spherical, I - Irregular), and the mean particle size. Most of the fillers are commercially available materials that are relevant for practical applications. Manufacturer and trade name are listed in column two. Only two fillers are lab samples that cannot be specified further. The particle sizes are given in **Table 3.2** using the percentile values D_{10}, D_{50}, and D_{90}, which are derived from the measurements of the particle size distribution. For evaluation, the Fraunhofer diffraction theory was applied (see e.g., [191]). In the case of spherical fillers, the measured particle sizes correspond to the particle diameter, while irregularly shaped particles are specified by the laser diffraction equivalent diameter. Matsuyama und Yamamoto [191] discuss the meaning of this equivalent parameter and its influence on particle size distribution. D_{10}, D_{50}, and D_{90} indicate the particle sizes below which $10\ \%$, $50\ \%$ and $90\ \%$ of the particle volume is present. The specific surface area S_{V} of the fillers is also given, which was calculated from the size distribution under the simplified assumption of a spherical particle shape and a smooth particle surface for all fillers. Basically, it is the particle surface area in relation to the particle volume.

The thermal conductivities of the filler particles are based on the literature ranges shown in **Table 2.1**, page 23. The actual values may differ due to purity, porosity, crystallinity, and in the case of aluminum, depend on surface oxidation and alloying elements. Measuring the thermal conductivity of the filler particles is difficult due to their small size and inhomogeneous structure. While local methods such as Raman thermography, as demonstrated by Stoib et al. in 2014 [192] and more recently by Özden et al. [193] on small iron sulfide crystals, may be applicable in some cases, they require homogeneous and isotropic materials. The fillers used in this work do not fulfill these conditions.

In view of these constraints, the decision has been made to use representative literature values (**Table 3.2**) for modeling and simulation in this work. This can be justified by the fact, that the exact thermal conductivity of the filler material plays a minor role for the effective thermal conductivity of the composite (see chapter 4.4). Rather, geometric factors such as particle distribution and packing density tend to dominate the effective thermal conductivity. Therefore, the use of approximate reference values appears sufficient for the purposes of this work.

The respective particle density, required for sample preparation, is given in the last column of **Table 3.2**. Measurements were performed using a pycnometer with a total volume of approximately $27\ \mathrm{ml}$ and ethanol as the reference liquid. The varying densities of the fillers, also within a material type, are due to different purities and porosities of the fillers. **Figure 3.1** additionally shows laser scanning microscopic images of all fillers listed in **Table 3.2**. All individual images have been created with the same setup and show the fillers at the same magnification. The selection contains fillers of different size classes (compare Alox-S-01 and Alox-S-63), with a very broad size distribution (see Alox-S-22 and Alox-S-40), and a clearly different particle morphology (compare Alox-S-63, ATH-I-75, and Al-I-88).

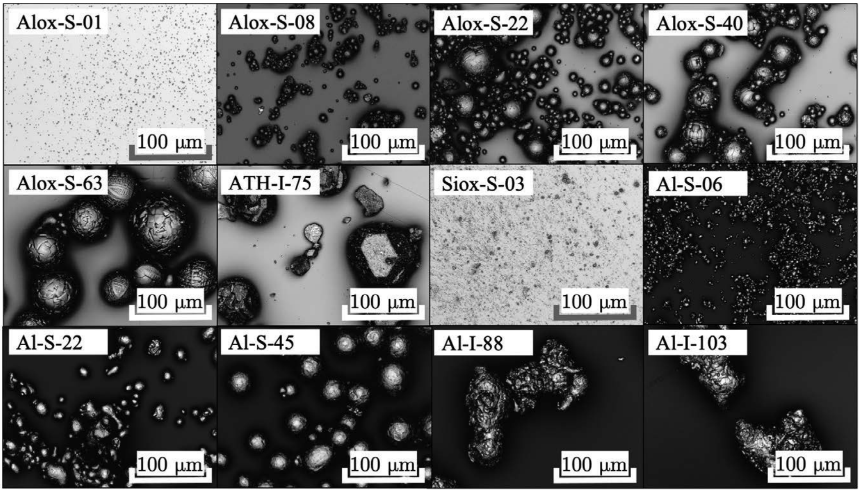

Figure 3.1. Laser microscopic images of fillers.
Images taken with a Keyence 3D laser scanning microscope VK-X100K with a 100x magnification lens.

3.1.3 SUBSTRATES

This section presents the substrates used in the experimental studies on heat conduction across filled polymer to substrate transitions (FPS transitions). These were made of aluminum sheet metal (AlMg3; EN AW-5754) with a thickness of $2\ \mathrm{mm}$. The thermal conductivity of the alloy used is $\lambda_{\mathrm{S}} = 130\ \mathrm{W\ m^{-1}K^{-1}}\ \pm 5\ \%$ at $300\ \mathrm{K}$ [194]. Different surface structures were created by grinding or sandblasting. The resulting surface characteristics can be described using the surface parameters from DIN EN ISO 25178-2:2023-09 [195]. For the evaluation and further reconstruction, the surface structure of the prepared substrates was digitized with a laser scanning microscope[5]. The surface height $z(x, y)$ was measured with an x and y step size of $0.68\ \mathrm{\mu m}$ at a z resolution of $0.05\ \mathrm{\mu m}$ and exported in tabular form. **Figure 3.2** visualizes the digitized surface structures and shows an illustrative light microscopic image of the corresponding surface. A unique ID is defined for each substrate type for simpler further reference. SUB-R0 was prepared by grinding with P800 silicon carbide (SiC) sandpaper, while SUB-R1 to SUB-R4 were prepared by sandblasting. The sandblasting was performed with glass beads of different grades, through an $8\ \mathrm{mm}$ nozzle with a blasting pressure of $0.5\ \mathrm{MPa}$. For SUB-R1 to SUB-R4, glass beads of increasing size from $(40 \ldots 70)\ \mathrm{\mu m}$ up to $(400 \ldots 600)\ \mathrm{\mu m}$ were used. Further details follow in **Table 3.3**, page 48. The increasing coarseness of the substrate surfaces is visible

---

[5] Keyence 3D laser scanning microscope VK-X100K with a 20x magnification lens

in both the height profiles and the microscopic images in **Figure 3.2**. **Figure 3.3** illustrates the evaluation of the surface parameters according to DIN EN ISO 25178-2:2023-09 [195] based on the measured height data $z(x, y)$. The surface's central plane is defined as the reference plane ($z = 0$), ensuring that the arithmetic mean of all height values is zero.

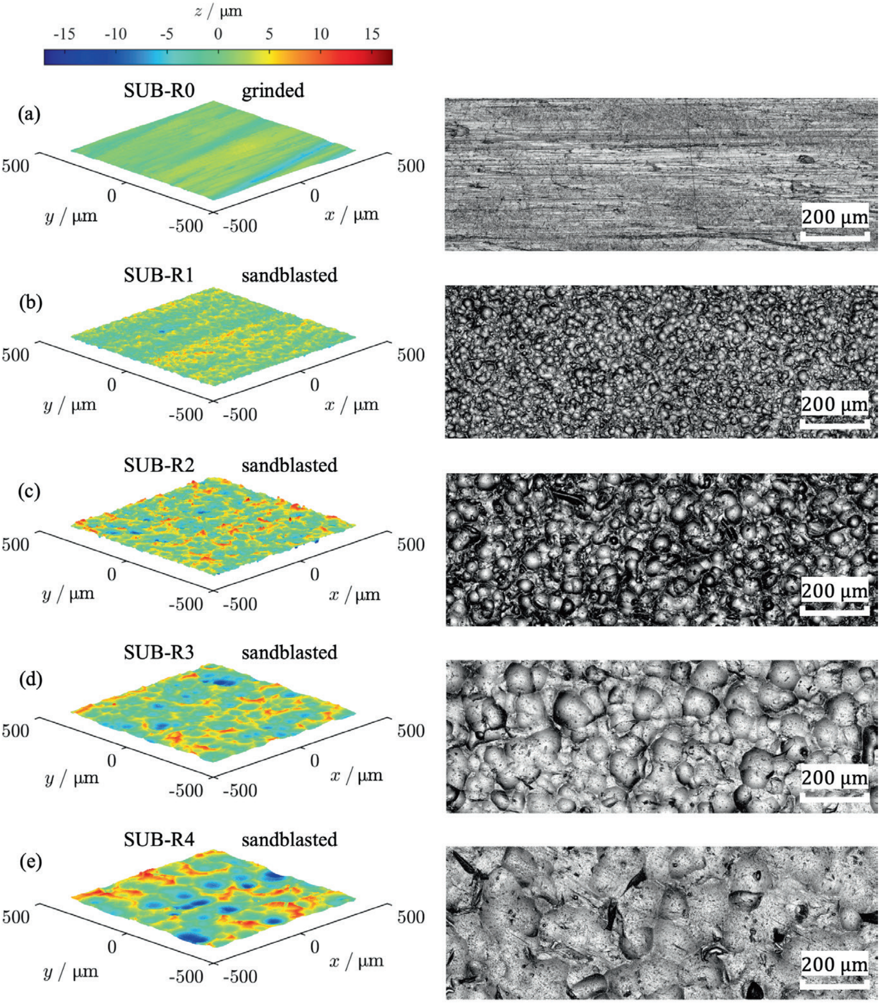

Figure 3.2. Height profile and microscopic images of aluminum substrates.
Height data and images taken with a Keyence 3D laser scanning microscope VK-X100K with a 20x magnification lens.

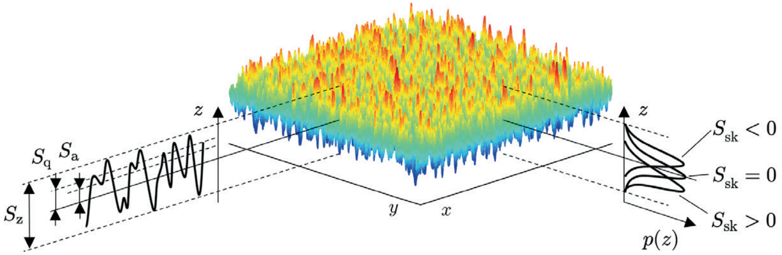

Figure 3.3. Illustration of surface parameters.
Simplified representation of the surface parameters according to DIN EN ISO 25178-2:2023-09 [195]. The evaluation is based on the complete surface and not on the simplified illustrative extracted two-dimensional profile.

Three height parameters are derived from the measured data. The maximum height

$$S_\mathrm{z} = \max(z(x,y)) - \min(z(x,y)) \tag{3.1}$$

describes the maximum distance between the highest asperity and the lowest valley of the analyzed area A. The prepared substrates exhibit a maximum height of $S_\mathrm{z} = (14.294 \ldots 60.685)\ \mu\mathrm{m}$.

$$S_\mathrm{a} = \frac{1}{A} \iint_{\tilde{A}} |z(x,y)|\ \mathrm{d}x\mathrm{d}y \tag{3.2}$$

describes the arithmetic mean height of the surface, calculated as an integral mean value over the evaluation area $\tilde{A}$ [195]. Arithmetical mean heights of $S_\mathrm{a} = (1.382 \ldots 3.562)\ \mu\mathrm{m}$ were evaluated for the prepared substrates.

The root mean square roughness [195]

$$S_\mathrm{q} = \sqrt{\frac{1}{A} \iint_{\tilde{A}} z^2(x,y)\ \mathrm{d}x\mathrm{d}y} \tag{3.3}$$

is the square root of the mean squared height values. $S_\mathrm{q} = (1.796 \ldots 4.458)\ \mu\mathrm{m}$ was evaluated for the utilized substrates. In addition, the skewness of the surfaces is evaluated with [195]

$$S_\mathrm{sk} = \frac{1}{A\ S_\mathrm{q}^3} \iint_{\tilde{A}} z^3(x,y)\ \mathrm{d}x\mathrm{d}y\ . \tag{3.4}$$

For a symmetrical probability distribution $p(z)$ of the height data, $\mathrm{S_{sk}}$ becomes zero, see **Figure 3.3**. For a distribution shifted in the direction of positive heights, $\mathrm{S_{sk}} < 0$ is evaluated, while for a distribution shifted in the direction of negative heights, $\mathrm{S_{sk}} > 0$ is evaluated. The ground surface SUB-R0 has a clearly negative skewness of $\mathrm{S}_{\mathrm{sk}} = -0.9747$. The sandblasted surfaces exhibit the typical skewness of $\mathrm{S}_{\mathrm{sk}} \approx 0$, which is expected due to their typical Gaussian height distribution [196]. To additionally characterize the spatial structure of the surfaces, the autocorrelation length S_{al} is evaluated and listed in **Table 3.3**. According to DIN EN ISO 25178-2:2023-09 [195], the autocorrelation function $f_{\mathrm{ACF}}(t_x, t_y)$ is calculated with

$$f_{\mathrm{ACF}}(t_x, t_y) = \frac{\frac{1}{B}\iint_{\widetilde{B}} \; z(x,y) z(x+t_x, y+t_y) \;\, \mathrm{d}x\mathrm{d}y}{\frac{1}{A}\iint_{\tilde{A}} \; z^2(x,y) \;\, \mathrm{d}x\mathrm{d}y} \, . \tag{3.5}$$

It describes the correlation of a surface with the same surface displaced by (t_x, t_y), where $\widetilde{B}$ is the intersection of the correlated surfaces at the displacement (t_x, t_y) [195]. The autocorrelation length is the smallest horizontal distance at which the autocorrelation function decays to a specified value s. It is evaluated with [195]

$$S_{\mathrm{al}} = \min_{t_x, t_y \in R} \sqrt{t_x^2 + t_y^2} \, , \tag{3.6}$$

where $R = \{(t_x, t_y)\colon f_{\mathrm{ACF}}(t_x, t_y) \leq s\}$. The threshold $s = 0.2$ is set according to DIN EN ISO 25178-3:2012-11 [197]. **Table 3.3** summarizes the preparation parameters and the surface characteristics of the substrates used within the scope of this work. Each surface preparation results in a characteristic property profile of the substrate. In the case of sandblasted substrates SUB-R1 to SUB-R4, the application of coarser blasting material leads to a coarser lateral surface structure and thus an increasing autocorrelation length S_{al}. The surface height characteristics however, are only partially dependent on the grain size of the blasting material used. There is a tendency towards increasing height parameters for coarser blasting abrasives, but SUB-R2 has by far the greatest maximum height $S_{\mathrm{z}} = 60.685\ \mu\mathrm{m}$. The root mean square roughness for SUB-R2 as well as the arithmetical mean height hardly differ from those of the SUB-R4 substrate. In general, the prepared substrates cover a wide range of surface characteristics. The sample preparation using the presented substrates is described in section 3.3.3.

Table 3.3. Overview substrates and surface parameters.
Preparation parameters and surface parameters of five substrates made from aluminum alloy AlMg3. Surface parameters derived from measured surface height profile, see **Figure 3.2**.

		Height	**Skewness**	**Auto correlation length**
ID	**Surface preparation**	S_z S_a / µm S_q	S_{sk} / −	S_{al} / µm
SUB-R0	Grinding SiC P800	14.294 1.382 1.796	−0.9747	36.47
SUB-R1	Sandblasting Glass beads (40 ... 70) µm	29.703 2.025 2.540	−0.0106	26.68
SUB-R2	Sandblasting Glass beads (90 ... 150) µm	60.685 3.526 4.445	−0.0832	37.66
SUB-R3	Sandblasting Glass beads (200 ... 300) µm	32.208 2.863 3.618	−0.0387	50.32
SUB-R4	Sandblasting Glass beads (400 ... 600) µm	36.441 3.562 4.458	−0.1681	72.79

3.2 MEASURING THERMAL CONDUCTIVITY WITH THE STEADY-STATE CYLINDER METHOD

After an introduction to the basics of thermal conductivity measurements, the specific apparatus used in this work is presented. Following is then a description of the evaluation method including exemplary measurement results. Finally, the uncertainties of the steady-state cylinder method are discussed.

3.2.1 INTRODUCTION TO THERMAL CONDUCTIVITY MEASUREMENTS

To determine the thermal conductivity of a sample, it must be exposed to a temperature difference and the resulting heat flow measured. Alternatively, a heat flow is applied and the resulting temperature difference measured. Depending on the characteristics of the sample material, the magnitude of its thermal conductivity, and its dimensions, there are various measurement methods available. Following [32,38,41], these methods can generally be divided into:

- steady-state methods, and
- transient methods.

In the case of steady-state methods, time-invariant temperature differences or heat flows are imposed. Transient methods are characterized by applying or measuring temporally varying signals. These can be pulses, steps, or periodic functions. In general, measurements with steady-state boundary conditions take longer time, as it is necessary to wait until the temperature field in the sample and measurement setup is stable. Transient measurements can be carried out much faster. Recent review articles summarize state-of-the-art methods for e.g., filled polymer composites [6], insulating materials [198], thermoelectric materials [199], or energy storage materials [200]. In principle, the methods are all very similar, but adapted in detail to the respective sample properties and characteristics. In principle, only thermal conductivity can be determined with steady-state methods, whereas the transient methods also allow for analysis of thermal storage effects, described by the specific heat capacity c. The measured quantity is thus sometimes the thermal diffusivity, defined as

$$a = \frac{\lambda}{\rho \, c} , \tag{3.7}$$

where ρ denotes the density of the material. The most common transient techniques are the 3 - ω - method, the transient hot wire, bridge, and disc methods, as well as the laser flash analysis. The 3 - ω - method proposed by Cahill [201,202] is based on a periodic heating signal, and is particularly suitable for thin layers. An alternating current at angular frequency ω is applied to a metal line on the sample surface, causing a temperature oscillation. The resulting oscillating voltage response with frequency 3ω at the metal line is measured. Amplitude and phase shift of the voltage signal contain information about the thermal conductivity of the sample material.

Transient hot wire, bridge, and disc methods all work similarly but differ in the structure and function of the sensor. They have a specific sensor geometry subjected to an electrical current and thereby heated, for example in the case of the hot wire method, a thin wire. The temperature measured at the sensor over time is then a measurement for the thermal conductivity of the surrounding sample. If the temperature in the sensor increases faster with the same heating power, the surrounding sample has a lower thermal conductivity. The methods are specified e.g., in [203–205].

The last example to be mentioned is laser flash analysis, first introduced by Parker et al. in 1961 [206], and currently specified in e.g., ASTM E1461-13 (2022) [207], or DIN EN ISO 22007-4:2024-04 [208]. This method is also relevant in the context of this work, as it was used for method comparison, see section 3.3.7. In laser flash analysis, a sample is heated on one side with a laser or xenon light flash. On the opposite side, the temperature increase of the sample over time is determined in a contactless manner using an infrared detector. The thermal diffusivity of the material can be derived from this time-dependent temperature signal. Details on the method and the evaluation can be found in [206]. If the heat capacity is known, or also measured, the thermal conductivity of the material can be determined using **Eq. (3.7)**.

Steady-state methods are all based on the same general idea. A time-invariant heat flux is applied to the samples in a one-dimensional manner, and the resulting temperature drop along the sample is determined. The ratio of the temperature difference to the heat flux is the sample's specific thermal resistance; and from this, the thermal conductivity can be obtained. A distinction can be made based on the direction of the heat flow. There are some methods in which longitudinal heat flow is applied, while in others a radial heat flow results from the internal heating and external cooling of a circular sample [38].

Since all methods are based on the same theory, no further description of the individual specifications is provided. For filled polymers and in particular thermal interface materials (TIMs), the steady-state cylinder method has been established, as specified in ASTM D5470-17 [184]. The measurement range is well suited for testing filled polymer composites, and equally suitable for testing viscous liquids and elastic to rigid solids. It was used to determine the thermal conductivity of filled polymers in e.g., [122,130,169,177]. A detailed introduction to the measuring apparatus and the measurement principle follows in the next sections.

3.2.2 MEASUREMENT PRINCIPLE AND APPARATUS

A commercially available steady-state apparatus (TIM-Tester[6]) was used to perform measurements according to ASTM D5470-17 [184]. The device is designed to determine the thermal resistance of thermal interface materials (TIMs) in the form of thermal grease, sheets, or pads. **Figure 3.4** shows a picture of the measuring section and illustrates the general measurement principle. The sample is placed between two cylindrical aluminum bars, referred to as heat flow meter bars in [184], as they not only apply a heat flow through the sample but are also used to determine it. An electric heater heats the upper side of the upper bar to a constant hot temperature T_h, while the lower side of the lower bar is kept at a constant cold temperature T_c through a coolant mass flow. Neglecting lateral heat losses along the measuring section between heater and coolant, the heat flow through upper and lower bar as well as the sample is assumed to be one-dimensional. The heat flow through the sample can be described as heat flow through an infinitely extended plate.

---

[6] TIM-Tester: Device for measuring thermal resistances according to ASTM D5470-17. Built and distributed by [Center for heat management] Zentrum fuer Waermemanagement (ZFW), 70174 Stuttgart, Germany.

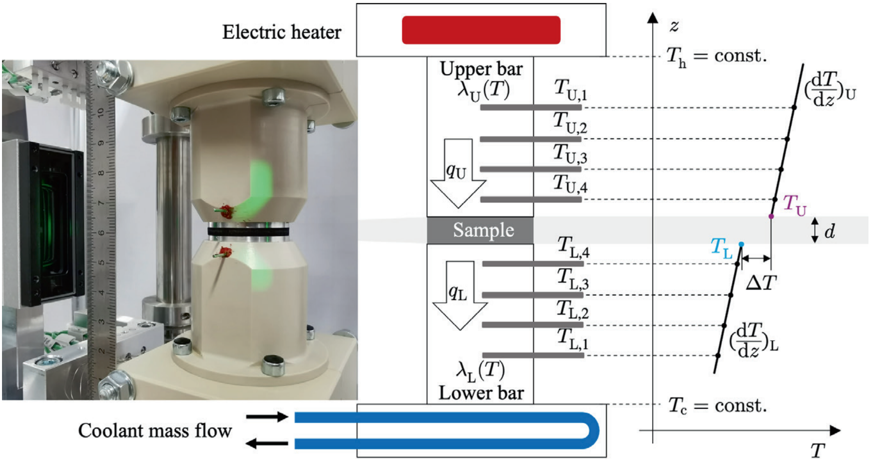

Figure 3.4. Measuring section of TIM-Tester and measurement principle.

As **Figure 3.4** illustrates, the temperature in the aluminum bars decreases linearly from top to bottom. Four thermocouples are mounted in both the upper and lower bars. Using the measured temperatures $T_{\mathrm{U},i}$ and $T_{\mathrm{L},i}$ with the z coordinates of the thermocouples, a linear regression can be performed for the lower and the upper bar. The temperature profiles in the two bars are then extrapolated to the surface of the aluminum rods using linear relationships with the constant gradients $(\frac{\mathrm{d}T}{\mathrm{d}z})_\mathrm{U}$ and $(\frac{\mathrm{d}T}{\mathrm{d}z})_\mathrm{L}$, allowing for calculation of the temperatures T_U and T_L at the contact surfaces to the sample. Using four thermocouples, the accuracy of the method is improved, and measurement errors can be compensated for. Both the aluminum bars and the sample have the same heat-transferring cross-sectional area. The measurements are carried out under steady-state conditions. All measured values are constant over time. The heat flux in the upper bar is evaluated as

$$q_\mathrm{U} = -\lambda_\mathrm{U}(T)\left(\frac{\mathrm{d}T}{\mathrm{d}z}\right)_\mathrm{U} , \tag{3.8}$$

where $\lambda_\mathrm{U}(T)$ is the well-known temperature-dependent thermal conductivity of the aluminum, from which the upper bar is fabricated. For the lower bar the heat flux is evaluated as

$$q_\mathrm{L} = -\lambda_\mathrm{L}(T)\left(\frac{\mathrm{d}T}{\mathrm{d}z}\right)_\mathrm{L} , \tag{3.9}$$

where $\lambda_\mathrm{L}(T)$ is again the thermal conductivity of the aluminum. Both heat fluxes should be the same when one neglects heat loss; however, in reality the lateral heat loss leads to deviations from this equality. For further evaluation, the heat flux through the sample is therefore calculated as the mean value of the upper and lower heat flux with

$$q = \frac{q_\mathrm{U} + q_\mathrm{L}}{2} \, . \tag{3.10}$$

Finally, the overall specific thermal resistance of the sample is evaluated as

$$r = \frac{T_\mathrm{U} - T_\mathrm{L}}{q} = \frac{\Delta T}{q} \, , \tag{3.11}$$

assuming equal heat-transferring cross-sectional areas in aluminum bars and sample. This resistance value contains the contact resistances between the sample and aluminum bars. For this reason, it cannot be used directly to evaluate the thermal conductivity of a bulk material. The further evaluation procedure is described in section 3.2.5. The thickness of the sample is also required for this, which is determined in-situ. A laser micrometer is installed for this purpose, which continuously measures the distance between two reference pins attached to the aluminum bars near the sample. The zero point of this measuring system is set at the beginning of each series of measurements at the relevant contact pressure and temperatures to minimize the effects of thermal expansion and compression set.

The diameter of the aluminum bars is $30\ \mathrm{mm}$ and the length of the cylindrical segment is $60\ \mathrm{mm}$. The upper cylinder is fixed, and the lower cylinder is positioned by a hydraulic lifting unit. This allows a constant surface pressure to be applied to the specimen. A load cell is installed above the heated bar for control purposes. To compensate for angular misalignments between the two aluminum bars or imperfectly flat specimen surfaces, the upper bar is equipped with a floating mount and can adapt to the specimen or the lower cylinder when surface pressure is applied.

3.2.3 SAMPLE PREPARATION

The thermal conductivities of the filled polymers prepared in this study were determined solely in the cured state. While the steady-state cylinder method also permits measurements on uncured, pasty samples, preliminary studies have shown that better reproducibility is achieved with cured samples. Sedimentation may occur during measurement, particularly in samples with low filler content, which can significantly distort the measurement result. An additional advantage of analyzing cured samples is the ability to prepare cross-sections of the microstructure for further investigation. As the investigation of microstructural influences is the focus of this work, this is an important advantage. **Figure 3.5** illustrates the sample preparation process. After weighing the components (liquid polymer A+B component, fillers, additives, see chapter 3.1), these were first mixed and then degassed in a vacuum chamber, see parts (a) and (b). A maximum volume of $70\ \mathrm{ml}$ per mixture was created. The composites were placed in open containers and kept in a vacuum chamber for about ten minutes at room temperature and approx. $0.8\ \mathrm{Pa}$. The resulting mixtures ranged from a liquid to paste-like consistency, based on the filler concentration.

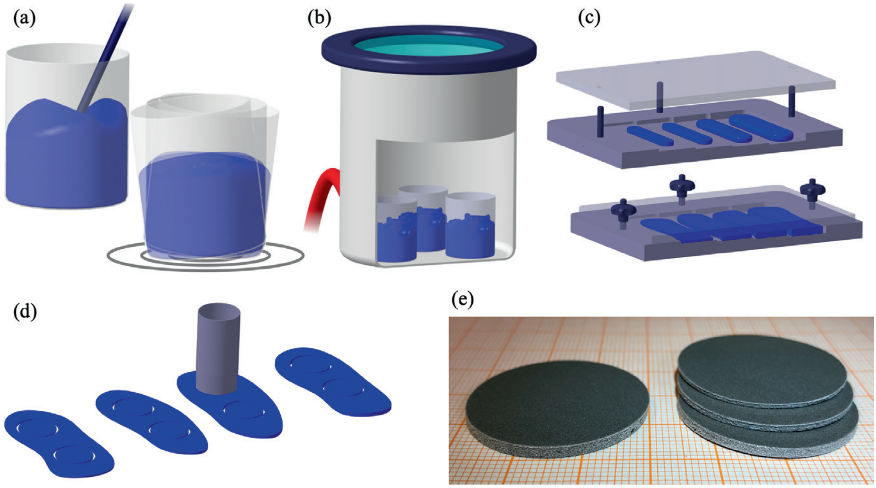

Figure 3.5. Sample preparation for steady-state cylinder method.
The composites are mixed manually and with a vortex shaker Vortex-Genie™ 2 from Scientific Industries SI™ (a). The composites are then degassed in a vacuum chamber (b). The samples are cured into sheets in an aluminum mold (c). Discs are cut out of the cured sheets (d). Samples of different thicknesses are prepared for measurements using the steady-state cylinder method (e).

The mixtures were then poured into a mold within a few minutes, ensuring the time was well below the pot life of the polymers, see part (c) of **Figure 3.5**. The mold is made of aluminum and covered with Polytetrafluoroethylene (PTFE) foil for better extraction of the samples. It has various mold shells in which the composites were cured to sheets of $n = 4$ different thicknesses. The thicknesses varied depending on the characteristics of the composite and were typically between $0.5\ \mathrm{mm}$ and $3.0\ \mathrm{mm}$. The samples were cured at room temperature, without applying surface pressure. The curing duration was determined in a preliminary study and chosen based on the longest curing time required for epoxy E01 (see **Table 3.1**, page 40). Within the first five days, there was a measurable change in the thermal conductivity and Young's modulus. To ensure full crosslinking and account for possible variations in environmental conditions or material properties, two additional days were added, resulting in a total curing time of seven days prior to further processing. After curing the sheets, they were cut to discs with a diameter of $\left(30^{+0.5}_{-0.0}\right)\ \mathrm{mm}$, see parts (d) and (e) of **Figure 3.5**. Preliminary studies have shown that the diameter tolerance of the samples does not have a significant effect with the typical thermal conductivities $\leq 6\ \mathrm{W\ m^{-1}\ K^{-1}}$, as the spreading effect is not yet pronounced compared to the highly conductive aluminum bars of the apparatus.

All samples with silicone rubber as the polymer matrix were placed directly on the aluminum bars of the measurement apparatus. For the samples with the comparatively rigid epoxy matrix, a 1: 1 water-glycol mixture was applied as a contact agent between samples and aluminum bars. While the soft silicone-based samples are good at compensating for surface irregularities, the epoxy-based samples had the contact agent reducing the thermal contact resistance between the sample and the aluminum bars.

Process-related uncertainties occur when weighing the components. For each sample, the actual masses were recorded, and the corresponding filler volume fractions were recalculated accordingly. The filler volume fractions reported in the following refer to these corrected values and are therefore presented without the remaining small uncertainty for the sake of simplicity.

3.2.4 MEASUREMENT PROCEDURE

This chapter briefly summarizes the applied parameters and environmental conditions present during the performed measurements. The apparatus was operated in a room with controlled environmental conditions. Within this room, the temperature was kept at (25 ± 1) °C, and the relative humidity at $(50 \pm 10)\ \%$. Before each series of measurements, the heater and cooler of the apparatus were pre-tempered for at least two hours so that the temperatures of all components stabilized. After the thickness measurement was tared, the samples were placed between the aluminum bars and the desired surface pressure was applied. For the rigid epoxy samples, $2\ \mathrm{MPa}$ was applied and for the more softer silicone samples, $(0.02 \ldots 0.1)\ \mathrm{MPa}$ was set. The higher the pressure, the lower the thermal contact resistance between the sample and the aluminum bars. In the case of soft samples, the pressure can simultaneously lead to significant compression of the sample, and therefore a noticeable change in its thermal conductivity. In a preliminary study, the effects of surface pressure were determined, and a material-dependent surface pressure was defined that lies within a range of low sensitivity.

Next, steady-state conditions were allowed to stabilize before the actual measurement. Following [184], the temperatures in the aluminum bars must not change by more than $\pm 0.1\ \mathrm{K}$ within five minutes. Once the specified thermal equilibrium is reached, the measurement can be triggered. The specific thermal resistance of the sample is calculated from the measured temperatures and stored together with the thickness, the applied pressure, an estimation of the systematic measurement uncertainty $\Delta r_{i,\mathrm{SYS}}$, and the other boundary conditions by the apparatus control software for further processing. Measurements were carried out at an average sample temperature of (25 ± 1) °C. This is done using a heater and cooler temperature setting of $T_{\mathrm{h}} = 311\ \mathrm{K} /\ T_{\mathrm{c}} = 285\ \mathrm{K}$ (38 °C / 12 °C). $n = 4$ samples of different thicknesses were analyzed for each composite.

3.2.5 EVALUATION

The measured values are subsequentially evaluated. The specific thermal resistances $r_i \pm \Delta r_{i,\mathrm{SYS}}$ and the in-situ measured thicknesses d_i for all $n = 4$ samples are used. The measured specific thermal resistances also include the thermal contact resistances towards the aluminum bars, so that only the apparent thermal conductivity, as defined in **Figure 2.3**, page 18, can be calculated with the individual measured values. It is obtained using

$$\lambda_{\mathrm{app},i} = \frac{d_i}{r_i} \; . \tag{3.12}$$

Assuming that the thermal conductivity and contact resistances are identical for all measured samples of varying thicknesses, a linear increase in specific thermal resistance with sample thickness can be expected. This assumption is valid when the sample thickness is much larger than the characteristic dimensions of the microstructure and the surface structure remains consistent.

A linear regression is performed, using the four measured specific thermal resistances and the corresponding thicknesses. The specific thermal resistance is expressed as

$$r(d)_{\mathrm{fit}} = \alpha_0 + \alpha_1 \; d \; . \tag{3.13}$$

Details on the calculation of the regression parameters α_0 and α_1 can be found in appendix B.1. Based on **Eq. (3.12)**, the thermal conductivity of the bulk material can be determined as the inverse of the slope in **Eq. (3.13)**, not including the contact resistances, as

$$\lambda = {\alpha_1}^{-1}. \tag{3.14}$$

Figure 3.6, **Figure 3.7**, and **Figure 3.8** show the described evaluation for three exemplary measurements on samples with low, medium, and high thermal conductivity. The four measured data points of the specific thermal resistance for specimens of different thicknesses, and the corresponding systematic uncertainties are plotted.

Furthermore, the linear regression line is shown, according to **Eq. (3.13)**. The evaluated thermal conductivity, as well as a systematic and a random uncertainty component are specified in **Figure 3.6**, **Figure 3.7**, and **Figure 3.8**. The uncertainty calculation and a discussion of the measurement uncertainty contributions in the given examples can be found in section 3.2.6.

In addition, specific thermal contact resistances that have been evaluated form the measurement results are shown in the respective figures. The evaluation and discussion of these contact resistances are described in section 3.2.7.

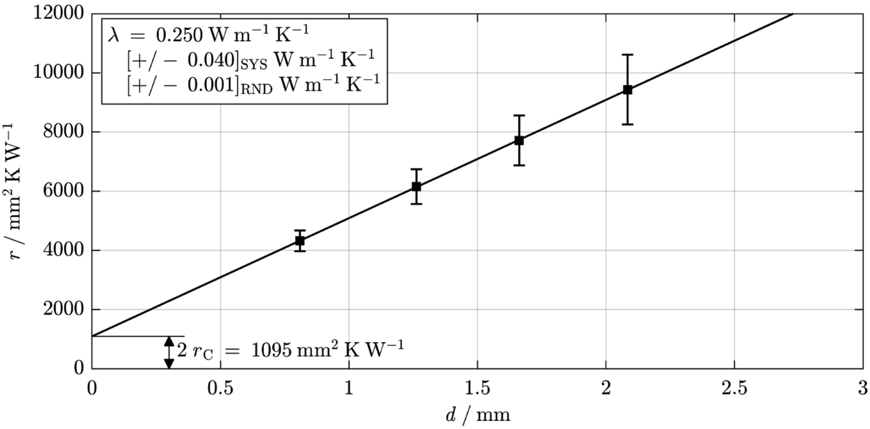

Figure 3.6. Evaluation of a thermal conductivity measurement of a sample with low thermal conductivity.

Exemplary measurement results for the unfilled, and cured epoxy E01.

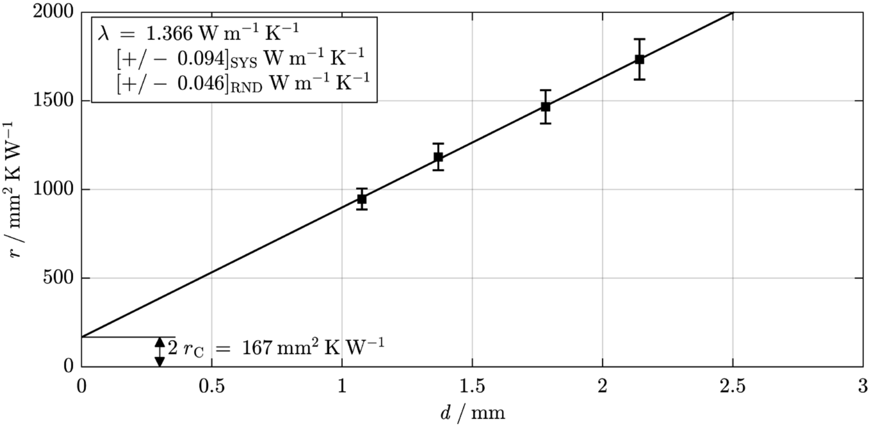

Figure 3.7. Evaluation of a thermal conductivity measurement of a sample with medium thermal conductivity.

Exemplary measurement results for a filled and cured epoxy composite. Polymer: Epoxy E01. Filler: Alumina, $\phi = 0.5$.

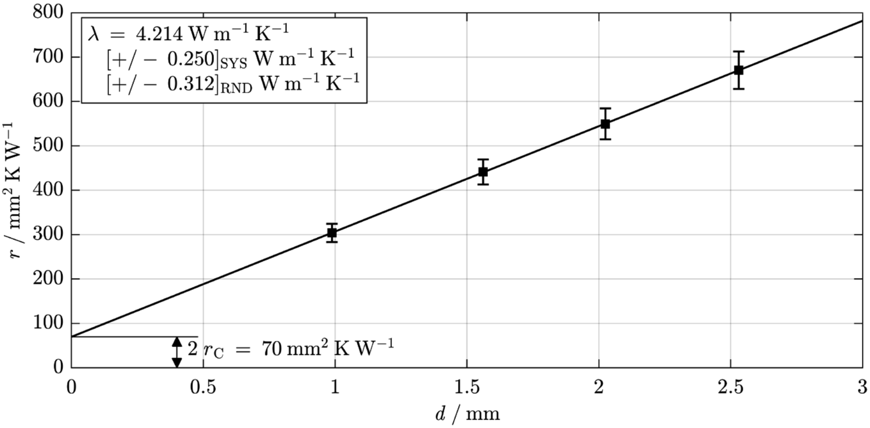

Figure 3.8. Evaluation of a thermal conductivity measurement of a sample with high thermal conductivity.

Exemplary measurement results for a filled and cured epoxy composite. Polymer: Epoxy E01. Filler: Aluminum and alumina blend, $\phi = 0.75$.

3.2.6 DISCUSSION OF MEASUREMENT UNCERTAINTIES

This section describes the origin and magnitude of the uncertainties when measuring with the steady-state cylinder method. In addition, the estimation of the total uncertainty of the primary target value, the thermal conductivity is presented. Random and systematic uncertainty components are processed separately. The systematic uncertainty evaluated for each obtained thermal conductivity is originally based on the internal uncertainty estimation in the control system of the "TIM-Tester". A systematic uncertainty component $\Delta r_{i,\mathrm{SYS}}$ is determined for each measured specific thermal resistance r_i. It is based on a superposition of the uncertainties originating from:

- the temperature measurement,
- the thermal conductivity of the aluminum bars,
- deviations in the aluminum bars' diameter,
- the thermocouples' positions, and
- a misalignment of the aluminum bars' center axis,

and evaluated, depending on heater and coolant temperatures. Comprehensive discussions of the uncertainties in the steady-state cylinder method can be found in [209–211]. The systematic uncertainty components in the measurements of this study were $\Delta r_{i,\mathrm{SYS}}/r_i = (6 \ldots 8)\ \%$ for most of the measured samples. An increase with very high thermal resistances occurs because the heat flow decreases and the effects of ambient losses increase [209]. With unfilled samples (e.g., **Figure 3.6**), this effect is already very pronounced and $\Delta r_{i,\mathrm{SYS}}/r_i \approx 12.5\ \%$ was evaluated for the thickest sample. For samples with very low thermal resistances, the uncertainty also increases, since the temperature drop across the sample is small and the impact of the uncertainties in the temperature extrapolation is large [209]. However, this range was not reached with the samples in this study. Systematic uncertainty in the determination of the sample thickness can be neglected, as this has no impact on the evaluation of the gradient of the function $r(d)_{\mathrm{fit}}$ to be evaluated. Appendix B.2 provides additional details on the uncertainty analysis and the uncertainty propagation procedures used to estimate both the systematic component $\Delta\lambda_{\mathrm{SYS}}$ and the random component $\Delta\lambda_{\mathrm{RND}}$ of the evaluated thermal conductivities.

The total uncertainty of the measurement can be expressed as the sum of the independent systematic and random components $\Delta\lambda_{\mathrm{SYS}}$ and $\Delta\lambda_{\mathrm{RND}}$. For easier interpretation, the values are given separately in the evaluations in **Figure 3.6**, **Figure 3.7**, and **Figure 3.8**. While the random uncertainties are not significant for the poorly thermally conductive sample in **Figure 3.6**, the systematic uncertainties are particularly large. As the thermal conductivity increases, the random uncertainties increase as well, but the systematic uncertainty decreases. There are two reasons for this. First, the general random uncertainty of $\Delta r_{\mathrm{RND}} \approx 20\ \mathrm{mm^2\ K\ W^{-1}}$, determined as the mean standard deviation from repeated measurements on the same sample, becomes more significant. Second, variations between individual samples increase, as samples with high filler content are more difficult to produce consistently. Air inclusions or surface irregularities become more likely under these conditions.

For a general overview of the uncertainty components for samples with good or poor thermal conductivity, **Figure 3.9** shows a summary of the uncertainties for the measurements carried out as part of this work.

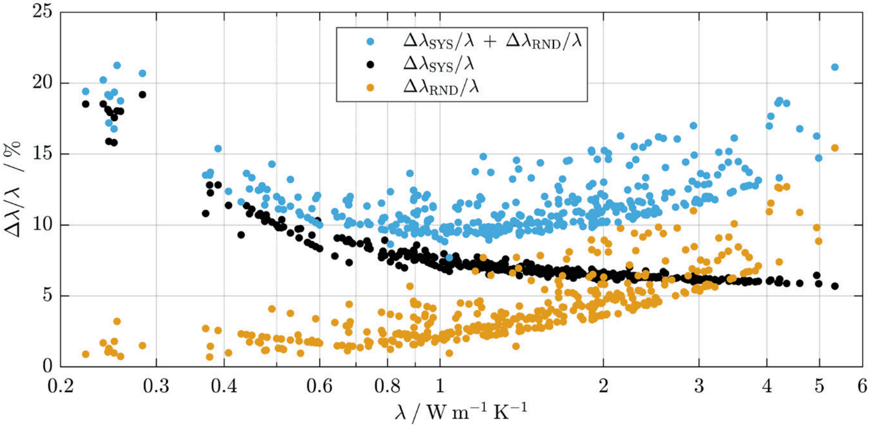

Figure 3.9. Systematic and random uncertainty components of thermal conductivity measurements. Systematic evaluation of uncertainty components in 384 measurements, performed within the scope of this work.

As the sample's thermal conductivity increases, the systematic uncertainty components decrease, while the random uncertainty components increase. In total, the minimum obtainable uncertainties are just under $10\ \%$. Most samples can be measured with a cumulative uncertainty of $< 15\ \%$, except for the lowest and highest thermal conductivities. The unfilled polymers with $\lambda < 0.3\ \mathrm{W\ m^{-1}\ K^{-1}}$ stand out. The method has reached its resolution limits with the selected sample size. Even lower thermal conductivities can no longer be measured precisely.

3.2.7 EXTENSION: EVALUATION OF THERMAL CONTACT RESISTANCES

As mentioned previously, the specific thermal resistances measured using the steady-state cylinder method include the contact resistances between the sample and the surfaces of the aluminum bars. A common approach to estimate these contact resistances is to extrapolate the linear regression of measured resistance values (see **Eq. (3.13)**) to a sample thickness of $d = 0$, as shown in **Figure 3.6**, **Figure 3.7**, and **Figure 3.8** [160,161,209,211]. This yields the combined resistance of both interfaces. If the upper and lower contact resistances are assumed to be equal, their sum can be expressed as

$$2\ r_{\mathrm{C}} = \alpha_0\ , \tag{3.15}$$

where α_0 is the r-axis section in **Eq. (3.13)**. However, this approach is not meaningful for the studies conducted in this work. The interface between the aluminum bars and the cured polymer composites, modified with a contact agent, does not reflect a practically relevant contact scenario. This evaluation is more applicable when analyzing thermal greases or other paste-like materials. By adjusting the surface structure of the aluminum bars in the measurement setup, the contact conditions of an actual application can be approximated, allowing for a more realistic measurement of the thermal contact resistance.

However, even for paste-like samples, the method has a fundamental limitation, as the presented evaluation strategy only approximates the contact resistances macroscopically and reduces them to planar phenomena. Yet, shown in **Figure 2.3**, page 18, thermal contact resistance is influenced by the entire contact zone. Already the pure surface roughness ensures that the temperature drop occurs over a certain distance. When the microstructural heterogeneity of filled polymers is also considered, extrapolation to zero-gap thickness oversimplifies the interface behavior and blurs important effects.

Furthermore, considerable material changes can occur during the measurement. When testing paste-like samples, it is typical to start with a large gap width, i.e., a large sample thickness d, and gradually reduce the gap during the measurement. This displaces excessive material from the gap. During this deformation process, however, it must be assumed that the microstructure of the material in the boundary zones changes considerably. Particles are pushed into direct surface contacts or form stacked particle layers. Abo Ras [211] discussed these phenomena with thermal grease in 2020. It is no longer sufficient to assume constant material and contact properties during the gradual change in sample thickness. The impact on the described extrapolation and evaluation cannot be estimated without considering the microscale effects.

3.3 MEASURING THERMAL CONTACT RESISTANCES USING MICRO THERMOGRAPHY

The central objective of this work is to investigate the microstructural effects on the heat transport properties of filled polymers. This includes not only the thermal conductivity of the bulk material but also the phenomena at filled polymer to substrate transitions (FPS transitions) and the arising contact resistances. A new measurement method based on micro thermography was developed to enable the experimental investigation of thermal contact resistances. This chapter introduces the new measurement method, describes the apparatus used, the evaluation strategy, and the uncertainties and limitations associated with the measurements. The new measurement method has already been presented and described in detail in [0]. In some places, reference is made to [0] for the consideration of peripheral and detailed topics as well as further experimental results.

3.3.1 INTRODUCTION TO THERMAL CONTACT RESISTANCE MEASUREMENTS

The measurement of thermal contact resistances is carried out following the same basic principles as the measurement of thermal bulk resistances or thermal conductivities. A temperature difference is applied, and the heat flow is measured, or vice versa. However, the fact that thermal contact resistance phenomena take place in a very confined space, i.e., very thin layers, makes resolution more difficult. The measurement of local temperature differences is limited by the size of conventional temperature probes, such as thermocouples. Extrapolation methods are usually used to approximate the resistances in the contact area or zones, as explained in section 3.2.7. In 2018, Xian et al. [212] reviewed several transient and steady-state methods for measuring thermal contact resistances. While many studies, e.g., [86,90,92,93,97], focus on the measurement of thermal contact resistance between solids, there are only a few that include filled polymers, e.g., [159,161,213]. However, they all depend on macroscopic approximations, e.g., zero-gap extrapolation. There is no study in which FPS transitions are resolved microscopically. Some interesting approaches [88,89,214,215] have been published that use infrared thermography in combination with steady-state and transient methods to enable higher spatial resolution for local temperature measurements. Thermal resistances are determined from heat flow and temperature differences. Locally finely resolved temperature measurements also enable the determination of locally resolved thermal resistances. While sensor contact always disturbs the temperature field and limits the local resolution, thermography can enable locally finely resolved measurements. However, the technique has not yet been applied to directly resolve the temperature differences at the interfaces between filled polymers and solid surfaces. In previous studies involving filled polymers, temperature measurements were still conducted outside the sample and extrapolated, as with the steady-state cylinder method, e.g., [214,215].

The measurement method developed as part of this work also uses infrared thermography, with temperatures measured directly at the transition from the solid surface to the filled polymer, not outside the sample. Temperature differences and thus thermal resistances are finely resolved locally without disturbing the temperature field. This method promises detailed insights into local thermal resistances and thus into the effects of the microscopic material structure in FPS transitions. Thus, it should be possible to investigate the effects of surface structure, filler quantity, filler size and filler material.

3.3.2 MEASUREMENT PRINCIPLE AND APPARATUS

A measuring apparatus for the thermal characterization of multi-layered samples was developed and built. The multi-layered samples consist of two aluminum substrates and an intermediate layer of filled polymer. The function is based on the steady-state cylinder method, as presented in chapter 3.2, see **Figure 3.10**. The samples are placed between two aluminum bars, with the upper side of the upper bar heated electrically to T_h and the lower side of lower bar cooled to a low temperature T_c by means of coolant flow.

The mechanical design is considerably simplified compared to the steady-state cylinder method in chapter 3.2. Since only fully cured sample materials with negligible elasticity are measured, position and force control of the aluminum bars are not necessary. The lower bar is fixed, and the upper bar is pressed onto the multi-layered samples from above using a manual clamping device. Thermal contact resistances between the sample and the aluminum bars are irrelevant, as the measurements are limited to the inner part of the sample.

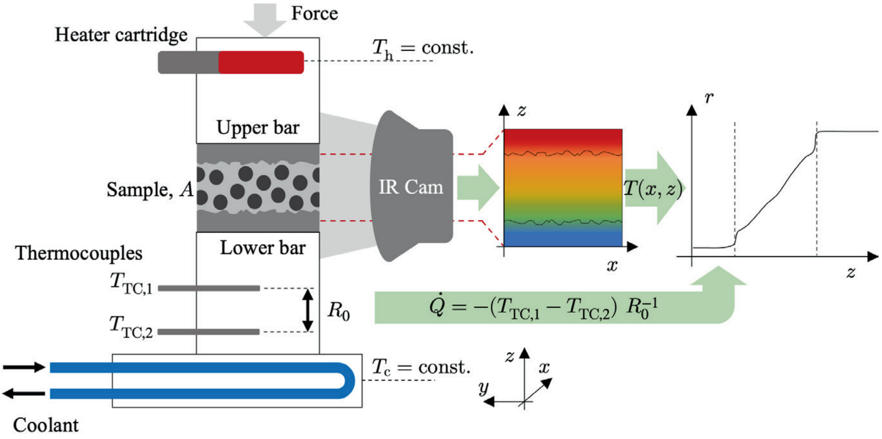

Figure 3.10. Schematic illustration of the micro thermography apparatus and the measurement principle. Modified from [0], CC BY 4.0, https://creativecommons.org/licenses/by/4.0.

The two aluminum bars and the samples have a square cross-section of $A = 20 \times 20\ \mathrm{mm}^2$ in heat flow direction. A one-dimensional heat flow $\dot{Q}$ is assumed, flowing from the upper bar, through the sample and through the lower bar into the coolant. The measurement is conducted under steady-state conditions. Unlike the steady-state cylinder method, where temperature profiles are measured along the aluminum bars and extrapolated to the sample surface, this setup captures temperature differences directly within the sample layers, without physical contact, see **Figure 3.10**.

For this purpose, an infrared camera[7] with an additional close-up lens $0.5\times$ is fixed to the apparatus to image the temperature field on the side surface of the sample. The pixel dimension with this setup is $14.836\ \mu\mathrm{m}$, which corresponds to approximately half the native detector resolution. The utilized camera system has a MicroScan mode in which a rapidly oscillating deflection unit shifts the sensed area by half a pixel dimension. By superimposing four individual images with slight local offsets, a thermal image is created with twice the resolution in each image direction. **Figure 3.11** shows the micro thermography apparatus and exemplary temperature data. The measuring section with an inserted sample and the adjusted IR camera is shown in part (a). Part (b) shows superimposed extractions from a sample micrograph and captured temperature field.

In part (c), a full temperature field captured on an exemplary sample is presented, and part (d) shows an averaged temperature profile $\bar{T}(z)$ derived from the thermal image. Assuming z is the direction of heat flow, local temperature gradients along z can be converted into local thermal resistances using the known heat flux. The heat flux is determined from a reference section in the lower bar, where two thermocouples are positioned at a known distance. The temperature difference between them, along with the known thermal resistance R_0 is used to calculate the heat flow, as shown in **Figure 3.10**.

3.3.3 SAMPLE PREPARATION

The multi-layered samples were prepared from aluminum substrates (EN AW-5754) with an area of $100 \times 100\ \mathrm{mm}^2$, and filled polymer composites based on the epoxy polymer E01. The sample preparation process described below requires a fully cured, grindable polymer composite. The studies are therefore limited to this polymer. No loss of generality is expected for the subsequent studies on the effects of the materials microstructure. The surface structure of the aluminum substrates was modified by sandblasting, as described in detail in section 3.1.3. They were then cleaned with isopropanol before further processing. The preparation process of the central particle-polymer composites is identical to the process presented in section 3.2.3. **Figure 3.12** illustrates the preparation process of the complete multi-layered samples, which involves several steps.

---

[7] InfraTec VarioCAM® HD head 980

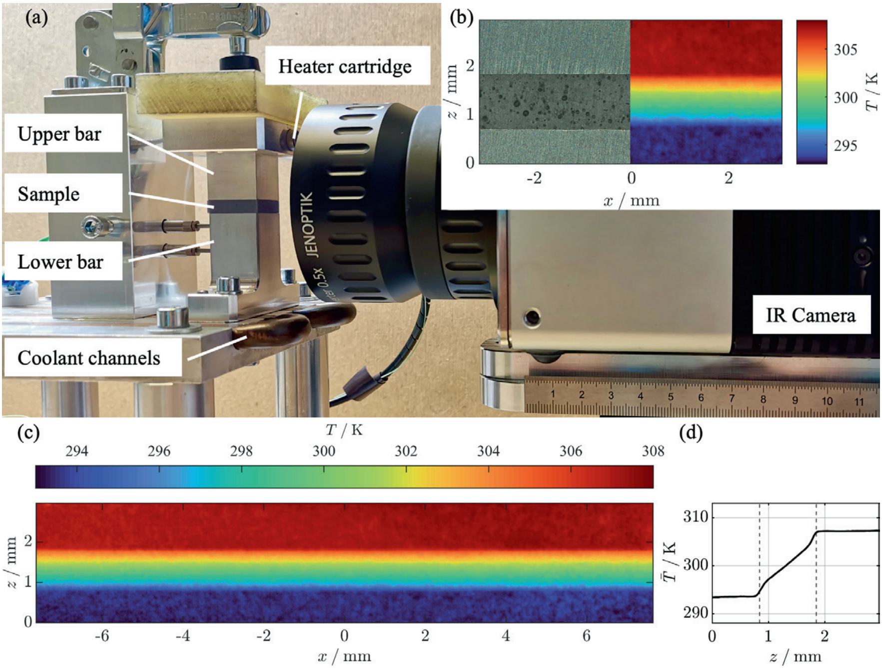

Figure 3.11. Micro thermography apparatus and exemplary measured temperature field. Image of the apparatus with measuring section and IR camera (a). Section of a micrograph and corresponding thermal image (b). Full thermal image (c). Average temperature curve along z direction on sample surface (d).

The prepared particle-polymer composites were applied to an aluminum substrate, and another substrate placed on top, see part (a). Spacers with a thickness of $(0.9 \ldots 1.2)$ mm were used to adjust the distance between the substrates and thus the layer thickness of the filled polymer. The multi-layered structure was fixed in place with four screws and then cured at room temperature for at least seven days, see part (b) of **Figure 3.12**. The multi-layered samples were then cut to the approximate final dimensions of $20 \times 20 \times 5$ mm^3 using a waterjet cutter, see part (c). The side surfaces of the samples were ground and polished, see parts (d) and (e) of **Figure 3.12**. Finally, the side surface to be analyzed was coated with an acrylic resin-based graphite spray. For thermography, it is necessary to have a surface with uniform emissivity, which is not fulfilled with aluminum and filled polymers. While the absolute level of emissivity is not critical, it is essential to minimize surface reflectivity to avoid distortion of the thermal image caused by reflections of the IR detector's own radiation. To address this, a coating with high emissivity, and therefore low reflectivity, was applied to the sample surface. In a preliminary study, the emissivity of the utilized graphite coating was determined to be $\varepsilon = 0.98 \pm 0.01$.

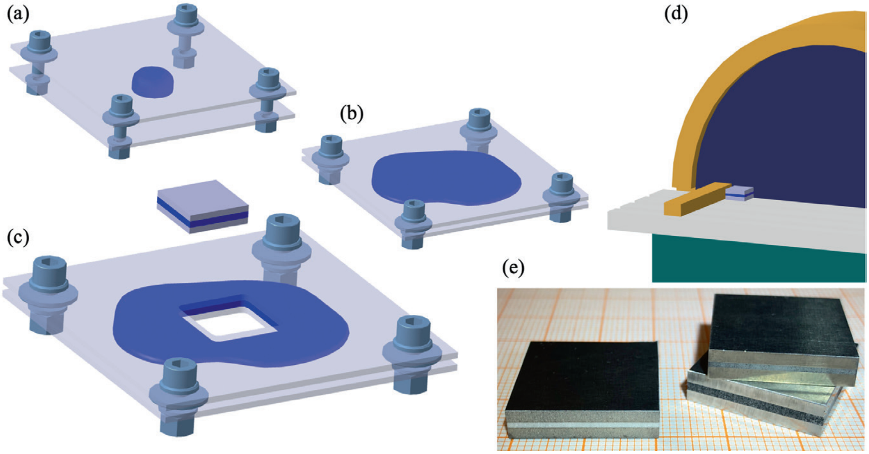

Figure 3.12. Sample preparation for micro thermography.
Application of filled polymer composite between substrates (a). Joining the substrates at a defined distance using spacers (b). Cutting the sample from the central area of the multi-layered structure (c). Grinding and polishing the side sample surfaces (d). Prepared samples before graphite coating (e).

3.3.4 CALIBRATION PROCEDURE

Like the steady-state cylinder method, the micro-thermography technique relies solely on temperature measurements. To minimize uncertainty, the thermocouples used are calibrated for the steady-state cylinder method. IR camera systems generally exhibit lower absolute accuracy than thermocouples and are subject to calibration limitations. Additional sources of uncertainty in the micro-thermography measurements include variations in emissivity, reflected ambient radiation, and environmental heat losses. Another significant consideration is the spatial assignment of temperature values. The raw thermal image does not provide spatial information, so local coordinates must be assigned, introducing further uncertainty. Consequently, measurements are not made in absolute terms but are instead compared to a well-known reference sample. An initial calibration procedure compensates for the uncertainty effects mentioned. The calibration process was carried out before each series of measurements, or if the measurement conditions or ambient temperature changed. For the latter, a threshold of $1\ \mathrm{K}$ is used as the limit for recalibration. The thermal reference resistance R_0 in the lower aluminum bar serves as the calibration parameter. This is particularly suitable because it directly influences the heat flow and, consequently, the measured thermal resistance values. An absolute determination of this reference resistance would be subject to high uncertainty due to temperature measurement errors, uncertainty in the distance between the thermocouples, or ambient losses. To calibrate the system, a well-known reference material with thermal resistance similar to that of the multi-layered samples is required. For the measurements conducted in this study, a reference sample was fabricated from stainless steel 304. Stainless steel 304 is listed as a reference material by the National Physical Laboratory (NPL), UK [216], and its thermal conductivity has been extensively studied, e.g., [217–220]. The batch of the material used for the reference sample was examined using laser flash analysis, according to ASTM E1461-13 [207]. The thermal conductivity was calculated from the separately measured values of thermal diffusivity, density, and heat capacity. For the relevant temperature range of $288\ \mathrm{K}$ to $303\ \mathrm{K}$,

$$\lambda_{\mathrm{ref}}(T_{\mathrm{ref}}) = [6.859 + 0.027\,T_{\mathrm{ref}}/\mathrm{K}]\ \mathrm{W\ m^{-1}\ K^{-1}} \qquad \pm\,4.8\ \% \tag{3.16}$$

was obtained [0]. The uncertainty value is based on [216], after determining good agreement with [217–220]. The average deviation in relation to the literature values is $2.6\ \%$ in the investigated temperature range. The reference sample was prepared with the dimensions $20 \times 20 \times 5\ \mathrm{mm}^3$. A flat groove with a width of $\Delta z_{\mathrm{M}} = 3.0\ \mathrm{mm}$ and a depth of $0.2\ \mathrm{mm}$ was milled into one of its side surfaces. The excess rib surfaces were polished, while the base of the groove was coated with the same graphite spray used on the actual samples. At the beginning of a series of measurements, the reference sample is placed in the micro thermography apparatus and a series of heater and coolant temperature combinations is then run, with a calibration measurement carried out for each combination. While the coolant was kept at a constant $288\ \mathrm{K}$, the heater temperature was increased from $303\ \mathrm{K}$ to $343\ \mathrm{K}$ in $5\ \mathrm{K}$ steps. **Figure 3.13** illustrates the calibration procedure, based on the well-known reference sample with thermal conductivity λ_{ref} and heat-transferring cross-sectional area A_{ref}.

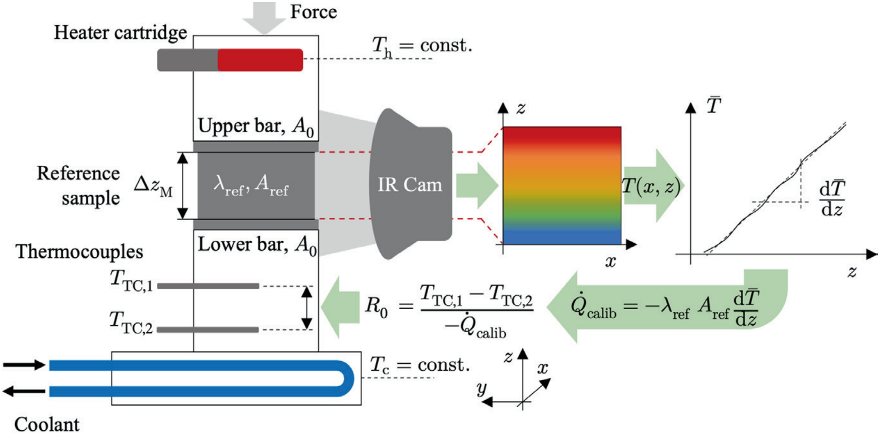

Figure 3.13. Calibration procedure for micro thermography apparatus. Modified from [0], CC BY 4.0, https://creativecommons.org/licenses/by/4.0.

To calibrate the spatial assignment of the temperature field and the temperature measurement at the same time, the evaluation window in the thermography software IRBIS® 3[8] is aligned with the edges of the flat groove in the reference sample surface. These are easily recognized by the difference in emissivity (groove - graphite coated and rib - polished). This alignment is illustrated in **Figure 3.13** by the red dashed lines between reference sample and IR camera. After reaching thermal equilibrium at each temperature set, according to the criterion in ASTM D5470-17 [184], the temperature field on the reference sample's surface is captured. Since the reference sample is homogeneous along the x axis (into the image plane), the temperature field can be averaged along this direction.

The obtained temperature curve $\bar{T}(z)$ is then approximately linear in the central area and might be disturbed by boundary effects at the lower and upper end. The temperature gradient $\mathrm{d}\bar{T}/\mathrm{d}z$ on the reference sample surface is calculated using linear regression. The calibration heat flow in the reference sample can be calculated with

$$\dot{Q}_{\mathrm{calib}} = -\lambda_{\mathrm{ref}}(T_{\mathrm{ref}})\ A_{\mathrm{ref}}\ \frac{\mathrm{d}\bar{T}}{\mathrm{d}z}\ , \qquad \textbf{(3.17)}$$

where T_{ref} is the mean reference sample temperature and A_{ref} is the heat-transferring cross-sectional area of the reference sample. Using this heat flow, the apparent thermal reference resistance can be expressed as

$$R_0 = \frac{T_{\mathrm{TC,1}} - T_{\mathrm{TC,2}}}{-\dot{Q}_{\mathrm{calib}}}\ , \qquad \textbf{(3.18)}$$

where $(T_{\mathrm{TC,1}} - T_{\mathrm{TC,2}})$ is the temperature difference measured across the lower aluminum bar. The average temperature T_0 of the two thermocouples in the lower aluminum bar is then calculated as a reference for the thermal reference resistance.

After running through various heater and coolant temperature combinations (T_{h} / T_{c}), a calibration curve $R_0(T_0)$ is obtained, see **Figure 3.14**. This curve is approximated by a linear fit and expressed as e.g.,

$$R_0(T_0) = [-0.0028\,T_0/\mathrm{K} + 1.0837]\ \mathrm{K\ W^{-1}}\ . \qquad \textbf{(3.19)}$$

This calibration result can be used to evaluate all subsequent measurements under the same ambient conditions.

---

[8] InfraTec GmbH, Germany

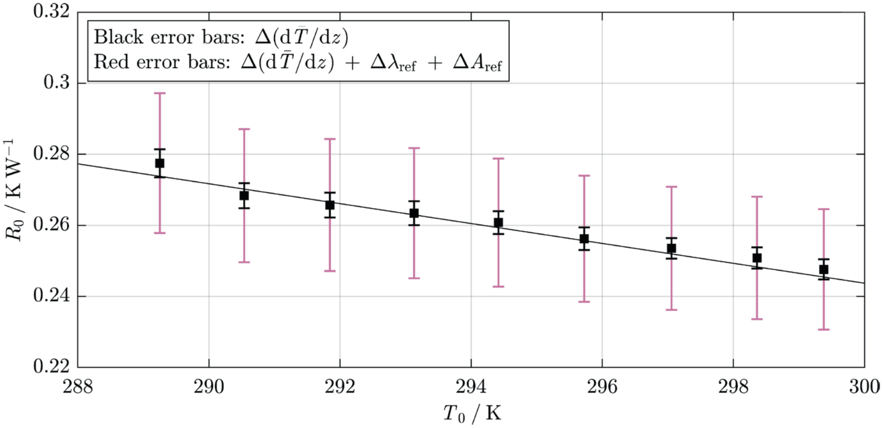

Figure 3.14. Result of a calibration run in the micro thermography apparatus. Based on [0].

In the calibration process described, all environmental influences and uncertainties are neglected. These include:

- absolute errors in temperature measurement with the IR camera,
- an inaccurate z coordinate assignment to the pixels of the thermal image,
- absolute errors in temperature measurement with the thermocouples,
- environmental heat losses at the side surfaces of the measuring section by radiation or convection
- temperature field disturbance by the thermocouples in the lower aluminum bar,
- reflected ambient radiation on the reference samples' surface,
- reflected radiation of the IR detector from the reference samples' surface,
- deviations or non-uniformities in the emissivity of the reference samples' surface,
- further optical inaccuracies of the setup.

These uncertainties are directly reflected by the calibration result $R_0(T_0)$. Since they are all systematic uncertainties, it can be assumed that they are identical for the measurements directly following under the same conditions. Reapplying $R_0(T_0)$ for the evaluation of the actual measurement helps to compensate for these uncertainty effects. The black error bars shown in **Figure 3.14** illustrate the uncertainty contribution from determining the temperature gradient through the reference sample. The red, significantly larger error bars also include the uncertainty contributions of the thermal conductivity of the reference sample and its area.

A detailed description of the uncertainty analysis can be found in section 3.3.7 and appendix B.3. It is apparent from **Figure 3.14** that a large part of the total uncertainty is due to the reference sample. Only the uncertainty in the temperature gradient is method related, and with an even better-known reference material, a more accurate measurement would be possible.

3.3.5 MEASUREMENT PROCEDURE

The measurements with the micro thermography method were carried out under controlled ambient conditions. Due to the described calibration process, the absolute ambient conditions are less important, however the measuring procedure requires constant thermal conditions. In addition, the average temperature at the reference resistance R_0 must be as close as possible to the ambient temperature. This results in sample-specific heater temperatures between $318\ \mathrm{K}$ and $328\ \mathrm{K}$. The effects were investigated in advance using numerical simulation and are discussed in detail in [0]. The coolant was kept at a constant inlet temperature of $288\ \mathrm{K}$ for all measurements performed within this study. Since micro thermography is a steady-state measurement method in which all components must be in thermal equilibrium, the micro thermography apparatus was pre-heated for at least two hours before each series of measurements. For each measurement, the sample is inserted and fixed with the mechanical clamping device. A water-glycol mixture is injected between the aluminum bars and the multi-layered samples as a contact agent to ensure uniform thermal contact, and the thermal equilibrium must then be reached. The criterion from ASTM D5470-17 [184] was used to evaluate the thermal equilibrium. Finally, the thermal image is recorded, and the raw data are saved as a two-dimensional matrix $T(x,z)$. It is imperative that the identical local alignment is set in the thermography software as in the previous calibration process, see section 3.3.4. For this purpose, the same evaluation window is set in the IRBIS® 3 software as for the previous calibration. Furthermore, the temperatures of the thermocouples in the lower aluminum bar are recorded.

3.3.6 EVALUATION

Before further evaluation, the recorded two-dimensional temperature fields $T(x,z)$ are numerically sharpened to reduce camera and detector-related blurring. While this process does not increase physical resolution, it enhances image clarity, making transitions between sample layers more visible. Since the optical setup is consistent across all measurements, a general point spread function is determined, and a reverse Gaussian low-pass filter[9] is applied. A standard Wiener filter[10] is used beforehand to reduce high-frequency noise. The temperature field $T(x,z)$ is then averaged along the x-direction, which is assumed to be homogeneous, by calculating the arithmetic mean for each pixel row. The

---

[9] MATLAB® built-in function *imsharpen*() with $\mathrm{Radius} = 2.3$, $\mathrm{Amount} = 0.2$, and $\mathrm{Threshold} = 0$ (default).

[10] MATLAB® built-in function *wiener2*() with $\mathrm{Neighborhood\ size} = [5\ 5]$.

resulting temperature curve $\bar{T}(z)$, shown in **Figure 3.11**, page 63, represents the temperature variation along the heat flow direction. A method for considering variations along the x-direction, to analyze local thermal contact resistances, is discussed in section 6.4.4. The heat flow through the sample can be determined with

$$\dot{Q} = -\frac{T_{\mathrm{TC},1} - T_{\mathrm{TC},2}}{R_0(T_0)} \,. \tag{3.20}$$

The thermal resistance contributions of the sample layers are finally obtained from the local derivative of the temperature profile $\mathrm{d}\bar{T}/\mathrm{d}z$, the heat flow $\dot{Q}$, and the cross-sectional area of the sample A

$$\frac{\mathrm{d}r}{\mathrm{d}z} = \frac{A}{-\dot{Q}} \frac{\mathrm{d}\bar{T}}{\mathrm{d}z} \,. \tag{3.21}$$

For simplicity, the differential notation is chosen, even if only discrete temperature values are available from the thermal images. However, these are available in a fine local resolution such that neither a discrete notation nor a discrete representation is appropriate. For easier analysis and extraction of the thermal contact resistances, $\mathrm{d}r/\mathrm{d}z$ according to **Eq. (3.21)** is integrated and can be illustrated as shown in **Figure 3.15**. The presented measurement result is that of a typical multi-layered sample with two aluminum substrates and a particle-filled polymer in between. The integrated specific thermal resistance growth along z direction is presented.

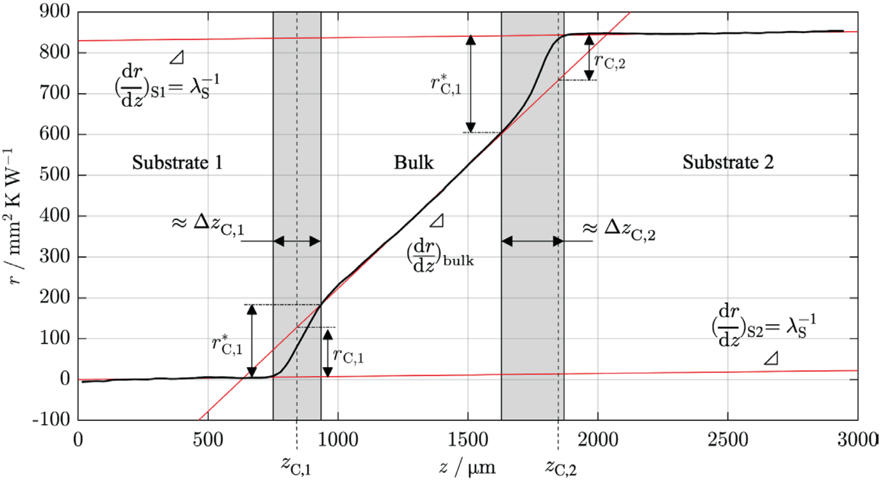

Figure 3.15. Exemplary micro thermography result.
Cumulative thermal resistance curve across a multi-layered sample with two aluminum substrates and a filled polymer interlayer. Polymer: Epoxy E01. Filler: Alox-S-63, $\phi = 0.5$, $D_{50} = 63.4$ µm. Results are given in **Table 3.4**. Based on [0].

The two interfaces between substrate and filled polymer are located at $z_{\mathrm{C},1}$ and $z_{\mathrm{C},2}$, and visualized with black dashed vertical lines. The positions were determined ex-situ, using a digital light microscope[11]. Difficulties and definition gaps that arise with this approach are discussed in chapter **6.3**. With rough surfaces, there is always the question about the reference height to be evaluated. There is hardly any resistance increase visible above and below the interfaces, since the thermal conductivity of the substrates (AlMg3; EN AW-5754) is very high ($\lambda_\mathrm{S} = 130\ \mathrm{W\ m^{-1}K^{-1}}\ \ \pm 5\ \%$ at 300 K [194]) and therefore their contribution to thermal resistance is low. In the bulk zone of the filled polymer layer, an approximately linear increase in specific thermal resistance is observed. This corresponds to a constant effective thermal conductivity of the filled polymer, which can again be determined from the inverse of the slope. In the example shown in **Figure 3.15**, it is

$$\lambda_\mathrm{eff} = \left(\frac{\mathrm{d}r}{\mathrm{d}z}\right)^{-1}_{\mathrm{bulk}} = 1.66\ \mathrm{W\ m^{-1}K^{-1}}\ . \tag{3.22}$$

For simplified analysis, the three approximately linear thermal resistance curves along the z axis in the substrates and in the bulk of the filled polymer are approximated using linear functions. This is shown by the red lines in **Figure 3.15**. In the contact zones, shaded in grey, there is a clear deviation of the resistance curve from the ideal linear behavior. The deviations can be explained by FPS transition effects and are caused by the thermal contact resistances, which have already been analyzed from a macroscopic perspective in other works, e.g., [8,9,159–161,213].

Unlike previous steady-state methods, which could only derive contact resistances macroscopically via temperature field extrapolation, this approach enables direct visualization of these resistances with spatial resolution. The contact zones between the substrates and the filled polymer can be distinguished from the bulk zone in **Figure 3.15**. This marks a significant advancement: the thermal contact resistances become visible and locally evaluable. However, despite numerical sharpening, the visualized resistance curve contains a remaining blurriness. It has not been possible within the scope of this work to quantify this remaining blurriness, or the potential distortion caused by the sharpening process with a standardized point spread function. As a result, the identification of the beginning and end of the contact layers is subject to considerable uncertainty and cannot be made with exactness. Nevertheless, this method provides a valuable comparative insight. Using the same measurement setup and conditions, different FPS transitions can be compared for tendencies, e.g. whether one FPS transition has thicker or thinner contact zones than another. The unsharpened raw data consistently shows smoother, more blurred resistance curves, which result in broader contact zones. Sharpening the data helps to better approximate the actual

---

[11] Keyence VHX with a dual-light high-magnification zoom lens VH-Z250R and an xy-measurement system VH-M100E

layer thicknesses, but the true values remain at an unquantifiable distance due to the limited spatial resolution which is given by the physical resolution limit in the used spectral range of $(7.5 \dots 14)$ $\mu\mathrm{m}$ (Abbe limit) and the point spread function of the optical system. For a quantitative evaluation of the thermal contact resistances, several strategies are available. Chapter 6.3 discusses those strategies, the different results obtained, and the uncertainties in detail. Only a rough introduction is provided here. **Table 3.4** summarizes the evaluation results for each layer and interface, gained from the micro thermography analyses shown in **Figure 3.15**. Based on previous steady-state methods, the first and simplest option is to extrapolate the linear relationship of the bulk zone and search for the intersections with the interface heights. In **Figure 3.15**, the thermal contact resistances determined this way are labeled $r_{\mathrm{C},1}$ and $r_{\mathrm{C},2}$.

Table 3.4. Results of exemplary micro thermography measurement, corresponding to **Figure 3.15**.

Bulk		**Contact**		
λ_{eff} / $\mathrm{W\ m^{-1}K^{-1}}$	**No.**	r_{C} / $\mathrm{mm^2\ K\ W^{-1}}$	r^*_{C} / $\mathrm{mm^2\ K\ W^{-1}}$	Δz_{C} / $\mu\mathrm{m}$
1.66 ± 0.18	1	122 ± 13	175 ± 18.6	184
	2	110 ± 11.7	236 ± 25.1	241

In the example shown, $r_{\mathrm{C},1} = 122\ \mathrm{mm^2\ K\ W^{-1}}$ and $r_{\mathrm{C},2} = 110\ \mathrm{mm^2\ K\ W^{-1}}$ were determined. Compared to the total thermal resistance for the layer of roughly $r_{\mathrm{tot}} \approx 850\ \mathrm{mm^2\ K\ W^{-1}}$, the two contact resistances account for a considerable proportion. This evaluation strategy is suitable if the results are to be used subsequently to calculate entire thermal dissipation paths and to add up several layers in series connections. However, it does not offer any added value for the analyses in this work, as the effects in the broad FPS transitions are not considered. For this purpose, a second evaluation strategy is additionally shown in **Figure 3.15**. The z positions at which the measured thermal resistance curve diverges from the ideal linear increases are identified. The areas found are declared as boundary layers, see grey shading in **Figure 3.15**. The width of the boundary layers and the total resistance contribution of these layers are evaluated, the latter referred to as r^*_{C}. In the example given, $\Delta z_{\mathrm{C},1} \approx 184\ \mu\mathrm{m}$ and $r^*_{\mathrm{C},1} \approx 175\ \mathrm{mm^2\ K\ W^{-1}}$ are determined for the first boundary layer. For the second boundary layer, $\Delta z_{\mathrm{C},2} \approx 241\ \mu\mathrm{m}$ and $r^*_{\mathrm{C},2} \approx 236\ \mathrm{mm^2\ K\ W^{-1}}$ are obtained. This evaluation ignores the fact that the image blurriness and the sharpening process influence the identified divergence points and result in non-quantifiable errors. The values should therefore not be used as an absolute result but may be used to compare different FPS transitions that were examined with the same setup. The uncertainty in the layer thickness cannot be quantified and is therefore not specified. The uncertainty of the specific thermal contact resistances given in **Table 3.4** refers only to the uncertainties in the resistance, but not to the uncertainties in finding the divergence position. The second evaluation strategy includes all parts and contributions of the substrate surface, FPS transition, and close-to-surface particle packing. Local analyses can be carried out in the further course of the work and if necessary, a separation of the effects of substrate and particle layers in local analyses. A detailed discussion of the definition and evaluation of boundary layers is provided in chapter 6.3.

3.3.7 DISCUSSION OF MEASUREMENT UNCERTAINTIES

This section deals with the estimation of the resistance-related uncertainties of the new micro thermography method. The calibration process described in section 3.3.4 compensates for numerous sources of error. Nevertheless, systematic and random uncertainties remain, which are evaluated and discussed separately. Appendix B.3 provides the detailed uncertainty analysis and propagation calculations. The analysis of systematic uncertainty is carried out in two steps. First, the uncertainty of the calibrated thermal reference resistances R_0, according to **Eq. (3.18)**, page 66, is determined. In the second step, the systematic uncertainty of the actual measurement result, the specific thermal resistance r of the sample, is estimated. **Figure 3.16** shows the results of the uncertainty estimation for the calibration results given in **Figure 3.14**, page 67, and the results of the uncertainty estimation for eight exemplary samples.

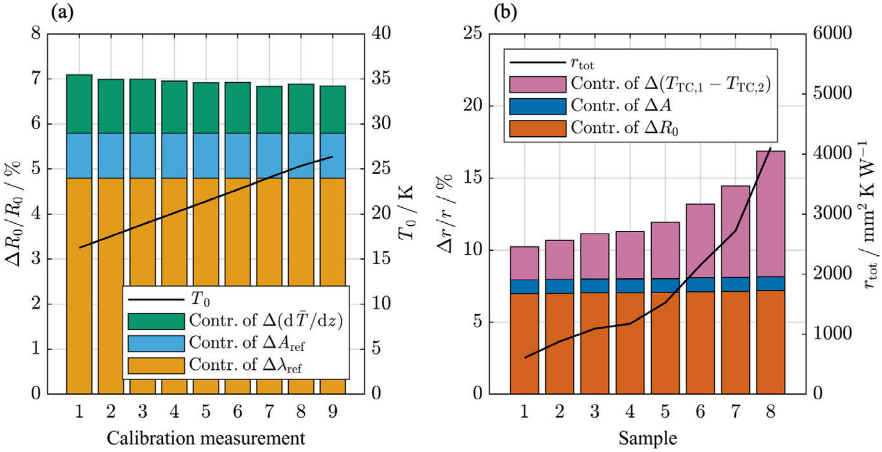

Figure 3.16. Exemplary results of systematic uncertainty analysis.

Results of systematic uncertainty estimation for the calibration run, already presented in **Figure 3.14** in part (a). Estimated systematic uncertainties for nine exemplary samples, measured with micro thermography in part (b). Modified from [0], CC BY 4.0, https://creativecommons.org/licenses/by/4.0.

The results shown are to be understood as an example, since the calibration results and thus also the uncertainty analysis vary slightly from measurement series to measurement series. However, the general order of magnitude remains the same. Part (a) of **Figure 3.16** shows the estimated uncertainty of the thermal reference resistance and its components for nine calibration measurements at different reference temperatures T_0, achieved by variation of the heater temperature, as described in section 3.3.4. Almost $70\ \%$ of the uncertainty is caused by possible errors in the reference samples' thermal conductivity $\Delta\lambda_{\mathrm{ref}}$. This fact was already mentioned in the previous section and shown in **Figure 3.14**, page 67. If a reference with even better-known thermal conductivity is available, more reliable (absolute) results can be achieved with micro thermography. The uncertainty contribution of ΔA_{ref} is roughly $1\ \%$. The uncertainty contribution coming from the evaluation of the temperature gradient $\mathrm{d}\bar{T}/\mathrm{d}z$ accounts for slightly more than $1\ \%$ and drops marginally with temperature. In total, the uncertainty in reference resistance determination is $\Delta R_0/R_0 \approx 7\ \%$. Part (b) of **Figure 3.16** shows the estimated uncertainty and the contributions of the specific thermal resistance of eight exemplary samples with different total specific thermal resistances. The samples were selected to cover the complete range of relevant total resistances. The relative uncertainty increases with total thermal resistance, which is almost solely caused by the increasing relevance of the uncertainties in temperature difference measurements. This is due to the decrease of the heat flow and thus the absolute temperature difference. Especially for small and medium total specific thermal resistances up to $3000\ \mathrm{mm}^2\ \mathrm{K\ W}^{-1}$, the contribution of the uncertainty of the reference resistance is dominant. For higher specific thermal resistances, the contribution of the uncertainty of the temperature difference measurement is of a similar magnitude. The contribution of the uncertainty in the sample area is almost constant at approx. $1\ \%$. In the relevant range of sample resistances, the estimated total systematic uncertainty is $\Delta r/r = (10 \ldots 17)\ \%$. The uncertainty analysis is based on an estimation of the maximum error and is therefore a worst-case scenario. Further confidence in the method can be achieved through cross-comparison with other measurement methods. As no other method is available with microscopic resolution of thermal resistances, a comparison was carried out using measured thermal conductivities of bulk samples. The micro thermography results were compared with measurements using the steady-state cylinder method, according to ASTM D5470-17 [184], and measurements using laser flash analysis, according to ASTM E1461-13 [207]. The latter were again based on the separate measurement of thermal diffusivity, density, and heat capacity. Details on the laser flash analysis can be found in [206]. Twelve filled polymer samples were prepared with different filler concentrations and filler types to achieve thermal conductivities in the relevant range of $0.25\ \mathrm{W\ m}^{-1}\ \mathrm{K}^{-1}$ up to approx. $2\ \mathrm{W\ m}^{-1}\ \mathrm{K}^{-1}$. **Figure 3.17** compares the effective thermal conductivities of the twelve measured samples using the three methods.

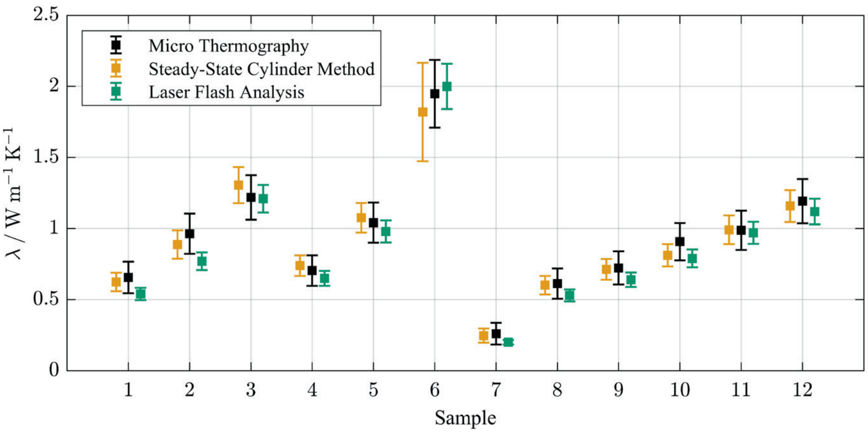

Figure 3.17. Results of cross-comparison of micro thermography, steady-state cylinder method (ASTM D5470-17), and laser flash analysis (ASTM E1461-13).

Measured thermal conductivities of twelve filled polymer samples of different filler concentration. Polymer: Epoxy E01. Filler: alumina and aluminum. The error bars show the assigned systemic uncertainties of the methods. Based on [0].

Very good agreement within the error bars of the measured thermal conductivities for all samples confirms the success of the error compensation by the described calibration process, as well as the suitability of the method for measuring thermal resistances in the relevant order of magnitude.

As in case of the steady-state cylinder method, the random uncertainties were also analyzed in addition to the systematic uncertainties of the method. To assess the reproducibility of the micro thermography technique, a series of repeatability tests was conducted using selected samples. Measurements were repeated on the same side surface, as well as on the other three side surfaces of the samples. Additionally, multiple nominally identical samples were fabricated and compared. Across repeated measurements on a single surface and between the different side surfaces of a given sample, only minor variations $< 5\ \%$ were observed, indicating good measurement repeatability. However, significant local variations were found within individual surfaces. This phenomenon will be discussed in section 6.4.4. Furthermore, differences of up to $25\ \%$ were detected between the measured thermal contact resistances of two samples that were prepared under identical conditions. In contrast, the bulk thermal conductivity of the filled polymer showed much lower variability of $< 10\ \%$ across the same sample set.

These findings lead to an important conclusion: the reproducibility of the measurement method itself is considerably higher than the reproducibility of the physical phenomenon under investigation. This is primarily attributed to the stochastic nature of thermal contact resistance formation (see chapter 6.4). Local variations in particle-to-substrate contact, particle aggregations, and surface roughness result in varying thermal contact behavior, even between samples that appear identical on a macroscopic level.

Furthermore, the measurements were not examined in the complete volume of the sample, but only on one of the four side surfaces with the structure present there and in the immediate proximity. The method is therefore more suitable for resolving the local effects on individual, well-known samples than for carrying out systematic studies. For a comparison of differently prepared samples to each other, numerous repetitions would have to be carried out to compensate for sample and structure-related variations. If the microscopic structure of a sample or the surface to be measured is known from microscopic imaging analyses, micro thermography is very suitable. The results can be directly correlated with the structural properties. Given the method's high reproducibility, additional statistical evaluation was not performed.

4 EFFECTIVE THERMAL CONDUCTIVITY OF SINGLE-SCALE FILLED POLYMERS

This chapter starts with the simplest case: single-scale filled polymers. These are characterized by the use of only one filler with a monomodal particle size distribution. A continuation of the previous considerations of chapter 2.4.2 is presented. Numerous experimental and numerical studies on model systems were carried out to investigate the effects of various polymer and filler properties on the effective thermal conductivity. These studies and the results obtained are presented and discussed mainly focusing on the isolated investigation of microscopic packing effects. This work aims to achieve a comprehensive quantification of these phenomena by developing and utilizing a new microscale simulation method, since it is challenging to extract detailed information about individual packing phenomena solely from experimental data. The method is based on detailed representations of the filler packings at the microscale, allowing for a fundamental investigation of their impact on the effective thermal conductivity. The microstructure models are fully parameterized using measurable quantities, which enables their direct adaptation to real filler systems without requiring empirical adjustment of model parameters. Chapter 4.1 describes the new calculation method. Chapter 4.2 follows with mostly numerical studies on the effect of the filler's maximum packing density on effective thermal conductivity. The impacts of the packing's compaction, the particle size distribution, and the particle morphology are discussed. Chapter 4.3 deals with dispersion effects. Chapter 4.4 follows with numerical and experimental studies and presents the effects of thermal filler and polymer properties. Chapter 4.5 presents an experimental validation of the microscale simulation approach and the findings from chapters 4.2 - 4.4. Finally, chapter 4.6 gives a comprehensive picture and conclusion of the investigated parameters, their interactions and the factors affecting them.

4.1 PREDICTING THE EFFECTIVE THERMAL CONDUCTIVITY USING MICROSCALE SIMULATIONS

Thermal microscale simulations offer several advantages when conducted alongside experimental studies. Fillers at the micro- and nanoscale exhibit complex property profiles, including chemical composition, morphology, surface structure, particle size distribution, and interactions with the polymer matrix. In experiments, these properties are inseparable, making it difficult to isolate the influence of individual parameters. In contrast, numerical simulations allow targeted variation of specific filler characteristics, and thus enable the isolated study of packing effects. Moreover, simulations can provide insights into heat transfer at the particle level, which are not accessible through macroscopic thermal conductivity measurements. While the micro thermography method introduced in chapter 3.3 offers spatially resolved resistance data, it does not allow detailed analysis of local heat paths. Numerical simulations also offer practical benefits: they can replace or complement experiments, accelerate development, and provide results even before materials or mixtures are physically available. This can be an important factor in the early stages of filler design.

4.1.1 INTRODUCTION TO NUMERICAL SIMULATION OF HEAT CONDUCTION IN FILLED POLYMERS

Modeling and calculating the effective thermal conductivity of filled polymers has long been established in research and development using a variety of methods. The simplest and most common variant is the application of theoretical and semi-empirical models, as presented in section 2.4.2, e.g., [119,120,122,130,165,168,169,173]. However, the use of these models is limited to simplified, qualitative studies, as these are restricted to a few parameters. They are usually not solely based on measurable parameters, therefore making quantitative predictions of the effective thermal conductivity, especially for medium to higher filler concentrations difficult. As soon as the particles approach each other spatially and the geometric interplay becomes decisive, microstructure simulations offer a more suitable and accurate approach.

This chapter introduces the general concept of microstructure simulations and presents the currently published techniques. The limitations of existing approaches and the motivation for developing a new calculation technique are discussed. Microstructure simulations physically model the heat conduction through the heterogeneous structure of a filled polymer and derive the effective thermal conductivity based on the resulting relationship between heat flux and temperature field. The previously published methods can be divided into two groups:

- random network models (RNM), and
- full-field techniques.

Recent work explaining and applying methods from these groups in detail has been published by Chowdhury et al. in 2018 [221] (RNM), and Sharma in 2022 [136] (full-field). Both require the definition of a representative volume element (RVE), as resolving the full application-scale microstructure is computationally expensive.

RNMs simplify the microstructure by representing each particle as a point mass and modeling thermal paths as one-dimensional thermal resistors between particles. These models are limited to spherical particles and rely on empirical calibration. A fundamental model for describing the thermal resistance between two particles in a continuous matrix was introduced by Batchelor and O’Brien [222], who analytically described the heat transfer through a narrow cylindrical zone between two adjacent particles. Their model incorporates the particle diameters and inter-particle distances to estimate local thermal resistances. This approach has been widely adopted [221,223,224] and further refined in subsequent studies, e.g., [225,226].

RNMs enable fast, resource-efficient calculations; however, the achievable accuracy is limited due to the simplified modeling of geometric microstructures and thus simplified thermal paths. In contrast, full-field techniques represent the microstructure in more detail. They allow the inclusion of arbitrary particle shapes and more realistic heat conduction paths. These techniques typically use finite element, finite difference, or finite volume solvers.

The finite element method (FEM) has been used most frequently [135,136,227–232]. Whenever microscopically detailed full-field simulations were performed, it was concluded that the structural heterogeneity and the details of the microscopic particle-polymer arrangement are important [135,136,228,229,231,232]. However, these studies are often limited to a few selected microstructures and primarily serve to support specific experimental work. A comprehensive, systematic study of the microstructural effects on the effective thermal conductivity is lacking in the literature. This can be attributed to fact that the detailed representation of the microstructure of filled polymers still reaches the limits of computing capacity today. The recent review article by Zhai et al. (2018) [139] comprehensively summarizes various calculation approaches. They cover both theoretical and semi-empirical models as well as numerical simulations. The authors conclude that there is a strong demand for a precise and universal calculation method for the effective thermal conductivity of particulate composites, as all existing techniques have strict limitations. Zhai et al. as well as Hu and Yang [233] emphasize the importance of multi-scale simulations, starting at the atomic level, and reaching up to the macroscopic effects.

Table 4.1 categorizes the calculation methods described and lists possible calculation scopes. Four different calculation techniques are compared regarding their resolution potential and suitability for describing differently sized RVEs. The size of the RVE is expressed as a multiple of the volumetric median particle size D_{50}. Filler properties such as the particle morphology, the maximum packing density, and most importantly the width of the particle size distribution determine how large an RVE must be modeled to fully represent the material behavior.

The first column classifies effective medium approaches (EMAs), which do not resolve the material's microstructure explicitly and therefore require no computational meshing. As a result, both memory usage (Mem.) and computational time (Comp.) are negligible. The second column describes random network models (RNMs), which use a simplified thermal network to represent the particle packing. Due to their idealized microstructural representation, RNMs are generally considered applicable only for representative volume elements (RVEs) with a size $\geq 4 \times D_{50}$. The method offers rapid computation with minimal memory demand.

Table 4.1. Comparison of calculation techniques for effective thermal conductivity of filled polymers. A classification of effective medium approaches (EMA), random network models (RNM), and full-field techniques. Column 3 describes the new full-field calculation approach developed as part of this work. Representation of the typical memory requirement (Mem.) and the typical calculation times (Comp.), depending on the size of the RVE to be described. The calculation times given are rough guideline values based on the calculations carried out as part of this project using the same computing hardware (AMD EPYC™ 9274F). Full-field FEM simulations were carried out using Ansys® Material Designer, 2023 R1.

		1 EMA	**2 RNM**	**3 Full-field this work**	**4 Full-field FEM**
Resolved packing		×	✓	✓	✓
Resolved particles		×	×	✓	✓
Mesh		none	Simplified network	Case-independent, structured	Case-dependent, unstructured
RVE Size	$\mathbf{1 \times D_{50}}$	Mem.: neglig. Comp.: < 1 s	🟥	🟥	10^5 elements Mem.: ≈ 5 GB Comp.: ≈ 12 s
	$\mathbf{2 \times D_{50}}$		🟥	🟥	$5 \cdot 10^5$ elements Mem.: ≈ 18 GB Comp.: ≈ 2 min
	$\mathbf{3 \times D_{50}}$		🟥	$27 \cdot 10^6$cells Mem: ≈ 4 GB Comp.: ≈ 1 h	$1.4 \cdot 10^6$ elements Mem.: ≈ 73 GB Comp.: ≈ 20 min
	$\mathbf{4 \times D_{50}}$		Mem.: neglig. Comp.: ≈ 1 s		$3 \cdot 10^6$ elements Mem: ≈ 200 GB Comp.: ≈ 1.5 h
	$\mathbf{5 \times D_{50}}$				🟥
	$\mathbf{6 \times D_{50}}$				🟥
	$\mathbf{> 6 \times D_{50}}$		Increasing packing modeling runtimes		

The FEM-based full-field technique (column 4) resolves both particle geometry and packing structure in detail. A case-specific computational mesh is used. As is typical for FEM, the mesh is unstructured, making it well suited for representing complex particle geometries. Depending on the specific filler properties, the method can be applied starting at $1 \times D_{50}$. The number of mesh elements scales with the number of particles, leading to a significant increase in memory requirements as RVE size increases.

To quantify this, simulations were performed using Ansys® Material Designer (2023 R1) on RVEs containing ideally spherical particles with a log-normal size distribution with a logarithmic standard deviation of $\log(\sigma) = 0.4$. **Table 4.1** summarizes the required memory and computation times. In particular, the enormous increase in storage requirements is seen to correlate with the number of mesh elements required as the size of the RVE increases. For $> 4 \times D_{50}$, it was unreasonable to perform a simulation with today's practical hardware capacity and calculation time. However, even at $4 \times D_{50}$, the number of resolvable particles (~$1{,}000$) was insufficient to statistically represent the target size distribution, which would require at least $6{,}000$ particles. For details on the required number of particles and RVE size, see section 4.1.2 and appendix C.1.

The new full-field technique developed within this work (column 3) addresses this limitation by retaining the high geometric resolution of FEM-based approaches while simplifying meshing and numerical computation. The computational meshes are case-independent and structured. The structured meshes limit the memory requirement in this study to ≈ 4 GB, for a mesh with 27 mio. cells and permit accelerated calculation on the graphics processing unit (GPU), see section 4.1.4. The method takes up the basic features of the finite cell method, used in structural mechanics [234]. Details on the computational mesh and compensation of the resulting loss of accuracy are described in section 4.1.5. The boundary conditions used in the new full-field technique limit the method to RVE $\geq 3 \times D_{50}$, see section 4.1.4. Regardless of the method used, **Table 4.1** shows that very long runtimes of the packing modeling occur for RVEs $> 6 \times D_{50}$. This did not lead to any restrictions in the context of this work but must be communicated as a general restriction for all methods, considering today's computing capabilities.

4.1.2 MICROSTRUCTURE MODELING WITH SPHERICAL PARTICLES

The first step of every microscale simulation process is the modeling of the materials microstructure. There are existing approaches, that derive microstructural models from experimental data, e.g., scanning electron microscopy [235–237], but these methods do not allow the creation of artificial material models. Since the objective of this work is to carry out systematic studies on the properties of the microscopic packing structure, completely virtual filler packing models were created. The modeling approaches are adapted from established granular bed modeling since filler concentrations close to the maximum packing density are of interest. Many fillers used in practical applications have approximately spherical particles, see references in chapter 2.5. These are the basis for the explanation of the packing modeling in this section. An extension to arbitrary particle morphologies is presented in section 4.1.3.

The modeling of dense particle arrangements, especially for spherical particles, has been the subject of numerous publications in recent decades with a variety of objectives. Some studies investigated the maximum achievable packing density, while others modeled packings to later perform physical simulations of diffusion, flow, or electricity. In general, most of the published approaches can be assigned to one of the following groups:

- Collective rearrangement methods, e.g., in [238–241], and
- Sequential addition methods, e.g., in [242–248].

Using a collective rearrangement method, all particles are randomly placed within the RVE initially and then further stepwise adjustments are made to either the particle sizes, the particle positions, or both. One option is to start with a random dense packing, allowing overlaps at the beginning and optimize the positions and sizes afterwards to eliminate all overlaps. Alternatively, the packing can begin as random and loose, and then be compacted as much as possible by virtually shaking or vibrating. Both methods can achieve a dense packing of particles. In general, collective rearrangement methods are computationally expensive, especially when considering large numbers of particles. Furthermore, limiting the resulting size distribution can be difficult when the sizes of single particles must be adjusted during the rearrangement steps.

Particles are added in a stepwise fashion in a sequential addition algorithm, with size and position defined directly. If the positions are selected randomly, large gaps remain between the single particles and the resulting packing density is low. Therefore, methods have been developed where each new particle is added in contact with the existing packing. A very popular method, known as the spherical growth procedure, is based on the early work of Norman in 1971 [242] and Adams and Matheson in 1972 [243], and has since been applied and expanded upon in several studies [245–248]. A container is filled with particles, starting with either one central particle or a small cluster of a few particles in the middle of the volume, with all subsequently added particles placed at positions where they contact the existing packing. The packing grows from the center outwards by adding particles step by step, until the desired volume is filled. The new positions are selected in such a way that each newly positioned particle touches three existing particles. This ensures that all gaps are filled, for the densest packing. This method permits the quick growth of particle packings while maintaining the desired size distribution. Matheson [249] reported resulting inhomogeneities in packing density using this method and proposed an alternative in 1974. Instead of growing the filler packing from a central point, a flat surface was used as the basis for filler packing growth. Another variant is to reverse the methodology and start with positioning the individual filler particles at the edge of the RVE and grow the filler packing inwards [250,251]. With this method, it is noticeably hard to handle the last remaining gap in the center of the volume, but the effect of the central void is smaller with larger total volumes. Another sequential addition algorithm is the dropping method. Visscher and Bolsterli [252] reported the use of this method already in 1972, and Santiso and Müller [244] applied this method to large systems with up to 20,000 particles in 2002. The sequentially added particles are "dropped" from a random position above the volume to be filled. After hitting the existing particles, rolling is modeled until a stable position is reached. As with the spherical growth procedure, the existing gaps are filled most effectively for dense packing. In addition to the collective rearrangement and sequential addition methods, several combined procedures have been developed where individual particles or clusters are added and then the packing is compacted by collective rearrangement [253,254].

A sequential addition algorithm was also implemented as part of this work, based on the assessment that the control of the desired size distribution and homogeneity is much easier than when using collective rearrangement methods. A spherical growth procedure was programmed, which has the disadvantage of possible radial inhomogeneities reported by Matheson [249]. The produced packings were therefore carefully examined regarding their homogeneity and found to be sufficiently homogeneous. Further details will follow after the explanations of the spherical growth procedure.

Figure 4.1 illustrates the spherical growth procedure for the numerical modeling of filler packings. For the sake of simplicity, the process is shown in 2D and with equally sized spheres. However, 3D simulations were carried out without restriction of particle size. MATLAB®[12] was used to program and run the algorithm. First, an RVE is defined. Only cube-shaped RVEs with a case-dependent size $\Delta x_\mathrm{m} \times \Delta y_\mathrm{m} \times \Delta z_\mathrm{m}$ were modeled. Before particle placement, a random sample of $100{,}000$ particle sizes is prepared, from which the particles are selected sequentially. For the preparation of the random sample, an experimentally determined or a theoretically defined particle size distribution can be used. A theoretically defined particle size distribution is discretized into 145 logarithmically spaced intervals, which are used to represent the size distribution in the random sample. To maintain the desired particle size distribution during the entire packing generation process, batches of 20 randomly selected particles are created. Each batch is adjusted to best match the required size distribution and morphology characteristics. Those prepared batches are then positioned within the RVE sequentially. The first particle is positioned in the center of the RVE, see part (a) of **Figure 4.1**. The next particles with diameter D_i are placed in contact to the existing packing in the center of the RVE.

---

[12] MATLAB®: R2022a, R2023b, R2024a

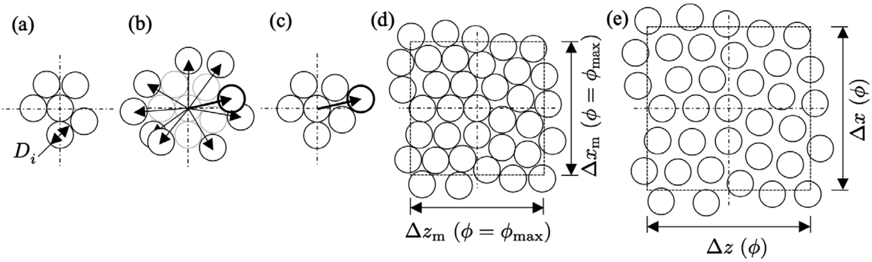

Figure 4.1. Schematic illustration of spherical growth procedure.
Simplified 2D illustration of a process, which is carried out in three dimensions. Numerical generation of a dense filler packing with all particles in contact with each other in (a) – (d). Expansion of the entire RVE, keeping relative particle positions, while maintaining the particle sizes to adjust the filler volume fraction in (e).

To find the best position for each particle to be positioned, N different possible positions around the existing packing are explored. Therefore, the particles are numerically shifted radially outwards from the center of the RVE, until no overlaps with the previously placed particles remain, see part (b). The directions are selected randomly and out of N possible particle positions, the one with the closest distance to the RVE center is selected, see part (c). All others are rejected. This ensures efficient filling of all gaps between the filler particles. The higher N, the more likely that perfect positions for a very dense particle arrangement are found. Thus, increasing N increases the achievable packing density. Section 4.2.1 deals with the effects of varying N, and thus achieving different packing densities. The packing procedure ends when no further particles can be added within the defined RVE. Particles that overlap the RVE boundaries are cut off during the subsequent meshing process. In the final packing (d), all particles are in contact with their neighboring particles. This state is referred to as ϕ_max configuration. For equally sized spheres and N being between 500 and $500{,}000$, packing densities between 0.578 and 0.641 were attained. This range is in line with literature values for maximum packing densities of sphere packings.

Random packing of spheres has been widely studied experimentally, numerically, and theoretically [243,249,255–259]. The achieved packing densities always depended on the experimental methods, or the packing algorithm employed in simulations. It has been established that the densest random particle arrangements approach a packing density of $\phi \approx 0.637$, known as random dense packing or random close packing. While this value is generally accepted as the maximum achievable for random sphere packing, its stochastic nature prevents a precise definition [256]. Nevertheless, the term "random close packing" is also adapted in this work to describe packings with equally sized spheres that have a packing density of $\phi \approx 0.64$ in the ϕ_max configuration. Achieving higher packing densities with equally sized spheres requires crystalline substructures or fully crystalline arrangements, such as the face-centered cubic packing, which has a maximum packing density of

$\phi_{\mathrm{max}} = \pi/(3\sqrt{2}) = 0.74048\ldots$ [257,258]. The ϕ_{max} configuration is of limited applicability for thermal simulations of filled polymers. To set a desired filler volume fraction $\phi < \phi_{\mathrm{max}}$, the entire RVE including the particle positions is expanded uniformly in all three spatial directions to $\Delta x \times \Delta y \times \Delta z$ while maintaining the particle sizes, see part (e) of **Figure 4.1**. The result is a homogeneous, random packing structure with the desired filler volume fraction ϕ based on a specified ϕ_{max} configuration. The interpretation of this relationship is discussed in chapter 4.2.

The ϕ_{max} configuration can be adjusted by varying N, enabling the modeling of fillers with different packing characteristics. In addition to N, ϕ_{max} is also influenced by the particle shape and size distribution. **Figure 4.2** shows the process of deriving multiple filler volume fractions based on one ϕ_{max} configuration using a filler packing of Alox-S-22 as an example. Central cross-sections of the RVE are shown. Initially, the ϕ_{max} configuration was modeled in an RVE with $\Delta x_{\mathrm{m}} = \Delta y_{\mathrm{m}} = \Delta z_{\mathrm{m}} = 90$ µm. $\phi_{\mathrm{max}} = 0.68$ is reached with $N = 5{,}000$. The stepwise expansion up to $\Delta x = \Delta y = \Delta z = 136$ µm reduces the filler volume fraction down to $\phi = 0.2$. The resulting filler packings are perfectly homogeneous as local accumulation or individual particle-particle contacts are impossible with this procedure. This aspect and alternative modeling approaches are discussed in chapter 4.3.

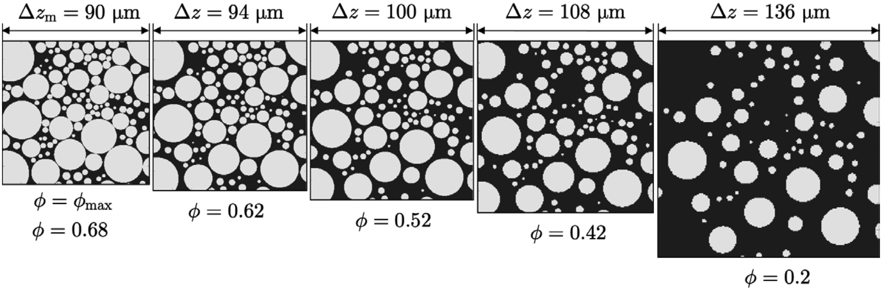

Figure 4.2. Expansion of the RVE to adjust the filler volume fraction.
Cross-sections of a particle filled RVE during an expansion process (from left to right), starting at the maximum packing density of $\phi = \phi_{\mathrm{max}} = 0.68$, ending at $\phi = 0.20$. All packing models with $\phi < \phi_{\mathrm{max}}$ are based on the same initial ϕ_{max} configuration. Filler: Alox-S-22.

One of the biggest challenges in modeling RVEs is determining an appropriate size that balances computational efficiency and statistical representativeness. Smaller RVEs provide higher geometric resolution but may not capture the full particle size distribution of the filler and variability of the random packing behavior. On the other hand, larger RVEs can better compensate for local packing variations and thus reduce statistical variance in repeated simulations. As RVE size increases, local heterogeneities tend to homogenize at the global level, and the variability between independently modeled packings decreases. This convergence behavior has been investigated in numerous studies to define minimum

RVE sizes that ensure statistically reliable simulation results. If the RVE is too small, the modeled packing may not be representative, leading to large variations in the results and poor reproducibility.

Two criteria were checked to assess the representativeness of RVEs:

1. The deviation between desired and modeled particle size distribution: If D_{10}, D_{50}, and D_{90} deviate less than two percent from the target value, the filler packing is assumed to be representative. Details on the evaluation and an exemplary comparison between the desired and modeled particle size distribution are provided in appendix C.1.
2. The stability of the thermal simulation: Modeling a too small RVE causes a strongly non-linear temperature curve along the heat flow direction (z-axis), see section 4.1.4. This leads to a high uncertainty in the linear regression used to extract the effective thermal conductivity. An uncertainty threshold of $1~\%$ in the regression slope is defined as acceptable, ensuring the RVE is sufficiently large to compensate for local internal variations. As a result, the uncertainty in the simulated effective thermal conductivity is an order of magnitude lower than that of the experiments, see section 3.2.6.

The following findings were made in a series of test simulations and packing studies:

- Fillers with a broad size distribution increase the microstructure randomness and thus ensure a higher linearity in the temperature curve. Therefore, smaller RVEs may be sufficient to achieve a good linear regression.
- For fillers with a broad size distribution, larger RVEs are required for a representative size distribution.
- Irregularly shaped filler particles increase the microstructure randomness, thus smaller RVEs suffice to achieve a good linear regression.

The first two effects mentioned are opposing and overlap, so that no generally valid statement on the required RVE size is possible. The dominant effect depends on the individual filler properties. Based on those findings, the RVEs were modeled with a filler dependent size between three and six times the median particle size D_{50}. A size of $6 \times D_{50}$ was necessary for equally sized spheres. When introducing a size distribution for spheres, the necessary RVE size dropped to $4 \times D_{50}$, before increasing again to $6 \times D_{50}$ for very wide size distributions. For strongly irregular particle shapes and medium broad size distributions, the necessary RVE size dropped even further to $3 \times D_{50}$.

The preliminary studies described were conducted on a representative selection of modeled RVEs and additionally showed that repeated simulations with identical setups yield a standard deviation of less than $1~\%$. This not only confirms the adequacy of the selected RVE size but also provides a solid basis for estimating the statistical uncertainty in all subsequent simulations. Since the uncertainty margin is very small compared to the experimental uncertainty, it is treated as constant in the following analyses and not reassessed for each individual model. An exemplary study on model reproducibility is provided in appendix C.1. Due to the meshing procedure described in the section 4.1.4, the filler volume fraction of the simulated models is known exactly, so that no uncertainty needs to be considered here.

Before performing the thermal simulations on the modeled RVEs, the filler packings must also be checked for homogeneity, randomness, and isotropy. Numerous methods and indicators have already been described in various publications. In general, the homogeneity can easily be checked by dividing the RVE into several sub-volumes and calculating the standard deviation of local properties [241,248]. Another method to check the properties of a filler packing is evaluation of the radial distribution functions, e.g., [244,249,252,259]. A radial distribution function quantifies how the particle density varies with the distance to a reference particle in a packing structure and can be used to identify unwanted structuring.

The most prominent criterion, which was also chosen for the evaluation of filler packings in this work is the coordination number, the average number of contacting neighbors per particle. The coordination number was already analyzed in the early works of Bernal and Mason in 1960 [260], Tory et al. in 1968 [261] and Visscher and Bolsterli in 1972 [252], but continues to be used in later work, e.g., Yang et al. 1996 [239], Kristiansen et al. 2005 [262], An et al. 2005 [263]. The coordination number is reported to be around six for a random dense packing of equally sized spheres with $\phi_{\max} \approx 0.64$ and drops for lower packing densities, or with the introduction of a size distribution. Lattice structures exhibit significantly higher coordination numbers. For example, in a body-centered-cubic packing it is eight, while in hexagonal close and face-centered-cubic packings, all particles have twelve contacting neighbors. The local coordination number can be used to assess the randomness of modeled packings. If local coordination numbers of ≥ 7 are determined, a crystalline sub-volume must be assumed, and the generated packing is discarded. This risk solely exists for packings of equally sized spheres. With the previously described packing algorithm, globally averaged coordination numbers of up to 5.2 were achieved for the densest filler packings with $\phi_{\max} \approx 0.64$. This is slightly lower than the literature value of six mentioned above. The slightly lower coordination number results from the differences in the packing algorithm. Instead of looking for positions with at least three contact partners, the positioning of new particles is based on selection of the position closest to the center from a limited random sample. Presumably this method increases the randomness of filler packings, which is fairly advantageous, but at the same time reduces the coordination numbers.

The homogeneity and geometrical isotropy of the packings are evaluated based on position-dependent coordination numbers and filler volume fractions. **Figure 4.3** shows an example of the calculated filler volume fractions and coordination numbers for a random medium dense packing of equally sizes spheres.

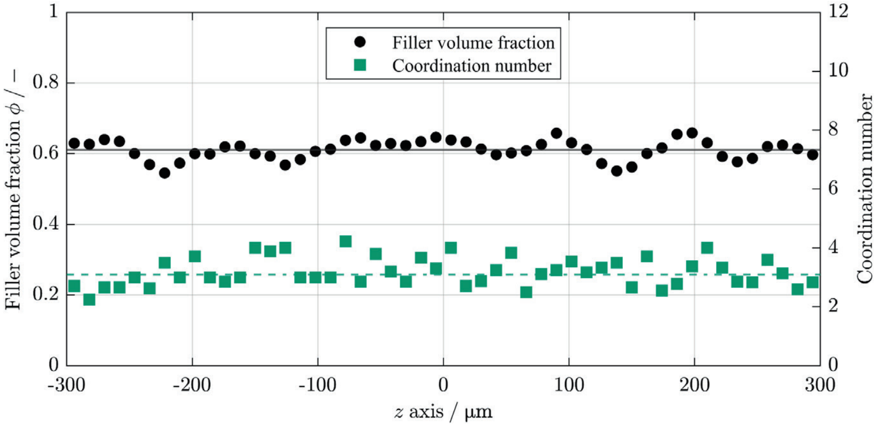

Figure 4.3. Packing evaluation along the z axis of a modeled RVE.
Filler volume fraction and local coordination number along the z axis. Random medium dense packing of equally sized spheres with $\phi_{\text{max}} = 0.61$.

Shown is the evaluation along the z axis, which is the primary heat flow direction in the subsequent thermal simulations. Evaluations along the other spatial directions were carried out additionally and typically showed no differences. For the analysis, the packing with particles of 100 µm in diameter is divided into 12 µm slices. The analyzed packing has an average coordination number of 3.1. Both filler volume fraction and coordination number show random variations, but neither systematic trends nor inhomogeneity are detected.

4.1.3 MICROSTRUCTURE MODELING WITH ARBITRARY PARTICLE MORPHOLOGIES

Finally, an extension to the presented technique for modeling arbitrary particle morphologies is provided. Clearly the spherical particles are the simplest case, as they can be described with merely three spatial coordinates and one diameter. It is unnecessary to specify an orientation. There are numerous primitive particle shapes for which only minor additions to the algorithm would have to be made. However, since complex and realistic particle shapes are also considered in the further development, the utilized method is directly suitable for arbitrary particle morphologies. The description is based on the example of real, digitized particle morphologies, but artificial shapes can also be represented, see section 4.2.3. An interesting method, in which arbitrary particle shapes are composed of a finite number of spheres of the same or different sizes was used by Smith and Midha in 1997 [255] and Zhao et al. in 2011 [264], for example. A disadvantage here is that the surfaces of the abstracted bodies are never completely smooth, when formed with a reasonable number of base spheres. The surfaces always have a characteristic structure created by the spheres. An alternative method was used by Jia and Williams [265] (2D) and Gan et al. [266], based on pre-meshing the volume to be filled and positioning the digitized particles that are represented by point clouds. This approach is also pursued in the present study. Particles are digitized using a 3D laser scanning microscope[13]. The gained images are first processed with an image analysis software[14]. High frequency noise is automatically removed, and the resulting height data from the scans are stored in tabular form. The images have a spatial resolution of $0.14\ \mu\mathrm{m}$ in the x and y directions and the scan resolution in z direction is $0.08\ \mu\mathrm{m}$. The height data are further processed using MATLAB®. **Figure 4.4** illustrates the main steps of the digitization process. In the first step, the upper half of the particle is extracted by truncating the height data at half the maximum height (orange line), see part (a). A point cloud, representing the captured surface is generated in the second step, see part (b). This point cloud is based on the x and y resolution of the image and reduced to $1/25$ of the original resolution in **Figure 4.4** for better visualization.

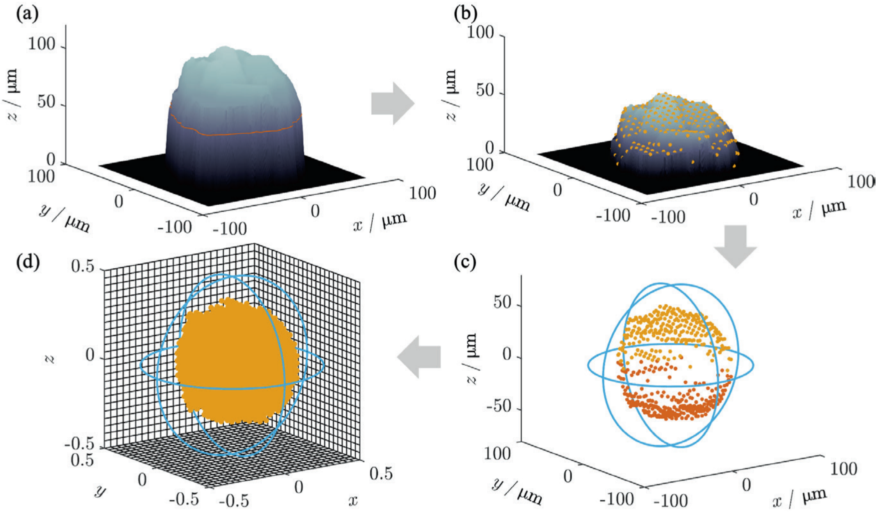

Figure 4.4. Filler particle digitization process.
Height data obtained during a single particle scan (a). Reduced data and point cloud representing the particle's upper half (b). Extracted and mirrored point cloud with spherical envelope (c). Pixel based representation of particle volume (d). All illustrations are reduced to $1/25$ of the original resolution for better visualization.

---

[13] Keyence VK-X100K with a 100x magnification lens

[14] Keyence VK-H1XAD

The point cloud is mirrored to represent the lower surface of the particle that cannot be captured, see part (c). Finally, a volumetric point cloud is generated that represents the filling volume of the particle, see part (d). By superimposing a numerical grid with the same spatial resolution, a pixel-wise representation of the particle volume is obtained. In this step, the size of the particle model is normalized to one based on the size of an enveloping sphere. These particle data sets are stored for further use in microstructure modeling. Tensors are stored with a logic "1" for particle volume and a logic "0" for empty volume. No absolute size information is stored with the particles.

It is also important to note that mirroring the particle data is a simplification, however it is assumed that the morphological characteristics (geometrical structure, shape, and roughness) of the particles are adequately represented this way. The randomness required to represent a complete particle packing is achieved by digitizing ten different particles per filler and then randomly rotating and scaling them.

The pixel-wise representation of the digitized particles can be visualized using a suitable rendering software, see **Figure 4.5**. Three exemplary laser microscope images of digitized particles are shown in (a) - (c). The corresponding rendered 3D particle models derived from them are shown in (d) - (f). The rendered images were generated using the rendering software MATLAB® Volume Viewer.

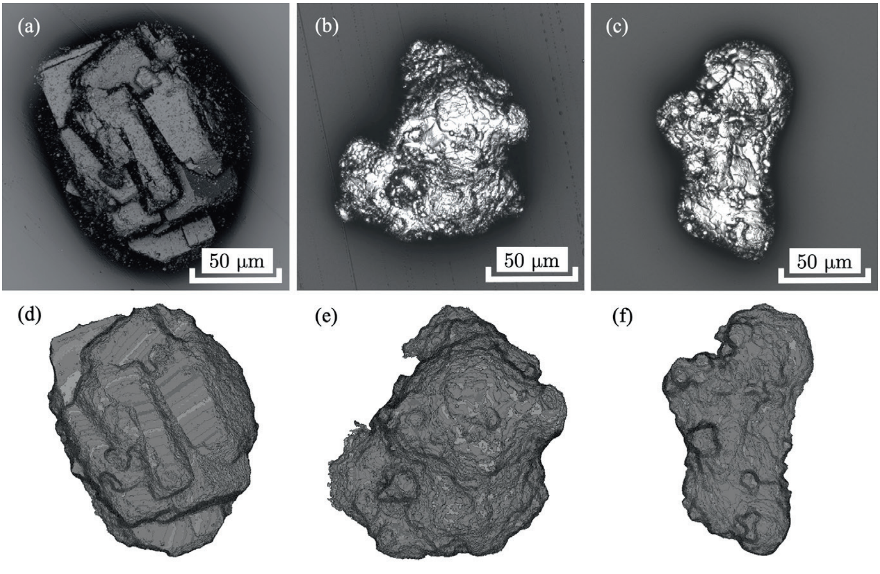

Figure 4.5. Digitization results of exemplary filler particles.

Laser microscope images, taken with a Keyence 3D laser scanning microscope VK-X100K with a 100x magnification lens in (a) – (c). Corresponding 3D particle models derived from the laser microscopic data in (d) – (f). Fillers: ATH-I-75 (a), Al-I-88 (b), and Al-I-103 (c).

These representations are based on the original resolution of the digitization. The completely different morphological characteristics of the particles, and thus the need for individual digitization can be seen from these three examples.

Packing modeling is then carried out based on the digitized particle models. There is a basic difference between packing modeling with ideal spheres and arbitrarily shaped particles. For the latter, the complete RVE is pre-meshed. The cube-shaped volume is divided into $n = n_x = n_y = n_z = 50 \ldots 300$ cube-shaped cells per spatial direction. This step is necessary for subsequent processing and therefore does not involve any additional effort. **Figure 4.6** illustrates the filler packing modeling procedure based on digitized particle models. Ten digitized particle models are available, which are represented by size-normalized logical tensors and can be called up one after the other (a). The sequence is determined randomly. As several hundred to a few thousand particles must be positioned per RVE, the particle models are repeated frequently. After selecting the next particle model, the absolute size of the particle and its orientation are adjusted. The size is determined according to the desired particle size distribution.

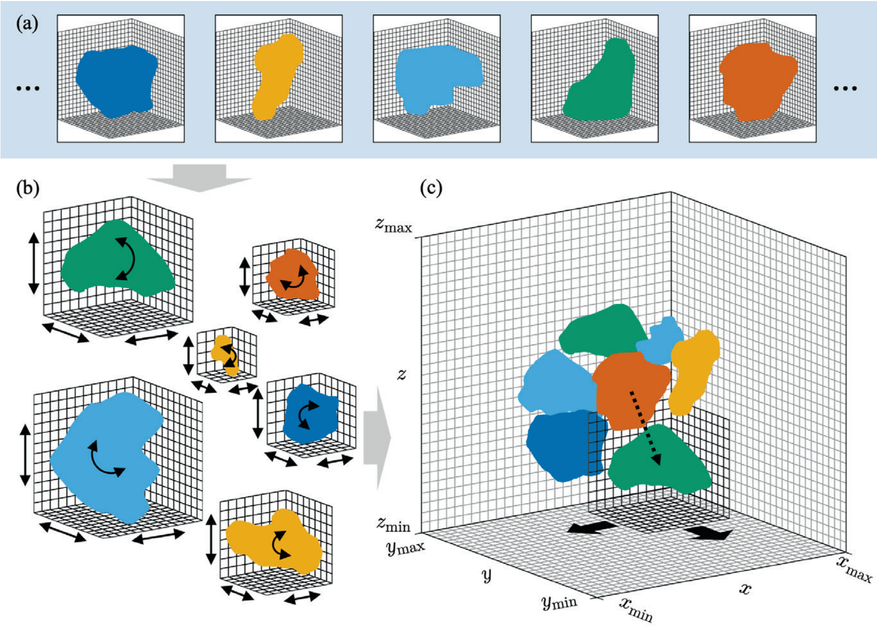

Figure 4.6. Filler packing modeling with arbitrarily shaped particles.
Simplified illustration of the packing process, based on digitized particle models, represented with numerical grids. Digitized and stored particle data sets (a). Scaling and rotation process for randomly selected particles (b). Sequential insertion of the particles to the RVE by superimposing the RVE and particle grids (c).

When converting to this size, the particle models are projected onto numerical grids that have the same spatial resolution as the mesh of the RVE. Therefore, the particle models are resolved with a different number of mesh cells per spatial direction based on their size, see part (b) of **Figure 4.6**. The number of mesh cells per particle and spatial direction are typically between ten for the smallest particles in the packing and 200 for the largest particles. In the illustration, the spatial resolution is again significantly reduced for better visualization of the grids. After the size has been determined, the logical tensor is generated in the final size, and the particle model is randomly rotated with the angles α, β, and γ around the z, y, and x axis. No preferred direction is considered in the standard procedure. A different procedure considering a particle alignment is described in section 4.2.3. The rotation is done with a simple coordinate transformation. For each tensor cell i, containing a logic "1", a transformation from the original coordinates x_i, y_i and z_i to the rotated coordinates ${x'}_i, {y'}_i$ and ${z'}_i$ is performed with

$$\begin{pmatrix} {x'}_i \\ {y'}_i \\ {z'}_i \end{pmatrix} = R' \begin{pmatrix} x_i \\ y_i \\ z_i \end{pmatrix} , \tag{4.1}$$

where $R^{\acute{}}$ is the rotation matrix for the rotation of axis in Euclidean space

$$\begin{gathered} R^{\acute{}} = R^{\acute{}}_z(\alpha)\ R^{\acute{}}_y(\beta)\ R^{\acute{}}_x(\gamma) \\ = \begin{bmatrix} \cos\alpha & -\sin\alpha & 0 \\ \sin\alpha & \cos\alpha & 0 \\ 0 & 0 & 1 \end{bmatrix} \begin{bmatrix} \cos\beta & 0 & \sin\beta \\ 0 & 1 & 0 \\ -\sin\beta & 0 & \cos\beta \end{bmatrix} \begin{bmatrix} 1 & 0 & 0 \\ 0 & \cos\gamma & -\sin\gamma \\ 0 & \sin\gamma & \cos\gamma \end{bmatrix} . \end{gathered} \tag{4.2}$$

Finally, the prepared particle grids can be inserted into the pre-meshed RVE, see part (c) of **Figure 4.6**. If both these grids have the same spatial resolution, the particle grids can be used like bricks and moved cell by cell in all directions. This means that the spherical growth method described previously can be used without restriction. N possible positions are determined for each particle by moving it radially outwards from the center of the RVE in N randomly selected directions, until no more overlap with existing particles is detected. In the case of arbitrary shaped particles, this gradual movement is performed cell by cell. Particle overlap can be identified as a multiple assignment of individual cells in the grid.

Figure 4.7 shows an example of four modeled RVEs and a summary of the input parameters. Parts (a) and (c) show modeled filler packings with spherical particles. There is either a random packing of equally sized spheres (a), or log-normal size distributed spheres with $\log(\sigma) = 0.4$ (c). In (b), a packing of equally sized spherocylinders with a length-to-diameter ratio of $L/D = 5$ is shown. Part (d) shows a packing of irregularly shaped, digitized aluminum particles (Al-I-88).

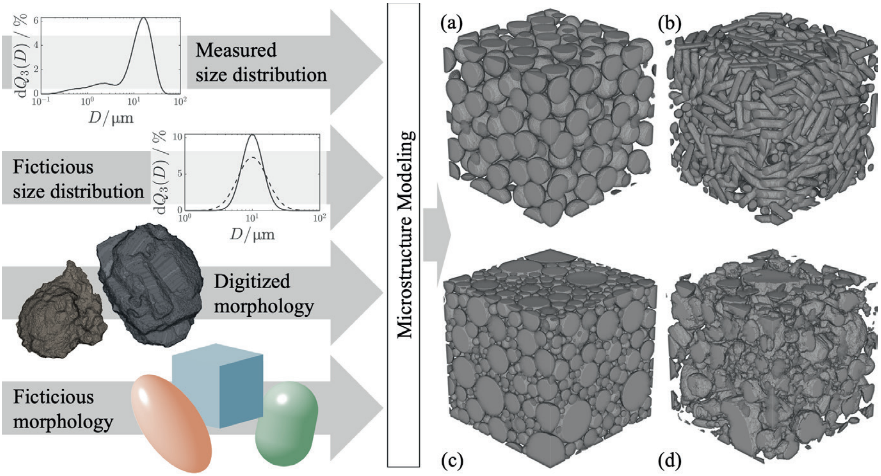

Figure 4.7. Microstructure modeling based on experimental or artificial input data. Exemplary images of generated filler packings in $\phi_{\max}$ configuration. Random packing of equally sized spheres in (a). Random packing of spherocylinders with $L/D = 5$ in (b). Random packing of spherical particles with log-normal size distribution and $\log(\sigma) = 0.4$ in (c). Random packing of digitized aluminum particles of irregular shape in (d), representing Al-I-88.

The microstructure modeling method is based on a particle size distribution, particle morphology input, as well as the specified modeling parameter N to adjust the resulting packing density. For details, see chapter 4.2. Both the particle size distribution and the particle morphology can be modeled artificially. This is particularly suitable for basic parametric studies and analyses, see e.g., sections 4.2.2 and 4.2.3. However, it is also possible to base the models on real measured filler data and thus achieve results that are as close to reality as possible, see chapter 4.5.

4.1.4 COMPUTATION OF MICROSCALE HEAT CONDUCTION

After modeling the materials' microstructures in cube-shaped RVEs, the models are meshed, boundary conditions are defined, and the system is solved using a steady-state heat conduction solver. The meshing process discretizes the calculation space spatially, which is a necessary step for the subsequent application of the numerical solver. If the RVE has already been pre-meshed for packing generation with arbitrarily shaped particles, this step is skipped. As already introduced, a case-independent, structured mesh with equally sized, cube-shaped mesh cells is used. A case-dependent mesh would have the advantage that local areas can be resolved with different levels of resolution. The resolution potential of the method used here is lost in geometrically complex areas and the resolution can be finer than necessary in irrelevant areas. Nevertheless, the advantage of the significantly lower storage requirement of a structured mesh predominates. Accuracy losses are compensated for by using a dynamic mesh. This newly developed approach qualifies the method for calculations of large RVEs with $> 4 \times D_{50}$, which would demand excessive memory and computation time when using current commercial FEM software. **Figure 4.8** illustrates the comparatively simple meshing process in the case of a structured mesh.

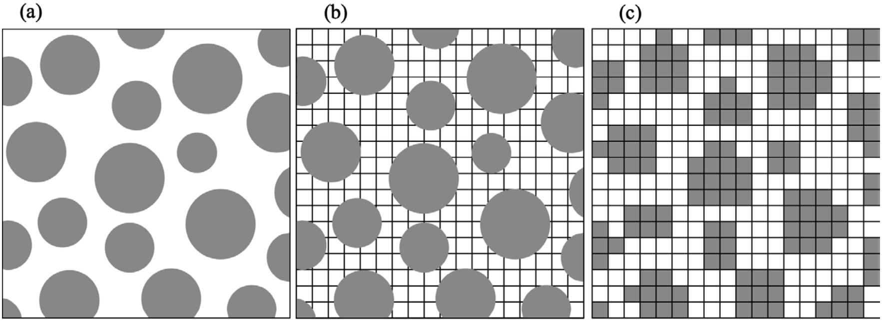

Figure 4.8. Process of meshing a modeled microstructure RVE with equally sized cube-shaped mesh cells.

Schematic illustrations of central cross-sections. Filler packing in (a). Filler packing and superimposed grid in (b). Discretized RVE in (c).

For the sake of simplicity only central cross-sections are shown, although the process is volumetric. The generated, and typically expanded filler packing is overlaid with a numerical grid of $n = n_x = n_y = n_z = 50 \ldots 300$ equally sized cube-shaped mesh cells. The particle's thermal conductivity is defined for all mesh cells located with at least $50\ \%$ of their volume within a particle domain, and all for all other cells, the polymer's thermal conductivity is set. A thermal interfacial resistance can be set at interfaces between cells if they represent a boundary between particle and polymer, see chapter 4.4. The result is a spatially discretized representation of the RVE, ready for thermal simulation in the next step. Each mesh cell is considered as an isothermal volume and projected onto its center point. Each mesh cell has exactly six clearly defined neighboring cells in the structured grid with which it can interact. The coefficient matrix required for the calculation is therefore significantly narrower than for unstructured grids with arbitrary interactions between individual cells. A mesh with $n = 300$ has $27\ \mathrm{mio.}$ cells in total and a storage demand of $216\ \mathrm{MB}$ per physical quantity in double precision.

A process of steady-state heat conduction through the RVE in the negative z direction is simulated. For this purpose, a constant temperature difference is applied to the boundaries of the RVE between $z = z_{\mathrm{min}}$ and $z = z_{\mathrm{max}}$, see part (a) of **Figure 4.9**.

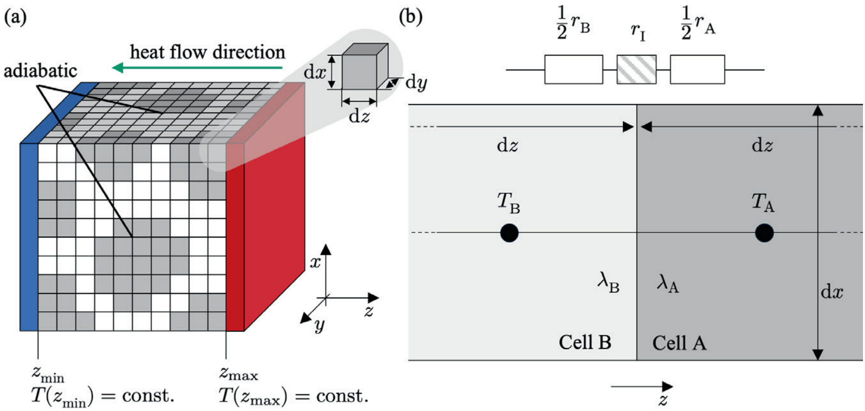

Figure 4.9. Simulation setup for steady-state heat conduction through RVE.
Simplified illustration of the meshed RVE with boundary conditions in (a). Basic principle of local thermal resistance modeling in (b).

In general, any temperature difference can be applied, and if the simulation is carried out with temperature-independent material values, the absolute temperature level is irrelevant, too. To remain within the typical range of practical applications, Dirichlet boundary conditions with

- $T(z_{\min}) = 293$ K, and
- $T(z_{\max}) = 353$ K

are set. The other four side surfaces are treated as adiabatic walls; thus Neumann boundary conditions are set:

- $q_x(x_{\min}) = q_x(x_{\max}) = 0$, and
- $q_y(y_{\min}) = q_y(y_{\max}) = 0$.

Physically, the applied Dirichlet boundary conditions are not fully accurate for a flat cross-section through a heterogenic material. However, a constant heat flux boundary condition would also be imprecise. Only periodic boundary conditions, such as those applied by Tian et al. [135] or by the Ansys® Material Designer, would be exact from a physical point of view. However, the periodic boundary conditions must already be considered in the packing modeling. It was found that the effect on the packing structure is especially significant for relatively small volumes. For this reason, certain errors due to the incorrect boundary conditions are initially accepted, but later considered in the evaluation process. A more detailed evaluation and discussion of the different boundary conditions was published by Sharma [136] in 2022. After applying the boundary conditions, the resulting heat flow between all mesh cells representing the microscale heat conduction paths is calculated using a finite volume method (FVM) algorithm. MATLAB® was used to program and run the algorithm. Based on Fourier's law, see **Eq. (2.1)**, the balance equation

$$\frac{\partial}{\partial x}\left(\lambda_x \frac{\partial T}{\partial x}\right) + \frac{\partial}{\partial y}\left(\lambda_y \frac{\partial T}{\partial y}\right) + \frac{\partial}{\partial z}\left(\lambda_z \frac{\partial T}{\partial z}\right) = 0 \tag{4.3}$$

can be derived for three-dimensional steady-state heat conduction at each location within the volume. λ_x, λ_y, and λ_z are the thermal conductivities in the three spatial directions. Applied to a grid of $n_x \times n_y \times n_z$ mesh cells with the uniform side length $\mathrm{d}x = \mathrm{d}y = \mathrm{d}z$, the discrete form

$$\frac{\Delta T_{-x}}{r_{-x}} + \frac{\Delta T_{+x}}{r_{+x}} + \frac{\Delta T_{-y}}{r_{-y}} + \frac{\Delta T_{+y}}{r_{+y}} + \frac{\Delta T_{-z}}{r_{-z}} + \frac{\Delta T_{+z}}{r_{+z}} = 0 \tag{4.4}$$

can be formulated for each cell. $\Delta T_{\text{""}}$ denotes the temperature difference between the cell under consideration and the adjacent cell in the indexed direction. $r_{\text{""}}$ denotes the corresponding specific thermal resistance between the two cell centers, see part (b) of **Figure 4.9**. If A is the cell under consideration, then the effective one-dimensional specific thermal resistance towards the adjacent cell B in negative z direction is

$$r_{-z} = \frac{1}{2} r_{\mathrm{B}} + (r_{\mathrm{I}}) + \frac{1}{2} r_{\mathrm{A}} \ , \tag{4.5}$$

where r_{B} is the specific thermal resistance of cell B with $r_{\mathrm{B}} = \mathrm{d}z/\lambda_{\mathrm{B}}$, and r_{A} is the specific thermal resistance of cell A with $r_{\mathrm{A}} = \mathrm{d}z/\lambda_{\mathrm{A}}$. r_{I} is an optional thermal interfacial resistance to be considered. This scheme can describe the interaction resistances between all middle cells. For boundary cells in the x and y directions, the interaction terms towards the adiabatic boundary must be set to zero. For the boundary cells in the positive and negative z directions, a further fictitious cell layer without any thermal resistance and with a constant temperature is added. **Eq. (4.4)** represents a heat flow balance with the summands being the heat fluxes conducted to or from the adjacent cells in all spatial directions. Under steady-state conditions, this energy balance must hold for each cell.

Based on an initial temperature field guess, a numerical iteration scheme is applied to obtain the steady-state temperature field inside the RVE. Many different iteration schemes are available for such applications. For this study, the basic Jacobi scheme is applied, which is a method of simultaneous displacements. It is best suited for very large meshes with numerous cells, as it can be implemented in vectorized form on the GPU and thus enables almost case-independent short calculation times. Details are provided in appendix C.2. For further evaluation, the fully converged temperature field and the corresponding heat fluxes for each mesh cell are stored and post-processed.

4.1.5 EVALUATIONS

Besides the converged thermal fields, only spatial information about the RVE is necessary. The converged fields can be used to visualize the results and to qualitatively analyze the microscale heat conduction paths. **Figure 4.10**, **Figure 4.11**, and **Figure 4.12** show exemplary evaluations of different simulated RVEs. Part (a) of the figures shows a central cross-section through the microscale packing structure of the RVE. An ideally spherical filler is shown in **Figure 4.10**, and two fillers with irregular grain shape based on particle digitization are shown in **Figure 4.11** and **Figure 4.12**. Part (b) of the figures shows the steady-state heat flux field in the same cross-section and part (c) shows the respective steady-state temperature field. The heat is conducted in the opposite direction to the z axis. The temperature fields are highly inhomogeneous with no flat isothermal cross section in the entire RVEs. At the RVE boundaries, the imposed Dirichlet boundary conditions artificially influence the temperature distribution, disturbing the actual inhomogeneity of the internal field. As a result, the boundary regions must be excluded during subsequent evaluation. In part (b) of the figures, the formation of good heat-conducting paths through the particle network can be recognized. Paths that carry a high heat flux run along the heat flow direction from particle to particle. An increase in the heat flux can be seen at the narrow points between the particles. Nevertheless, there are no percolation paths in the true sense of the word, since all RVEs were expanded homogeneously and thus all particles were pulled apart equally.

For a quantitative evaluation and extraction of the effective thermal conductivity of the RVE, Fourier's law in one-dimensional notation must be used. The effective thermal conductivity can be calculated with

$$\lambda_{\mathrm{eff}} = \frac{-q_z}{\mathrm{d}\bar{T}/\mathrm{d}z}\,, \tag{4.6}$$

where q_z is the heat flux through the RVE in z direction and $\mathrm{d}\bar{T}/\mathrm{d}z$ is the mean temperature gradient within the RVE. The negative sign indicates the heat flow direction. The heat flux must be equal for all mesh cell layers to maintain an energy balance and can be easily derived from the converged heat flux field data.

To determine the mean temperature gradient for **Eq. (4.6)**, the evaluation region must first be defined. As already described, the Dirichlet boundary conditions at z_{min} and z_{max} are not physically correct. The disturbance of the temperature field protrudes approximately one particle size into the RVE. This effect can be observed most clearly in part (d) of **Figure 4.12**. Consequently, the two boundary regions up to the marked boundary level, see dashed lines in part (d) of **Figure 4.10**, **Figure 4.11**, and **Figure 4.12**, are ignored in the calculation. Only the temperature gradient of the zone in between is calculated.

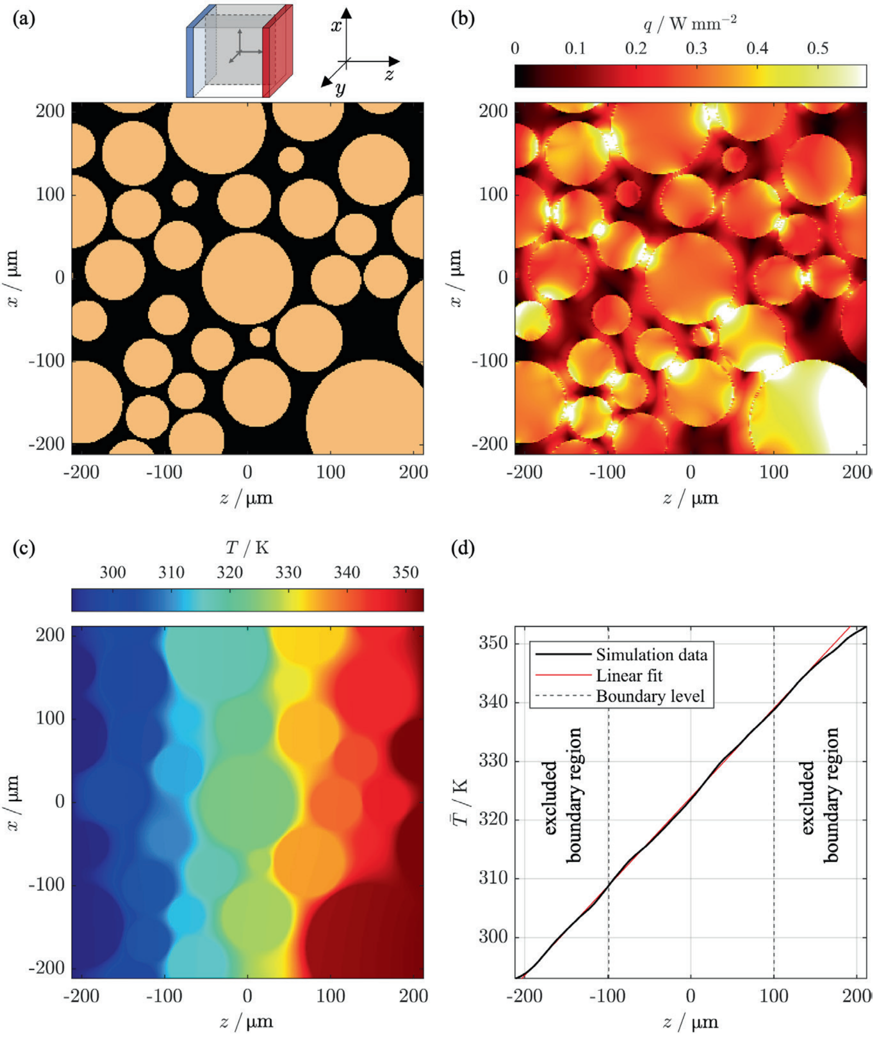

Figure 4.10. Results of microscale heat conduction simulation 1 (ideally spherical filler).

Central cross-sections of geometry (a), steady-state heat flux field (b), steady-state temperature field (c), and average temperature curve along heat flow direction (d). Polymer: $\lambda_{\mathrm{C}} = 0.25$ W m^{-1} K^{-1} (e.g., epoxy). Filler: Spheres with log-normal size distribution with $\log(\sigma) = 0.2$, $D_{50} = 100$ µm, $\phi_{\max} = 0.66$, $\phi = 0.56$, $\lambda_{\mathrm{D}} = 35$ W m^{-1} K^{-1} (e.g., alumina). $\lambda_{\mathrm{eff}} = 1.26$ W m^{-1} K^{-1}.

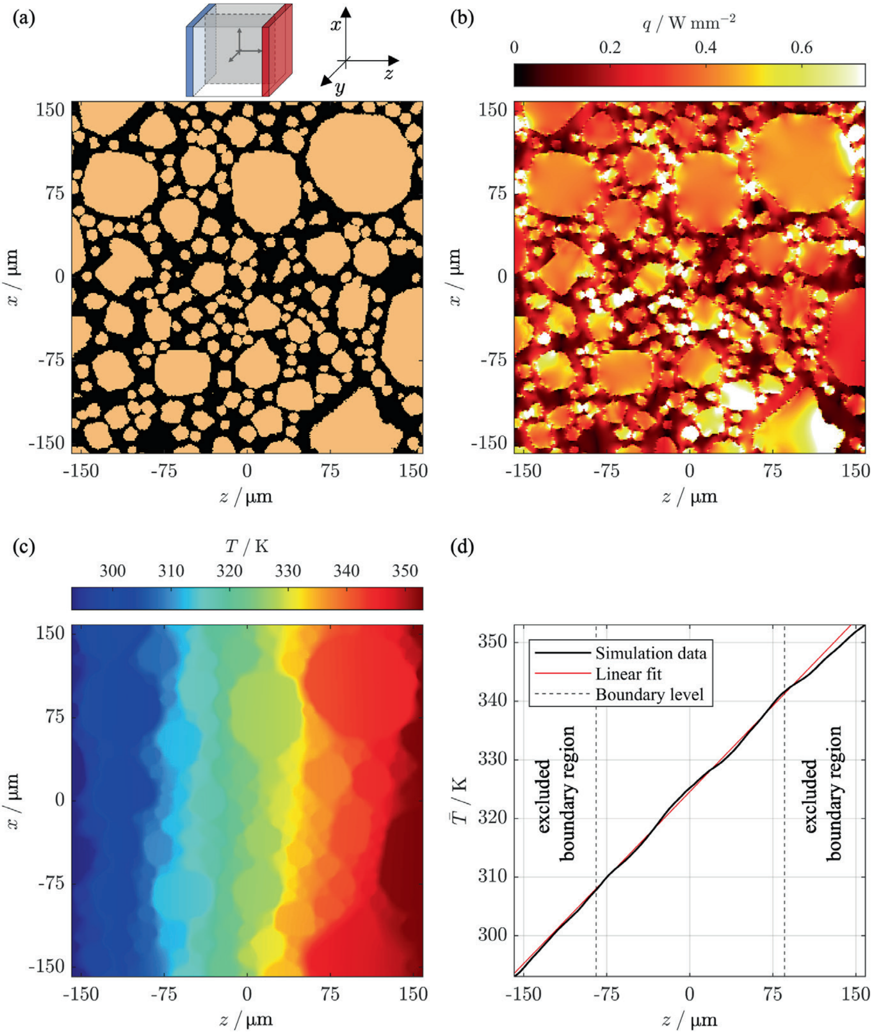

Figure 4.11. Results of microscale heat conduction simulation 2 (irregular particle morphology). Central cross-sections of geometry (a), steady-state heat flux field (b), steady-state temperature field (c), and average temperature curve along heat flow direction (d). Polymer: $\lambda_C = 0.25$ W m^{-1} K^{-1} (e.g., epoxy). Filler: ATH-I-75 with digitized morphology. $D_{50} = 74.6$ µm, $\phi_{max} = 0.64$, $\phi = 0.56$, $\lambda_D = 10$ W m^{-1} K^{-1}. $\lambda_{eff} = 1.28$ W m^{-1} K^{-1}.

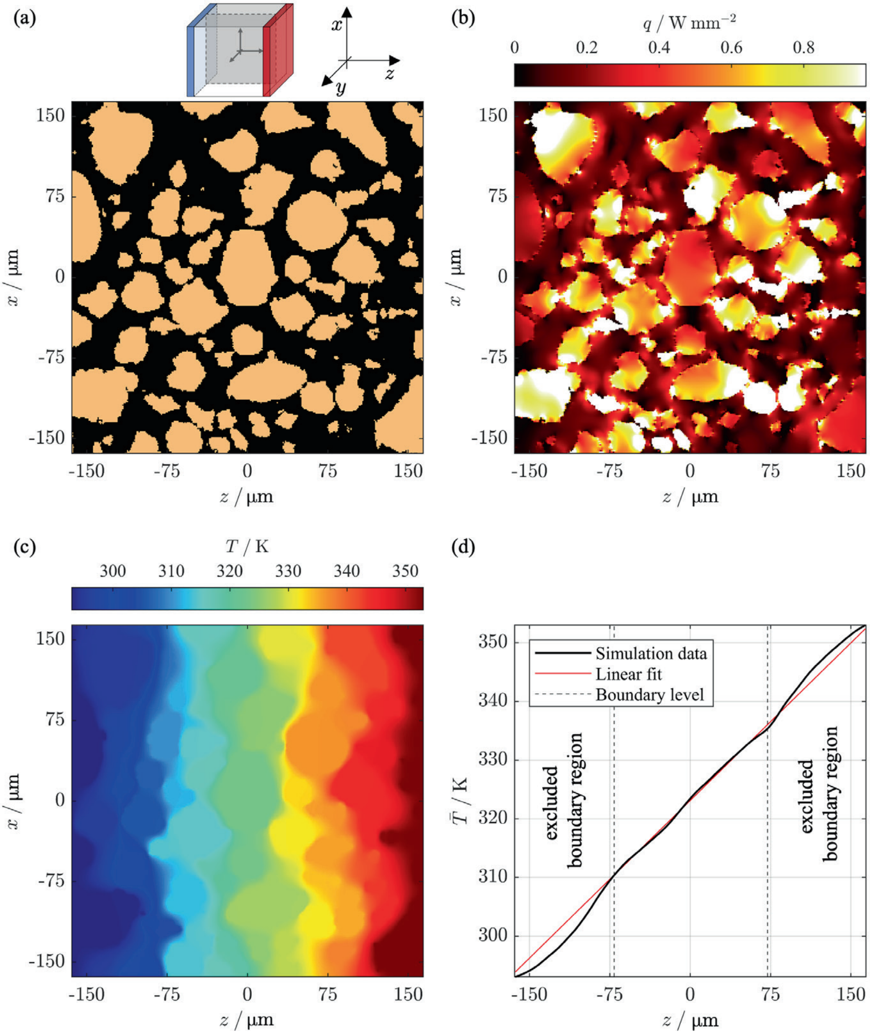

Figure 4.12. Results of microscale heat conduction simulation 3 (irregular particle morphology). Central cross-sections of geometry (a), steady-state heat flux field (b), steady-state temperature field (c), and average temperature curve along heat flow direction (d). Polymer: $\lambda_C = 0.25$ W m^{-1} K^{-1} (e.g., epoxy). Filler: Al-I-103 with digitized morphology, $D_{50} = 103.1$ µm, $\phi_{\max} = 0.42$, $\phi = 0.38$, $\lambda_D = 150$ W m^{-1} K^{-1}. $\lambda_{\text{eff}} = 1.26$ W m^{-1} K^{-1}.

For the mean temperature gradient, the mean value of all mesh cells per mesh layer is calculated, see black curves in part (d) of the figures. A linear regression is then performed over all mesh layers of the middle zone, see red line in part (d) of the figures. The thickness of the boundary zones is set to the volumetric median particle diameter. The Neumann boundary conditions on the remaining four outer surfaces of the RVE, which are also incorrect, have a much smaller effect on the evaluated thermal conductivity. Since the defined boundary conditions cause a heat flow with a preferred z direction, the local transverse heat flows at the boundaries are negligible. Therefore, a further restriction of the evaluation region is unnecessary. The evaluated effective thermal conductivities of the three simulation examples are given in the captions of the respective figures.

Finally, the aforementioned dynamic mesh approach is explained. In principle, the simple structured, case-independent meshing has several advantages. A clear disadvantage is the loss of resolution in geometrically detailed sub-areas. This is particularly relevant for filler concentrations close to the maximum packing density, as there are only very small interparticle distances, and the particles can fuse together due to the lack of resolution. This leads to a significant overestimation of the effective thermal conductivity. To compensate for this disadvantage in the developed method, the affected calculations are carried out using a dynamic mesh. In the first step, a simple and quick calculation of the RVEs is carried out with a very coarse resolution of $n = n_x = n_y = n_z = 50$. After completion and evaluation, step-by-step refinement and recalculation is carried out until the resolution limit of $n = n_x = n_y = n_z = 300$ is reached, see **Figure 4.13**.

For the example shown, with a filler volume fraction close to the maximum packing density, the individual particles are not properly resolved for $n \leq 150$ and may fuse together due to the lack of resolution. **Figure 4.14** shows the progression of the calculated effective thermal conductivity for these configurations as well as for four other filler volume fractions of the same filler packing with an increasing number of mesh cells. The blue data points ($\phi = 0.63$) show the results corresponding to the dynamically meshed RVE in **Figure 4.13**.

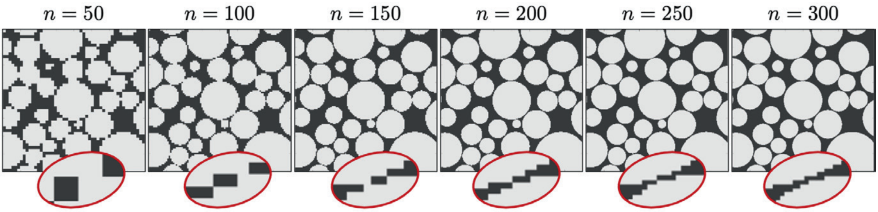

Figure 4.13. Stepwise refinement of RVE meshing using the dynamic mesh.
Central cross-sections of meshed RVE and magnified sections of a particle proximity. Filler: Spheres with log-normal size distribution with $\log(\sigma) = 0.2$, $D_{50} = 100\ \mu\text{m}$, $\phi_{\max} = 0.66$, $\phi = 0.63$.

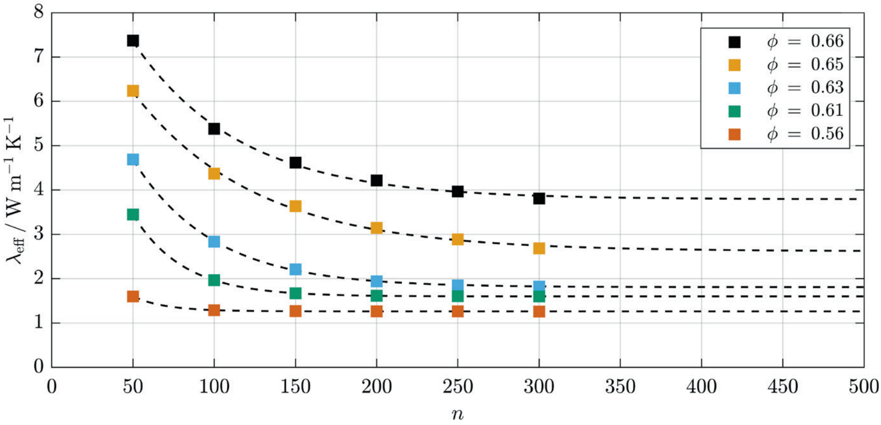

Figure 4.14. Results of dynamic mesh simulations.

Progression of evaluated effective thermal conductivity for $n = 50 \ldots 300$. Polymer: $\lambda_C = 0.25$ W m^{-1} K^{-1} (e.g., epoxy). Filler: Spheres with log-normal size distribution with $\log(\sigma) = 0.2$, $D_{50} = 100$ µm, $\phi_{\mathrm{max}} = 0.66$, $\phi = 0.56$, $\lambda_D = 35$ W m^{-1} K^{-1} (e.g., alumina).

In addition, the results for two configurations with higher and two configurations with lower filler concentration are shown. There is always a decay of the evaluated effective thermal conductivities with the number of mesh cells per spatial direction n. While the results for the lower filler volume fractions $\phi = 0.56$ and $\phi = 0.61$ already stabilize at $n > 200$, the results for higher filler volume fractions and especially the ϕ_{max} configuration with $\phi = \phi_{\mathrm{max}} = 0.66$ are still decreasing even with $n = 300$. While the RVE are not resolved finely enough at $n = 300$, the intermediate results obtained during the dynamic mesh calculations allow an approximation of the further decay behavior of the results with increasingly finer meshes.

In such cases, the effective thermal conductivity is evaluated by extrapolation to $n \to \infty$. For this purpose, a model of type $\lambda_{\mathrm{eff}} = a + b\exp(-c\ n)$ is fitted to the simulation results and $\lambda_{\mathrm{eff}}(n \to \infty) = a$ is evaluated, see **Figure 4.14**. The selected model assumes that the effective thermal conductivity is increased due to fused particles at a coarse mesh resolution. With increasing number of mesh cells n, the probability of such numerical artifacts decreases and the error decays exponentially. The parameter a represents the error-free effective thermal conductivity with an infinitely fine mesh. b describes the magnitude of the described artifacts and c is an empirical decay coefficient that depends on the specific packing structure and model parameters. The average root mean square error of the fits in relation to the simulations shown in **Figure 4.14** is 1.3 %. Across all simulations performed in this work, the root mean square error of the fit was < 5 %, confirming the general suitability of the model for extrapolating effective thermal conductivity values at higher resolutions. The precondition is of course, that sufficient data can be collected up to $n = 300$ to provide a stable forecast. This requires that the microstructure of the RVE is not too complex and that the calculations with $n = 300$ are already close to the result. In the calculations carried out as part of this study, up to $n = 600$ would have been necessary to generate reliable values without extrapolation. Such calculations, with 216 mio. mesh cells demand unreasonable calculation times with today's hardware. The calculation methodology and details on the hardware used are provided in appendix C.2. An experimental validation of the method is shown in chapter 4.5. A good agreement with experimental data confirms that the presented approach is effective and that reliable results can be achieved with a manageable use of resources and in a reasonable amount of time. The considerations in the following sections show which input parameters are of particular importance for the simulation and must be considered when modeling real materials for experimental validation.

4.2 EFFECT OF THE FILLERS MAXIMUM PACKING DENSITY

The qualitative parametric studies with the semi-empirical Lewis and Nielsen model in chapter 2.4.2 have already shown that the maximum packing density of the filler packing has a significant effect on the increase in the effective thermal conductivity over the entire range of possible filler volume fractions, see **Figure 2.6**, page 26. Tabulated guide values of maximum packing density for clearly defined or well-studied packing structures are available for the Lewis and Nielsen model. These can only provide a rough orientation at best for fillers with complex property profiles with irregular particle shapes, arbitrary size distributions, and unique dispersion behavior. In this chapter, the newly introduced simulation method is used to study the effect of the maximum packing density and secondary parameters with a direct impact on the maximum packing density, such as particle size distribution and particle morphology.

4.2.1 MICROSCALE PACKING STRUCTURE

A fundamental feature of the introduced microscale simulation approach is that each investigated packing structure is based on a predefined $\phi_{\max}$ configuration. This approach accounts for the fact that different fillers in different polymers can be packed to different densities, as different microscale packing structures are formed, depending on the mixing process. For structured particle arrangements, such as the simple cubic packing (SCP), the cubic close packing (CCP, face-centered cubic lattice), or the hexagonal close packing (HCP), the $\phi_{\max}$ configuration would be clearly defined. For random particle arrangements, the maximum packing density depends largely on the mixing process and the degree of compaction. Accordingly, the literature reports a range of values. In 1969, Scott and Kilgour [258] reported an experimentally determined maximum packing density of

$\phi_{\max} \approx 0.64$ for a random dense packing of equally sized spheres. Since then, this value has been reproduced in numerous other experimental studies and simulations to a good approximation [243,249,255,258,259]. For a less compact arrangement, a so-called random loose packing, Scott and Kilgour [258] reported a value of $\phi_{\max} \approx 0.61$. The introduced microscale simulation approach allows for the modeling of different packing configurations and enables the analysis of how the packing structure and compactability of a filler influence the effective thermal conductivity at any $\phi < \phi_{\max}$. For random packing structures, the degree of compaction can be set by varying N, the number of possible particle positions considered during packing generation. **Figure 4.15** shows the results of a first purely simulative study, considering two structured and three random particle arrangement of equally sized spheres. Part (a) presents the simulation results, while part (b) shows the corresponding 1σ uncertainty from repeated simulations with random packings, estimated as described in section 4.1.2. $\lambda_C = 0.25$ W m^{-1} K^{-1} is set for the polymer and $\lambda_D = 35$ W m^{-1} K^{-1} is set for the filler, representing an alumina filler in an epoxy matrix. Thermal interfacial resistances between filler particles and polymer are neglected.

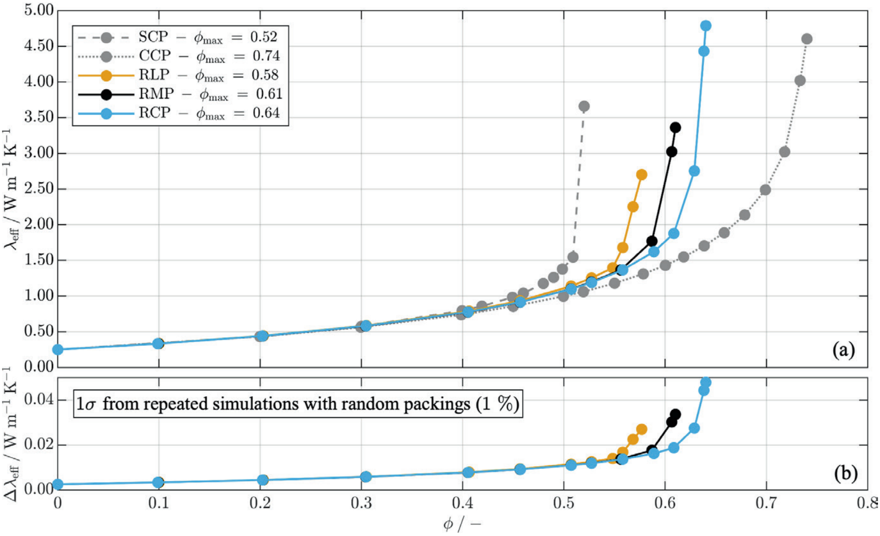

Figure 4.15. Effective thermal conductivity of a filled polymer as a function of filler volume fraction, considering different packing structures.

Simulation results are shown in (a). The corresponding 1σ uncertainty, estimated as described in section 4.1.2, is shown in (b). Polymer: $\lambda_C = 0.25$ W m^{-1} K^{-1} (e.g., epoxy). Filler: Equally sized spheres, $D = 100$ µm, $\lambda_D = 35$ W m^{-1} K^{-1} (e.g., alumina). Packing structures: SCP (Simple cubic packing), CCP (Close cubic packing), RLP (Random loose packing with $N = 500$), RMP (Random medium packing with $N = 5{,}000$), RCP (Random close packing with $N = 500{,}000$).

A simple cubic packing (SCP) with $\phi_{\max} = 0.52$ and a cubic close packing (CCP) with $\phi_{\max} = 0.74$ are considered as the respective limits of the lowest and highest possible maximum packing densities. Maximum random packing densities between $\phi_{\max} = 0.58$ and $\phi_{\max} = 0.64$ are achieved by varying N, the number of possible particle positions considered during packing generation, between 500 and $500{,}000$. The packing structures are referred to as random loose packing (RLP), random medium dense packing (RMP), and random close packing (RCP), see **Figure 4.15**.

For all packing structures, the expected superlinear increase of effective thermal conductivity with filler volume fraction is observed. There is a sharp increase in the effective thermal conductivity just before the maximum packing density is observed, beginning between $\phi = 0.45$ and $\phi = 0.65$. For $\phi < 0.4$ it seems irrelevant how the microstructure is modeled, with particle-particle interactions having no notable effect. For $\phi > 0.4$ the packing structure is significant.

This may explain why simple effective medium approaches (EMAs) can provide good results for low filler volume fractions without empirical adjustment, but normally fail for high filler volume fractions, see section 2.4.2. Even if the unrealistic, structured particle arrangements are excluded, there remains a considerable difference between the remaining random particle arrangements, dependent upon their degree of compaction and thus their maximum packing density. In the range of $0.56 < \phi < 0.64$, effective thermal conductivities of $1.36\ \mathrm{W\ m^{-1}\ K^{-1}} < \lambda_{\mathrm{eff}} < 4.79\ \mathrm{W\ m^{-1}\ K^{-1}}$ are predicted, see part (a) of **Figure 4.15**. For $\phi = 0.61$, the range between the differently compacted random structures is as high as $1.88\ \mathrm{W\ m^{-1}\ K^{-1}} \leq \lambda_{\mathrm{eff}} \leq 3.36\ \mathrm{W\ m^{-1}\ K^{-1}}$. The medium dense filler packing (RMP) is used as a starting point in several of the following studies.

4.2.2 WIDTH OF THE PARTICLE SIZE DISTRIBUTION

In addition to the microscale particle arrangement, the particle morphology and size distribution also have an effect on the maximum packing density [264,267,268]. In this section, the spherical particle shape is retained, but a particle size distribution is introduced. A systematic study on the effects of particle morphology is presented in the next section. Microscale fillers often have broad size distributions as a result of mining or manufacturing processes, see **Table 3.2**, page 41. Log-normal size distributions, or those closely approximating log-normal behavior, are of particular relevance, as they are commonly observed in both technical and natural processes. To investigate the effects of the particle size distribution, the random medium dense packing (RMP) of equally sized spheres from the previous section is taken as a basis and compared with packings with log-normal size distribution. Ideal log-normal size distributions with a volume weighted distribution integral

$$Q_3(D) = \frac{1}{2}\left(1 + \operatorname{erf}\left(\frac{\log(D) - \log(D_{50})}{\log(\sigma)}\right)\right) , \tag{4.7}$$

are modeled, where D is the particle diameter, D_{50} is the volumetric median particle diameter, and $\log(\sigma)$ is the variable logarithmic standard deviation. The volumetric median particle diameter D_{50} is set to $100\ \mu\mathrm{m}$, and $\lambda_\mathrm{C} = 0.25\ \mathrm{W\ m^{-1}\ K^{-1}}$ and $\lambda_\mathrm{D} = 35\ \mathrm{W\ m^{-1}\ K^{-1}}$ are set, as in section 4.2.1. In addition to the RMP of equally sized spheres, taken from section 4.2.1, four RMPs of spherical particles with logarithmic standard deviations between $\log(\sigma) = 0.2$ and $\log(\sigma) = 0.5$ were modeled. As explained in section 4.1.2, the continuous size distribution given in **Eq. (4.7)** is discretized and represented by a random sample of particle sizes. The evaluation of how accurately the modeled packing represents the target distribution is described in detail in section 4.1.2 and appendix C.1. Part (a) of **Figure 4.16** shows the calculated effective thermal conductivity as a function of filler volume fraction, without accounting for thermal interfacial resistances between filler particles and polymer. Part (b) shows the corresponding 1σ uncertainty from repeated simulations with random packings, estimated as described in section 4.1.2.

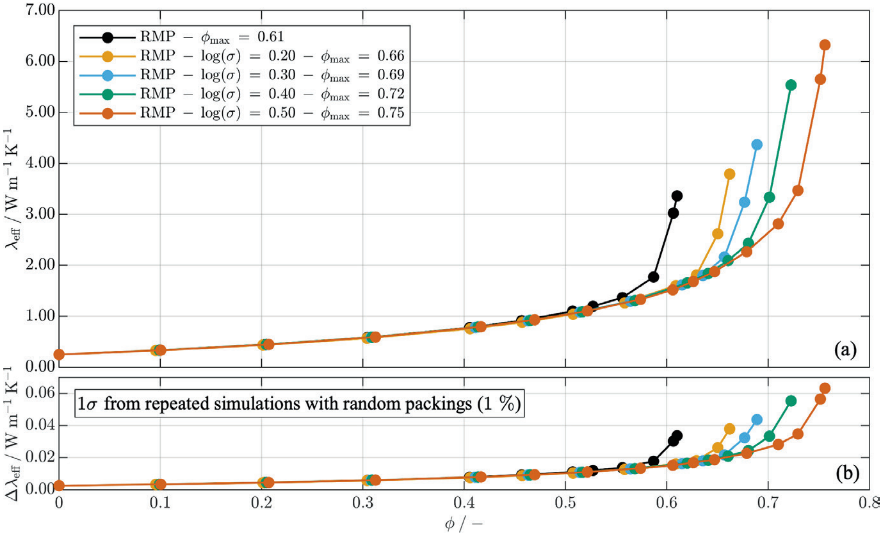

Figure 4.16. Effective thermal conductivity of a filled polymer as a function of filler volume fraction, considering a variable width of the particle size distribution.

Simulation results are shown in (a). The corresponding 1σ uncertainty, estimated as described in section 4.1.2, is shown in (b). Polymer: $\lambda_\mathrm{C} = 0.25\ \mathrm{W\ m^{-1}\ K^{-1}}$ (e.g., epoxy).

Filler: Spheres, $D_{50} = 100\ \mu\mathrm{m}$, $\lambda_\mathrm{D} = 35\ \mathrm{W\ m^{-1}\ K^{-1}}$ (e.g., alumina). Packing structure: RMP ($N = 5{,}000$).

In this study, hardly any difference is observed for $\phi < 0.55$, but for higher filler volume fractions, the calculation results diverge notably for the different filler characteristics. The RMP of equally sized spheres reaches its maximum packing density at $\phi_{\max} = 0.61$ and the thermally conductive paths are formed at an early stage. The RMP of spheres with $\log(\sigma) = 0.5$ reaches a maximum packing density of $\phi_{\max} = 0.75$. Accordingly, a steep increase in the effective thermal conductivity can only be observed for high filler volume fractions $\phi > 0.7$. All packings are modeled with $N = 5{,}000$ and thus have the same degree of compaction. It can already be summarized from the last two sections that the width of the particle size distribution determines the maximum achievable packing density, but the degree of compaction of the formed filler packings has a superimposed effect of a similar magnitude. For a reliable, quantitative calculation, both the size distribution and the degree of compaction must be precisely known.

4.2.3 PARTICLE MORPHOLOGY

Another filler property with a noticeable impact on the maximum achievable packing density is particle morphology. The microscale modeling approach introduced above also allows this effect to be systematically investigated. While some fillers are specifically manufactured with a spherical particle shape to reduce the increase in viscosity with the addition of fillers, there are others that have completely different morphologies due to the manufacturing process. As the overview in chapter 2.5 has shown, fillers with a fiber or platelet-like morphology are regularly used if a strong increase in effective thermal conductivity is desired even at low filler volume fractions. However, the viscosity of the composite also increases. In addition to fibrous and platelet-like materials, there are others with a completely irregular shape, see section 3.1.2. Since it is difficult to derive general statements from the analysis of arbitrary particle morphologies, the simulation results for various primitive particle shapes are presented in this section. **Figure 4.17** shows ten modeled random loose packings (RLP) with equally sized particles of different morphology. All packings were modeled geometrically isotropically. No preferred orientation of the particles was applied. The packings are sorted by descending sphericity. The following shapes were modeled:

- spheres (a),
- short (b) and long (i) spherocylinders,
- prolate (c) and oblate (d) spheroids,
- short (e) and long (f) truncated cones,
- short (g) and long (j) cylinders, and
- cubes (h).

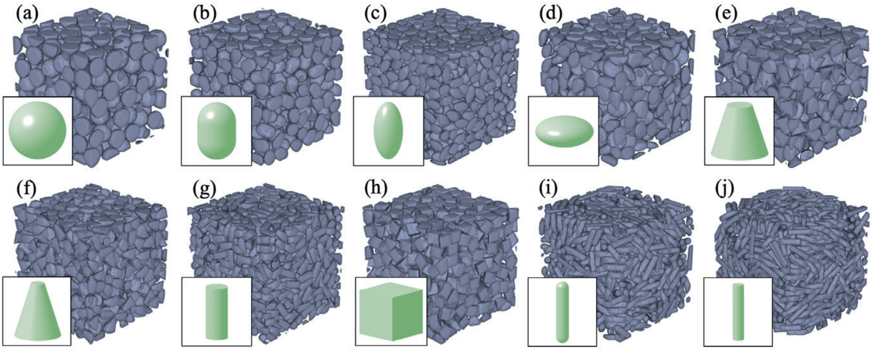

Figure 4.17. Filler packings of equally sized particles with different morphology. RLP ($N = 500$). Sorted by descending sphericity.

Table 4.2 lists the geometry details of the different shapes, the achieved maximum packing densities (RLP), the sphericity, and the roundness of the particles modeled. The size of the differently shaped particles is defined by the diameter of a spherical envelope ($D = 100\ \mu\mathrm{m}$). Several descriptors are required for a sufficient description of a particle shape, e.g., sphericity, roundness, and surface roughness. The latter is omitted here, since only smooth particle surfaces were modeled. The definition of sphericity and roundness goes back to the early work of Wadell [269] from 1935. Both are still used today when describing granular matter. The sphericity S compares the surface of the present particle A_D with that of an ideal sphere of the same volume V_D. It is calculated with [270]

$$S = \frac{\sqrt[3]{36\ \pi\ V_\mathrm{D}^2}}{A_\mathrm{D}}\ . \qquad \textbf{(4.8)}$$

The sphericity of the modeled particles is given in **Table 4.2**. The roundness R_p is the ratio of the average corner radii to the radius of the maximum inscribed circle or sphere. Wadell's [269] original definition is based on the manual analysis of several perpendicular 2D cross-sections. More recent approaches evaluate the roundness of particles numerically, analyzing the entire 3D particle morphology, e.g., [270–273]. The roundness values given in **Table 4.2** are based on a 2D analysis, according to Wadell [269]. This appears sufficient in this case, as these are clearly defined, primitive particle shapes. Spheres have $S = R_\mathrm{p} = 1$. Increasing the specific surface of the particle, decreases the sphericity. For the evaluation of roundness, the edge characteristic is important. Completely sharp-edged particles have a roundness $R_\mathrm{p} = 0$, such as the cubes.

Table 4.2. Geometry data and maximum packing density of modeled primitive particle morphologies. Maximum packing densities of filler packings, modeled with $N = 500$ (RLP). Sphericities calculated using **Eq. (4.8)**.

Index	Morphology	Geometry details	$\phi_{\mathbf{max}}$	$\boldsymbol{S}$	$\boldsymbol{R}_{\mathbf{p}}$
(a)	Sphere		0.53	1	1
(b)	Spherocylinder short	$L/D = 1.5$	0.51	0.968	1
(c)	Prolate spheroid	$D_X : D_Y : D_Z = 1 : 0.5 : 0.5$	0.50	0.929	0.6
(d)	Oblate spheroid	$D_X : D_Y : D_Z = 1 : 1 : 0.5$	0.50	0.913	0.6
(e)	Truncated cone short	$D_1 : D_2 : L = 1 : 2.26 : 2.01$	0.47	0.834	$0.\bar{1}$
(f)	Truncated cone long	$D_1 : D_2 : L = 1 : 3.5 : 4$	0.45	0.815	$0.\bar{1}$
(g)	Cylinder short	$L/D = 2.37$	0.44	0.812	$0.\bar{1}$
(h)	Cube		0.44	0.806	0
(i)	Spherocylinder long	$L/D = 5$	0.37	0.732	1
(j)	Cylinder long	$L/D = 5$	0.34	0.697	$0.\bar{1}$

Figure 4.18 presents the calculated effective thermal conductivities, achieved with the packings shown in **Figure 4.17**. Again, the combination of $\lambda_C = 0.25\ \mathrm{W\ m^{-1}\ K^{-1}}$ for the polymer and $\lambda_D = 35\ \mathrm{W\ m^{-1}\ K^{-1}}$ for the filler, representing an alumina filler in an epoxy matrix, is set. Part (a) of **Figure 4.18** shows the calculated effective thermal conductivity as a function of filler volume fraction ϕ. The expected superlinear increase is apparent for all morphologies.

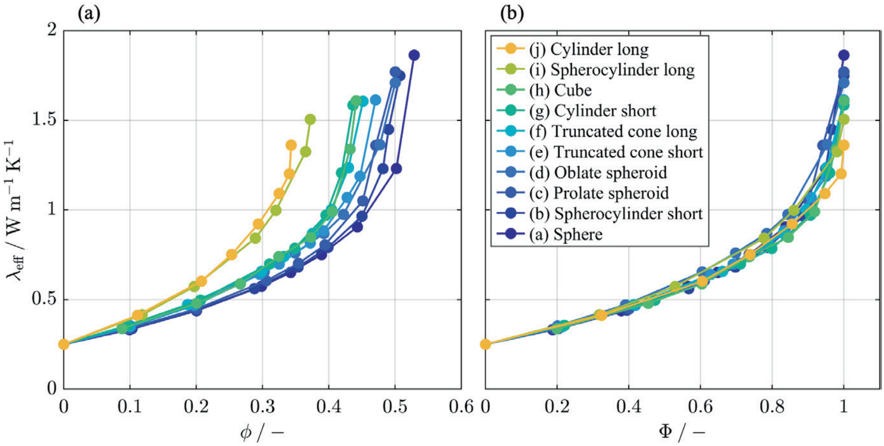

Figure 4.18. Effective thermal conductivity of a filled polymer as a function of filler volume fraction (a) and filler loading level (b), considering different particle morphologies.

Polymer: $\lambda_C = 0.25\ \mathrm{W\ m^{-1}\ K^{-1}}$ (e.g., epoxy). Filler: $D_{50} = 100\ \mu\mathrm{m}$, $\lambda_D = 35\ \mathrm{W\ m^{-1}\ K^{-1}}$ (e.g., alumina). Packing structure: RLP ($N = 500$). Error bars are omitted for clearer visualization. The 1σ margin of the simulations is $\pm\ 1\ \%$, estimated as described in section 4.1.2.

The individual curves are color-graded in order of increasing sphericity. While the two particle shapes with the lowest sphericity (long cylinders (j), and long spherocylinders (i)) form the earliest thermally conductive paths, the effective thermal conductivity with the use of spheres is the lowest over the entire range of filler volume fraction and a steep increase is only calculated for high filler volume fractions $\phi > 0.5$. In contrast to the evaluations in the previous sections, the curve of the effective thermal conductivity only appears to be compressed or stretched with the filler volume fraction. It makes sense to carry out further evaluation with a standardized filler volume fraction. Part (b) of **Figure 4.18** shows the same results, but with respect to the normalized axis of the filler loading level Φ, defined as,

$$\Phi = \frac{\phi}{\phi_{\max}} \,. \tag{4.9}$$

As can be seen by comparing parts (a) and (b) of **Figure 4.18**, the effect of the particle morphology is dominated by the effect of maximum packing density. Normalizing the filler volume fraction with the maximum packing density compensates for its effect. Only at high filler volume fractions $\Phi > 0.9$ there is still a considerable spread of up to $1\ \mathrm{W\ m^{-1}\ K^{-1}}$. To supplement this, **Figure 4.19** shows a representation of the calculated effective thermal conductivities as a function of the sphericity (a) and the maximum packing density (b).

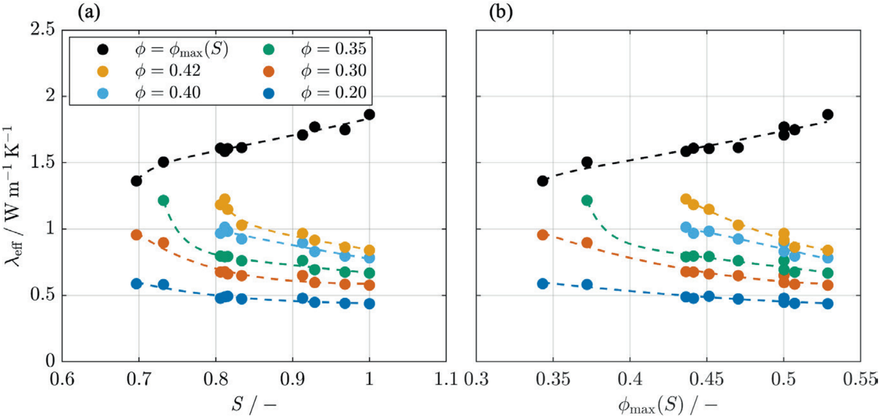

Figure 4.19. Effective thermal conductivity of a filled polymer as a function of sphericity (a) and maximum packing density (b), considering different filler volume fractions.

Polymer: $\lambda_C = 0.25\ \mathrm{W\ m^{-1}\ K^{-1}}$ (e.g., epoxy). Filler: $D_{50} = 100\ \mu\mathrm{m}$, $\lambda_D = 35\ \mathrm{W\ m^{-1}\ K^{-1}}$ (e.g., alumina). Packing structure: RLP ($N = 500$).

Note that the colored data points correspond to constant filler volume fractions ϕ, while the black data points correspond to particle morphology-dependent maximum packing densities $\phi_{\max}(S)$. Error bars are omitted for clearer visualization. The 1σ margin of the simulations is $\pm\ 1\ \%$, estimated as described in section 4.1.2.

The evaluations shown are for filler volume fractions from $\phi = 0.20$ to $\phi = 0.42$, and for $\phi = \phi_{\max}(S)$. The effective thermal conductivity of the $\phi_{\max}$ configurations, i.e., for filler beds with polymer instead of a filling gas, increases with the sphericity and the maximum packing density, as also reported by Fei et al. [270]. For all filler volume fractions $\phi < \phi_{\max}$, the effective thermal conductivity decreases with the sphericity and the maximum packing density. This reduction is attributed to inefficient heat paths in the filled polymer, caused by the polymer layers between the particles and the lack of direct particle-particle proximity. In all simulations performed, the maximum packing density shows a strong correlation with the sphericity of the filler particles. This is further supported by the similarity of the two representations in (a) and (b). It can therefore be concluded that the relevant morphological effects can, to a large extent, be described solely by the sphericity. In contrast, a clear effect of the particles' roundness R_{p} could not be found, thus no additional illustration is provided. The results shown are based on geometrically isotropic packings without any preferred direction of the individual particles. A clear effect of orientation on the effective thermal conductivity is to be expected, especially in the case of highly non-spherical fillers, such as the fiber-like cylinders or spherocylinders in **Figure 4.17** part (i) and part (j). A further simulative study has been carried out to quantify this effect. The geometrically isotropic packing of the long spherocylinders from **Figure 4.17** part (i) is used as reference. Additional packings are modeled with the same particles and the same packing compaction. During the random rotation of the individual particles however, an increased probability of orientation along the heat flow direction z is set. The achieved level of alignment τ is evaluated with

$$\tau = \frac{\sum_{i=1}^{m} v_{z,i}}{\sum_{i=1}^{m}(v_{x,i} + v_{y,i} + v_{z,i})}\,, \tag{4.10}$$

where m is the number of particles in the RVE, $\vec{v}_i$ is the orientation vector of particle i, and $v_{x,i}$, $v_{y,i}$, and $v_{z,i}$ are its direction components. $\tau = 1/3$ represents the geometrically isotropic modeling in which the probability of particle orientations in all three spatial directions is the same. For $\tau = 1$, all particles are perfectly aligned in the z direction, i.e., in the direction of heat flow, see **Figure 4.20**. The packings are modeled with $N = 500$, resulting in a random loose packing, but depending on the level of alignment τ, different maximum packing densities are achieved. While $\phi_{\max} = 0.37$ is achieved for $\tau = 1/3$, $\phi_{\max} = 0.42$ is achieved for $\tau = 1$. Part (a) of **Figure 4.21** shows the effective thermal conductivities calculated with these RVEs at different filler volume fractions. Part (b) shows the corresponding 1σ uncertainty from repeated simulations with random packings, estimated as described in section 4.1.2. $\lambda_{\mathrm{C}} = 0.25\ \mathrm{W\ m^{-1}\ K^{-1}}$ is set for the polymer and $\lambda_{\mathrm{D}} = 35\ \mathrm{W\ m^{-1}\ K^{-1}}$ for the filler, representing an alumina filler in an epoxy matrix.

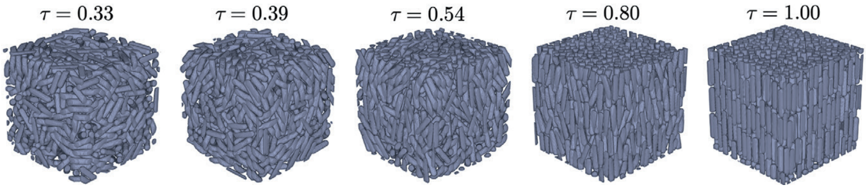

Figure 4.20. Spherocylindrical particle packings with different levels of alignment.

RLP ($N = 500$). Sorted by increasing level of alignment. Morphology data of the particle, see **Table 4.2**.

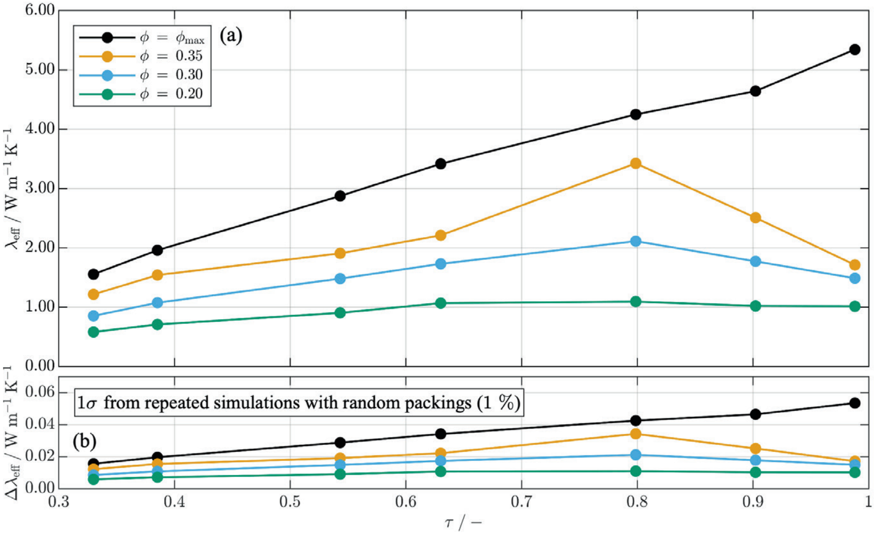

Figure 4.21. Effective thermal conductivity of a filled polymer with spherocylindrical particles as a function of the particles' level of alignment, considering different filler concentrations.

Simulation results are shown in (a). The corresponding 1σ uncertainty, estimated as described in section 4.1.2, is shown in (b). Polymer: $\lambda_{\text{C}} = 0.25$ W m^{-1} K^{-1} (e.g., epoxy). Filler: Long spherocylinders, see **Table 4.2**, $D_{50} = 100$ µm, $\lambda_{\text{D}} = 35$ W m^{-1} K^{-1} (e.g., alumina). Packing structure: RLP ($N = 500$).

The results are shown for the $\phi_{\max}$ configurations as well as for the filler volume fractions $\phi = 0.20$, $\phi = 0.30$, and $\phi = 0.35$. As expected, the effective thermal conductivity increases significantly with the level of alignment for the $\phi_{\max}$ configuration. From $\tau = 1/3$ to $\tau = 1$ there is an increase of 344 %. For the three curves with $\phi < \phi_{\max}$, there is also a general increase in the effective thermal conductivity with the level of alignment. However, there is an intermediate maximum at approx. $\tau = 0.8$. This non-monotonic behavior may initially appear counterintuitive. However, it must be considered that the maximum packing density also increases with the level of alignment and thus the relative particle distance increase, too. From $\tau = 0.8$ upwards, the additional positive effects of the alignment are counteracted by the increasing particle spacing. A slight inclination of the particles, see **Figure 4.20**, is advantageous compared to a perfect alignment. The resulting particle-particle proximities lead to better heat-conducting paths through the material. To summarize the last three sections, it can be concluded that the filler-specific morphology and particle size distribution, together with the degree of compaction of the filler packing have a direct influence on the achievable maximum packing density. This in turn defines the filler volume fraction above which effective thermal paths are formed in the material and leads to a steep increase in effective thermal conductivity. With this knowledge, the considerations of **Figure 4.7**, page 92, must be expanded. In addition to morphology and size distribution, the maximum packing density of the filler must be included as an input parameter. Packing structure and density are not only important for ϕ_{max} configurations. It is also important for all packings with $\phi < \phi_{\mathrm{max}}$ which particle arrangement is modeled and from which ϕ_{max} configuration it is derived.

4.2.4 AN EXPERIMENTAL APPROACH FOR DETERMINING THE MAXIMUM PACKING DENSITY

The simulation results in the previous sections have shown that the maximum packing density of a filler packing is of considerable importance. For proper calculations, it might be not sufficient to assume reference values, as proposed in the Lewis and Nielsen model. If the filler volume fraction comes close to the maximum packing density, the calculation results are significantly affected, see e.g., **Figure 4.15**, page 103. If real fillers are modeled, the individual maximum packing density of the packing structure must be known. This depends on both filler properties and microscale particle arrangement. If a random packing structure is assumed and its ability to be compacted is attributed to the filler, the maximum packing density can be regarded as a filler or filler-polymer combination property. The particle shape, size distribution, agglomeration effects, and the overall ability to be compacted are of great importance. While the effect of particle morphology and size distribution can be predicted in microstructure simulations, agglomeration effects and the overall ability to be compacted can only be determined experimentally.

A representative experimental approach is required to determine the maximum packing density as input for the simulation. In principle, different experimental methods can be considered:

- preparation of dry beds and determination of the volume,
- carrying out tapped density experiments,
- sedimentation trials with determination of the sediment density, or
- performing dispersion tests.

For the variety of fillers analyzed in this work, only dispersion tests were found to provide reasonable and reproducible values as input for the simulations. While reasonable results could also be achieved with coarser-grained fillers in the other experiments, it was primarily the fine-grained fillers that formed insufficiently dense packings in the other experiments due to their pronounced aggregation behavior, caused by inter-particle interactions.

For the dispersion tests, the experimental approach previously published by Hodgson et al. [274] is adopted and modified. Hodgson et al. performed rheological experiments with soda-lime glass spheres in a glycerol–water mixture. The transition from a dry-looking granular material to a flowable suspension was investigated. It was found that the mixing method has a major impact on the rheological behavior of the mixture in this transition area. Both low- and high-shear mixing were carried out; however, in this work only low shear mixing is applied to avoid grinding up the filler particles.

Mixtures are prepared in transparent $20\ \mathrm{ml}$ polypropylene cans, filled to half maximum and a defined quantity of dry filler is added. A comparatively thin liquid, ethanol, is used to suppress the effects of the continuous phase as much as possible and to determine a purely geometric $\phi_{\max}$ value, dependent solely on the filler. In the first step, a small amount of ethanol is added, so that the mixture is still dry and crumbly. The filler volume fraction is well above the maximum packing density. Subsequently, further drops of ethanol ($0.1\ \mathrm{ml} - 0.5\ \mathrm{ml}$) are added stepwise and the suspension is mixed each time for 60 seconds with a vortex shaker[15] at a mixing speed of $2000\ \mathrm{rpm}$. After each mixing process, the result is visually assessed and the transition from a dry, crumbly mixture to a flowable, paste-like suspension is observed, see **Figure 4.22**. The process and the results for four exemplary fillers are shown. From left to right, suspensions with increasing amounts of ethanol and thus decreasing filler concentration are presented. The observed transition region between a dry, crumbly mixture with $\phi > \phi_{\max}$ to the overwetted state $\phi < \phi_{\max}$ is marked with a grey background.

After an initial identification of this region, the actual transition point of the maximum packing density is approached with finer resolution by reducing the ethanol quantities added in the mixing steps. As the result, $\phi_{\max} = 0.700$ for Alox-S-01, $\phi_{\max} = 0.646$ for Alox-S-08, $\phi_{\max} = 0.644$ for ATH-I-75, and $\phi_{\max} = 0.431$ for Al-I-88 were approximated by gradually refining the steps.

For Alox-S-01, the comparatively broad size distribution (see **Table 3.2**, page 41) leads to a particularly high maximum packing density. In the case of Al-I-88, it is most probably the highly irregular grain shape (see **Figure 3.1**, page 44) that causes the comparatively low maximum packing density.

---

[15] Vortex-Genie™ 2 from Scientific Industries SI™

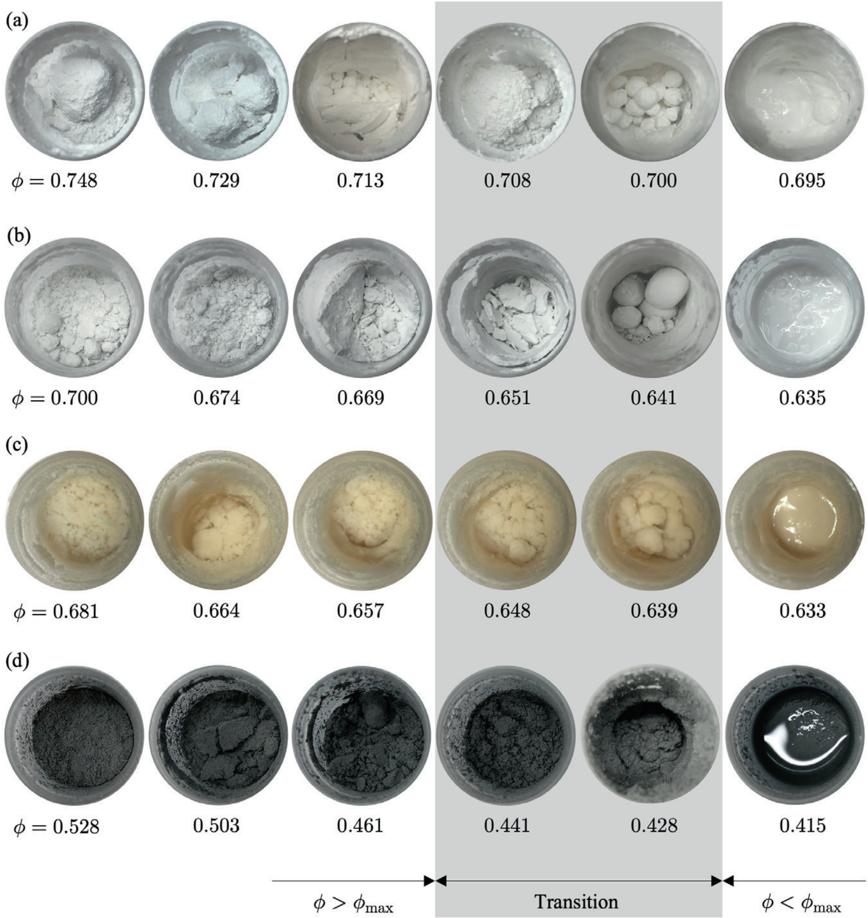

Figure 4.22. Experimental determination of maximum packing density.
Representative selection of images, taken during the maximum packing density experiment of four fillers with different characteristics. Alox-S-01, a fine-grained, spherical alumina filler is shown in (a). Alox-S-08, a medium-grained, spherical alumina filler is shown in (b). ATH-I-75, a coarse-grained aluminum hydroxide filler with irregular morphology is shown in (c). Al-I-88, a coarse-grained aluminum filler with irregular morphology is shown in (d).

The maximum packing densities of the individual fillers determined depending on their morphology, size distribution, aggregation behavior and surface characteristics, can be used as direct input parameters for simulations. By modifying N, the number of possible particle positions in the packing modeling, the model can be adjusted to the experimentally determined input, as described in section 4.1.2. As with the simulations, the maximum packing density found experimentally depends on the specific process. If other liquids or surfactants are used, or if other mixing processes are applied, different results can be expected. However, it has been found that the simulations created with the experimentally determined packing densities agree very well with measured values. This confirms that the method is suitable and representative for the materials and combinations investigated. A general validation of the microscale simulations using the experimentally determined maximum packing densities is presented in chapter 4.5.

4.3 EFFECTS OF THE SPATIAL FILLER PARTICLE ARRANGEMENT

All previous studies are based on packings, modeled with the spherical growth procedure described in section 4.1.2. An ideally homogeneous particle distribution in the RVE is considered, as the microstructural model for each individual filler volume fraction is generated by uniform expansion of a $\phi_{\max}$ configuration. Individual particle-particle contacts are excluded. This chapter deals with other spatial arrangements of the particles and the effect of local and global packing inhomogeneities on the effective thermal conductivity of a filled polymer.

4.3.1 INHOMOGENEOUS PARTICLE DISTRIBUTION

The first and most obvious approach is to modify the process of RVE expansion from a $\phi_{\max}$ configuration to any $\phi < \phi_{\max}$ and to generate locally inhomogeneous particle distributions during this procedure. For this purpose, an additional step is inserted into the microstructure modeling described in section 4.1.2, see **Figure 4.23**.

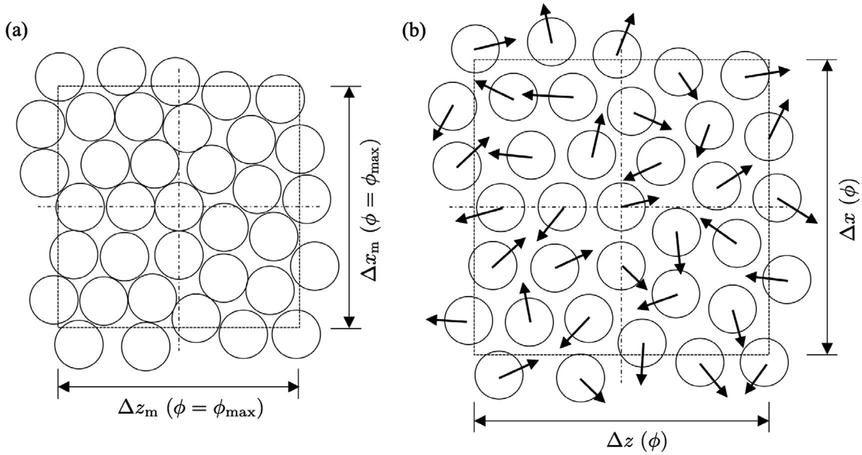

Figure 4.23. Packing modification by random particle displacement.
Schematic illustration of cross-section through modeled filler packing in $\phi_{\max}$ configuration in (a). Random particle displacement after RVE expansion to $\phi < \phi_{\max}$ in (b).

After expanding the densest packing configuration (a), all particles are individually displaced from their position in random directions, see part (b), and a kind of collective rearrangement is performed. Local voids and local accumulations of particles are created. The resulting packing structure deviates considerably from the structure originally generated using the spherical growth procedure. This can also show how representative the packings of the previous studies are and the extent to which deviations due to other modeling approaches can be estimated. The distance by which the individual particles are shifted is defined by a new parameter δ. This is defined globally for all particles and calculated according to

$$\delta = \frac{\Delta s_i}{\Delta s_{i,\max}} \,, \tag{4.11}$$

where Δs_i is the distance particle i is shifted and $\Delta s_{i,\max}$ is the maximum distance particle i could be shifted until a collision with any other particle occurs. The direction is randomly determined in advance for each particle. The higher δ, the greater the deviation of the packing structure from the initial homogeneous spatial arrangement. For $\delta = 1$, all particles are shifted towards contact with any other particle. Since particle displacement is only possible if there are gaps between the particles, this excludes the consideration of a $\phi_{\max}$ configuration. **Figure 4.24** shows the results of an exemplary study for $\phi < \phi_{\max}$ based on a random medium dense packing of equally sized spheres.

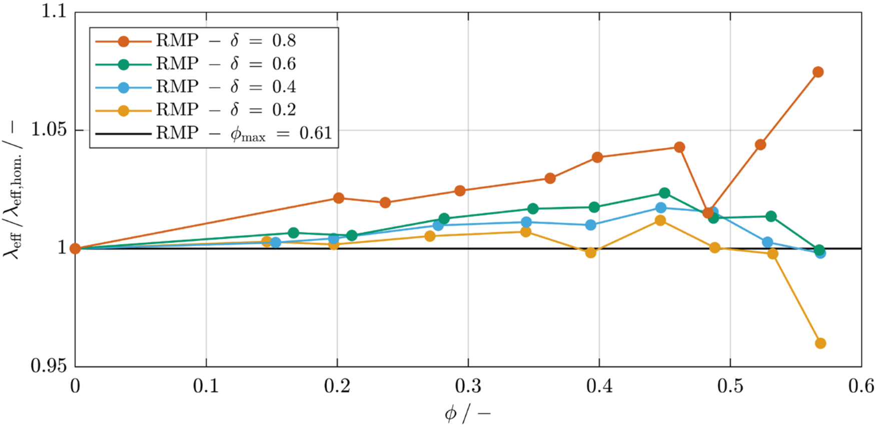

Figure 4.24. Change in effective thermal conductivity with inhomogeneous particle distribution. Calculated effective thermal conductivity with differently modified packing structures in relation to the calculated effective thermal conductivity with an ideally homogeneous filler packing. Polymer: $\lambda_C = 0.25$ W m^{-1} K^{-1} (e.g., epoxy). Filler: Equally sized spheres, $D = 100$ µm, $\lambda_D = 35$ W m^{-1} K^{-1} (e.g., alumina). Packing structure: RMP ($N = 5{,}000$).

The random medium dense (RMP) packing structure of equally sized spheres with $\lambda_{\mathrm{C}} = 0.25\ \mathrm{W\ m^{-1}\ K^{-1}}$ and $\lambda_{\mathrm{D}} = 35\ \mathrm{W\ m^{-1}\ K^{-1}}$ is adapted from the study already shown in **Figure 4.15**, page 103. The ratio of the calculated thermal conductivity to that of an ideally homogeneous particle distribution at the same filler volume fraction $\lambda_{\mathrm{eff}}/\lambda_{\mathrm{eff,hom}}$ is given.

Four curves for $0.2 \leq \delta \leq 0.8$ are shown in **Figure 4.24**. In general, the effective thermal conductivity increases with increasing δ and increasing filler volume fraction ϕ. However, the random modifications of the packing structures lead to strongly scattering results also containing microstructures with a slight reduction of effective thermal conductivity. Shifting the individual particles from their ideal position for a dense packing structure generally reduces the maximum packing density of the new microstructure and thus, as a logical consequence tends to increase the effective thermal conductivity.

Notably, the effect is very small at typically $< 5\ \%$, which confirms that the spherical growth procedure used probably does not suppress any significant effects that occur in other random packing structures. Not included here are cases in which the particles are shifted so that they touch each other. This would represent an agglomeration of particles and not just an inhomogeneous distribution of particles. The effect of agglomeration is examined and discussed in the next section. Presently, it can be concluded that the modeling approach using a spherical growth procedure with ideally homogeneous expansion of the RVE is reasonable since the effect of inhomogeneous particle distributions is of minor importance.

4.3.2 AGGLOMERATED FILLER PACKINGS

Agglomeration or aggregation is a well-known and common phenomenon with micro and nano scale fillers [4,29,56,275,276]. Several experimental studies have reported an increase in effective thermal conductivity with a higher degree of agglomeration, e.g., [4,56]. Burger et al. [29] discuss various experimental studies investigating the effect of agglomeration or varying degrees of dispersion on the effective thermal conductivity. However, the reported results are different and sometimes contradictory, with some studies observing higher thermal conductivity with better dispersion. These discrepancies are due to the complex interplay of several factors that are difficult to isolate in a purely experimental investigation. It is unclear how the agglomerates form, whether thin polymer layers remain between the particles, or whether there are air inclusions in the agglomerates. It is also very challenging to control the degree of agglomeration inside a sample, therefore the results are difficult to compare and evaluate. To examine the effect of agglomeration in isolation, a further simulative study with a controlled microstructure is carried out. Once again, an ideal random medium dense packing model of equally sized spheres is used as a starting point and modified stepwise. Unlike in the previous section, no random particle displacement is performed to generate particle-particle contacts, but a systematic agglomerate is formed in the center of the RVE. Since the RVE only represents a small, microscopic section of the entire material, there is no loss of generality. This approach does allow for agglomerates to be modeled in a very controlled manner, with a structure that can be clearly determined and quantified. To quantify the level of agglomeration, the parameter ψ is defined as

$$\psi = \frac{V_\mathrm{A}}{V_\mathrm{D}} , \tag{4.12}$$

where V_A is the volume of all particles forming the agglomerate and V_D is the volume of all particles within the evaluated zone of the RVE. Packing modeling is not modified; but the expansion process for setting the desired filler volume fraction is different. Instead of expanding all particle positions equally with the RVE size, N_ψ particles are kept in contact with each other in the center of the RVE. This means that in the outer area of the RVE, a lower mean filler volume fraction is modeled, while maintaining the maximum packing density in the center. The number of particles in the central agglomerate N_ψ is determined in such a way that the desired degree of agglomeration ψ is achieved, according to **Eq. (4.12)**. The agglomerates generated in this way have no preferred shape or orientation and represent the probable case that they arise purely randomly, not generated by macroscopically directed forces, such as shear forces.

Figure 4.25 shows cross-sections of RVEs modeled with different levels of agglomeration at a filler volume fraction of $\phi = 0.4$. The central agglomerate grows with increasing ψ from left to right. No modification is made for $\psi = 0$ with all particles evenly distributed. At $\psi = 0.4$, $40\ \%$ of the particle volume is agglomerated. The thermal simulation is carried out with these modified RVEs as described generally in chapter 4.1. A prerequisite for error-free evaluation is ensuring that the central agglomerate does not extend into the boundary areas cut off during the evaluation. This can be confirmed for up to $\psi \approx 0.4$ with the packing structure used for this investigation.

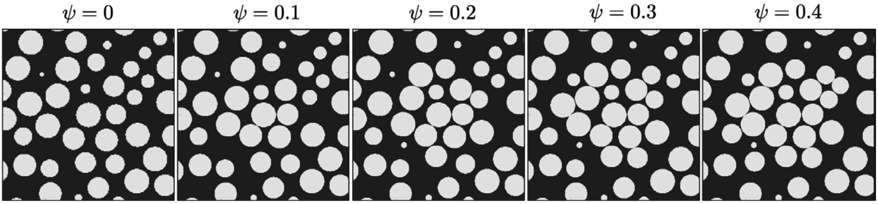

Figure 4.25. Packing structures with increasing level of agglomeration.
Central cross-sections of meshed RVE. Filler: Equally sized spheres, $D = 100\ \mu\mathrm{m}$, $\phi = 0.4$.
Packing structure: RMP ($N = 5{,}000$).

Figure 4.26 shows the simulation results with $\lambda_C = 0.25\ \mathrm{W\ m^{-1}\ K^{-1}}$ for the polymer and $\lambda_D = 35\ \mathrm{W\ m^{-1}\ K^{-1}}$ for the filler. All simulations are based on the same microscale packing model. This suppresses stochastic fluctuations caused by random packing structures, thus enabling the isolated analysis of the systematic agglomeration effects. For this reason, error bars are not shown. The effective thermal conductivity continues to increase superlinearly with the volume fraction, independent of the level of agglomeration. While the results for $\phi = 0$ and $\phi = \phi_{\max}$ are identical, the effective thermal conductivity increases significantly with increasing agglomeration for medium filler volume fractions. The results show a similar trend as in the previous section. Inhomogeneous distribution and the extreme case of agglomeration lead to an increase in the effective thermal conductivity.

The particles in the agglomerates form thermally conductive paths locally, which increase the overall thermal conductivity of the RVE although there is a lack of particles in other areas. If areas with high thermal conductivity are made available parallel to the poorly conductive zones, their effect predominates and the effective thermal conductivity increases. The largest increases in effective thermal conductivity are observed within the range $0.45 < \phi < 0.55$. An increase of $6\ \%$ compared to the non-agglomerated RMP configuration is calculated for $\psi = 0.1$, and for $\psi = 0.4$ the increase is approx. $35\ \%$.

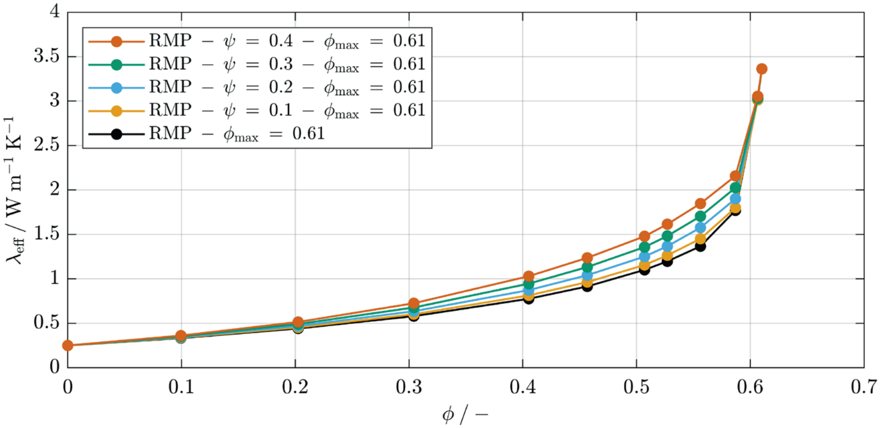

Figure 4.26. Effective thermal conductivity of a filled polymer as a function of filler volume fraction, considering different level of agglomeration.

Polymer: $\lambda_C = 0.25\ \mathrm{W\ m^{-1}\ K^{-1}}$ (e.g., epoxy). Filler: Equally sized spheres, $D = 100\ \mu\mathrm{m}$, $\lambda_D = 35\ \mathrm{W\ m^{-1}\ K^{-1}}$ (e.g., alumina). Packing structure: RMP ($N = 5{,}000$), equal for all simulations.

The newly developed simulation approach makes it possible to quantify the effect of agglomeration in isolation for a model system. A calculation for any other initial packing structure is possible. However, the question of the level of agglomeration in real materials remains open. Although the definition according to **Eq. (4.12)** appears straightforward, it is nevertheless difficult to determine the level of agglomeration in experimental samples. Imaging analysis of cross-sections offers limited insight due to the loss of three-dimensional structural information. Only advanced volumetric imaging methods such as micro-CT would be suitable to quantify agglomeration levels in real materials.

4.3.3 SEDIMENTED FILLER PACKINGS

While agglomeration phenomena mainly occur with small filler particles, large and heavy particles tend to sediment. Sedimentation also affects the global homogeneity of filler packings and can cause a change in thermal conductivity. This effect is also discussed based on a simulative study. To analyze both cases of heat flow along and perpendicular to the direction of sedimentation, another extension to the microscale modeling procedure is applied. After adjusting the filler volume fraction of the desired filler packing, all particles within the RVE are moved along the x or z axis. Sedimentation along the y axis, the second spatial direction perpendicular to the heat flow, does not require separate investigation, as the same results are expected as for the x axis. The state of complete sedimentation is modeled, as well as partially sedimented states. The sedimentation parameters

$$\beta_{\mathrm{sed},x} = \frac{\Delta x_i}{\Delta x_{i,\max}} \, , \tag{4.13}$$

and

$$\beta_{\mathrm{sed},z} = \frac{\Delta z_i}{\Delta z_{i,\max}} \tag{4.14}$$

are defined, where $\Delta x_{i,\max}$ and $\Delta z_{i,\max}$ are the maximum distances a particle i can sediment along the x or z axis until it is in contact with another particle. Δx_i and Δz_i are the actual sedimentation distances of particle i. For $\beta_{\mathrm{sed}} = 0$ there is no sedimentation and for $\beta_{\mathrm{sed}} = 1$ the state of complete sedimentation is modeled, see **Figure 4.27**. Part (a) of **Figure 4.27** shows four section views through RVEs with different states of sedimentation along the x axis, i.e., perpendicular to the heat flow direction. Part (b) shows the equivalent section views for sedimentation along the z axis. All section views show filler packings based on the same RMP configuration with $\phi = 0.4$. The appearance that complete sedimentation has not been achieved at $\beta_{\mathrm{sed}} = 1$ in **Figure 4.27** is due to the visualization showing only a two-dimensional cross-section of a three-dimensional filler packing. Particles that still have space to move in this image plane already collide with particles in other layers of the three-dimensional structure.

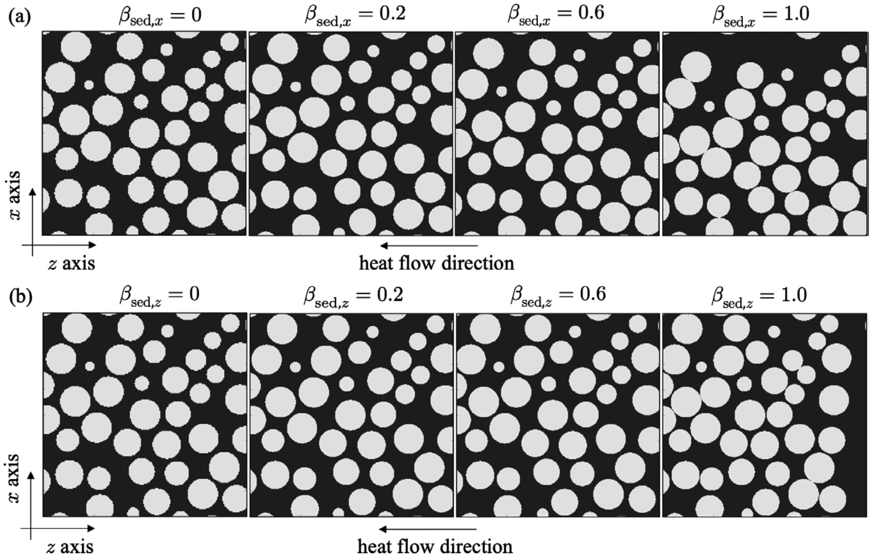

Figure 4.27. Packing structures with different states of sedimentation.
Central cross-sections of meshed RVEs. Filler: Equally sized spheres, $D = 100\ \mu\mathrm{m}$, $\phi = 0.4$. Packing structure: RMP ($N = 5{,}000$).

The simulation of heat conduction and determination of the temperature and heat flow field is carried out in the same way as described in chapter 4.1. However, an alternative strategy must be used for the evaluation. For the sedimented packings, the boundary zones cannot be excluded as this would result in a filler volume fraction error. Instead of evaluating the temperature gradient $\mathrm{d}\bar{T}/\mathrm{d}z$ in the middle of the RVE, an evaluation of the total temperature drop $\Delta T/\Delta z$ over the entire length of the RVE is carried out with

$$\frac{\Delta T}{\Delta z} = \frac{T(z_{\mathrm{max}}) - T(z_{\mathrm{min}})}{z_{\mathrm{max}} - z_{\mathrm{min}}}\,, \tag{4.15}$$

using the boundary conditions $T(z_{\mathrm{min}}) = 293\ \mathrm{K}$ and $T(z_{\mathrm{max}}) = 353\ \mathrm{K}$.

Figure 4.28 presents the simulation results for different states of sedimentation along the x and z axis. Again, $\lambda_{\mathrm{C}} = 0.25\ \mathrm{W\ m^{-1}\ K^{-1}}$ is set for the polymer and $\lambda_{\mathrm{D}} = 35\ \mathrm{W\ m^{-1}\ K^{-1}}$ is set for the filler, representing an alumina filler in an epoxy matrix. Thermal interfacial resistances between filler particles and polymer are neglected. Part (a) of **Figure 4.28** presents the results considering sedimentation in x direction. Part (b) presents the results considering sedimentation in z direction.

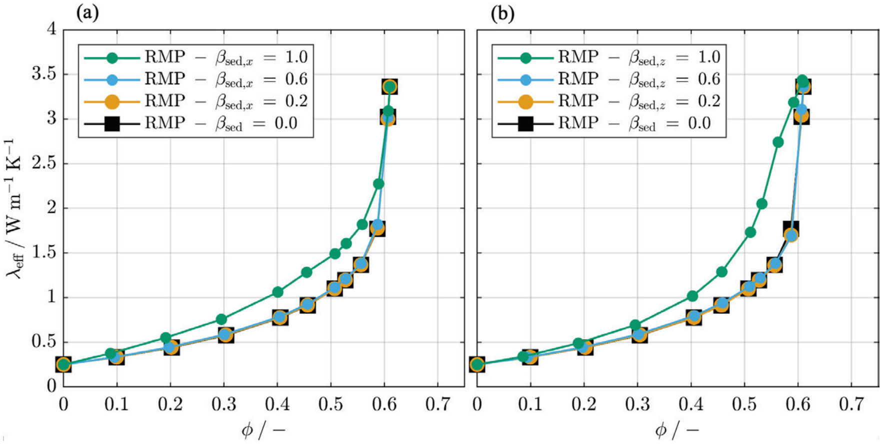

Figure 4.28. Effective thermal conductivity of a filled polymer as a function of filler volume fraction, considering different states of sedimentation.

Results considering sedimentation in x direction are shown in (a). Results considering sedimentation in z direction are shown in (b). Polymer: $\lambda_{\mathrm{C}} = 0.25$ W m^{-1} K^{-1} (e.g., epoxy). Filler: Equally sized spheres, $D = 100$ µm, $\lambda_{\mathrm{D}} = 35$ W m^{-1} K^{-1} (e.g., alumina). Packing structure: RMP ($N = 5{,}000$), equal for all simulations.

All simulations are based on the same microscale packing model. This suppresses stochastic variations caused by random packing structures, thus enabling the isolated analysis of the systematic sedimentation effects. For this reason, error bars are not shown.

The curves for $\beta_{\mathrm{sed}} = 0.2$ and $\beta_{\mathrm{sed}} = 0.6$ are almost analogous to the reference curve for the initial, non-sedimented RMP configuration in both cases. The complete sedimentation states $\beta_{\mathrm{sed},x} = 1$ and $\beta_{\mathrm{sed},z} = 1$ show significantly increased effective thermal conductivities over the entire range of filler volume fractions. While complete sedimentation along the x axis enhances the effective thermal conductivity by up to $40\ \%$ at a filler volume fraction of $\phi = 0.45$, complete sedimentation along the z axis causes an increase of $100\ \%$ at $\phi = 0.56$. The large increase in thermal conductivity could appear nonintuitive for packings sedimented in the z direction, since poorly thermally conductive polymer layers are formed which should significantly reduce thermal conductivity. But the complete sedimentation with $\beta_{\mathrm{sed},z} = 1$ leads to a densely packed bulk with continuous particle-particle contacts and thermal paths, causing a strong increases in thermal conductivity, so that the later series connection of very good and poorly conducting layers still conducts better than the homogeneous mixture. This analysis can be supported with a simplified analytical model. Assuming an ideal series connection of thermal resistances for sediment and polymer layer, the effective thermal conductivity of the RVE can be approximated as

$$\lambda_{\mathrm{eff}}^{\mathrm{apx.}} = \left[\lambda_{\mathrm{sed},z}^{-1} \frac{\Delta z_{\mathrm{sed},z}}{\Delta z_{\mathrm{tot}}} + \lambda_{\mathrm{C}}^{-1} \frac{\Delta z_{\mathrm{C}}}{\Delta z_{\mathrm{tot}}}\right]^{-1} . \tag{4.16}$$

For the sediment layer, the thermal conductivity can be approximated by that of the ϕ_{max} configuration, i.e., $\lambda_{\mathrm{sed},z} = \lambda_{\mathrm{eff}}(\phi_{\mathrm{max}}) = 3.4\ \mathrm{W\ m^{-1}\ K^{-1}}$ (see **Figure 4.15**, page 103). Based on **Figure 4.27** (b), the sediment occupies approximately $85\ \%$ of the RVE height at an initial filler volume fraction of $\phi = 0.4$. Therefore $\Delta z_{\mathrm{sed},z}/\Delta z_{\mathrm{tot}} = 0.85$ and $\Delta z_{\mathrm{C}}/\Delta z_{\mathrm{tot}} = 0.15$ are set. For the pure polymer we use $\lambda_{\mathrm{C}} = 0.25\ \mathrm{W\ m^{-1}\ K^{-1}}$. Inserting these values into **Eq. (4.16)** yields an effective thermal conductivity of $\lambda_{\mathrm{eff}}^{\mathrm{apx.}} = 1.18\ \mathrm{W\ m^{-1}\ K^{-1}}$, even more than with the microscale simulations ($\lambda_{\mathrm{eff}} = 1.02\ \mathrm{W\ m^{-1}\ K^{-1}}$). For comparison: A non-sedimented RMP configuration would result in $\lambda_{\mathrm{eff}}(\phi = 0.4) = 0.76\ \mathrm{W\ m^{-1}\ K^{-1}}$, see **Figure 4.15**, page 103.

It should be noted that the packing modeling described is an idealized and extreme case. The artificial sedimentation of particles by uniaxial movement without re-sorting and compaction of the particles in the sediment, as it occurs in real processes, leads to a sediment structure that is very dense in the direction of sedimentation, but very loose perpendicular to it. This results in efficient heat-conducting paths along the direction of sedimentation, while simultaneously forming the thickest possible sediment layer.

The results obtained with the simulations of sedimented filler packings are similar to those obtained with the previously presented studies on local inhomogeneities and agglomeration. Therefore, it can be concluded that if there are no forced particle-particle contacts, a local and global inhomogeneity does not notably affect the effective thermal conductivity of the composite. As soon as particle-particle contacts occur, there is a significant increase in thermal conductivity, even if only locally efficient heat paths are formed. Continuous percolation paths through the entire RVE are not required to achieve a significant increase in thermal conductivity.

4.4 EFFECTS OF THE THERMAL FILLER AND POLYMER PROPERTIES

After numerous studies on the effects of geometric packing phenomena were presented in the previous chapters, this chapter deals with the effects of the thermal conductivities of filler and polymer as well as a discussion of the impact of thermal interfacial resistances. Since these effects, as described in section 2.4.2, can be easily analyzed with effective medium approaches, they are already comparatively well understood and are only dealt with in this work for the sake of completeness. To isolate the effect of the filler's thermal conductivity, a purely simulative approach is employed. This allows for precise control of all other parameters, ensuring that the observed effects can be attributed solely to changes in the filler's thermal conductivity. For the analysis of the polymer's influence, both experimental and simulative results are discussed.

4.4.1 FILLER THERMAL CONDUCTIVITY

To analyze and quantify the impact of a filler's thermal conductivity on the effective thermal conductivity of a filled polymer, a basic random medium dense packing (RMP) model with equally sized spheres is chosen. The polymer's thermal conductivity is kept constant at $\lambda_{\mathrm{C}} = 0.25\ \mathrm{W\ m^{-1}\ K^{-1}}$, representing e.g., epoxy and the filler's thermal conductivity is varied systematically. **Figure 4.29** shows the simulation results for the complete range of filler volume fraction and λ_{D} between $1\ \mathrm{W\ m^{-1}\ K^{-1}}$ and $500\ \mathrm{W\ m^{-1}\ K^{-1}}$. The simulation results are represented as a surface plot and iso-λ_{eff}-lines are added to enhance interpretation. All simulations are based on the same microscale packing model. This suppresses stochastic fluctuations caused by random packing structures, thus enabling the isolated analysis of the systematic effects of the filler's thermal conductivity. For this reason, error bars are not shown. With increasing filler thermal conductivity, the superlinear increase in effective thermal conductivity with filler volume fraction becomes more pronounced. However, a saturation effect can also be observed: After reaching a certain threshold value in λ_{D}, a further increase in the conductivity of the filler leads to progressively smaller increases in λ_{eff}. This threshold varies depending on the filler volume fraction, ranging from a few $\mathrm{W\ m^{-1}\ K^{-1}}$ at low volume fractions to approximately $100\ \mathrm{W\ m^{-1}\ K^{-1}}$ at higher volume fractions. As soon as the iso-λ_{eff}-lines run parallel to the λ_{D} axis, the effective thermal conductivity remains almost unchanged, regardless of any further increase in the filler conductivity.

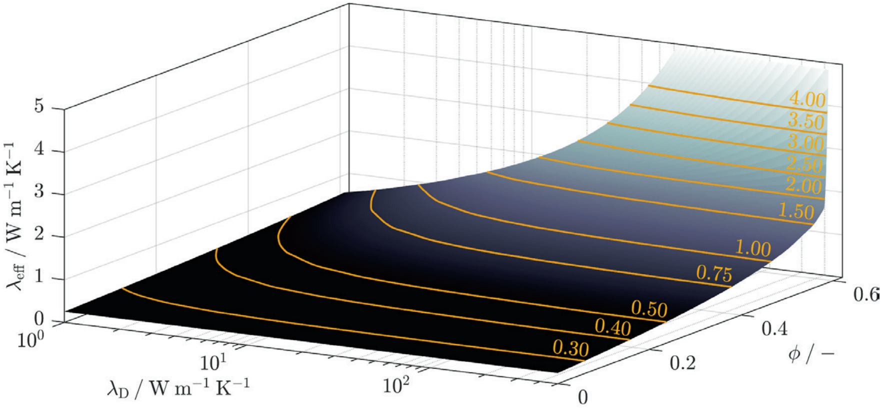

Figure 4.29. Effective thermal conductivity of a filled polymer as a function of the filler's thermal conductivity and filler volume fraction.

3D surface plot with iso-λ_{eff}-lines. Polymer: $\lambda_{\mathrm{C}} = 0.25\ \mathrm{W\ m^{-1}\ K^{-1}}$ (e.g., epoxy). Filler: Equally sized spheres, $D = 100\ \mu\mathrm{m}$. Packing structure: RMP ($N = 5{,}000$), equal for all simulations.

This aspect has already been investigated and discussed in section 2.4.2 using the Lewis and Nielsen model. It is a fundamental characteristic of composites with a continuous and disperse phase. In such materials, heat flows must always overcome the polymer, which is a poorly conductive continuous phase between the particles. As the filler conductivity increases, the polymer increasingly limits the overall conductivity of the composite. Above a filler concentration-dependent threshold, the bottleneck effect of the polymer predominates. Based on this observation, it can be concluded that when using fillers with high thermal conductivity from filler classes II and III (see section 2.4.2), no significant enhancement in effective thermal conductivity is to be expected only from the filler's thermal conductivity. Rather, the achievable effective thermal conductivity depends on the packing structure and the geometric formation of highly thermally conductive paths in the material. The studies in the previous chapters have shown that there is a much greater potential in adjusting the packing structure.

4.4.2 POLYMER THERMAL CONDUCTIVITY

The results presented in the previous section have indicated the significance of the polymer characteristics when using highly conductive fillers. The continuous polymeric phase is the limiting component and as previously discussed, the potential of polymers is restricted. Typical thermal conductivities of polymers are in the range of $\lambda_\mathrm{C} = (0.1 \dots 0.5)\ \mathrm{W\ m^{-1}\ K^{-1}}$ [1–4]. Additionally, the specific chemical, mechanical, and rheological properties of the materials limit the materials in this range that are suitable for each technical application. The simulative studies presented previously were based on a standard thermal conductivity of $\lambda_\mathrm{C} = 0.25\ \mathrm{W\ m^{-1}\ K^{-1}}$ for e.g., epoxy.

This chapter presents experimental and simulative results that quantify the impact of the polymer's thermal conductivity. For this purpose, three silicone rubbers are selected, that cure at room temperature and have thermal conductivities between $0.22\ \mathrm{W\ m^{-1}\ K^{-1}}$ and $0.28\ \mathrm{W\ m^{-1}\ K^{-1}}$. The fillers used are ATH-I-75, Alox-S-40, and Al-S-45, see **Table 4.3**. The fillers were selected to provide a similar microscopic packing structure. However, it is practically impossible to identify three fillers of different materials with otherwise identical characteristics.

Table 4.3. Filler selection for studying the effect of the polymer's thermal conductivity.

ID	Class	Description	Thermal conductivity λ_D / $\mathrm{W\ m^{-1}K^{-1}}$
Al-S-45	III	Spherical aluminum	≈ 150
Alox-S-40	II	Spherical alumina	≈ 35
ATH-I-75	I	Irregularly shaped aluminum hydroxide	≈ 10

Measurements were carried out using the steady-state cylinder method, according to ASTM D5470-17 [184], see chapter 3.2. For the simulations, the particle shape of ATH-I-75 was digitized as described in section 4.1.3, and Al-S-45 as well as Alox-S-40 were modeled with ideally spherical particle shape. The measured size distributions and maximum packing densities were considered during packing modeling, as described in sections 4.1.2 and 4.1.3. **Figure 4.30** (a) – (c) present the measured and simulated thermal conductivities of several cross combinations of the fillers and polymers selected as a function of filler volume fraction. Part (d) shows the results at a fixed filler volume fraction of $\phi = 0.4$, plotted against the polymer thermal conductivity λ_C. Overall good agreement is observed between the experimental and simulative results. In **Figure 4.30** (a) – (c), the sets of curves are sorted from left to right in ascending order of polymer thermal conductivity. It is immediately apparent that the thermal conductivities achieved with ATH-I-75 are significantly below the thermal conductivities achieved with Al-S-45 and Alox-S-40.

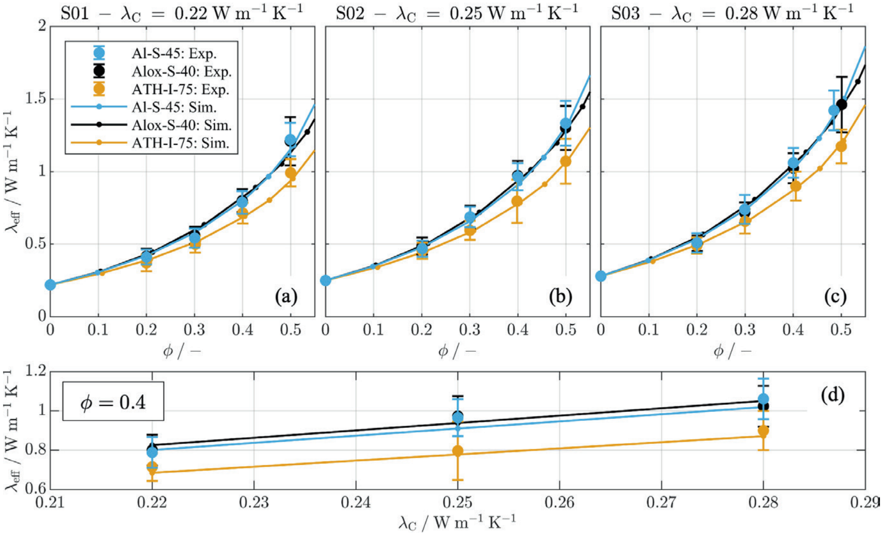

Figure 4.30. Effective thermal conductivity of a filled polymer as a function of filler volume fraction, considering different polymer-filler combinations.

Effective thermal conductivity as a function of filler volume fraction for different polymers in (a) - (c). Effective thermal conductivity as a function of polymer thermal conductivity for $\phi = 0.4$ in (d). Large data points represent experimental results (steady-state cylinder method) and solid lines with small data points represent microscale simulation results. Error bars represent the sum of random and systematic uncertainties in experimental determination of thermal conductivity, see section 3.2.6. Error bars of the simulations are omitted for clearer visualization. The 1σ margin of the simulations is $\pm$ 1 %, estimated as described in section 4.1.2. For details on the fillers, see **Table 4.3**. Microstructure modeling parameters, see **Table 4.4**, page 131.

No significant difference between the two higher thermally conductive fillers could be resolved experimentally. The simulation results predict only a slightly higher thermal conductivity with Al-S-45 at very high filler volume fractions $\phi > 0.5$.

An upward trend in the experimental and simulative results is observed with increasing thermal conductivity of the polymer. This can be seen particularly well in the exemplary representation for $\phi = 0.4$ in part (d) of **Figure 4.30**. While the experimental results do not allow a clear conclusion due to the large error intervals, simulations predict an almost linear relationship between effective and polymer thermal conductivity. Across the dataset, samples with Al-S-45 and S02 have an 18 $\%$ higher thermal conductivity than those with S01. The thermal conductivities of the samples with Al-S-45 and S03 are 28 $\%$ higher than those with S01. On average, the experimental results also approximate the proportionality well. However, this proportionality has limitations. Simulations have shown that it holds only when the ratio of filler to polymer thermal conductivity remains constant. Experimentally verifying this behavior is challenging due to the limited availability of suitable fillers. A further discussion of the findings follows in the summary in chapter 4.6.

A more detailed analysis of the simulation results in **Figure 4.30** reveals two effects that are not intuitive at first glance. First, the calculated effective thermal conductivities with Alox-S-40 at the lower filler volume fractions of $\phi < 0.45$ are higher than the thermal conductivities with Al-S-45, yet the ratio is inverted for $\phi > 0.45$. It can also be seen that the distance between the curve calculated with ATH-I-75 and the other two fillers decreases for higher filler volume fractions $\phi > 0.5$. These effects are caused by the characteristics of the microstructure of the selected materials. Even when specifically selected for similar property profiles, there will be differences in particle morphology, maximum packing density, size distribution, and level of agglomeration. This once again confirms the necessity of the previously presented purely simulative studies for isolated consideration of the microstructural effects.

4.4.3 THERMAL INTERFACIAL RESISTANCES BETWEEN FILLER PARTICLES AND POLYMERS

As mentioned in section 2.4.2, there have already been numerous theoretical and experimental studies on the effects of thermal interfacial resistances between filler particles and polymers [2–4,56,57]. However, these have led to partly contradictory statements and no clear result, see section 2.4.2. There are many possible explanations for this. First, the problem with experimental studies is that the effect is superimposed by other influences and is difficult to isolate. Secondly, a wide variety of composites in different ranges of thermal conductivities, even beyond filled polymers, are compared. The qualitative effect of thermal interfacial resistances was covered in section 2.4.2 using the theoretical model of Jiajun and Xiao-Su [154]. They lead to a reduction in the effective thermal conductivity over the entire range of filler volume fractions. The effect increases when the particle size decreases and thus the specific surface area increases.

The thermal interfacial resistances between polymer and nano or micro filler particles are not directly experimentally accessible. Measurements on contacts with a larger surface area are more conceivable and were e.g., carried out for the combination of alumina and epoxy by Yang et al. [277] using the time-domain thermoreflectance method. Theoretical predictions from first principles are very difficult [2]. Instead, simplified models can be used to predict the order of magnitude to be expected, such as the acoustic mismatch model (AMM) or the diffuse mismatch model (DMM), see chapter 2.2. Essentially this involves analyzing the differences in the acoustic properties of the two contact partners and the associated probability of phonons to be transmitted across the interface. The greatest difference in acoustic properties would be expected between polymer and the filler with the highest density and stiffness. The relevant filler in this work is alumina. Therefore, an analysis of the thermal interfacial resistances between alumina and a polymer should suffice to estimate the greatest possible impact. In [152,153,278,279] values of thermal interfacial resistances are given for several material combinations calculated by the AMM.

For example: For a polyethylene-alumina interface, Devpura et al. [153] reported $r_\mathrm{I} = 6.6 \cdot 10^{-5}\ \mathrm{m}^2\ \mathrm{K}\ \mathrm{W}^{-1}$ at 5 K and $r_\mathrm{I} = 9.6\ \cdot 10^{-9}\ \mathrm{m}^2\ \mathrm{K}\ \mathrm{W}^{-1}$ at 300 K. This is a very broad range which includes the value $r_\mathrm{I} = 1.25 \cdot 10^{-7}\ \mathrm{m}^2\ \mathrm{K}\ \mathrm{W}^{-1}$ measured by Yang et al. [277] at a non-modified alumina-epoxy interface without temperature information. For applications at ordinary temperatures ($290\ \mathrm{K} \ldots 420\ \mathrm{K}$), the expected range might be limited to $10^{-9}\ \mathrm{m}^2\ \mathrm{K}\ \mathrm{W}^{-1}$ to $10^{-7}\ \mathrm{m}^2\ \mathrm{K}\ \mathrm{W}^{-1}$. For further discussion, the results of a simulative study using the newly developed microscale simulation approach are used. Once again, the microstructure model of the random medium dense packing of equally sized spheres is used as a reference. $\lambda_\mathrm{C} = 0.25\ \mathrm{W}\ \mathrm{m}^{-1}\ \mathrm{K}^{-1}$ is set for the polymer and $\lambda_\mathrm{D} = 35\ \mathrm{W}\ \mathrm{m}^{-1}\ \mathrm{K}^{-1}$ is set for the filler, representing an alumina filler in an epoxy matrix. Calculations are performed with particles of different sizes and thermal interfacial resistances between $10^{-9}\ \mathrm{m}^2\ \mathrm{K}\ \mathrm{W}^{-1}$ and $10^{-5}\ \mathrm{m}^2\ \mathrm{K}\ \mathrm{W}^{-1}$. This also covers the order of magnitude predicted by Devpura et al. [153] at $5\ \mathrm{K}$.

Figure 4.31 presents the results and illustrates the effect of thermal interfacial resistances. All simulations are based on the same microscale packing model. This suppresses stochastic variations caused by random packing structures, thus enabling the isolated analysis of the systematic effects of the filler's thermal conductivity. For this reason, error bars are not shown. While the calculations with particles of $D = 100\ \mathrm{\mu m}$ only predict a slight reduction with $r_\mathrm{I} = 10^{-5}\ \mathrm{m}^2\ \mathrm{K}\ \mathrm{W}^{-1}$, the effective thermal conductivity for particles with $D = 1\ \mathrm{\mu m}$ already drops from $r_\mathrm{I} = 10^{-7}\ \mathrm{m}^2\ \mathrm{K}\ \mathrm{W}^{-1}$. For $r_\mathrm{I} = 10^{-5}\ \mathrm{m}^2\ \mathrm{K}\ \mathrm{W}^{-1}$, a reduction in thermal conductivity can be expected compared to that of the polymer with $\lambda_\mathrm{C} = 0.25\ \mathrm{W}\ \mathrm{m}^{-1}\ \mathrm{K}^{-1}$.

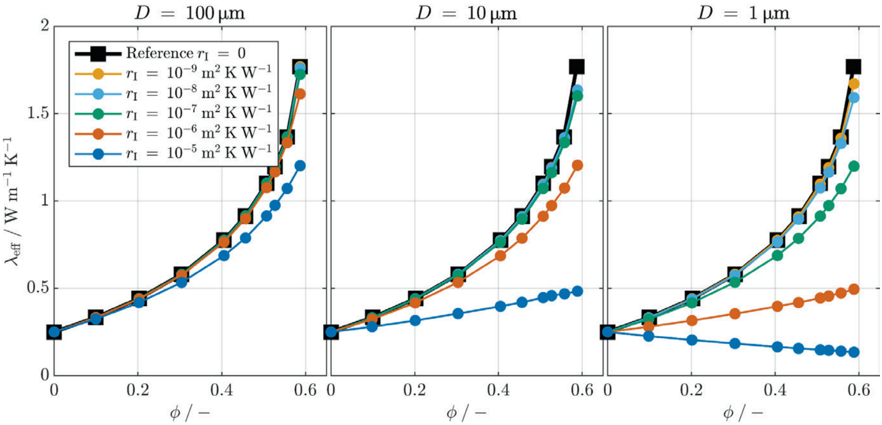

Figure 4.31. Effective thermal conductivity of a filled polymer as a function of filler volume fraction, considering thermal interfacial resistances and different particles sizes.

Polymer: $\lambda_C = 0.25\ \mathrm{W\ m^{-1}\ K^{-1}}$ (e.g., epoxy). Filler: Equally sized spheres, $D = 100\ \mu\mathrm{m}$, $\lambda_D = 35\ \mathrm{W\ m^{-1}\ K^{-1}}$ (e.g., alumina). Packing structure: RMP ($N = 5{,}000$), equal for all simulations.

The results presented are in good qualitative agreement with the results obtained with the model of Jiajun and Xiao-Su in section 2.4.2, and the results published by Hasselman and Johnson [155] and Every et al. [156]. However, for the expected range of thermal interfacial resistances ($r_I = (10^{-9} \dots 10^{-7})\ \mathrm{m^2\ K\ W^{-1}}$, at ordinary temperatures), no significant effect is observed for particle sizes of $D = 100\ \mu\mathrm{m}$ and $D = 10\ \mu\mathrm{m}$. Even for $D = 1\ \mu\mathrm{m}$, only a slight reduction of 8 % at $\phi = 0.3$ and 17 % at $\phi = 0.5$ is predicted.

It should also be mentioned that no measurable dependence of effective thermal conductivity on particle size was observed for any of the fillers tested (see section 3.1.2). This supports the conclusion that interfacial thermal resistances are negligible in typical filled polymers at ordinary temperatures. This follows the assessment of Devpura et al. [153] and Schmidt [152]. However, there might be certain applications and material combinations in which thermal interfacial resistances lead to a noticeable reduction in the effective thermal conductivity. This may be the case for very low temperatures or for very high matrix thermal conductivities, as in e.g., [150,151,227].

4.5 EXPERIMENTAL VALIDATION OF MICROSCALE SIMULATIONS

In this section, broad experimental validations of the developed and applied simulation method are presented. In addition, the phenomena shown in chapters 4.2 - 4.4 are discussed based on experimental data. A reasonable comparison of measured and simulated data is only possible if all significant filler properties are modeled in sufficient detail. The previous sections have shown that precise knowledge of the filler thermal conductivity tends to be less important for fillers in class II and III. Rather, it is the geometric packing structure that determines the increase in effective thermal conductivity with the filler volume fraction.

Figure 4.32 shows the parameters used in the simulation model to describe real fillers. First, the particle size distribution of the fillers, measured with a laser particle sizer[16], is imported and represented in the packing modeling. Second, the maximum packing densities experimentally obtained according to section 4.2.4 are used to set the level of compaction for the initial packing models in the $\phi_{\max}$ configurations. Furthermore, the particle morphology is modeled as spherical or based on the digitized particle models of the respective fillers. Then finally, the level of agglomeration is set, which is the only parameter for which a purely experimental determination has not been sufficient. Only a rough estimate of the level of agglomeration can be made based on a microscopic cross-section analyses. A refined assessment of the level of agglomeration for the simulation was done using measured thermal conductivities and a calibration of the model. **Table 4.4** summarizes the applied model parameters for the fillers already introduced in **Table 3.2**, page 41. Fillers from all three classes were used. Most of them have an ideal or at least approximately spherical shape, and ATH-I-75 and Al-I-88 were digitized.

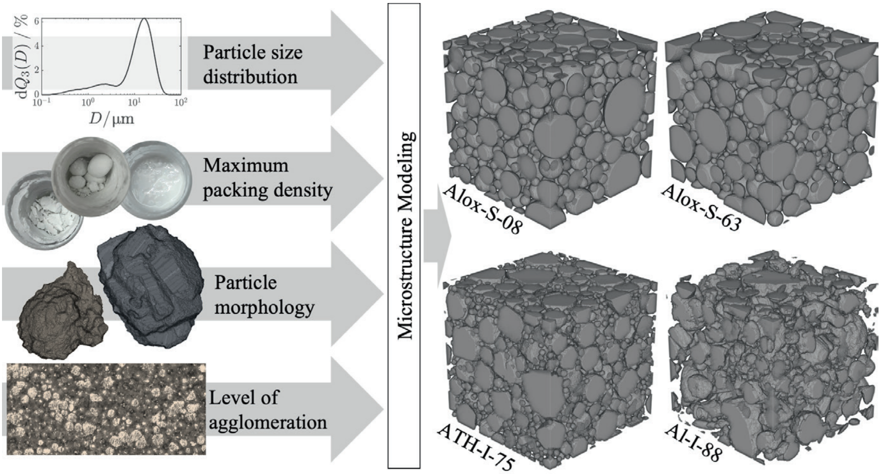

Figure 4.32. Microstructure modeling based on experimental input data.
Illustration of experimental input data and exemplary images of modeled filler packings in $\phi_{\max}$ configuration: Alox-S-08, Alox-S-63, ATH-I-75, and Al-I-88.

---

[16] Fritsch Analysette 22 NanoTec

Table 4.4. Overview of fillers and microstructure modeling parameters.

ID	Morphology	Sphericity S / −	Thermal conductivity λ / W m^{-1} K^{-1}	Max. packing density $\phi_{\max}$ / −	Level of agglomeration ψ / −
Alox-S-01	Ideally spherical	1	35	0.700	0.00
Alox-S-08	Ideally spherical	1	35	0.646	0.13
Alox-S-22	Ideally spherical	1	35	0.679	0.05
Alox-S-40	Ideally spherical	1	35	0.652	0.12
Alox-S-63	Ideally spherical	1	35	0.660	0.15
ATH-I-75	Irregular, dig.	0.96	10	0.644	0.20
Siox-S-03	Ideally spherical	1	1.4	0.712	0.15
Al-S-06	Ideally spherical	1	150	0.630	0.12
Al-S-22	Ideally spherical	1	150	0.640	0.15
Al-S-45	Ideally spherical	1	150	0.625	0.10
Al-I-88	Irregular, dig.	0.91	150	0.431	0.30
Al-I-103	Irregular, dig.	0.91	150	0.470	0.00

Due to the limited availability of specific data and suitable measurement methods, the thermal conductivities of the fillers in the model are based on general literature values, see **Figure 2.5**, page 22. The maximum packing densities range from $\phi_{\max} = 0.431$ to $\phi_{\max} = 0.712$, but Alox-S-01, Siox-S-03, and Al-I-88 stand out. With Alox-S-01 and Siox-S-03, the particularly high maximum packing densities are caused by their broad size distributions. In the case of Al-I-88, the low maximum packing density is mainly determined by the strongly aspherical morphology ($S = 0.91$). The level of agglomeration for the selected fillers was between $\psi = 0.00$ and $\psi = 0.30$. No thermal interfacial resistances were considered in thermal modeling. For measurements made with the steady-state cylinder method, $4 - 6$ samples per filler were prepared with different filler volume fractions and using Epoxy E01 as the polymer. Simulations with $8 - 10$ individual filler volume fractions were carried out in the same range. Spline interpolation was used to generate intermediate results for visualization. **Figure 4.33** presents a general validation of the microscale simulation method by comparing all simulated thermal conductivities with experimental results. In addition to the data points, part (a) of **Figure 4.33** also contains the reference line for ideal agreement as well as the ± 10 % and ± 20 % deviation thresholds, based on the measured values. There is very good agreement between simulation and measurement. Error bars are omitted for better visualization. As discussed in detail in section 3.2.6, the measurement uncertainties with the steady-state cylinder method are sample-related and in the range of $(10 \dots 15)$ %. Part (b) of **Figure 4.33** displays a histogram of the deviations between simulated and measured values. 89 % of the simulations exhibit a deviation ≤ 10 %, i.e. are within the ± 10 % thresholds. 99 % of the simulations exhibit a deviation ≤ 20 %, i.e. are within the ± 20 % thresholds. The mean absolute deviation is 4.1 %. The standard deviation is 4.3 %. The individual analysis of the measurement and simulation results, dependent upon the filler volume fraction, and of the fillers in comparison, allows for further interpretation and validation of the previous simulation results. For example, the effect of the morphology dependent maximum packing density can be revealed by comparing the fillers Al-S-45 and Al-I-88, see **Figure 4.34**. Both fillers are coarse-grained aluminum with high thermal conductivity and a similar size distribution, but with completely different grain morphologies. While Al-S-45 contains almost ideal spheres, the particles of Al-I-88 are strongly irregular, see **Figure 3.1**, page 44. This leads to a considerably lower maximum packing density and the formation of good heat-conducting paths already at lower filler volume fractions, see **Table 4.4**. Both, the measured and simulated curves in **Figure 4.34** show a significantly earlier increase in the effective thermal conductivity with filler volume fraction for Al-I-88.

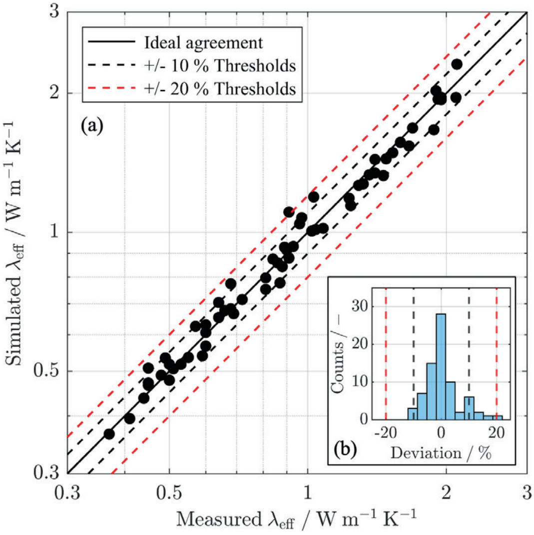

Figure 4.33. General validation of the microscale simulation approach for single-scale filled polymers. Comparison of calculated thermal conductivities with measured thermal conductivities using the steady-state cylinder method in (a). Histogram of deviations in (b). Polymer: Epoxy E01. Fillers: see **Table 4.4**, page 131, $0.2 < \phi < 0.6$.

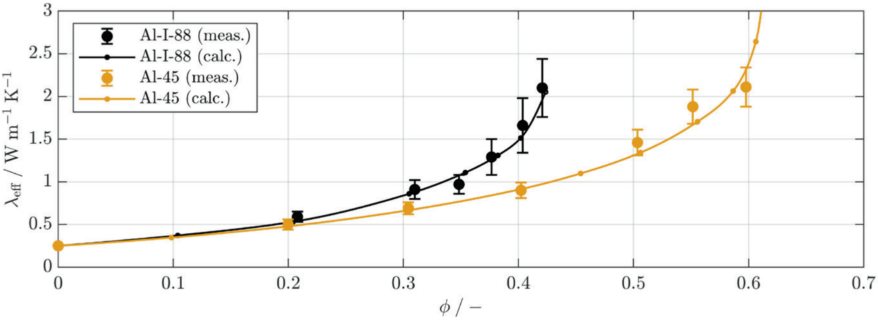

Figure 4.34. Effective thermal conductivity as a function of filler volume fraction, comparing alumina fillers with different particle morphologies.

Thermal conductivity measurements (large data points) and simulations (solid lines with small data points) for filled polymer composites consisting of epoxy E01 and the fillers Al-S-45 and Al-I-88. Error bars of the simulations are omitted for clearer visualization. The 1σ margin of the simulations is $\pm$ 1 %, estimated as described in section 4.1.2.

For example, to reach $\lambda_{\text{eff}} = 2$ W m^{-1} K^{-1}, $\phi \approx 0.58$ is necessary for Al-S-45, while $\phi \approx 0.42$ already is sufficient when using Al-I-88. A more detailed analysis of the contributions of particle size distribution, particle morphology, and agglomeration is difficult solely based on experimental data. Using simulations, these effects can be examined in detail in chapters 4.2 - 4.4. Experimental evidence of thermal interfacial resistances, or rather evidence of their negligible effects, is even more difficult to examine. A decreasing effective thermal conductivity with decreasing particle sizes would be an indication for thermal interfacial resistances. However, the effect overlaps considerably with other packing phenomena. **Figure 4.35** compares the measured and simulated curves for the fillers Alox-S-08, Alox-S-22 and Alox-S-40 as an example. All fillers are almost perfectly spherical, see **Figure 3.1**, page 44, with similar size distributions. The volumetric mean particle sizes differ, with $D_{50} = 7.9$ µm for Alox-S-08, $D_{50} = 22.2$ µm for Alox-S-22, and $D_{50} = 63.4$ µm for Alox-S-63. As shown in **Figure 4.35**, there is no clear dependence of the effective thermal conductivity on the particle size. The achievable thermal conductivities with Alox-S-08 are systematically higher than those with Alox-S-22. The individual curves differ significantly due to the packing effects such as maximum packing density, particle size distribution, and agglomeration. Either there is no measurable effect of thermal interfacial resistances, or they are lost in combination with other phenomena. The fact that **Figure 4.33** confirms the very good model agreement despite the simulations completely neglecting thermal interfacial resistances suggests that the former is the case, and the effects are negligible.

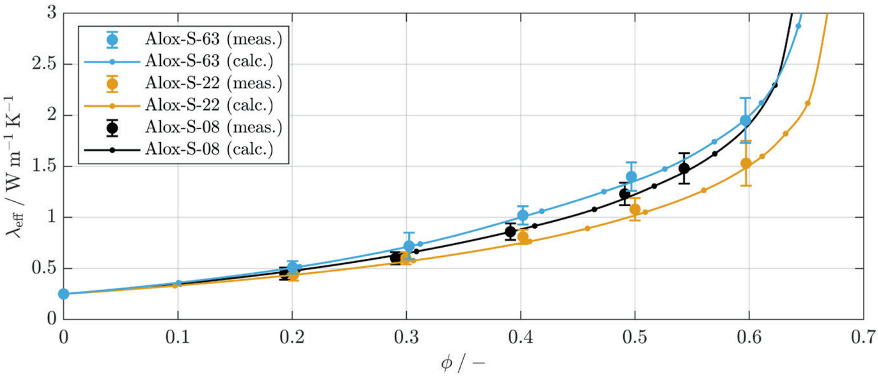

Figure 4.35. Effective thermal conductivity as a function of filler volume fraction, comparing alumina fillers with different mean particle sizes.

Thermal conductivity measurements (large data points) and simulations (solid lines with small data points) for filled polymer composites consisting of epoxy E01 and the fillers Alox-S-08, Alox-S-22, and Alox-S-63. Error bars of the simulations are omitted for clearer visualization. The 1σ margin of the simulations is $\pm$ 1 %, estimated as described in section 4.1.2.

In summary, the experimental results in this chapter show that the presented simulation approach is very well suited to make quantitative predictions for real fillers with complex property profiles. The precondition is the detailed modeling considering all relevant parameters. At the same time, the experiments confirm the existence of the phenomena analyzed by simulation in the previous chapters. The experimental studies alone do not permit an isolated analysis and thus comprehensive study of different parameters due to the superposition of effects.

4.6 CHAPTER SUMMARY AND CONCLUSION

In the first sections of this chapter, the effects of the microscopic packing structure were discussed. Then, the microscopic particle distribution was dealt with. This was followed by analysis of the effects of the thermal filler and polymer properties. Finally, all effects are combined to formulate a comprehensive picture about the effective thermal conductivity of single-scale filled polymers. Across all experimental and simulative studies, there was a superlinear increase in effective thermal conductivity with filler volume fraction. In contrast to the electrical conductivity, no sudden jump was observed that would indicate percolation, see e.g., [149]. This observation was also described by Burger et al. [29]. It can be explained by the fact that the thermal conductivities of polymers and fillers are of a similar order of magnitude, whereas there is a gap of several orders of magnitude in the electrical conductivities.

Even if the qualitative curve of the effective thermal conductivity versus filler volume fraction was always similar for geometrically isotropic filler packings, numerous thermal and especially microscopic geometric parameters could be identified that strongly affect the curve quantitatively, see **Figure 4.36**.

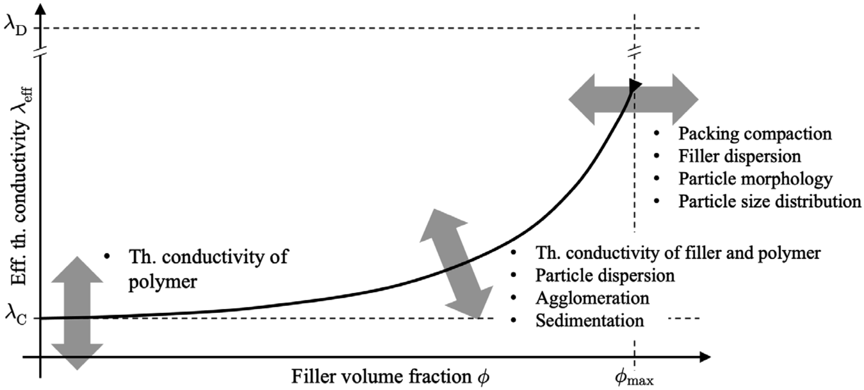

Figure 4.36. Summary of effects on effective thermal conductivity of single-scale filled polymers.

The curve starts at the thermal conductivity of the unfilled polymer λ_C, and the steep end of the curve is defined by the maximum packing density ϕ_{max}. This must be determined individually for each filler as it depends largely on the filler dispersion, the particle morphology, the particle size distribution, and the compactability of the filler. The growth rate and the curvature are determined by the filler's thermal conductivity λ_D and the particle dispersion. In sections 4.3.2 and 4.3.3 it was shown that agglomeration and sedimentation phenomena generally lead to an increase in the effective thermal conductivity.

The qualitative curve for effective thermal conductivity versus filler volume fraction is always the same for geometrically isotropic filler packings, but scales or shifts with the stated parameters. Therefore, it is appropriate to choose a dimensionless representation and quantitatively summarize as many parameters as possible. For this purpose, three dimensionless quantities are defined:

- The thermal conductivity magnification Λ, as the ratio of the effective thermal conductivity λ_{eff} to the initial thermal conductivity of the polymer (continuous phase) λ_C

$$\Lambda = \frac{\lambda_{eff}}{\lambda_C} \, , \tag{4.17}$$

- the ratio of the raw material thermal conductivities (TC ratio) κ with

$$\kappa = \frac{\lambda_\mathrm{D}}{\lambda_\mathrm{C}}\,, \tag{4.18}$$

where λ_D is the thermal conductivity of the filler particles (disperse phase), and

- the filler loading level Φ as the ratio of the actual filler volume fraction ϕ to the maximum packing density of the respective filler ϕ_max

$$\Phi = \frac{\phi}{\phi_\mathrm{max}}\,. \tag{4.19}$$

With these three dimensionless parameters, the results can be presented very clearly, see **Figure 4.37**.

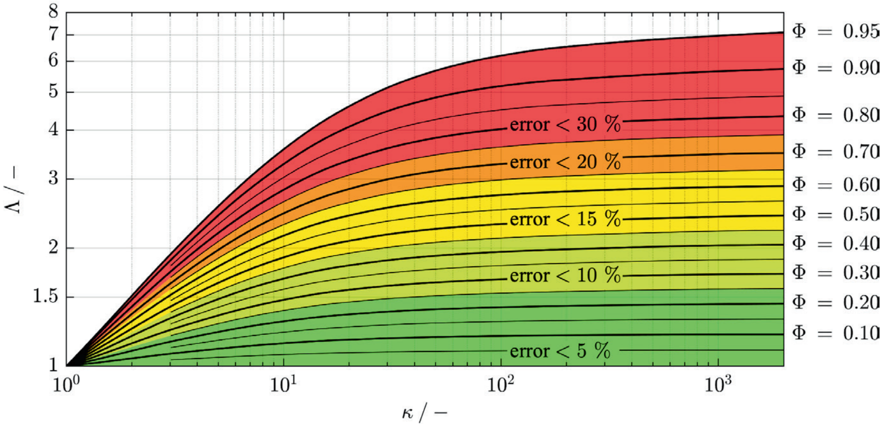

Figure 4.37. Thermal conductivity magnification as a function of TC ratio and filler loading level. Filler: Equally sized spheres, $D = 100$ µm. Packing structure: RMP ($N = 5{,}000$). No thermal interfacial resistances. Thin isolines represent the mean value of the adjacent thick isolines.

The graph shows simulation results for Λ as a function of κ and Φ for a simple model system with equally sized spherical particles in a medium dense packing arrangement. For better clarity, the TC ratio κ is plotted along the abscissa instead of filler concentration, which is instead indicated by isolines. The saturation phenomenon discussed in sections 4.4.1 and 4.4.2 can be seen most clearly in this illustration. So far, this has only been discussed based on absolute thermal conductivities. It becomes apparent that $\kappa \approx 100$ marks the sensitivity threshold for most filler loading levels Φ. With higher TC ratios, a noteworthy effect is only achieved for high filler loading levels of $\Phi > 0.8$. For instance, increasing κ from 10^2 to 10^3, raises Λ by 6.7 % at $\Phi = 0.8$ and by 12.4 % at $\Phi = 0.95$.

If class II or III fillers with medium to high thermal conductivity are used, then no great improvement is expected in most cases by increasing the thermal conductivity of the fillers utilized. On the other hand, a further increase in the filler loading level always leads to an increase in thermal conductivity magnification, with the precondition that the maximum has not already been reached. Although the presented results were determined using only a simple model system, they have a wide range of applicability due to the standardized representation of input and output variables. Comparison with all the 173 calculation results obtained during the studies has shown that

- log-normal particle size distributions with a logarithmic standard deviation $\log(\sigma)$ of up to 0.5,
- random loose to random dense particle arrangements with $\phi_{\max} = 0.58$ to 0.64, based on the reference of equally sized spheres, and
- primitive particle shapes with sphericities between 0.7 and 1.0 (cubes, spherocylinders, spheroids, truncated cones, cylinders, etc.)

are taken with an error of

$< 5\%$ for $\Phi < 0.25$,

$< 10\%$ for $\Phi < 0.45$,

$< 15\%$ for $\Phi < 0.65$,

$< 20\%$ for $\Phi < 0.75$, and

$< 30\%$ for $\Phi < 0.95$.

The representation in **Figure 4.37** can verifiably depict many of the investigated parameters for a good approximation. It does not replace microscale simulations for quantitative predictions but is useful for quick estimations on the order of magnitude of the achievable effective thermal conductivity. What the dimensionless representation does not cover are the particle dispersion phenomena, discussed in chapter 4.3 and the effects of a particle alignment, discussed in section 4.2.3.

Another important finding, when looking at **Figure 4.37**, is that even with very high filler loading levels $\Phi \geq 0.95$, achievable thermal conductivity magnifications are limited to only $\Lambda < 8$ with this simple model system. For an epoxy with $\lambda_{\mathrm{C}} = 0.25\ \mathrm{W\ m^{-1}\ K^{-1}}$, this corresponds to an effective thermal conductivity of $2\ \mathrm{W\ m^{-1}\ K^{-1}}$. The highest thermal conductivity of a single-scale filled polymer measured in this work was $2.1\ \mathrm{W\ m^{-1}\ K^{-1}}$, see **Figure 4.33**, page 132. This aligns reasonably well with the limit of $\Lambda \approx 8$, especially when considering the increasing uncertainty associated with the generalized representation in **Figure 4.37**. By definition it is impossible to produce a composite with $\Phi = 1$, as this corresponds to the random extreme case in which every particle in the packing touches its neighbors. It may be conceivable to set $0.95 < \Phi < 1$, however the experimental studies in this work have shown that it is difficult to achieve this range. It is always associated with significant losses in the mechanical and rheological properties of the materials. This means that an initial performance limit for single-scale filled polymers can be derived at this point. Based on the simulations, it can be concluded that the effective thermal conductivity is a maximum of around eight times the thermal conductivity of the polymer. The statement was confirmed experimentally for the silicone and epoxy polymers used. No validation was performed for other polymers and polymer-filler combinations.

To complete the conclusion, it should be mentioned based on **Figure 4.16**, page 105, that an increasing width of the particle size distribution not only leads to higher maximum packing densities but also to higher effective thermal conductivities at filler volume fractions close to the maximum packing density. Therefore, there may be fillers for which the maximum achievable thermal conductivity magnification is > 8, i.e., fillers that have a very high maximum packing density and at the same time a very high thermal conductivity. However, the selection of fillers analyzed in this work does not contain such a filler. Another option would be to use filler packings with aligned particles, see section 4.2.3, but this requires specialized manufacturing processes.

5 EFFECTIVE THERMAL CONDUCTIVITY OF MULTI-SCALE FILLED POLYMERS

The summary in chapter 4.6 has shown that the achievable effective thermal conductivity with single-scale filler packings is strictly limited. To achieve higher thermal conductivities, alternative solutions must be found other than simply increasing the filler volume fraction or the filler's thermal conductivity. For many applications requiring highly thermally conductive polymer composites, possible solutions are multi-scale or hybrid filler packings, see chapter 2.5. Particularly high filler volume fractions are only achievable by combining different size classes in a filler blend. While the previous chapter provides information on the important factors influencing the effective thermal conductivity of single-scale filled polymers, this chapter focuses on combining individual fillers in multi-scale filler packings.

5.1 PREDICTING THE EFFECTIVE THERMAL CONDUCTIVITY USING A MULTI-STEP APPROACH

In chapter 4, microscale simulation models provided valuable insights into the heat transport processes in single-scale filled polymers. They were successfully used to analyze and quantify the impact of individual microstructure parameters in isolation, gaining insights that would have been inaccessible in experimental studies. Multi-scale filled polymers will also be investigated using both experimental and numerical studies. Reliable calculation approaches can remain useful outside of this work in the explicit development of products. When developing materials and adjusting material proportions in multi-scale filler blends, there are numerous degrees of freedom that make purely experimental approaches very time-consuming and costly. Simulations and simplified model studies can help to narrow the experimental search field.

5.1.1 NECESSITY FOR A MULTI-STEP APPROACH

The microscale simulation method developed in this work (see chapter 4.1) cannot be directly applied to multi-scale filled polymers due to the characteristics of commonly used filler blends, as discussed in the following section. The objective of using multi-scale filler packings is to achieve higher absolute filler volume fractions without a significant increase in viscosity. The processability often limits the permissible filler concentrations and thus the achievable effective thermal conductivity.

If a polymer is modified with a single-scale filler, both the effective thermal conductivity and the effective viscosity increase superlinearly with filler volume fraction. The viscosity diverges when the maximum packing density $\phi_{\max}$ of the filler is reached. For equally-sized spheres, this limit is $\phi_{\text{max}} \approx 0.64$ [243,249,255–259], as already discussed in section 4.2.1. Fillers used in practical applications always have a size distribution of the individual particles, and the wider the size distribution, the higher the maximum packing density [241,268,280,281], see section 4.2.2. A theoretical limit is formed by the Apollonian sphere packing with $\phi_{\text{max}} = 1$ [282]. A combination of two differently sized fillers to form a binary mixture with a bimodal particle size distribution has a higher achievable maximum packing density than with the individual components. The finer filler particles can fill the gaps between the larger particles, and increasing the disparity between the combined particle sizes increases the maximum packing density of the blend [283–285]. If the particle sizes remain within a feasible range for the application, additional smaller or larger filler fractions can always be added, resulting in even higher maximum packing densities. The limit depends on the application, as very small particles lead to a significant increase in the composite's viscosity, while very large particles limit the minimum achievable layer thickness.

Recent decades have shown an increase in the number of studies into the packing of granular matter using theoretical and experimental methods, as well as with numerical simulation methods. The aim was to obtain detailed knowledge about the maximum packing density of individual materials and material combinations. Most frequently studied were binary mixtures of ideally spherical materials [244,262,283,284]. However, additional studies have included other particle shapes [286] or ternary mixtures [287–290]. Further details on the rheology of filled polymers, packing effects, and the influence of maximum packing density can be found for example in the comprehensive review published in 2017 by Rueda et al. [291].

Figure 5.1 shows an exemplary ternary filler blend, consisting of three spherical alumina fillers of different particle sizes. The filler blend consists of Alox-S-63, Alox-S-08, and Alox-S-01 in a volumetric ratio of $40{:}\,20{:}\,10$. Laser microscope images are shown at different magnification levels in parts (a) - (c). Part (d) presents the measured differential particle size distribution of the individual fillers, as well as combined in the blend. Materials and proportions were carefully selected for fillers with clear size differences so that the effect of the increased maximum packing density is expected to be maximized. Alox-S-63 was selected as the coarsest filler, with the largest particles being up to $200\ \mu\text{m}$ in size. Alox-S-01 was used as the smallest filler with fine-grained particles down to $100\ \text{nm}$. Even finer fillers would lead to an excessive increase in viscosity, while even coarser particles would limit the minimum gap width when used as a thermal interface material. The proportions were adjusted in such a way that the filler loading levels Φ of all individual fillers are as low as possible. Thus, each filler is still as far away as possible from its individual maximum packing density.

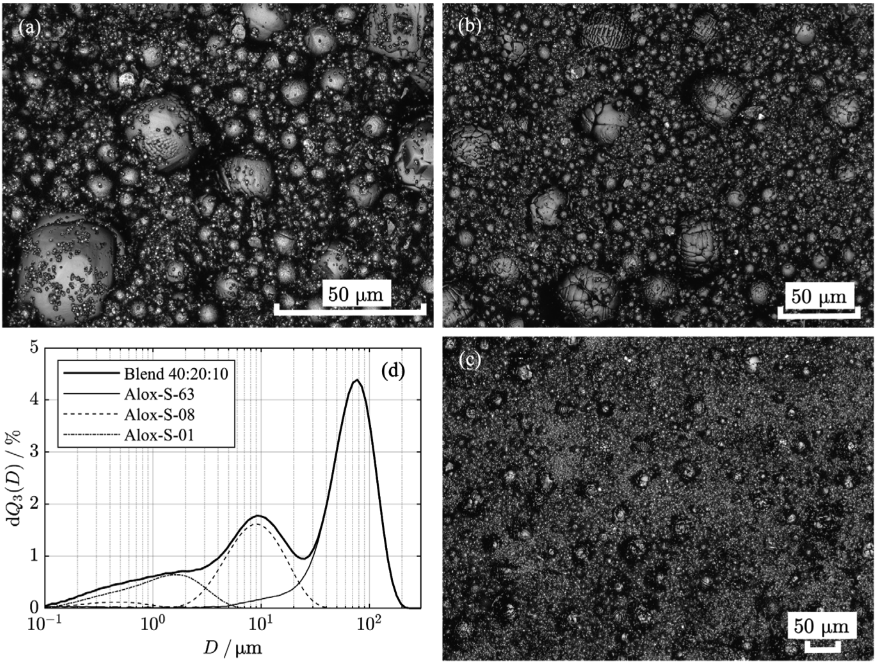

Figure 5.1. Laser microscope images and differential particle size distribution of an exemplary ternary filler blend.

Spherical alumina fillers Alox-S-63, Alox-S-08, and Alox-S-01 in a volumetric ratio of 40: 20: 10. Laser microscopic images of the filler blend in parts (a)-(c), taken with a Keyence 3D laser scanning microscope VK-X100K with different levels of magnification. Differential particle size distributions in (d), measured using the laser particle sizer Fritsch Analysette 22 NanoTec (laser diffraction).

The result is a mixture in which the largest particles appear to float in a bed of small particles. Direct contact between the particles of the largest fraction is unlikely. The presented blend and its filler proportions are in line with the results of the material developments in [177,178,182,292]. The filler mixture shown in **Figure 5.1** has particles with sizes that extend over four orders of magnitude. Therefore, it cannot be represented in a single detailed microstructure model without incurring excessive memory usage and computation time. The size of the required RVE would be based on the average particle size of the coarsest fraction, as described in section 4.1.2. The smallest particles would then be significantly smaller than the realizable local resolution of the RVE. A complex material structure with such different length scales exceeds the limits of the proposed microscale simulation method. Instead, a multi-step homogenization approach is introduced in the following chapter, with which the individual fillers are locally resolved step by step and considered hierarchically. The term homogenization refers to the process of determining effective macroscopic material properties (in this case thermal conductivity) for a microscopically inhomogeneous material. Multi-step homogenization approaches for predicting the effective thermal conductivity of filled polymers have already been used in the past. They have proven to be particularly suitable for describing multi-component blends, which do not necessarily have to be multi-scale. Ngo and Truong [293], for example, studied composition effects on the effective thermal conductivity of a composite with a binary filler system. They analyzed fundamental effects, such as the impact of the fillers' thermal conductivities or the volumetric ratio of the fillers, by applying both full-field simulations and multi-step homogenizations. In their multi-step homogenization approach, different theoretical and semi-empirical models, such as the Lewis and Nielsen model [145–148], were embedded to describe the different filler fractions individually before combining their contributions. Lu [294] also presented a multi-step application of the Lewis-Nielsen model [145–148] in 2016. The effective thermal conductivity of polymer composites with hybrid filler packings (boron nitride and multiwalled carbon nanotubes) of up to $\phi = 0.31$ was calculated. Zhu et al. [295] performed two-step calculations to predict the effective thermal conductivity of fiber-particle hybrid composites.

5.1.2 THE GENERAL HOMOGENIZATION SCHEME

Figure 5.2 schematically shows a ternary mixture of three arbitrary granular fillers, in which the individual proportions are adjusted in such a way that each fraction i is present in a filler volume fraction $\phi_i \ll \phi_{\max,i}$. To estimate the effective thermal conductivity of such a mixture, the originally complex filler structure is decomposed into a hierarchy of nested single-scale filler packings. This allows each fraction's contribution to be isolated and evaluated individually, while still accounting for filler-specific properties and interactions across length scales. First, a very small local RVE of the microstructure, containing only the smallest filler fraction, is extracted, see red square in **Figure 5.2**, part (a).

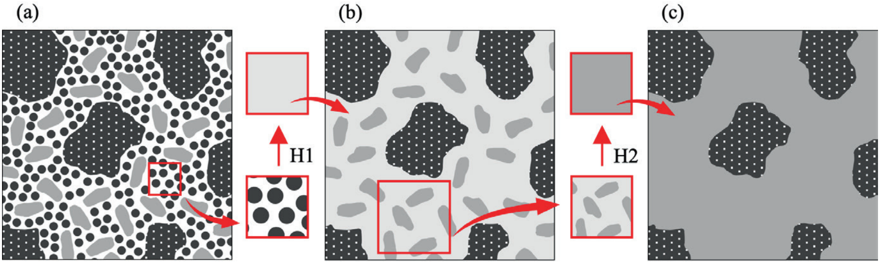

Figure 5.2. Illustration of general multi-step homogenization scheme.
Starting from a ternary filler blend in (a) and carrying out a first homogenization step H1 with the fine-grained fraction, a binary blend (b) is obtained. A second homogenization step H2, which is carried out with the medium-grained fraction, results in a single-scale filler packing (c).

The required size of this RVE is determined by the average particle size of the smallest fraction, see section 4.1.2. The effective thermal conductivity of this microscopically resolved RVE is calculated, and the result is substituted in during the first homogenization step (H1) to represent the first domain of the total system consisting of polymer matrix and the smallest filler fraction (b). The resulting microstructure in (b) is already significantly simplified, but still includes filler particles of different scales and domains. Again, a sub-RVE (red square) is extracted, that contains the homogenized phase (from H1) and the medium-sized filler fraction. The thermal conductivity, calculated using microscale simulations, is again used to homogenize (H2) the domain so that only a single-scale filler packing remains in (c). This process is repeated iteratively until all filler fractions have been incorporated. In the last step, the effective thermal conductivity of the entire RVE can be calculated. This multi-step homogenization approach is based on the assumption that each filler fraction occupies its own nested domain in the microstructure and behaves locally like a single-scale system. Each domain contributes hierarchically and multiplicatively to the overall improvement in thermal conductivity. Therefore, the cumulative effect of all filler fractions can be expressed by the following product formula:

$$\lambda_{\mathrm{eff}} = \lambda_{\mathrm{C}} \prod_{i=1}^{n} \Lambda_i \ . \tag{5.1}$$

Here, Λ_i represents the thermal conductivity magnification of filler fraction i. The n filler fractions of the blend are indexed in descending order of particle size. The individual thermal conductivity magnifications can be calculated with the microscale simulations described in chapter 4.1 and depend, among other filler-specific microstructural effects, on the TC ratio κ_i and the relative filler loading Φ_i^{r}

$$\Lambda_i(\kappa_i, \Phi_i^{\mathrm{r}}, \dots) \ . \tag{5.2}$$

The TC ratio κ_i relates the thermal conductivity of the filler particles $\lambda_{\mathrm{D},i}$ to the thermal conductivity of the surrounding continuous phase:

$$\kappa_i = \frac{\lambda_{\mathrm{D},i}}{\lambda_{\mathrm{C},i}} \ . \tag{5.3}$$

For $i = n$, the smallest fraction with the finest particles, this is the thermal conductivity of the polymer $\lambda_{\mathrm{C},n} = \lambda_{\mathrm{C}}$. For all fractions $i < n$, this is the effective thermal conductivity of the previous homogenization step $(i + 1)$

$$\lambda_{\mathrm{C},i} = \lambda_{\mathrm{eff},(i+1)} \ . \tag{5.4}$$

The relative filler loading Φ_i^r is calculated based on the relative filler volume fraction ϕ_i^r. It describes the volume concentration of a filler fraction in the domain assigned to it. It excludes the volume fraction $\phi_{1,i}$ occupied by the larger fractions with

$$\phi_i^\mathrm{r} = \frac{\phi_i}{1-\phi_{1,i}} = \frac{\phi_i}{1-\sum_{k=1}^{i-1}\phi_k} \,. \tag{5.5}$$

In principle, thermal interfacial resistance between the individual filler particles and the polymer can also be considered when calculating Λ_i. However, as the studies in section 4.4.3 have shown that their effect is negligible for the material combinations investigated in this work, they are disregarded in the following analyses.

The flowchart in **Figure 5.3** illustrates the implementation of the described calculation approach, including the preparatory calculation of the relative filler volume fractions according to **Eq. (5.5)**, and the subsequent calculation loop with microscale simulations for each fraction.

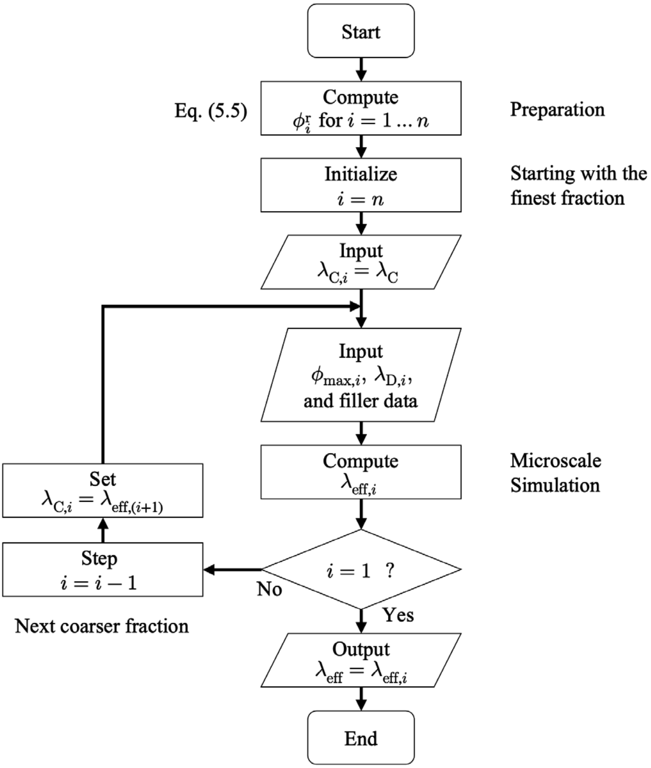

Figure 5.3. Flowchart of the general multi-step homogenization scheme.

While the product notation in **Eq. (5.1)** provides a compact representation, it is important to note that the overall effective thermal conductivity cannot be determined in a single step. Instead, it must be evaluated sequentially, starting from the smallest filler scale and progressing upwards.

The statistical reliability of the multi-step homogenization approach depends on the precision and repeatability of the underlying microscale simulations. As explained in section 4.1.2, these simulations yield a standard deviation of approximately 1 $\%$ in repeated runs. Within the multi-step homogenization, several single-scale simulations are combined to model the effective thermal conductivity of multi-scale filled polymers. Each individual simulation introduces its own uncertainty, and when these simulations are multiplicatively combined, the total uncertainty propagates according to

$$\left(\frac{\Delta\lambda_{\mathrm{eff}}}{\lambda_{\mathrm{eff}}}\right)_{\mathrm{multi}} = \sqrt{\sum_{i=1}^{n}\left(\frac{\Delta\Lambda_i}{\Lambda_i}\right)^2_{\mathrm{single}}} \ , \qquad \textbf{(5.6)}$$

where $(\Delta\Lambda_i/\Lambda_i)_{\mathrm{single}}$ are the independent and uncorrelated uncertainties of the individual microscale simulations of approximately 1 $\%$, and $(\Delta\lambda_{\mathrm{eff}}/\lambda_{\mathrm{eff}})_{\mathrm{multi}}$ is the resulting 1σ uncertainty of the multi-scale simulation. In extreme cases, this would be 1.7 $\%$ for a ternary filler blend ($n = 3$) and 2.0 $\%$ for a quaternary filler blend ($n = 4$). They are therefore significantly smaller than the uncertainties of the measurements with the steady-state cylinder method which are in the range of $(10\ldots15)$ $\%$. To eliminate the uncertainties of multi-scale simulations in systematic studies as presented in chapters 5.3 and 5.4, a static geometric packing model can be used for all single-scale calculations. This procedure ensures that variations due to random packing configurations are eliminated, allowing to focus on the systematic effects of different filler properties in the respective fractions.

Chapter 5.2 presents a general experimental validation of the multi-step homogenization approach. For this purpose, several polymer composites were prepared with arbitrary binary, ternary, and quaternary mixtures of granular fillers, and their effective thermal conductivities were measured. The simple superposition of the single-scale simulations according to **Eq. (5.1)** already shows a good model agreement. However, this approach tends to overestimate the effective thermal conductivity of the composite at medium to high total filler volume fractions. This overestimation is presumably due to the lack of consideration for microstructural packing effects, which do not occur in single-scale filled polymers and only appear when several size fractions are mixed. A model extension which takes these multi-scale packing effects into account is described in the next section 5.1.3. Further details and the results of the experimental model validation are shown in chapter 5.2.

5.1.3 CONSIDERING INTERFACIAL TRANSITION ZONES (ITZ)

In the field of granular matter and packing theories, wedging, loosening, and wall effects are well-known in packings with a multimodal particle size distribution [284,296–299]. These are all geometric effects that influence the packing structure, primarily determined by the material composition and, most importantly, the volumetric proportions. A loosening effect occurs when the particles of the smaller fraction are too large for the gaps between the particles of the coarser-grained fraction and push them apart. Wedging occurs when the particles of the larger fractions are so close together that only individual particles of the smaller fraction have space between them, and no packing of the smaller fraction can form.

The wall effect is the disturbance of the packing structure of a fine-grained filler domain at the boundary to the particles of coarse-grained fractions. In the filled polymers considered in this work, none of the individual fractions are close to their individual maximum packing density. As a result, neither wedging nor loosening effects are expected. There is always sufficient space between particles of the large fraction for the formation of fine-grained particle packings in between. However, wall effects are always present in multi-scale systems due to the size disparity between filler particles. The domain boundary layers where these geometric disturbances occur, are referred to as interfacial transition zones (ITZ), especially in concrete research and development [300,301]. This expression is been adapted for the further descriptions. In concrete research, it is more about the mechanical properties and the achievable packing densities, but the fundamental effect behind this is purely geometric, causing a lower local filler volume fraction near the wall, or in multi-scale filled polymers near the next largest particle, see **Figure 5.4**. There are always larger gaps between particles directly at the wall, which can’t be filled any further as additional particles would collide with the wall or the particles of the coarser-grained fractions.

There are numerous studies in which the wall effect has been investigated experimentally, theoretically, or by means of numerical packing simulation, reviewed in [296,297,299]. The focus in these studies has been on calculating the porosity or the reduced volume fraction in the ITZ, while heat conduction through such layers has not yet been systematically investigated. A closely related phenomenon, the locally reduced filler volume fraction at a filled polymer to substrate transition (FPS transition), has already been introduced in **Figure 2.3**, page 18, and will be discussed in more detail in chapter 6. In this work, it is hypothesized that a lower filler concentration in the ITZ, combined with a higher concentration in the undisturbed bulk region, leads to a spatially inhomogeneous thermal conductivity within each filler domain. It is assumed that the reduced thermal conductivity in the ITZ dominates and the overall effective thermal conductivity of the multi-scale system decreases.

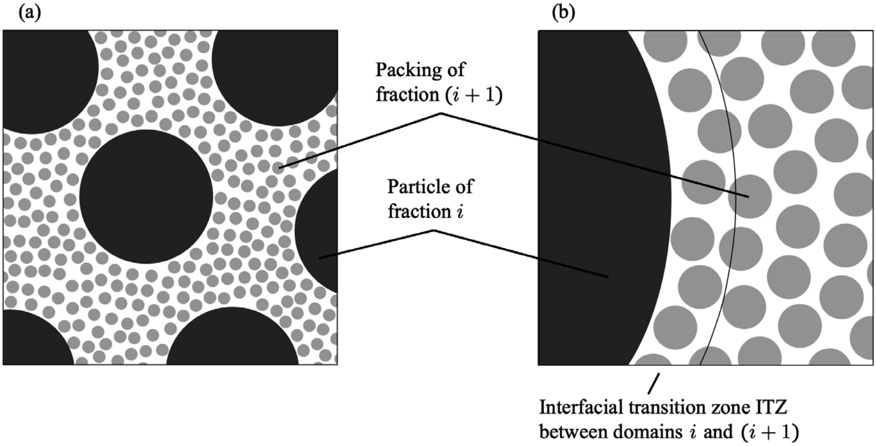

Figure 5.4. Interfacial transition zone (ITZ) between filler domains.
Binary filler blend, consisting of a coarse-grained and a fine-grained spherical filler (a). Detailed illustration of the domain boundary and the interfacial transition zone (ITZ) between the filler domains i and $(i + 1)$ in part (b).

In order to include ITZ effects in the multi-step homogenization approach without relying on computationally expensive microscale simulations for each individual case, a simplified, generalizable model is proposed. The aim is to approximate the thermal effects of ITZs using input parameters derived from a limited number of targeted simulations.

The geometric similarity between FPS transitions and ITZs allows simulation results from chapter 6.1 to be adapted to the analyses of ITZ behavior. The approach is intended to link the microscale origin of ITZ effects and their impact on the effective thermal conductivity of multi-scale filled polymers. It does not create a universally valid model. However, the semi-empirical correction introduced in this section creates an efficient calculation approach that is valid for a wide range of materials and combinations, see chapter 5.2.

Several simplified microstructural configurations are simulated to capture the essential parameters of ITZ behavior. The aim is to extract three key parameters that are necessary to approximate the ITZ effects on the effective thermal conductivity of a multi-scale filled polymer:

- The thickness Δr_{ITZ} of the ITZ,
- the reduced filler volume fraction ϕ_{ITZ} in the ITZ, and
- the reduced thermal conductivity λ_{ITZ} in the ITZ.

The implementation of the calculations is described in chapter 6.1. The resulting data is processed to extract dimensionless parameters that can be generally applied in an extended homogenization model. The simulations were carried out with ideally smooth substrate surfaces and spherical particles. Particle size distribution and filler loading level were varied, with a random particle-substrate distance (PSD) selected for the particles close to the substrate, see section 6.4.2, **Figure 6.19**, page 196.

Figure 5.5 summarizes the simulation results. Shown in part (a) is the dimensionless ITZ thickness $A1$, defined in **Eq. (5.7)**. Part (b) shows the ratio of the filler volume fractions in ITZ and undisturbed bulk $A2$, defined in **Eq. (5.8)**, while part (c) shows the ratio of thermal conductivities in ITZ and undisturbed bulk $A3$, defined in **Eq. (5.9)**.

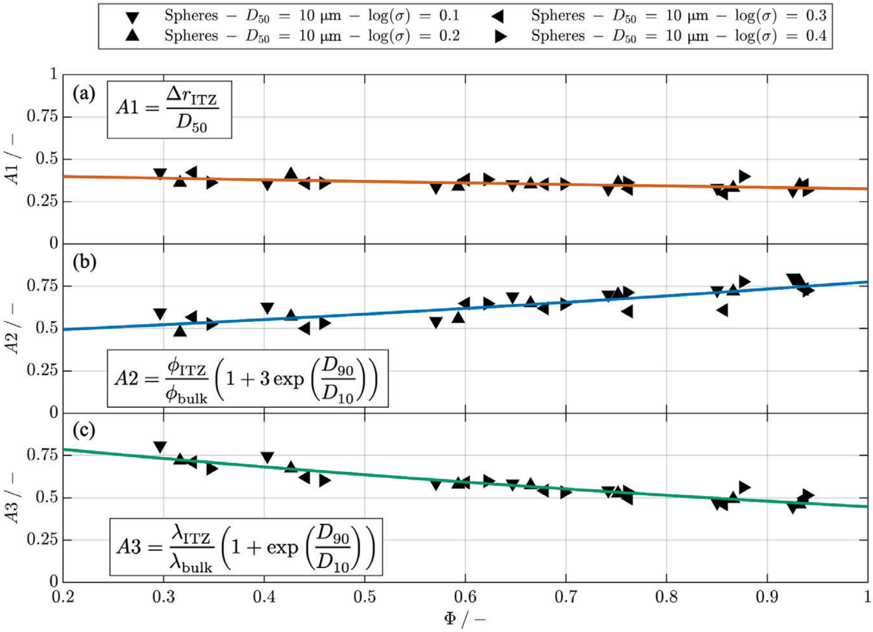

Figure 5.5. Summarized results of microscale simulations on ITZ effects.

Dimensionless representation of the three central effects in an ITZ. The dimensionless ITZ thickness $A1$, depending on the filler loading level and width of the particle size distribution is shown in (a). The filler concentration ratio of ITZ to bulk $A2$ is shown in (b). The thermal conductivity ratio of ITZ to bulk $A3$ is shown in (c). All simulations were carried out using the simulation approach presented in chapter 6.1. Polymer: $\lambda_{\mathrm{C}} = 0.25$ W m^{-1} K^{-1} (e.g., epoxy). Filler: Spheres with log-normal size distribution with $\log(\sigma) = 0.1 \ldots 0.4$, $D_{50} = 10$ µm, $\phi_{\max} = 0.55$, $\lambda_{\mathrm{D}} = 35$ W m^{-1} K^{-1} (e.g., alumina). Substrate: Ideally flat, $\lambda_{\mathrm{S}} = 130$ W m^{-1} K^{-1} (e.g., aluminum alloy). Full surface wetting.

To enable an integration into the multi-step homogenization approach, the extracted dimensionless parameters are approximated by exponential fits. These fits make the results easily transferable and applicable in subsequent modeling steps. The choice of exponential fits is based on the geometric nature of the ITZ effects. Over the relevant range of filler loading level, the parameter trends are almost linear but exhibit a slight curvature. This behavior reflects the underlying geometric constraints, such as the saturation of the dimensionless ITZ thickness $A1$ and the ratio of thermal conductivities in ITZ and undisturbed bulk $A3$ at high filler loading levels, as well as the nonlinear increase in the ratio of filler volume fractions $A2$. Exponential functions were chosen as they capture the asymptotic behavior of the observed geometric effects.

While the dimensionless ITZ thickness $A1$ is independent of the particle size distribution, both the filler volume fraction ratio $A2$ and the thermal conductivity ratio $A3$ show a pronounced dependence on it. This influence is considered during normalization by introducing empirically derived terms $(1 + 3\exp(D_{90}/D_{10}))$ for $A2$ and $(1 + \exp(D_{90}/D_{10}))$ for $A3$. These expressions scale the fitted relationships with respect to the width of the particle size distribution, expressed by the ratio of D_{90} to D_{10}, and ensure that the effects of increasing width of the particle size distribution are accounted for. $A1$ decreases slightly with the filler loading level. It can be approximated with

$$A1 = \frac{\Delta r_{\mathrm{ITZ}}}{D_{50}} = 0.4189 \;\; \exp(-0.2513 \; \Phi) \; . \tag{5.7}$$

The ITZ thickness Δr_{ITZ} is on average around $0.4 \cdot D_{50}$. The filler volume fraction ratio $A2$ depends significantly on the filler loading level Φ and shifts with increasing width of the particle size distribution. It can be approximated with

$$A2 = \frac{\phi_{\mathrm{ITZ}}}{\phi_{\mathrm{bulk}}} \left(1 + 3\exp\left(\frac{D_{90}}{D_{10}}\right)\right) = 0.4413 \;\; \exp(0.5640 \; \Phi) \; . \tag{5.8}$$

The ratio of the thermal conductivities $A3$ falls with increasing filler loading level Φ and can be approximated with

$$A3 = \frac{\lambda_{\mathrm{ITZ}}}{\lambda_{\mathrm{bulk}}} \left(1 + \exp\left(\frac{D_{90}}{D_{10}}\right)\right) = 0.9050 \;\; \exp(-0.7050 \; \Phi) \; . \tag{5.9}$$

To take the wall effect as described by $A1$, $A2$, and $A3$ into account when calculating the effective thermal conductivity with the multi-step homogenization approach, a model extension is applied. This is based on the correction of the filler volume fractions in ITZ and bulk.

Figure 5.6 schematically illustrates this model extension considering the ITZs between filler domains. The index i refers to the coarser filler fraction around which an ITZ forms, while $(i + 1)$ denotes the finer filler fraction with a disturbed packing. However, this indexing is purely descriptive and becomes irrelevant during calculations, as each fraction in a multi-scale filled blend - except the largest - can form an ITZ, while each fraction - except the smallest - can define the boundaries for the next smaller fraction.

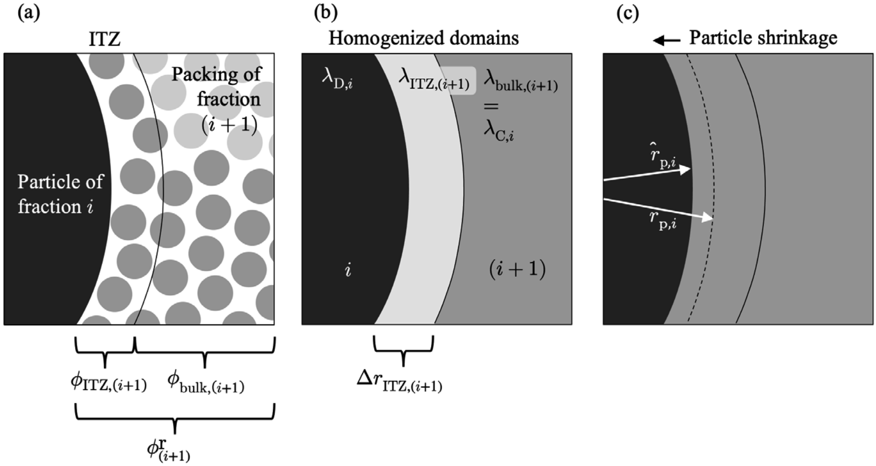

Figure 5.6. Schematic illustration of the model extension to consider the ITZ between filler domains. Detailed representation of the interfacial transition zone (ITZ) between the filler domains i and $(i+1)$ with labeling of the local filler volume fractions in part (a). Representation after homogenization of the ITZ and the filler packing $(i+1)$ with indication of the respective thermal conductivities in part (b). Illustration of the particle shrinkage process to represent the additional thermal resistance of the ITZ in part (c).

To represent the phenomena at the domain interfaces without having to resolve the structure microscopically, the filler volume fractions are modified of both the coarser-grained fraction i and the finer-grained fraction $(i+1)$. Part (a) of **Figure 5.6** illustrates the different filler volume fractions in the ITZ and bulk area of fraction $(i+1)$. From the materials composition, the only known property is the total relative filler volume fraction $\phi^{\mathrm{r}}_{(i+1)}$. For the subsequent homogenizations, the relative filler volume fraction must be corrected, so that it corresponds to the actual bulk filler volume fraction $\phi_{\mathrm{bulk},(i+1)}$.

ITZ and the remaining filler domain $(i+1)$ are homogenized in the further process, see part (b) of **Figure 5.6**. In order to reflect the effect of the lower thermal conductivity $\lambda_{\mathrm{ITZ},(i+1)}$ in the ITZ with the layer thickness $\Delta r_{\mathrm{ITZ},(i+1)}$, a particle shrinkage is then performed in the coarser-grained fraction i, see part (c) of **Figure 5.6**. The particle shrinkage $r_{\mathrm{p},i} \rightarrow \hat{r}_{\mathrm{p},i}$ is intended to replicate the additional thermal resistance that the ITZ in the adjacent finer fraction $(i+1)$ would introduce. In subsequent calculations, the shrunken particles are represented by an adjusted, reduced volume fraction for the coarser filler fraction. The flowchart in **Figure 5.7** illustrates the extended multi-step homogenization approach incorporating ITZ corrections. New or modified calculation steps compared to **Figure 5.3**, page 144, are highlighted in gray. These consist of two further preparation steps and one modification step, which are explained below.

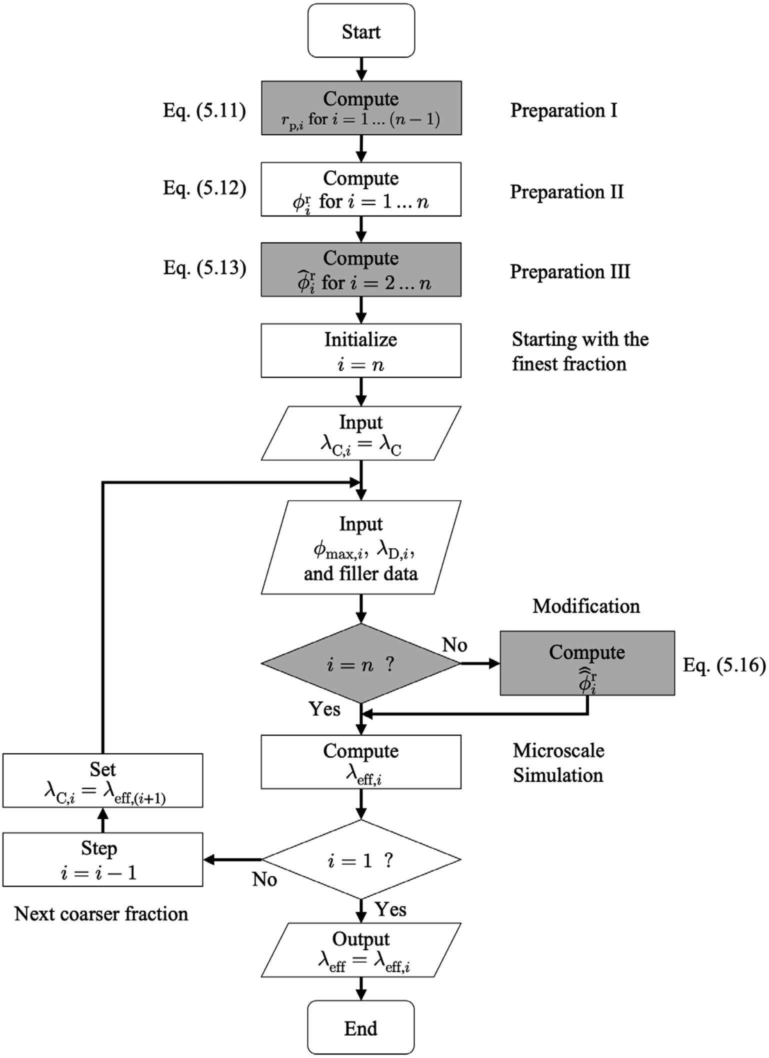

Figure 5.7. Flowchart of extended multi-step homogenization scheme with ITZ consideration.

Preparation Step I: Determination of an equivalent particle radius $r_{\mathrm{p},i}$ *for all fractions* i

Specifically for the ITZ extension, all particles within each fraction are treated as equally sized spheres, including irregularly shaped particles with arbitrary size distribution. In a first step, the equivalent radius $r_{\mathrm{p},i}$ is determined as a representative particle size for each filler fraction $i = 1 \dots (n-1)$ to be shrunk.

Since the phenomenon to be described is an interfacial effect, it is important to take the exact particle surface area into account despite geometric simplification. For this purpose, the equivalent radius is determined based on the specific surface area of the filler. The specific surface area $S_{\mathrm{V},i}$ of the granular fillers i can be easily calculated from the experimentally determined particle size distribution and represents the ratio of particle surface area $A_{\mathrm{D},i}$ to particle volume $V_{\mathrm{D},i}$

$$S_{\mathrm{V},i} = \frac{A_{\mathrm{D},i}}{V_{\mathrm{D},i}} \,. \qquad \textbf{(5.10)}$$

For equally sized spheres (simplified assumption), the equivalent radius is

$$r_{\mathrm{p},i} = \frac{3}{S_{\mathrm{V},i}} \,. \qquad \textbf{(5.11)}$$

Preparation Step II: Calculation of the relative filler volume fractions for all fractions i

This preparation step does not differ from the general multi-step homogenization scheme. The relative filler volume fractions ϕ_i^{r} of all size fractions are calculated using

$$\phi_i^{\mathrm{r}} = \frac{\phi_i}{1-\phi_{\mathrm{l},i}} = \frac{\phi_i}{1-\sum_{k=1}^{i-1}\phi_k} \,. \qquad \textbf{(5.12)}$$

They describe the volume concentration of a filler fraction in the domain assigned to it and exclude the volume fraction $\phi_{\mathrm{l},i}$ occupied by all larger fractions.

Preparation Step III: First correction of the filler volume fraction

As illustrated in part (a) of **Figure 5.6**, page 150, the ITZ towards coarser-grained fractions leads to an increase in the filler volume fraction in the bulk area of all fractions $i = 2 \ldots n$. The relative filler volume fraction ϕ_i^{r} must be corrected to $\phi_i^{\mathrm{r}} \to \hat{\phi}_i^{\mathrm{r}}$ so that it represents the actual bulk filler volume fraction $\hat{\phi}_i^{\mathrm{r}} = \phi_{\mathrm{bulk},i}$. This correction is derived geometrically, as detailed in appendix C.3. The corrected filler volume fraction in the bulk $\hat{\phi}_i^{\mathrm{r}}$ can be expressed as

$$\hat{\phi}_i^{\mathrm{r}} = \phi_{\mathrm{bulk},i} = \phi_i^{\mathrm{r}} \left[1 + \left(\frac{V_{\mathrm{ITZ}}}{V_{\mathrm{tot}}}\right)_i \left(\left(\frac{\phi_{\mathrm{ITZ}}}{\phi_{\mathrm{bulk}}}\right)_i - 1\right)\right]^{-1} , \qquad \textbf{(5.13)}$$

where $(\phi_{\mathrm{ITZ}}/\phi_{\mathrm{bulk}})_i = A2_i$ is the filler volume fraction ratio according to **Eq. (5.8)**, page 149, and $(V_{\mathrm{ITZ}}/V_{\mathrm{tot}})_i$ is the proportion of the volume of all ITZs towards particles of larger fractions in the total volume in which fraction i is dispersed. It is obtained with

$$\left(\frac{V_{\mathrm{ITZ}}}{V_{\mathrm{tot}}}\right)_i = \frac{\sum_{k=1}^{i-1}\phi_k\left(\left(1+\frac{\Delta r_{\mathrm{ITZ},i}}{r_{\mathrm{p},k}}\right)^3-1\right)}{1-\sum_{k=1}^{i-1}\phi_k}, \tag{5.14}$$

where $\Delta r_{\mathrm{ITZ},i}$ is the ITZ thickness according to **Eq. (5.7)**, page 149, $r_{\mathrm{p},k}$ are the equivalent particle radii of the coarser fractions according to **Eq. (5.11)**, and ϕ_k are the volume fractions of those coarser fractions.

Modification Step: Second correction of the filler volume fraction during homogenization

After the preparation steps I-III are completed, the further homogenization process is essentially the same as in the general homogenization scheme, see **Figure 5.2**, page 142. However, a modification step is introduced for all fractions $i = 1 \dots (n-1)$, see **Figure 5.7**, page 151. A correction of the particle radius $r_{\mathrm{p},i} \rightarrow \hat{r}_{\mathrm{p},i}$ and thus of the filler volume fraction $\hat{\phi}_i^{\mathrm{r}} \rightarrow \hat{\hat{\phi}}_i^{\mathrm{r}}$ is made in order to account for the ITZs caused by the next smaller fractions $(i+1)$, see part (c) of **Figure 5.6**, page 150.

Since the multi-step homogenization approach treats the fractions in descending order of size, the next smaller fraction is already homogenized when this modification is applied. The continuous phase to be considered has the thermal conductivity $\lambda_{\mathrm{C},i} = \lambda_{\mathrm{eff},(i+1)}$. The particles of fraction i are assumed to be spherical and uniformly surrounded by a thermally resistive spherical shell (ITZ) of thickness $\Delta r_{\mathrm{ITZ},(i+1)}$, as illustrated in part (b) of **Figure 5.6**, page 150. In order to reflect the effect of the lower thermal conductivity $\lambda_{\mathrm{ITZ},(i+1)}$ in the ITZ with the layer thickness $\Delta r_{\mathrm{ITZ},(i+1)}$, a particle shrinkage is then performed in the coarser-grained fraction i. The particle shrinkage $r_{\mathrm{p},i} \rightarrow \hat{r}_{\mathrm{p},i}$ is intended to replicate the additional thermal resistance that the ITZ in the adjacent finer fraction $(i+1)$ would introduce. The derivation of this particle shrinkage is described in appendix C.4. The result is

$$\hat{r}_{\mathrm{p},i} = \left[\frac{\left(\frac{1}{\lambda_{\mathrm{ITZ},(i+1)}}-\frac{1}{\lambda_{\mathrm{C},i}}\right)\left(\frac{1}{r_{\mathrm{p},i}}-\frac{1}{r_{\mathrm{p},i}+\Delta r_{\mathrm{ITZ},(i+1)}}\right)}{\left(\frac{1}{\lambda_{\mathrm{C},i}}-\frac{1}{\lambda_{\mathrm{D},i}}\right)}+\frac{1}{r_{\mathrm{p},i}}\right]^{-1}, \tag{5.15}$$

where $\lambda_{\mathrm{ITZ},(i+1)}$ represents the reduced effective thermal conductivity of the ITZ, which can be derived from **Eq. (5.9)**, page 149, and $\lambda_{\mathrm{D},i}$ denotes the thermal conductivity of the filler particles in fraction i. The resulting reduction in particle volume causes a reduction of the filler volume fraction in fraction i to

$$\hat{\hat{\phi}}_i^{\mathrm{r}} = \hat{\phi}_i^{\mathrm{r}} \left(\frac{\hat{r}_{\mathrm{p},i}}{r_{\mathrm{p},i}} \right)^3 \quad . \tag{5.16}$$

The original relative filler volume fraction $\hat{\phi}_i^{\mathrm{r}}$ is already a modified value from preparation step III, if the fraction i under consideration is not the coarsest fraction. If it is the coarsest, $\hat{\phi}_i^{\mathrm{r}}$ corresponds to the original relative filler volume fraction ϕ_i^{r} according to **Eq. (5.12)**. With the reduced filler volume fraction $\hat{\hat{\phi}}_i^{\mathrm{r}}$, the homogenization step can be carried out, see **Figure 5.7**, page 151.

With this model extension and substitute representation of the ITZs, the multi-step homogenization approach can account for the wall effect in particle packing without requiring microscopic resolution. Importantly, the prerequisite and limit of the model is that the filler volume fraction of the fraction to be modified is sufficiently small, such that two ITZs and an undisturbed bulk area can always form between two particles. This condition was met by all composites investigated in this work. The effect of the model extension on the accuracy of the simulation results is discussed in the following chapter.

5.2 EXPERIMENTAL VALIDATION AND FORMULATION STUDIES

Analogous to the procedure in chapter 4.5, this chapter provides an experimental validation of the presented calculation approach. Furthermore, the experimental results are used to discuss the first findings and identify parameters which influence the effective thermal conductivity of multi-scale filled polymers. 252 filled polymer composites with arbitrary binary, ternary, and quaternary mixtures of granular fillers were prepared for this purpose. The effective thermal conductivities were measured using the steady-state cylinder method according to ASTM D5470-17 [184], see chapter 3.2.

The utilized fillers were presented in section 3.1.2. They cover a wide range of characteristics and are

- of aluminum (Al), alumina (Al_2O_3), aluminum hydroxide ($Al(OH)_3$), and silica (SiO_2),
- with spherical and irregular shapes,
- with median volumetric particle sizes between $0.8\ \mu\mathrm{m}$ and $150\ \mu\mathrm{m}$, and
- used in total filler volume fractions from $\phi = 0.40$ to $\phi = 0.77$.

Epoxy E01[17] was used as the polymeric matrix. When defining the volume proportions of the fillers, the packing balance was carefully tuned according to [177,178,182,292], see section 5.1.1. This ensures good processability of the composites. The filler volume

---

[17] SikaBiresin® TD150 – TD165, details see **Table 3.1**.

fractions containing coarser-grained fractions are equal or higher than those of the finer-grained fractions. Individual filler loading levels of 0.08 … 0.80 were set with the average filler loading level of the fractions among all samples at 0.30. Only 7 % off the individual components within all filled polymer composites are used with a filler loading level > 0.65. All others are still far from their maximum packing density. The calculation approach presented in the previous chapter can therefore be used for all composites.

Figure 5.8 provides a comprehensive validation of the multi-step homogenization method by comparing all measured thermal conductivities with simulation results. **Table 5.1** supplements with a statistical analysis of model deviations. Part (a) and (c) of **Figure 5.8** show the results gained using the general homogenization scheme from section 5.1.2, while parts (b) and (d) correspond to the extended model considering domain interfaces, i.e., ITZs, as introduced in section 5.1.3. Parts (a) and (b) compare simulated and measured thermal conductivities. Error bars are not shown for the sake of better visualization. Parts (c) and (d) represent histograms of the deviations between simulated and measured values. The measurement uncertainties for the steady-state cylinder method depend on the sample quality and are in the range of (10 … 15) %. A good model agreement can already be achieved using the simple, general multi-step homogenization scheme.

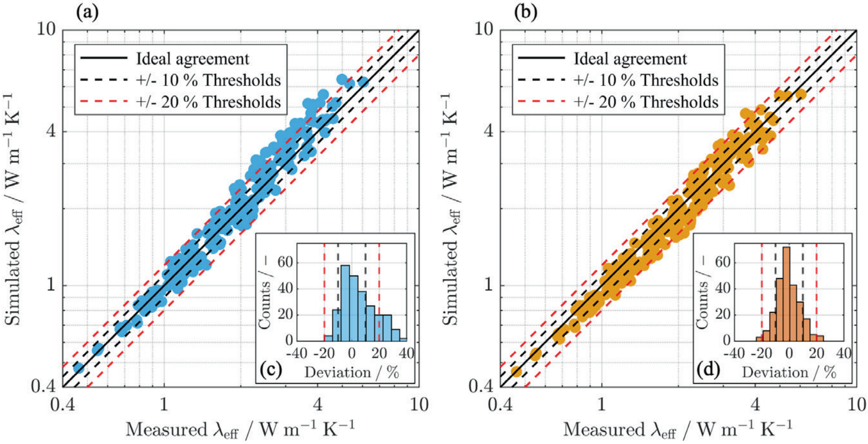

Figure 5.8. Validation of the multi-step homogenization approach for multi-scale filled polymers. Comparison of calculated thermal conductivities with measured thermal conductivities using the steady-state cylinder method in (a) and (b). Histogram of deviations in (c) and (d). Calculations were performed with the general homogenization scheme (section 5.1.2) in (a) and (c). Calculations were carried out with additional application of the model extension for ITZs (section 5.1.3) in (b) and (d). Polymer: Epoxy E01. Fillers: see **Table 4.4**, in binary, ternary and quaternary blends. Total filler volume fraction $0.40 < \phi < 0.77$.

Table 5.1. Statistical analysis of model validation, corresponding to **Figure 5.8**.

	General homogenization scheme (section 5.1.2)	**Incl. model extension for ITZs** (section 5.1.3)
Percentage of simulations within $\pm 10\ \%$ thresholds	$58\ \%$	$78\ \%$
Percentage of simulations within $\pm 20\ \%$ thresholds	$85\ \%$	$98\ \%$
Mean absolute deviation	$10.3\ \%$	$6.4\ \%$
Standard deviation	$8.7\ \%$	$5.1\ \%$

However, there is a systematic deviation between simulation and measurement for $\lambda_{\text{eff}} > 2\ \mathrm{W\ m^{-1}\ K^{-1}}$. The presented calculation approach tends to overestimate the effective thermal conductivity of the filled polymer. This deviation can be attributed to the packing effects at the domain interfaces, as described in section 5.1.3. If the additional model extension developed for this purpose is used, the model quality increases and there is better agreement between calculation and measurement, see part (b) of **Figure 5.8**. Noticeable deviations persist here too, both downwards and upwards. In addition to the measurement uncertainties contained therein, these can be attributed to the strong simplifications in the chosen extension approach. These include the treatment of all fillers as equally sized spheres and using modified filler volume fractions without microscopic resolution in the calculation. Nevertheless, the easy-to-use approach leads to significantly improved overall model quality.

With the general homogenization scheme, the maximum deviation between measurement and simulation is $41\ \%$. Using the model extension for ITZs, the maximum deviation falls to $29\ \%$. With the general homogenization scheme, $85\ \%$ of the simulations exhibit a deviation $\leq 20\ \%$, while with the model extension, $98\ \%$ of the simulations exhibit a deviation $\leq 20\ \%$. The mean absolute deviation is $10.3\ \%$ with the general homogenization scheme and $6.4\ \%$ with the model extension for domain interfaces, see **Table 5.1** and **Figure 5.8**.

As already discussed in the previous chapter, all fillers used have complex and individual property profiles. For this reason, the effects of the respective filler properties on the effective thermal conductivity of the multi-scale filled polymer can only be derived to a limited extent from purely experimental studies. Nevertheless, initial trends can already be extracted, which are then analyzed in detail in the following sections using the presented and validated calculation approach.

Figure 5.9 shows the results of a composition series with a ternary blend of spherical alumina. Epoxy E01 was combined with Alox-S-63, Alox-S-08, and Alox-S-01 in different proportions in twelve composites. The horizontal bars in the left part of **Figure 5.9** represent the filler volume fractions in each composite and the right side shows the measured and calculated effective thermal conductivities. Presented are both the results gained with the general homogenization scheme (black line) and the results gained with the additional usage of the model extension for ITZs (red line).

Since the same filler material with approximately the same thermal conductivity is used in all fractions, an increase in the effective thermal conductivity with the total filler concentration can be observed in all composites, regardless of the blend proportions. Depending on the proportions, different maximum filler volume fractions can be reached. The most highly filled samples are the composites C1.6 and C1.9, with the total filler volume fractions at $\phi = 0.72$.

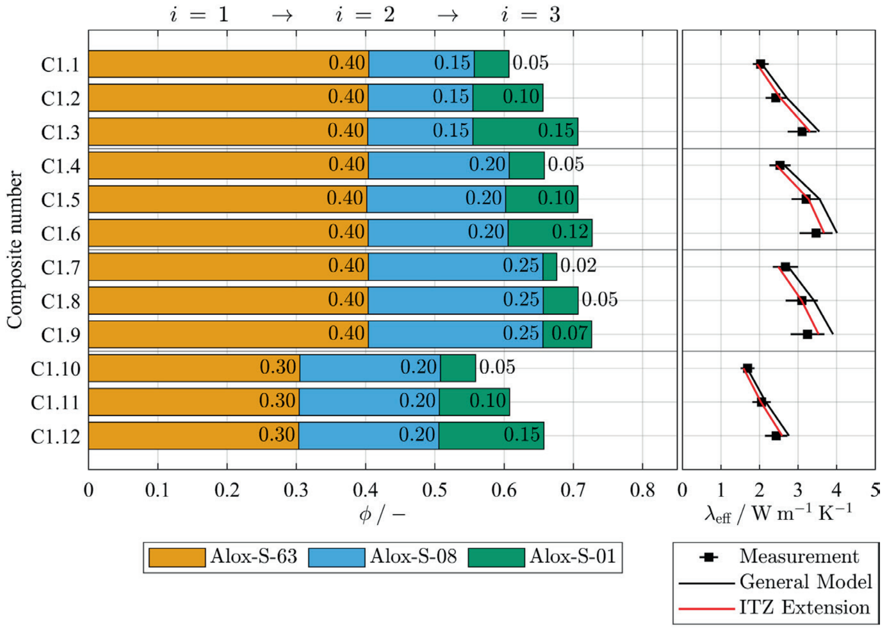

Figure 5.9. Results of composition series C1.

Filler content, measured, and calculated effective thermal conductivity of twelve composites. Polymer: Epoxy E01. Fillers: Alox-S-63, Alox-S-08, and Alox-S-01 in different proportions. Since the experimental uncertainties are significantly higher, error bars of the simulations are omitted for clearer visualization. The 1σ margin of the simulations is $\pm$ 1.7 %, estimated as described in section 5.1.2.

Measurements on composite C1.6 gave $\lambda_{\text{eff}} = 3.47\ \text{W m}^{-1}\ \text{K}^{-1}$ and for composite C1.9, $\lambda_{\text{eff}} = 3.25\ \text{W m}^{-1}\ \text{K}^{-1}$ was measured. The effects of filler-specific properties such as particle size distribution and maximum packing density can't be derived from these results. For this purpose, a simulative study with systematic variation of the maximum packing densities in the individual fractions is presented in chapter 5.3.

In a second and third composition series, different filler materials are combined in a ternary blend. **Figure 5.10** shows the results of those composition series. Epoxy E01 was used as the polymeric matrix. ATH-I-75 forms the coarsest fraction in both blends. The medium and fine-grained fractions consist of alumina and aluminum, and vice versa.

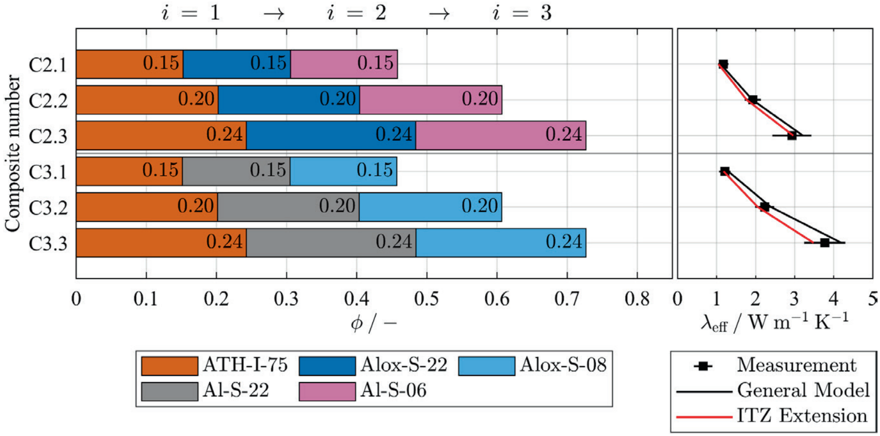

Figure 5.10. Results of composition series C2 and C3.
Filler content, measured, and calculated effective thermal conductivity of six composites. Polymer: Epoxy E01. Filler blend 2: ATH-I-75, Alox-S-22, and Al-S-06. Filler blend 3: ATH-I-75, Al-S-22, and Alox-S-08. Since the experimental uncertainties are significantly higher, error bars of the simulations are omitted for clearer visualization. The 1σ margin of the simulations is $\pm$ 1.7 %, estimated as described in section 5.1.2.

The fillers Alox-S-22, Alox-S-08, Al-S-22, and Al-S-06 are selected so that the medium and fine-grained fractions in both compositions have a similar property profile but consist of materials with significantly different thermal conductivities. To compensate the effect of different blend proportions, the individual filler volume fractions of each composite are chosen identically. Such a blend differs significantly from the optimal packing structures presented in [177,178,182,292] and is only used here to analyze the effect of composition. The simulation results with the general model and using the ITZ extension provide similar results, both within the error intervals of the experiments.

Both experimental and simulation results show that the filler mixture with the higher thermally conductive aluminum (class III filler with $\lambda_D \approx 150\ \text{W m}^{-1}\ \text{K}^{-1}$) in the middle fraction (C3), yields a higher effective thermal conductivity than the filler mixture with alumina (class II filler with $\lambda_\mathrm{D} \approx 35\ \mathrm{W\ m^{-1}\ K^{-1}}$) in the middle fraction (C2). This effect is less pronounced with a low total filler volume fraction of $\phi = 0.45$ (composites C2.1 and C3.1), but is well recognizable with composites C2.2, C2.3, C3.2, and C3.3 with $\phi = 0.6$ and $\phi = 0.72$. For composite C2.3, $\lambda_\mathrm{eff} = 2.93\ \mathrm{W\ m^{-1}\ K^{-1}}$, and for composite C3.3, $\lambda_\mathrm{eff} = 3.77\ \mathrm{W\ m^{-1}\ K^{-1}}$ was measured.

This is an interesting result when compared to the analysis on single-scale filled polymers in chapter 4, and especially the study in **Figure 4.30**, page 126. For single-scale filled polymers, it has been shown that the effective thermal conductivity is saturated even at moderate material thermal conductivities, and that the use of aluminum in comparison to alumina doesn't cause any significant increase in the effective thermal conductivity. However, the use of fillers with different thermal conductivities in the different fractions is much more important in multi-scale filled polymers. It appears that the aluminum filler can exploit its thermal performance significantly better when used in the medium fraction than in the fine-grained fraction. Since the selected fillers are similar but not identical (particle size distribution, agglomeration, maximum packing density, ...), the phenomenon can't be fully attributed to the difference in thermal conductivity of the fillers. It is possible that the effect is superimposed with other influences that can't be eliminated in an experimental study. For this reason, a simulative study is presented in chapter 5.4, in which fillers with different thermal conductivities, but otherwise identical, are combined in ternary blends.

5.3 EFFECT OF THE FILLERS' MAXIMUM PACKING DENSITIES

After the experimental studies in chapter 5.2, this and the following chapter focus on simulative studies. The effects of individual filler parameters are considered in isolation and studied systematically. In chapter 4.6 it has been shown that the characteristics of the enhancement in thermal conductivity with single-scale filled polymers can be attributed mainly to two central parameters:

- the filler loading level Φ, and
- the TC ratio of filler and continuous phase κ.

The filler loading level depends on the absolute filler volume fraction and the maximum packing density ϕ_max of the fillers. The latter depends on particle morphology, particle size distribution, and the degree of compaction of the filler packing. Effects such as agglomeration and sedimentation are not considered. In this chapter, the results of composition series C4, C5, and C6 are presented and discussed. These studies investigate the effect of the maximum packing density of the fillers used in the individual fractions. The next chapter will follow with composition series C7 and C8, in which the impact of the fillers' thermal conductivities is isolated. **Figure 5.11** shows the results of composition series C4, C5, and C6.

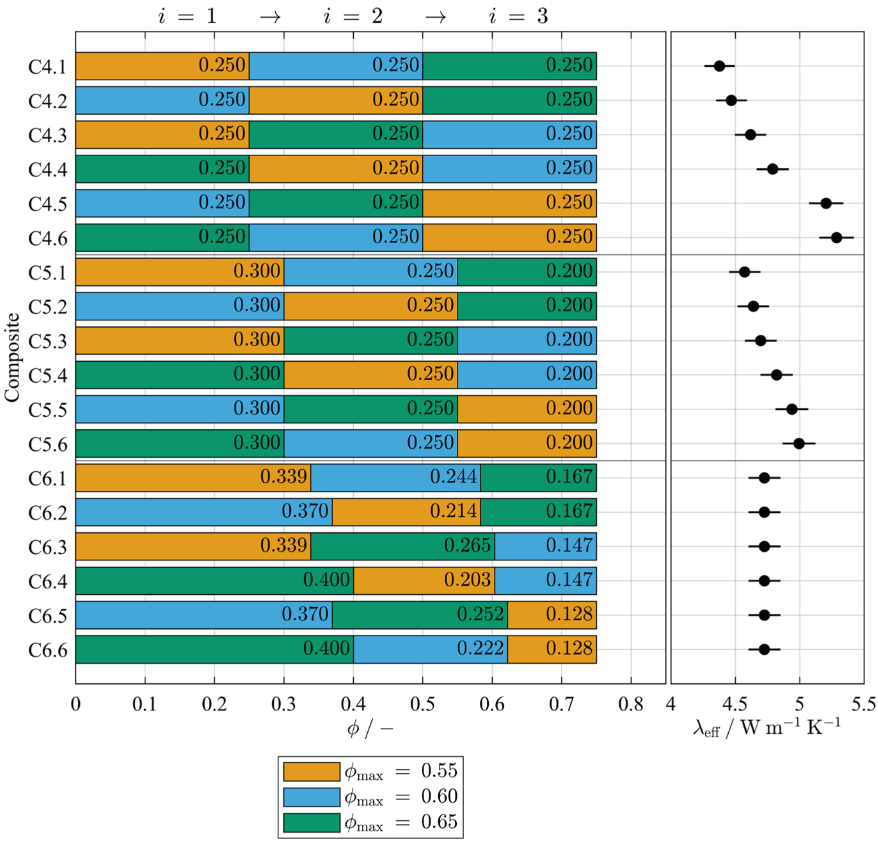

Figure 5.11. Results of simulative composition series C4, C5, and C6.
Filler content and calculated effective thermal conductivity of 18 composites. Polymer: $\lambda_C = 0.25$ W m^{-1} K^{-1} (e.g., epoxy). Fillers: $D_1 = 100$ µm, $D_2 = 10$ µm, $D_3 = 1$ µm, $\lambda_D = 35$ W m^{-1} K^{-1} (e.g., alumina). Varying maximum packing density of the individual fractions. Error bars represent the 3σ margin, corresponding to the 99.7 % confidence interval, estimated as described in section 5.1.2.

A polymer with $\lambda_C = 0.25$ W m^{-1} K^{-1} is studied with different ternary filler blends, with a constant total filler volume fraction of $\phi = 0.75$. For all filler fractions, $\lambda_D = 35$ W m^{-1} K^{-1} is defined. Maximum packing densities of $\phi_{\text{max,A}} = 0.55$, $\phi_{\text{max,B}} = 0.60$, and $\phi_{\text{max,C}} = 0.65$ are defined in the individual fractions and varied systematically. The modeled differences in maximum packing density may be influenced by the particle morphology, the particle size distribution, or simply the compactability of the fillers. Modeling and calculations are carried out using simple filler packings of equally sized spheres with $D_1 = 100$ µm, $D_2 = 10$ µm, and $D_3 = 1$ µm. The calculation results were normalized and converted to the desired maximum packing density for the respective calculations. In composition series C4, the filler blend consists of equal parts of the coarse-grained, medium-grained, and fine-grained fractions. In composition series C5, the parts of the largest fractions are increased and those of the smallest fractions reduced.

The blend thus tends towards packing structures according to [177,178,182,292]. The composites in composition series C6 are adjusted so that all fillers in their respective fractions have the same filler loading level Φ. While the calculated effective thermal conductivities are all identical in this case ($\lambda_{\text{eff}} = 4.73\ \mathrm{W\ m^{-1}\ K^{-1}}$), the results of composition series C4 and C5 show distinct differences. In composition series C4, the lowest effective thermal conductivity is $\lambda_{\text{eff}} = 4.38\ \mathrm{W\ m^{-1}\ K^{-1}}$ for composite C4.1, while the highest effective thermal conductivity is $\lambda_{\text{eff}} = 5.29\ \mathrm{W\ m^{-1}\ K^{-1}}$ for composite C4.6. This corresponds to an increase of approximately $21\ \%$. The results of composition series C5 show similar relationships, but less pronounced. Here, the minimum effective thermal conductivity of composite C5.1 with $\lambda_{\text{eff}} = 4.57\ \mathrm{W\ m^{-1}\ K^{-1}}$ and the maximum effective thermal conductivity of composite C5.6 with $\lambda_{\text{eff}} = 5.00\ \mathrm{W\ m^{-1}\ K^{-1}}$ are more similar.

The effect can be explained by the significantly different filler loading levels in the individual fractions. With identical filler volume fractions in all fractions, the relative filler volume fraction ϕ^{r} and thus the filler loading level, are generally highest in the finest fraction. A low maximum packing density in this fraction intensifies the effect and causes a significant increase in the thermal conductivity of this fine-grained fraction. Shifting the filler proportions to composition series C5 dampens the effect, and the further shift to study C6 completely compensates for it. Therefore, the mixture proportions are a crucial element when composing a multi-scale filler blend. The rheological effects of a filler blend must be accounted for as well when dealing with explicit product development. General guidelines are provided in [291,292]. But from a purely thermal point of view, we can conclude:

If the respective filler loading levels are the same in all fractions, the choice of fillers for the respective fractions is irrelevant (C6). If, in the other limiting case, all fractions contain identical absolute filler volume fractions (C4), the highest effective thermal conductivities can be achieved if fillers with higher maximum packing densities are used in the coarse-grained fractions and fillers with lower maximum packing densities are used in the finer fractions. This behavior can be easily interpreted using the multi-step homogenization approach described in chapter 5.1, as well as the main findings about single-scale filled polymers, summarized in chapter 4.6. Each fraction contributes multiplicatively to the overall increase in effective thermal conductivity. The higher the filler loading level of a given fraction, the more efficient it can form heat-conducting paths, and thus the greater its contribution. Filler loading level increases with higher relative volume fractions or lower maximum packing densities. Except for series C6, finer fractions typically have higher relative filler content due to the space occupied by coarser fillers. If a filler with a low maximum packing density is used in these fine fractions, this amplifies the effect, leading to a stronger increase in filler loading and a higher contribution to thermal conductivity. As a result, the overall effective thermal conductivity of the composite is significantly improved.

5.4 EFFECT OF THE FILLERS' THERMAL CONDUCTIVITIES

The investigation of single-scale filled polymers in chapter 4.4 has shown that the thermal filler properties are only of minor importance in the cases considered within this work. Even with moderate TC ratios of $\kappa \approx 100$, there is a saturation occurring and beyond that, the thermal conductivity of the filler no longer has a noticeable effect. However, the experimental composition series C2 and C3, shown in **Figure 5.10**, page 158, indicate that this finding cannot be directly transferred to multi-scale filled polymers. The replacement of the fillers in the medium and fine-grained fractions causes a significant change in the effective thermal conductivity, although the utilized fillers are both already above the saturation limit.

In the practical application of thermally conductive filled polymers, there are many reasons for using and combining different fillers. From a purely thermal point of view, the first choice is always clearly the filler with the highest thermal conductivity. Reasons for addition of thermally non-optimal fillers could be price, individual effects on viscosity, electrical insulation effects, density for lightweight construction applications, chemical compatibility with the polymer base, sedimentation-inhibiting effects, or a demand for flame-retardant effects.

For the case where fillers varying in thermal conductivity must be combined, it is crucial to know the appropriate fractions for the filler materials to achieve the highest possible effective thermal conductivity. In a simulative study in this chapter, the effect of the fillers' thermal conductivities on the effective thermal conductivity of a multi-scale filled polymer is investigated in isolation. The aim is to understand how different fillers interact in multi-scale blends and whether there is potential for optimization from a thermal point of view.

Composition series C7 and C8 consider different ternary mixtures consisting of fillers with different thermal conductivities and different sizes, but otherwise identical. The fictitious polymer under consideration has $\lambda_\mathrm{C} = 0.25\ \mathrm{W\ m^{-1}\ K^{-1}}$ and a total filler volume fraction of $\phi = 0.75$ is set. Each of the three size fractions consists of equally sized spherical particles, arranged in a random medium dense packing, with a maximum packing density of $\phi_{\mathrm{max},1} = \phi_{\mathrm{max},2} = \phi_{\mathrm{max},3} = 0.61$. The particle sizes are defined as $D_1 = 100\ \mu\mathrm{m}$, $D_2 = 10\ \mu\mathrm{m}$, and $D_3 = 1\ \mu\mathrm{m}$.

For the three different filler fractions, the thermal conductivities specified are

- $\lambda_{\mathrm{D,A}} = 10\ \mathrm{W\ m^{-1}\ K^{-1}}$ for a class I filler such as aluminum hydroxide $Al(OH)_3$,
- $\lambda_{\mathrm{D,B}} = 35\ \mathrm{W\ m^{-1}\ K^{-1}}$ for a class II filler such as alumina Al_2O_3, and
- $\lambda_{\mathrm{D,C}} = 150\ \mathrm{W\ m^{-1}\ K^{-1}}$ for a class III filler such as an aluminum alloy or aluminum nitride AlN.

The TC ratios, based on $\lambda_{\mathrm{C}} = 0.25\ \mathrm{W\ m^{-1}\ K^{-1}}$ are $\kappa_{\mathrm{A}} = 40$, $\kappa_{\mathrm{B}} = 140$, and $\kappa_{\mathrm{C}} = 600$. While κ_{A} is still well below the saturation limit of $\kappa \approx 100$, κ_{B} is slightly above, and κ_{C} is well above. In the composition series C7 and C8, each of the filler thermal conductivities is assigned to a size fraction and possible combinations are tested sequentially.

In composition series C7, equal filler volume fractions $\phi_1 = \phi_2 = \phi_3 = \phi/3 = 0.25$ and thus equal proportions are set in all fractions. Identical relative filler volume fractions $\phi_1^{\mathrm{r}} = \phi_2^{\mathrm{r}} = \phi_3^{\mathrm{r}}$ and thus equal filler loading levels $\Phi_1^{\mathrm{r}} = \Phi_2^{\mathrm{r}} = \Phi_3^{\mathrm{r}}$ are set in composition series C8. For a total filler volume fraction of $\phi = 0.75$, this results in $\phi_1 = 0.370$, $\phi_2 = 0.233$, and $\phi_3 = 0.147$. **Figure 5.12** shows the results of composition series C7 and C8. The calculated thermal conductivities range from $3.52\ \mathrm{W\ m^{-1}\ K^{-1}}$ for composite C8.1 to $4.84\ \mathrm{W\ m^{-1}\ K^{-1}}$ for composite C8.6. This corresponds to an increase of approximately $38\ \%$.

The results of both composition series are qualitatively the same, but the differences between the composites are more pronounced within series C8. If the more conductive fillers are used in the coarser fractions and the less conductive ones in the finer fractions, higher effective thermal conductivities are achieved than the other way round. In the composites with the lowest effective thermal conductivities C7.1 and C8.1, the fillers are used in fractions $i = 1$ to $i = 3$ with increasing thermal conductivity. The most conductive filler is present in the fine-grained fraction. The exact opposite is true for the most thermally conductive composites C7.6 and C8.6, where the highest thermally conductive individual filler is processed in the coarse-grained fraction and the lowest thermally conductive individual filler in the fine-grained fraction. This effect is much more pronounced with C8, which is due to a shift in the mixing ratio towards a higher proportion of the most conductive filler, which increases its impact.

The interpretation is most effectively framed using the multi-step homogenization approach introduced in chapter 5.1, which remains valid regardless of the number of fractions considered. This method starts with the finest fraction, which is always dispersed in the pure polymer matrix, exhibiting the behavior outlined in chapter 4.6, and limited by a saturation threshold of $\kappa \approx 100$.

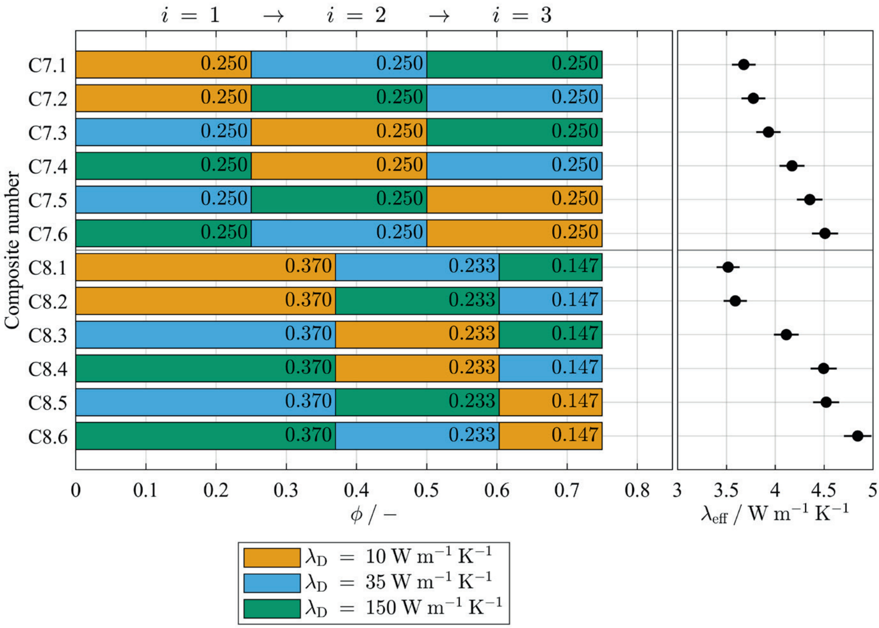

Figure 5.12. Results of simulative composition series C7 and C8.
Filler content and calculated effective thermal conductivity of twelve composites. Polymer: $\lambda_C = 0.25$ W m^{-1} K^{-1} (e.g., epoxy). Fillers: Equally sized spheres with $D_1 = 100$ µm, $D_2 = 10$ µm, $D_3 = 1$ µm, $\lambda_D = 35$ W m^{-1} K^{-1} (e.g., alumina). Packing structure in all fractions: RMP ($N = 5{,}000$), $\phi_{\max} = 0.61$. Varying thermal conductivity of the filler fractions. Error bars represent the 3σ margin, corresponding to the 99.7 % confidence interval, estimated as described in section 5.1.2.

Each subsequent coarser fraction is then dispersed into an increasingly homogenized and thermally enhanced phase, which is influenced by the preceding finer fractions. With each step, the thermal conductivity of the continuous phase increases, which in turn lowers the TC ratio κ for the next filler. This cascade effect makes the system increasingly responsive to higher filler conductivities. The thermal conductivity magnification Λ increases monotonically with the TC ratio κ but with continuously diminishing slope, see **Figure 4.37**, page 136. This explanation therefore applies regardless of the original TC ratio κ or the number of fractions n in the mixture. This is a very important finding that could not be fully substantiated by purely experimental studies. The experimental composition series C2 and C3 indicated such an effect, but the simulative composition series C7 and C8 along with the general interpretation were able to isolate and fully confirm it. This study results in valuable basic knowledge that provides a basis for the more targeted selection of fillers for multi-scale blends.

5.5 CHAPTER SUMMARY AND CONCLUSION

Chapter 5 began with the presentation of a new multi-scale homogenization approach for the calculation of the effective thermal conductivity of multi-scale filled polymers. It is based on the microscale simulation models from chapter 4.1 and the superposition of the thermal conductivity magnifications of all filler fractions in multi-scale filler blends. Comprehensive experimental validation has shown that the calculation approach is suitable for accelerating explicit product development as well as for fundamental studies on individual filler properties. Furthermore, experimental and simulative studies on filler blend compositions were presented and there was a detailed discussion of the resulting findings about the interactions of different fillers in multi-scale filler blends.

The various microstructural effects caused by particle morphology, particle size distribution, and packing compaction, initially discussed in chapter 4, were summarized in the maximum packing density of the individual fractions and investigated together. If the filler proportions are adjusted so that all fractions have the same filler loading level, then the filler composition is irrelevant. In all other cases, it has been shown that it is advantageous to use fillers with a lower maximum packing density in the finest fraction and a higher maximum packing density in the coarser-grained fractions. After it was established in chapter 4.4 that the filler's thermal conductivity often has no major effect on the effective thermal conductivity of single-scale filled polymers, the studies in chapter 5.4 have shown that there are indeed relevant effects in multi-scale filled polymers. Fillers with a TC ratio of $\kappa > 100$ that are already above their individual saturation limit can exploit their thermal performance in multi-scale filled polymers if they are used in the coarse-grained fraction.

As a basic rule, it can be deduced that fillers with higher thermal conductivity should always be used in the coarser-grained fractions if the aim is to increase the effective thermal conductivity. The finer-grained fractions increase the thermal conductivity of the continuous phase, which is present for the coarse-grained fractions, thus shifting the saturation limit towards higher TC ratios.

The proposed homogenization approach has proven to be widely applicable as it has been successfully tested on a variety of material combinations. However, it cannot be considered universally valid as it is based on numerous modeling assumptions that lack a general theoretical justification and may not be transferable to all systems. Consequently, the findings from this study apply primarily to the specific material combinations investigated. Nevertheless, these findings are logically derived from the calculation strategy itself, and for any material system where the assumptions of the model are valid, the observed effects are also to be expected.

6 THERMAL TRANSFER FROM FILLED POLYMERS TO SOLID SUBSTRATES

This chapter shifts the focus from the bulk thermal conductivity of particle-filled polymers to the study of filled polymer to substrate transitions (FPS transitions). The quantity of interest is the thermal contact resistance, as shown in **Figure 2.3**, page 18. Although thermal contact resistance plays a critical role in applications with thermal interface materials (TIM) and insulated metal substrates (IMS) [5,8–10,159–161], only a few studies (e.g., [159,161,213]) have so far investigated these resistances experimentally. Generally, macroscopic approximations have been used, as described in sections 3.2.7, 3.3.1, and 3.3.6. A detailed understanding of the heat transfer mechanisms governed by the microscopic material and packing structure at FPS transitions is still missing.

The experimental (chapter 3.3) and simulation methods (chapter 4.1) developed within this work allow a detailed analysis of heat conduction through filled polymers at the microscale. This chapter presents a first step in applying these new methods to FPS transitions and analyzing the microscopic origins of thermal contact resistance.

Chapter 6.1 presents the extension of the microscale simulation approach to FPS transitions. The concept of equivalent thermal height and the definition of geometric and thermal boundary layers are introduced in chapters 6.2 and 6.3. In chapter 6.4, these concepts are used to study the effects of the microscale packing and substrate structure for selected examples and model systems. In this work, only a limited parameter space can be systematically explored. However, the studies reveal systematic trends and allow to identify key parameters. Chapter 6.5 deals with the effects of the components' thermal conductivities. Specific aspects of very thin material layers, such as those used in IMS, are considered in chapter 6.6. Finally, the results are summarized in chapter 6.7.

6.1 ASSESSING THE PHENOMENON WITH MICROSCALE SIMULATIONS

In chapter 4 it has been shown that heat conduction in filled polymers can be modeled very well in microstructure simulations and that reliable quantitative predictions of the effective thermal conductivity are possible. The following sections describe how the simulation technique developed for this purpose is adapted for the investigation of FPS transitions. The discussions address only changes and special considerations. All other steps are identical to those outlined in chapter 4.1.

6.1.1 MICROSTRUCTURE MODELING

To simulate thermal transfer between a filled polymer and a substrate surface, a representative volume element (RVE) must be modeled containing a section of a substrate surface and the adjacent filler packing. The approach should allow both the representation of real materials and structures, as well as the generation of artificial models for fundamental parametric studies. In the first step, the height profile $z(x, y)$ is required for the substrate surface to be represented. This can be derived from one of the laser-microscopically digitized surface data sets of the physically present substrates described in section 3.1.3. Alternatively, artificial surface structures are generated using the MATLAB® code provided by Kanafi [302]. **Figure 6.1** shows an artificially generated surface with a root mean square roughness $S_\mathrm{q} = 1.0\ \mathrm{\mu m}$, and the corresponding surface roughness power spectrum $C(q_\mathrm{w})$, with q_w being the wave vector (magnitude). The surface roughness power spectrum $C(q_\mathrm{w})$ quantifies the contributions of different spatial frequencies to the overall roughness characteristics. A comprehensive discussion of the definition and the calculation formalism can be found in [196]. A roll-off wavevector $q_\mathrm{w,r} = 6 \cdot 10^5\ \mathrm{m}^{-1}$ was set for modeling, below which $C(q_\mathrm{w})$ remains approximately constant. The generated surface shown in part (a) has a size of $300 \times 300\ \mathrm{\mu m}^2$. It has periodic boundaries and can be repeated as often as required to enlarge it. The autocorrelation length is $5.43\ \mathrm{\mu m}$, and the skewness is zero. This surface structure is used in most of the following simulative studies. It qualitatively represents a typical roughness spectrum found in many technical surfaces [196]. By reusing the same randomly generated surface structure, stochastic variations that would arise from generating a new surface each time are minimized. This enables a focus on systematic changes during the analyses of the simulations, where the absolute roughness level is set by scaling the data set in the z direction, and the autocorrelation length is modified by scaling the data set along the x and y directions. The following modeling process is the same, whether using measured surface data or artificially generated datasets.

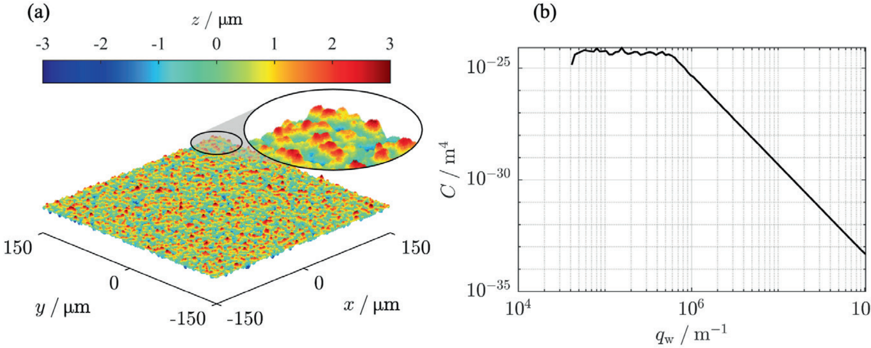

Figure 6.1. Artificial random rough surfaces and corresponding roughness power spectrum. 3D illustration of random rough surface, generated with the MATLAB® code provided by Kanafi [302] in (a). $S_\mathrm{q} = 1.0\ \mathrm{\mu m}$. Surface roughness power spectrum in (b).

Figure 6.2 visualizes the modeling process of the microstructure in RVEs, based on an arbitrary substrate surface. For the sake of simplicity, only two-dimensional sections are shown; however, the actual process is three-dimensional. MATLAB® is also used for implementation here. Cube-shaped RVEs with a case-dependent size $\Delta x = \Delta y = \Delta z$ are modeled, see part (a) of **Figure 6.2**. The heat flow is modeled from z_{max} to z_{min}. The substrate surface is placed in between, at $z_{\mathrm{min}} + 0.25\ \Delta z = 0$, using the arithmetic mean value

$$z_{\mathrm{a}} = \frac{1}{A} \iint_{\tilde{A}} z(x, y)\ \mathrm{d}x\mathrm{d}y\ . \tag{6.1}$$

of the height values $z(x, y)$ as reference for $z = 0$. If only the thermal transfer from an unfilled polymer to a substrate is to be simulated, the modeling process is complete at this point. To describe an FPS transition, the modeling of the adjacent filler packing follows, see parts (b) - (e) of **Figure 6.2**. In this example, particles are shown as equally sized spheres to simplify the explanation of the process.

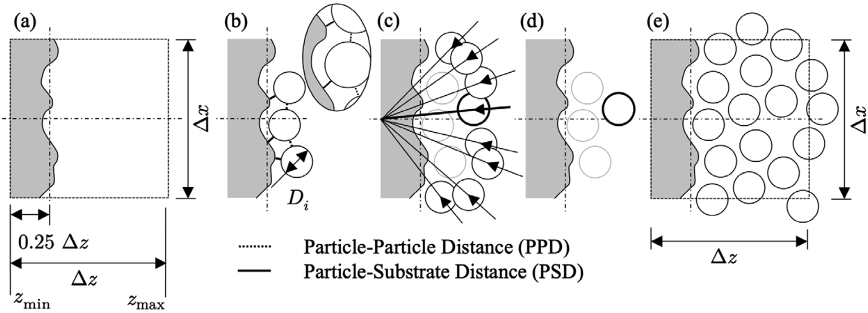

Figure 6.2. Schematic illustration of microstructure modeling process.
Simplified 2D illustration of the modeling process, carried out in three dimensions. Positioning of the substrate surface in (a). Modeling of the adjacent filler packing in (b) – (e).

The spherical growth procedure from section 4.1.2 is adapted and modified for this application. The seed point of the packing modeling is located centrally below the substrate surface at $z = z_{\mathrm{min}}$, see part (c) of **Figure 6.2**. The filler packing is generated from this point, i.e., growing from the substrate surface in z direction. If the filler packing grows towards the surface, it is difficult to control the remaining gaps and particle-substrate distances (PSDs). In contrast to the spherical growth procedure in section 4.1.2, the particles are not positioned in direct contact, but with a pre-defined minimum particle-particle distance (PPD) and a pre-defined minimum PSD, see part (b) of **Figure 6.2**. An expansion of the filler packing to adjust the filler volume fraction is not feasible, as it would alter the relative positioning between particles and the substrate surface. The packings must be modeled directly with the desired filler volume fraction, and this is set using the PPD. Apart from this, the packing modeling process is similar to the spherical growth procedure from section 4.1.2. For each particle, N possible positions are explored in random spatial directions and the position closest to the seed point is selected, see parts (c) and (d). The process is repeated until no more particles can be positioned within the RVE. Particles at the RVE boundaries are modeled with overlap and are cut off during the meshing process, see part (d). The algorithm must be slightly modified for modeling close-to-surface particle packings. Instead of starting the search for new positions at the seed point and moving the particles outwards step by step, as in **Figure 4.1**, page 83, the search for new possible particle positions is started outside the already generated filler packing and the particles are moved step by step towards the seed point. Therefore, they approach the particle packing from the outside, see part (c). The new possible particle position is the last possible position before the minimum distance to the substrate or other particles is exceeded. When modeling filler packings with equally sized spheres, this reversal of the procedure has no advantage. However, if fillers with a size distribution are modeled, this procedure avoids the excessive accumulation of fine-grained particles directly on the substrate surface in the gaps that remain between the larger particles. The resulting packing would otherwise have a locally variable particle size distribution. By reversing the procedure as described, it is possible to produce filler packings with a homogeneous size distribution. It can be assumed that the method avoids undesired microstructural ordering, as particles are placed in sequential batches of 20, each randomly selected to match the intended size distribution. With a total of more than $1{,}000$ particles positioned, statistical uniformity is further ensured.

The observations in chapter 4 have shown that modeling homogeneous packings with constant particle-particle distances leads to reliable results. Therefore, FPS transitions are also modeled with a constant particle-particle distance (PPD). However, particle-substrate distances (PSDs) naturally have a significant influence on the thermal resistance of the boundary layer. When all boundary particles are in direct contact with the substrate, efficient local heat conducting paths are formed, resulting in reduced thermal contact resistance. If thin polymer layers remain between the particles and the substrate, the thermal resistance increases. The effect of the particle arrangement close to the surface is discussed in chapter 6.4. All other models are based on the simplified assumption that the PSDs correspond to the PPDs. This leads to a very homogeneous particle distribution and assumes an equilibrium state in which all polymer layers have the same thickness. This reflects a case in which all interaction forces between substrate, polymer and particles are of equal magnitude and no external forces act, for example, to push the first particle layers towards the substrate surface. In a $\phi_{\max}$ configuration within the bulk region, all particles are in contact not only with their neighbors but also with the substrate. For all filler volume fractions $\phi < \phi_{\max}$, however, there is no longer any particle-substrate contact.

Unlike the simulations of effective thermal conductivity, the studies in this chapter focus on a local phenomenon directly at the substrate surface. To capture sufficient randomness, the RVE must be modeled significantly larger for this purpose. An RVE size of $9 \times D_{50}$ has been found to be a good compromise between the smallest possible RVE for high local resolution and a sufficiently large RVE for reproducible modeling of the stochastic contact phenomenon directly at the substrate surface. The stochastic variation is already partially limited by the constant surface structure. Nevertheless, repeated modeling of the adjacent particle packing leads to variations and locally random structures. Consequently, variations of up to $10\ \%$ can occur between identically configured simulations. Further details on simulation reproducibility are provided in section 6.3, and local variations are discussed in section 6.4.4.

The given RVE size refers to the $\phi_{\max}$ configuration. For smaller ϕ, and thus increasing particle distances, the modeled RVE size increases accordingly. **Figure 6.3** shows exemplary cross-sections through modeled RVEs with a transition zone between filled polymers with different filler volume fractions, and solid substrates. Central cross-sections of the RVE are shown. Unlike in chapter 4.1, this is not a single packing configuration that is modified by expansion to different filler volume fractions. Instead, each RVE is modeled separately with an individual PPD and PSD configuration. The $\phi_{\max}$ configuration is modeled in an RVE with $\Delta x_{\mathrm{m}} = \Delta y_{\mathrm{m}} = \Delta z_{\mathrm{m}} = 90\ \mu\mathrm{m}$. $\phi_{\max} = 0.55$ in the bulk region is reached with $N = 500$.

The other RVEs are based on a gradual increase of PPD and PSD up to $0.7 \times D$. At the same time, there are adjustments in the size of the RVEs. With a PPD of $0.7 \times D$, the RVE is $\Delta x = \Delta y = \Delta z = 153\ \mu\mathrm{m}$ in size. The filler volume fraction is $\phi = 0.24$. The investigations in this work are limited to composites with spherical particles.

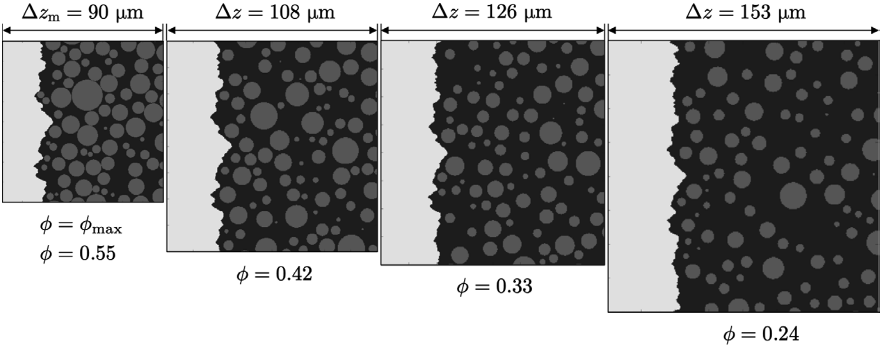

Figure 6.3. Modeled FPS transitions with varying filler volume fractions.

Cross-sections of RVEs with different filler volume fractions starting at the maximum packing density of $\phi = \phi_{\max} = 0.55$, ending at $\phi = 0.24$. RLP of spherical particles with log-normal size distribution with log $(\sigma) = 0.2$ and $D_{50} = 10\ \mu\mathrm{m}$. Substrate surface: Artificial random rough surface from **Figure 6.1**.

Figure 6.4 summarizes the input parameters of the modeling process and shows examples of modeled RVEs with FPS transitions. Parts (a) and (b) show modeled filler packings with equally sized, spherical particles in a packing close to an ideally flat substrate surface. Part (a) shows a packing in $\phi_{\max}$ configuration with $\phi_{\max} = 0.55$ in the bulk region. In (b), the filler volume fraction in the bulk region is $\phi = 0.24$. Part (c) shows a modeled filler packing of spheres with a log-normal size distribution and $\log(\sigma) = 0.2$. It is also a $\phi_{\max}$ configuration with $\phi_{\max} = 0.55$, close to an ideally flat substrate surface. The model in (d) differs only in the surface characteristics, as an artificial rough surface is modeled.

The microstructure modeling process is based on particle size distribution and surface data input. They can be defined artificially or based on experimental input to represent real materials, see chapter 6.4.

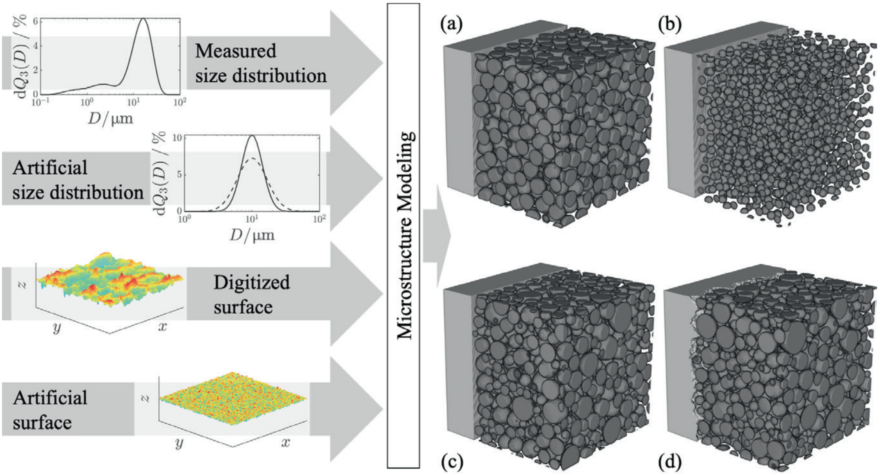

Figure 6.4. Microstructure modeling input data and results.
Exemplary images of modeled RVEs with FPS transitions. Random loose packing (RLP) of equally sized spheres with $\phi_{\max} = 0.55$ and ideally flat substrate surface in (a). RLP of equally sized spheres with $\phi = 0.24$ and ideally flat substrate surface in (b). RLP of spherical particles ($\log(\sigma) = 0.2$) with $\phi_{\max} = 0.55$ and ideally flat substrate surface in (c). RLP of spherical particles ($\log(\sigma) = 0.2$) with $\phi_{\max} = 0.55$ and a substrate with artificial random rough surface in (d).

6.1.2 COMPUTATION OF MICROSCALE HEAT CONDUCTION

After modeling the microstructure in the RVEs has been completed, the actual calculation of heat conduction is carried out, analogous to the procedure in section 4.1.4. The RVEs are meshed and boundary conditions for steady-state, one-dimensional heat conduction are defined. Once again, a structured mesh with equally sized cube-shaped mesh cells is used. All RVEs are meshed with $n = n_x = n_y = n_z = 300$. This limits both the resolution of the packing and surface structure, as well as the maximum size of the RVEs. An initial test has shown that $n = n_x = n_y = n_z = 300$ is sufficient to adequately resolve RVEs with up to $9 \times D_{50}$. Compared to the simulations of the effective thermal conductivity in chapter 4.1, slightly larger systematic errors are tolerated here. This is justified by the different objective of the current analysis, which focuses on qualitative investigations of the microstructural impacts on the thermal contact resistance at FPS junctions and not on precise quantitative predictions. Due to the coarser mesh resolution and the lack of a dynamic meshing scheme as in section 4.1.5, it must be assumed that mesh-related artifacts can occur at high filler concentrations, such as the artificial fusing of neighboring particles, leading to a local overestimation of the effective thermal conductivity. The exact extent cannot be quantified generally but is considered tolerable in the context of the study's objectives.

The particle packing is meshed in the same way as described in section 4.1.4. For the solid substrate volume, an addition is implemented in the meshing algorithm that checks all mesh cells for whether they lie below the specified substrate surface and, if so, defines the substrate thermal conductivity λ_{S}. The consideration of thermal interfacial resistances is omitted, as section 4.4.3 has shown that these resistances have a minimal impact for particles larger than 1 $\mu\mathrm{m}$. Again, a heat flow is modeled from $z_{\max}$ to $z_{\min}$. For this purpose, a steady-state temperature difference with

- $T(z_{\min}) = 293$ K, and
- $T(z_{\max}) = 353$ K

is applied to the RVE, see **Figure 4.9**, page 94. All other outer surfaces of the RVE are modeled adiabatically. The finite volume method (FVM) algorithm is applied, as described in section 4.1.4. A new convergence criterion must be defined for the simulations to investigate heat conduction through FPS transitions. In the simulations described in chapter 4.1, the residual of the effective thermal conductivity was used for this purpose. Since the effective thermal conductivity is determined as a global average, it compensates for inhomogeneities and local residual errors. For the simulations of FPS transitions, it is essential to fully converge the high temperature gradients near the substrate to obtain reliable results. When a temperature difference is applied, the result is a heat flow. This must be the same in all mesh layers along the heat flow direction to maintain the energy balance. The coefficient of variation of the heat flux according to

$$v_q = \frac{\sigma_q}{\bar{q}_z} = \sqrt{\frac{\sum_{i=1}^{n_z} (q_{z,i} - \bar{q}_z)^2}{n_z - 1}} \frac{1}{\bar{q}_z}. \qquad \textbf{(6.2)}$$

has shown to provide a robust measure for assessing convergence. $q_{z,i}$ is the z direction heat flux in the mesh layer i, calculated across all mesh cells of the layer, and $\bar{q}_z$ is the average of all z direction heat fluxes. A threshold of $v_q \leq 0.001$ is set, which was determined as part of a convergence study. The higher temperature gradients in these simulations require systematically more iterations, between 2 and 4 million in total.

6.1.3 EVALUATIONS

Spatial information about the RVE and converged temperature fields are used to evaluate heat conduction across the FPS transitions and to calculate thermal contact resistances. **Figure 6.5** shows an exemplary evaluation of a calculated RVE with an ideally smooth substrate surface and a filled polymer with a log-normal size distribution of spherical filler particles. Part (a) shows a central cross-section through the microstructure of the RVE with the substrate surface located at $z = 0$. Part (b) presents the steady-state heat flux field in the same cross-section, indicating the formation of good heat-conducting paths and the concentration of heat flows at the points of particle-particle and particle-substrate proximity. As a result, a clearly inhomogeneous heat flux field is observed in the first substrate layers directly below $z = 0$, which only becomes homogenized after a certain depth into the substrate due to its spreading effect. Part (c) shows the respective steady-state temperature field. The substrate volume is almost uniform in temperature and the volume of the filled polymer has a highly inhomogeneous temperature field. Part (d) shows the mean temperature curve along the z axis. A visualization of the data points or discrete representation is omitted for reasons of clarity.

As described in section 4.1.4, a Dirichlet boundary condition for a sectional plane through a filled polymer is not physically correct. The upper boundary region of the RVE at z_{max} must therefore be excluded for further evaluations. The boundary level is marked by a vertical dashed line in part (d) of **Figure 6.5**. Furthermore, part (d) clearly shows that the majority of the temperature drop across the RVE occurs within the filled polymer. Due to the substrate's comparatively high thermal conductivity of $\lambda_{\mathrm{S}} = 130\ \mathrm{W\ m^{-1}\ K^{-1}}$, it has no significant contribution to the thermal resistance and thus temperature drop of the composite. At a sufficient distance from the substrate surface, there is an almost linear increase in temperature with the z coordinate, apart from stochastic variations. This indicates an almost constant thermal conductivity in the bulk material, see also **Figure 4.10**, page 97, **Figure 4.11**, page 98, or **Figure 4.12**, page 99. In the FPS transitions however, there is a clear deviation from this curve. This area is of particular interest in this chapter because thermal contact resistances act here. For further evaluation, the specific cumulative resistance curve along the z axis is determined from the calculated temperature curve $\bar{T}(z)$. Every small temperature difference $\mathrm{d}\bar{T}$ along a small distance $\mathrm{d}z$ is caused by a specific thermal resistance contribution $\mathrm{d}r$ of the investigated layer.

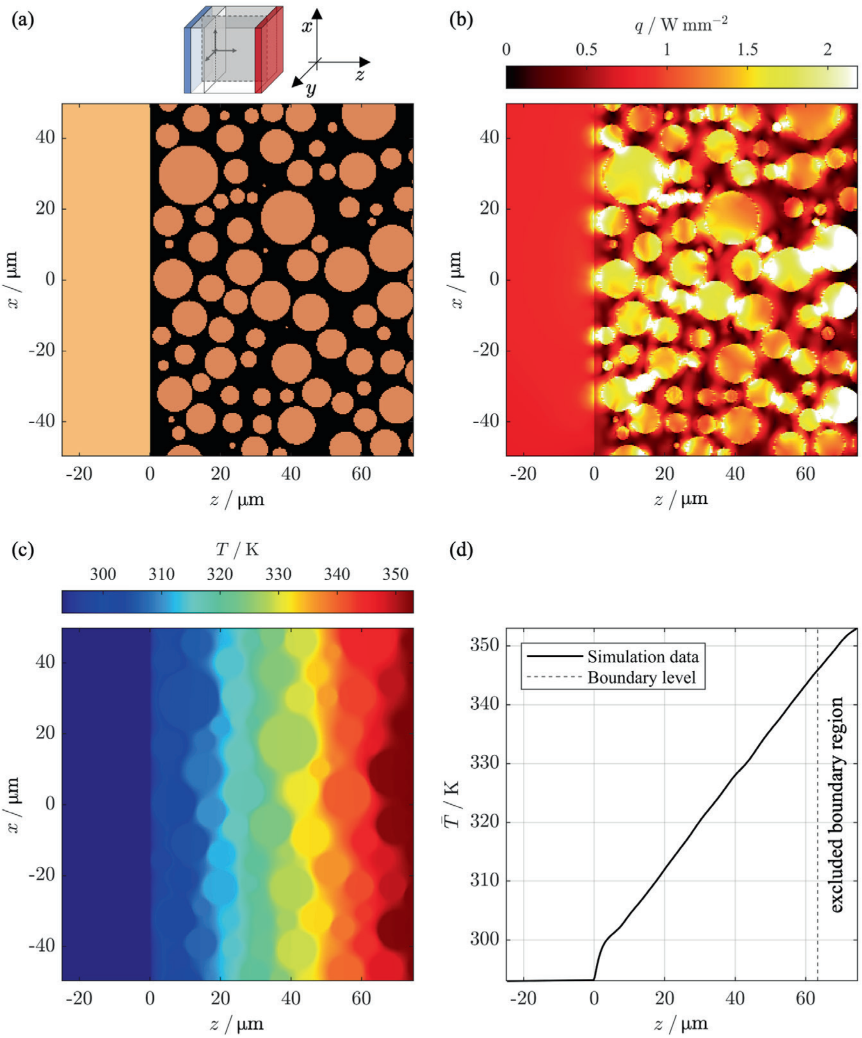

Figure 6.5. Results of microscale heat conduction simulation 4.

Central cross-sections of geometry (a), steady-state heat flux field (b), steady-state temperature field (c), and average temperature curve along heat flow direction (d). Polymer: $\lambda_C = 0.25$ W m^{-1} K^{-1} (e.g., epoxy). Filler: Spheres with log-normal size distribution with $\log(\sigma) = 0.2$, $D_{50} = 10$ µm, $\phi_{\max} = 0.55$, $\phi = 0.48$, $\lambda_D = 35$ W m^{-1} K^{-1} (e.g., alumina). Substrate: Ideally flat, $\lambda_S = 130$ W m^{-1} K^{-1} (e.g., aluminum alloy). Full surface wetting.

The specific local thermal resistance contribution can be formulated using the average heat flux $\bar{q}_z$ as

$$\frac{\mathrm{d}r}{\mathrm{d}z} = \frac{1}{\bar{q}_z}\frac{\mathrm{d}\bar{T}}{\mathrm{d}z} \; . \tag{6.3}$$

As with the micro thermography experiments in section 3.3.6, differential notation is used here for simplicity, even if only discrete temperature values are available in the resolution of the calculation mesh. With $r(z = z_{\mathrm{min}}) = 0$ and $\bar{q}_z = \mathrm{const.}$, the cumulative resistance curve can be expressed as

$$r(z) = \frac{1}{\bar{q}_z}\left(\bar{T}(z) - \bar{T}(z_{\mathrm{min}})\right) \; . \tag{6.4}$$

The result of the example in **Figure 6.5** is shown in **Figure 6.6**. Part (a) shows the complete cumulative specific resistance curve over the entire height of the RVE, and part (b) presents a magnified view of the actual FPS transition. Since the resistance contributions of the individual mesh layers are proportional to the temperature drop, the curve shown in (a) is qualitatively the same as the curve in part (d) of **Figure 6.5**. The total specific thermal resistance of the overall RVE with $\Delta z = 99$ µm is approx. 75 $\mathrm{mm^2\ K\ W^{-1}}$. The RVE can be divided into three sections along the z axis: Substrate, bulk, and a transition zone, which is called the boundary layer in the following.

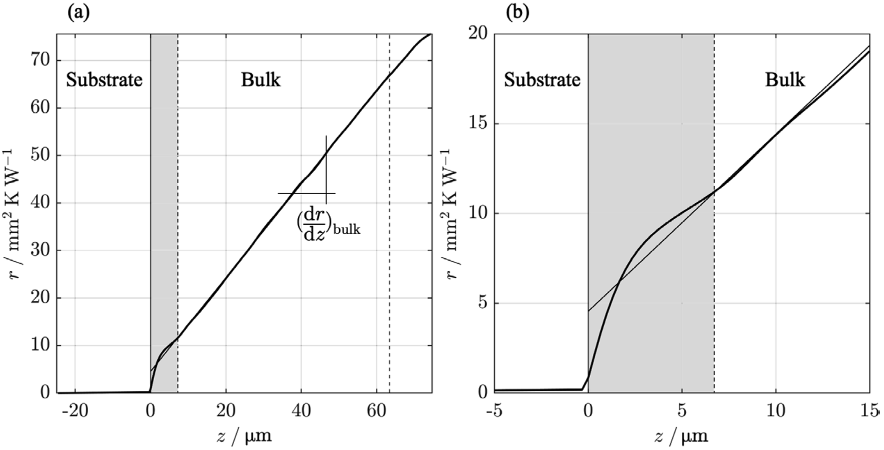

Figure 6.6. Cumulative thermal resistance curve across an FPS transition.
Illustration for the total simulated RVE in (a). Magnified view of the FPS transition in (b). Polymer: $\lambda_{\mathrm{C}} = 0.25$ W m^{-1} K^{-1} (e.g., epoxy). Filler: Spheres with log-normal size distribution with $\log(\sigma) = 0.2$, $D_{50} = 10$ µm, $\phi_{\mathrm{max}} = 0.55$, $\phi = 0.48$, $\lambda_{\mathrm{D}} = 35$ W m^{-1} K^{-1} (e.g., alumina). Substrate: Ideally flat, $\lambda_{\mathrm{S}} = 130$ W m^{-1} K^{-1} (e.g., aluminum alloy). Full surface wetting. $\lambda_{\mathrm{eff}} = 1.01$ W m^{-1} K^{-1}.

It is shaded in gray in **Figure 6.6**. At a sufficient distance of roughly 7 $\mu\mathrm{m}$ from the substrate surface, there is an approximately linear increase in specific thermal resistance with the z coordinate. This can be approximated by linear regression, and converted into the effective thermal conductivity of the filled polymer using

$$\lambda_{\text{eff}} = \overline{\left(\frac{\mathrm{d}r}{\mathrm{d}z}\right)^{-1}_{\text{bulk}}}. \tag{6.5}$$

In the example shown, this results in $\lambda_{\text{eff}} = 1.01$ W m^{-1} K^{-1}. The focus now shifts to the resistance contribution of the boundary layer, commonly referred to as thermal contact resistance on the macroscopic scale. In the example shown, it is approximately $10\ \mathrm{mm}^2\ \mathrm{K}\ \mathrm{W}^{-1}$ and thus of significant relevance. It is important to note that the contact resistance observed in this simulation is not caused by thermal interfacial resistances from an acoustic mismatch between materials or a resistance due to insufficient surface contact. Rather, it is just the disturbance of the microscopic filler packing by the substrate surface, leading to an increase in thermal resistance. This is a purely geometric, microstructural phenomenon, known as the wall effect in granular matter research [296,297,299].

For further evaluation, it is essential to clearly define and systematically evaluate the boundary layers and their thicknesses. A clear definition is crucial for isolating and quantifying the boundary layers' specific contribution to resistance. Chapter 6.3 deals with the question of defining this boundary layer and possible evaluation strategies for both micro thermography experiments and simulations. As a foundation, chapter 6.2 first considers the simpler case of heat transfer between unfilled polymers and substrate surfaces.

Furthermore, appendix D.2 provides a representative comparison between a simulated $r(z)$ curve across an FPS transition and one measured with micro thermography. Since the local microstructure of the sample is neither experimentally accessible nor theoretically predictable, the modeling is based on several assumptions and empirical adjustments to bring the simulation in line with the measurement. Nevertheless, simulation and experiment can be brought into good agreement, which confirms the fundamental suitability of both methods.

6.2 INTRODUCTORY INVESTIGATIONS WITH UNFILLED POLYMERS

Before returning to the topic of heat conduction across FPS transitions in the next chapter, this section presents basic considerations about heat transfer between unfilled polymers and substrate surfaces. The results provide an important foundation for the evaluation methods described in chapter 6.3. The transition from an ideally smooth substrate to a microscopically homogeneous unfilled polymer is thermally neutral, provided that thermal interfacial resistances can be neglected. There is a sharp transition in the temperature field between a substrate with high thermal conductivity and a polymer with lower thermal conductivity. However, if the substrate has a rough surface, then the expectation is a transition area of finite layer thickness. **Figure 6.7** shows the result of an exemplary simulation of heat conduction across an interface between a rough surface and a homogeneous polymer. A substrate with $\lambda_\mathrm{S} = 130\ \mathrm{W\ m^{-1}\ K^{-1}}$ (e.g., aluminum alloy) and with the artificially generated surface from **Figure 6.1**, scaled to $S_\mathrm{q} = 2.0\ \mathrm{\mu m}$ is modeled. For the polymer, $\lambda_\mathrm{C} = 0.25\ \mathrm{W\ m^{-1}\ K^{-1}}$ (e.g., epoxy) is set. The polymer completely wets the substrate surface in the model. Part (a) shows a central cross-section through the modeled RVE, where the substrate surface is located at $z = 0$, and aligned with its arithmetic mean height z_a. Part (b) shows the steady-state heat flux field in the same cross-section. While there is a homogeneous heat flux field at a sufficient distance from the interface, there is a strong concentration of heat flows on the asperities of the rough substrate. Even in the polymer layers just above the surface, a heat flow constriction and localization around these asperities can be detected.

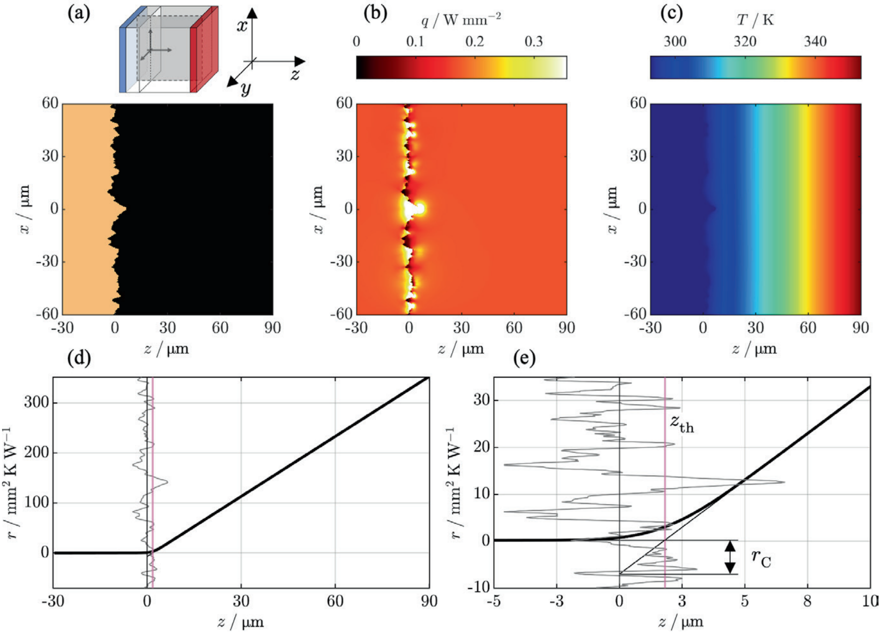

Figure 6.7. Evaluation of thermal transfer between an unfilled polymer and a rough substrate surface. Central cross-sections of geometry (a), steady-state heat flux field (b), and steady-state temperature field (c). Cumulative specific thermal resistance curves across the FPS transition at different magnification levels in parts (d) and (e). Polymer: $\lambda_\mathrm{C} = 0.25\ \mathrm{W\ m^{-1}\ K^{-1}}$ (e.g., epoxy). Substrate: Artificial random rough surface with $S_\mathrm{q} = 2.0\ \mathrm{\mu m}$, see **Figure 6.1**, $\lambda_\mathrm{S} = 130\ \mathrm{W\ m^{-1}\ K^{-1}}$ (e.g., aluminum alloy). Full surface wetting. Results: $r_\mathrm{C} = -7.24\ \mathrm{mm^2\ K\ W^{-1}}$, $z_\mathrm{th} = 1.81\ \mathrm{\mu m}$.

The substrate receives the main part of the heat flow via these paths of least resistance and then spreads it out again over the entire cross-sectional area just below the surface. The dark-colored polymer areas above the roughness valleys in the substrate play a minor role in heat conduction, as the parallel surface asperities protrude deep into the polymer layers providing paths of lower resistance. Part (c) shows the respective steady-state temperature field. Parts (d) and (e) present the evaluated cumulative thermal resistance curves across the interface at different levels of magnification. For orientation, the surface profile in the sectional plane shown in parts (a) - (c) is additionally illustrated in parts (d) and (e) in true z scale. Part (d) provides the complete cumulative thermal resistance curve over the entire height of the RVE, while part (e) shows a magnification on the layers of interest. The total specific thermal resistance of the overall RVE with $\Delta z = 120\ \mu\text{m}$ is approx. $350\ \text{mm}^2\ \text{K}\ \text{W}^{-1}$. The substrate with high thermal conductivity does not contribute significantly to the thermal resistance. In both regions, sufficiently far away from the interface, the cumulative thermal resistance curve is linear, as both material layers are modeled homogeneously. The evaluation of the thermal contact resistance is shown in simplified form in **Figure 6.8**. Part (a) shows the expected course of the cumulated specific thermal resistance $r(z)$ across an interface with an ideally smooth substrate and a sharp transition between the two materials, resulting in $r_\text{C} = 0$. Part (b) shows the course of the cumulative thermal resistance $r(z)$ across an interface with rough substrate surface and thus a similar curve as in the example shown in **Figure 6.7**. From a macroscopic point of view, it is reasonable to extrapolate the linear $r(z)$ curve from the polymer region to the virtual surface level $z = 0$. However, this results in a negative contact resistance r_C. In the example shown in **Figure 6.7**, r_C would be $-7.24\ \text{mm}^2\ \text{K}\ \text{W}^{-1}$.

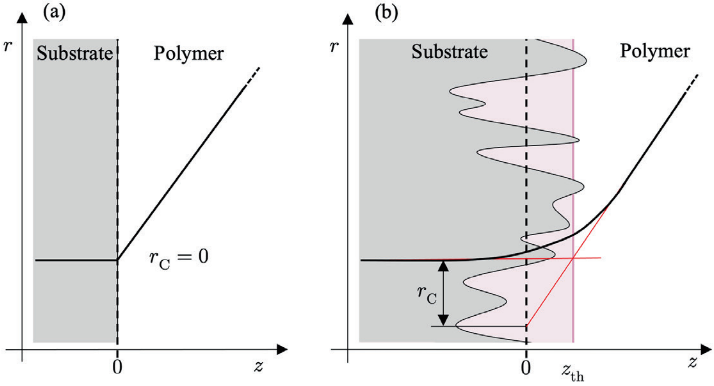

Figure 6.8. Illustration of cumulated specific thermal resistance across an unfilled polymer to substrate transition.

Interfaces with smooth substrate surface in (a) and with rough surface in (b). $\lambda_\text{S} \gg \lambda_\text{C}$.

The substrate-polymer interface with a rough surface exhibits a lower overall thermal resistance than an ideally smooth interface, as thermally effective surface asperities extend deep into the polymer. This effect persists as long as the substrate has a higher thermal conductivity than the polymer and the effect is not compensated by a strongly positive surface skewness S_{sk}. The height of the thermal contact resistance evaluated in this way depends largely on the definition of the $z = 0$ level. For a relevant evaluation, the microscopic surface level should be known. Unfortunately, this macroscopic surface level cannot be directly measured or evaluated for a microscopically rough surface, nor is it explicitly defined in surface characterization standards, e.g., DIN EN ISO 25178-2:2023-09 [195]. It likely falls between the arithmetic mean value of the surface profile and the maximum peak height but cannot be precisely determined. This challenge and the associated difficulties were already addressed in section 3.2.7, where the measurement of thermal contact resistance using the steady-state cylinder method was discussed, as well as in section 3.3.6, concerning the evaluation of micro thermography. Both experimental techniques require the determination of the $z = 0$ level. When the $z = 0$ level is measured on real samples, it depends on the contact pressure of the measuring tool, as surface asperities are deformed during the process. An optical measurement faces the same problem, as seen by the evaluation of simulated rough surface structures. This leads to the question of what a representative zero level is.

To address this, the concept of equivalent thermal height is proposed, which is intended to define the thermal zero level of a rough surface, based on its thermal effect. The equivalent thermal height z_{th} of a substrate-polymer interface is defined as the z coordinate at which the two linear thermal resistance curves, one from the substrate and one from the polymer layer, intersect, see part (b) of **Figure 6.8** and part (e) of **Figure 6.7**. Physically, z_{th} represents the position at which a theoretical, ideally smooth interface would need to be located in order to produce the same overall thermal resistance as the actual, rough interface under investigation. In this sense, z_{th} serves as a characteristic value that reflects the combined geometric and thermal behavior of the real interface. The interface studied in **Figure 6.7** provides an overall thermal resistance equal to that of an ideally smooth interface at $z_{\mathrm{th}} = 1.81\ \mu\mathrm{m}$. Positive values of z_{th} represent an interface with lower thermal resistance than an ideally smooth one and negative values of z_{th} represent an interface with higher thermal resistance. The relationship between equivalent thermal height and specific thermal contact resistance is given by

$$\frac{-r_{\mathrm{C}}}{z_{\mathrm{th}}} = \lambda_{\mathrm{C}}^{-1} - \lambda_{\mathrm{S}}^{-1}\ . \tag{6.6}$$

For the subsequent analyses of FPS transitions, the equivalent thermal heights provide a helpful starting point as they cover the effects of the pure substrate-polymer interface and thus allow a separation from the filler packing contributions.

Appendix D.1 provides supplementary simulation results on the effect of the surface structure on the expected thermal resistances and the equivalent thermal heights at interfaces between unfilled polymers and solid substrates. Also included are studies on the effect of incomplete surface wetting of the polymer on the substrate surface. However, as the micrographs of the samples prepared within the scope of this work showed no detectable air inclusions in the valleys of the substrate surfaces, complete surface wetting is continued to be assumed in all further studies.

6.3 DEFINITION OF THERMAL AND GEOMETRICAL BOUNDARY LAYER

After the previous chapter dealt with heat conduction across interfaces between unfilled polymers and substrate surfaces, this chapter introduces a novel concept for the evaluation of boundary layers at FPS transitions. As the exemplary simulation results in section 6.1.3 have already shown, it must be expected that the addition of a filler packing extends the thermal transition zone between the materials to a layer of significantly increased thickness. This increase results from the disturbance of the filler packing near the interface, which locally reduces the thermal conductivity of the filled polymer. Starting with the simplified case of an ideally smooth substrate surface, the simulation results already shown in **Figure 6.5**, page 174, are reassessed.

Figure 6.9 shows two different strategies for defining and analyzing the boundary layers. A spherical filler was modeled with log-normal size distribution and $\log(\sigma) = 0.2$. The volumetric median particle diameter is $D_{50} = 10\ \mu\mathrm{m}$. In parts (a) to (c), the central cross-sections of the geometry, the steady-state heat flux field, and the steady-state temperature field are shown analogous to **Figure 6.5**, page 174. In addition, parts (d) and (e) show the local filler volume fraction, and the cumulative specific thermal resistance for the range $-5\ \mu\mathrm{m} \le z \le +15\ \mu\mathrm{m}$. Part (e) is a magnified section of the results previously shown in **Figure 6.6**, page 175. It takes almost $5\ \mu\mathrm{m}$, about half the mean particle diameter, for the volume fraction of the filler to reach its plateau at the bulk level. This wall effect, which is a well-known geometric phenomenon commonly addressed in the analysis of granular materials and concrete mixtures [296,297,299], has already been described in section 5.1.3. It is the main reason for the steep initial increase in specific thermal resistance observed directly above the substrate at $z = 0$, before the curve changes to an almost linear trend in the undisturbed bulk region of the filled polymer. The boundary layers can now be defined and extracted based on either the geometric cause or the thermal effect. For the further use of the results and thermal design of FPS transitions, a purely thermal evaluation is more appropriate. For a systematic investigation of cause and effect, a geometric evaluation of the boundary layers seems more suitable. The following definitions apply in principle to both, micro thermography experiments and microscale simulations of FPS transitions.

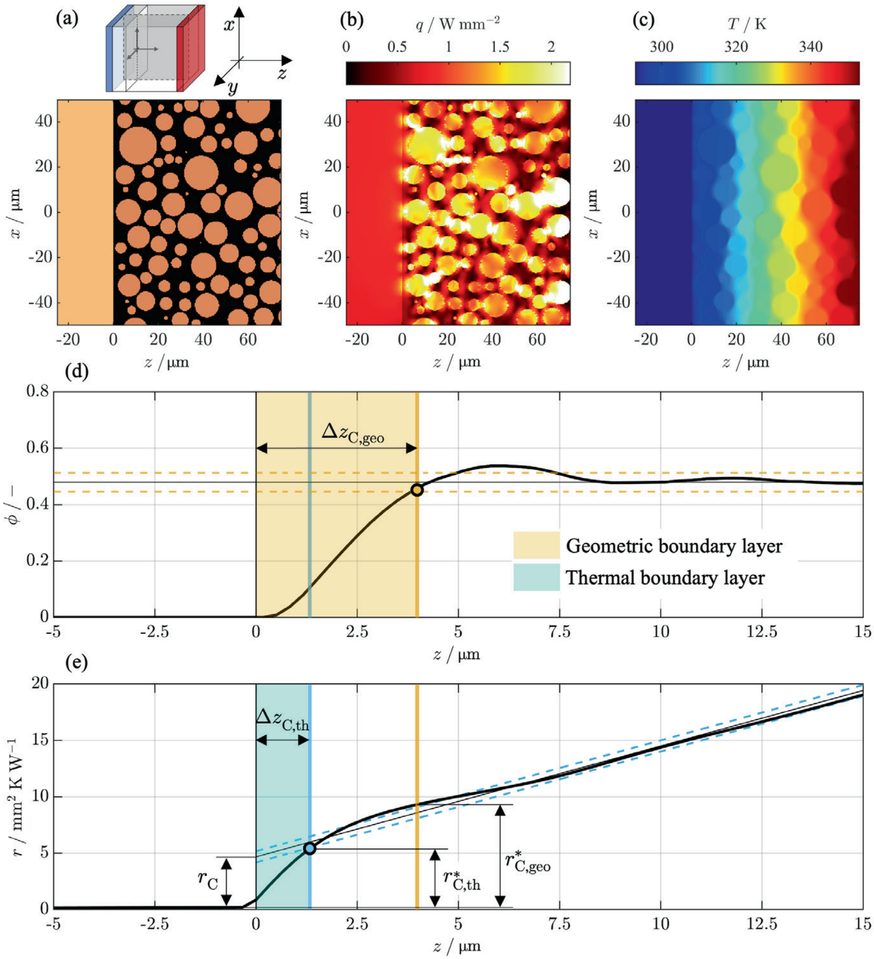

Figure 6.9. Evaluation of the boundary layer at an FPS transition with ideally flat substrate surface. Exemplary calculation results. Central cross-sections of geometry (a), steady-state heat flux field (b), steady-state temperature field (c), average filler volume fraction curve (d), and cumulative specific thermal resistance curve across the FPS transition (e). Polymer: $\lambda_C = 0.25$ W m^{-1} K^{-1} (e.g., epoxy). Filler: Spheres with log-normal size distribution with $\log(\sigma) = 0.2$, $D_{50} = 10$ µm, $\phi_{max} = 0.55$, $\phi = 0.48$, $\lambda_D = 35$ W m^{-1} K^{-1} (e.g., alumina). Substrate: $\lambda_S = 130$ W m^{-1} K^{-1} (e.g., aluminum alloy). Spatial resolution of the simulation: 0.3 µm. Results, see **Table 6.1**.

However, they are explained here using simulation results, as these offer higher spatial resolution and are unaffected by experimental artifacts. Nevertheless, it is important to note that it is not possible to evaluate the local filler volume fraction from the micro thermography results as they do not contain any information about the sample's microstructure.

In the case of an ideally smooth substrate surface, $z = 0$ is defined as the lower limit of both boundary layers, see part (d) and (e) of **Figure 6.9**. The apparent increase in the thermal resistance curve in the substrate area shortly before the interface is due to the limited resolution of the simulation. The upper limit of the boundary layers is numerically determined based on the shown $\phi(z)$ and $r(z)$ curves by identifying the transition from the interface-affected region to the undisturbed bulk. However, clearly defining this transition point is challenging. Due to the stochastic nature of particle packing, the filler volume fraction remains locally variable even in the bulk, and the thermal resistance curve shows a nonlinear increase. The following procedure has proven useful for identifying the transition:

For the geometric boundary layer, the mean filler volume fraction in the undisturbed bulk area is determined with the standard deviation σ of all data points in relation to this mean value. A 2σ band is then constructed around this mean, and approximately 95% of all data points in the bulk range are expected to be in this band, see dashed orange lines in part (d) of **Figure 6.9**. The z coordinate at which the $\phi(z)$ curve enters this band for the first time is then identified and defined as the upper boundary of the geometric boundary layer, see orange marking in part (d) or **Figure 6.9**. The boundary layer thickness determined in this manner is referred to as $\Delta z_{\mathrm{C,geo}}$ and in the example provided is $3.98\ \mathrm{\mu m}$. A standard deviation of $6\ \%$ was observed across ten repeated simulations with randomly generated filler packings.

The procedure for evaluating the thermal boundary layer is similar. Here, a regression line is determined for the $r(z)$ curve in the bulk region and the standard deviation band of all data points around this line is calculated. The evaluation is carried out with a 2σ band, as well. The upper limit of the thermal boundary layer is the z coordinate at which the calculated $r(z)$ curve initially enters this band. The boundary layer thickness found in this manner is referred to as $\Delta z_{\mathrm{C,th}}$ and is $1.33\ \mathrm{\mu m}$ in the example shown. Repeated simulations result in a standard deviation of $13\ \%$. The selection of the 2σ bands has proven to be suitable as it leads to lower variability of the results than the 1σ band, especially in the thermal evaluation. More stable results were not achieved with a 3σ band. At the same time, however, a thicker band systematically causes a thinner boundary layer. The boundary layer thickness must always be calculated iteratively, as the mean value of the volume fraction or the linear increase in resistance in the bulk area can only be correctly calculated if the end of the boundary layer, and thus the beginning of the bulk area, is known. Once the boundary layers have been identified, the resistance contributions of these boundary layers can be evaluated as $r^{*}_{\mathrm{C,geo}} = 9.12\ \mathrm{mm}^2\ \mathrm{K}\ \mathrm{W}^{-1}$ and $r^{*}_{\mathrm{C,th}} = 5.21\ \mathrm{mm}^2\ \mathrm{K}\ \mathrm{W}^{-1}$

for this example, see **Figure 6.9**. The standard deviation across repeated simulations is $5\ \%$ and $9\ \%$, respectively. The specific thermal contact resistance, evaluated by extrapolation to $z = 0$ is $r_\mathrm{C} = 4.37\ \mathrm{mm^2\ K\ W^{-1}}$, and the corresponding equivalent thermal height is $z_\mathrm{th} = -4.45\ \mathrm{\mu m}$. Repeated simulations yield a standard deviation of $6\ \%$ for both values. The negative thermal height indicates an FPS transition with higher thermal resistance than a transition between two ideally homogeneous materials (unfilled polymer and substrate). **Table 6.1** summarizes all evaluation results derived from the analysis shown in **Figure 6.9**. The variance across multiple simulations on this representative setup, expressed by the given standard deviations, is used to estimate the 1σ margin for all subsequent simulations involving a smooth substrate surface in sections 6.4.1 and 6.4.2.

The situation becomes somewhat more complex when a rough substrate surface is considered. In this situation, the effects of the thermal transition between substrate and polymer are superimposed with the impact of the particle packing with wall effect. **Figure 6.10** exemplarily shows calculation results and a boundary layer evaluation for an FPS transition with an artificial random rough surface with $S_\mathrm{q} = 2.0\ \mathrm{\mu m}$. Except for the substrate surface, all model parameters are identical to those in **Figure 6.9**, with a spherical filler with $\log(\sigma) = 0.2$ and $D_{50} = 10\ \mathrm{\mu m}$. Parts (a) to (c) show central cross-sections of the geometry, the steady-state heat flux field, and the steady-state temperature field. Parts (d) and (e) show the $\phi(z)$ and $r(z)$ curves for $-5\ \mathrm{\mu m} \le z \le +15\ \mathrm{\mu m}$. For better comprehension of the geometric relationships, the surface profile along a central sectional plane is additionally indicated in parts (d) and (e). In the example shown, both the $\phi(z)$ and $r(z)$ curves start to increase considerably below $z = 0$.

The boundary layers are no longer confined to the filled polymer but extend over larger distances of the roughness profile into the substrate. Henceforth, the boundary layers are divided into two sections. One section is located below the $z = 0$ reference level, and the other is above. The upper limit of the geometric and thermal boundary is defined in the same way as in the previous example with an ideally smooth substrate surface. The definition of the lower limits needs to be modified.

Table 6.1. Results of microscale simulations, corresponding to **Figure 6.9**.

Bulk	Projection		Geometric boundary layer		Thermal boundary layer	
λ_eff / W m^{-1} K^{-1}	r_C / $\mathrm{mm^2\ K\ W^{-1}}$	z_th / $\mathrm{\mu m}$	$\Delta z_\mathrm{C,geo}$ / $\mathrm{\mu m}$	$r^*_\mathrm{C,geo}$ / $\mathrm{mm^2\ K\ W^{-1}}$	$\Delta z_\mathrm{C,th}$ / $\mathrm{\mu m}$	$r^*_\mathrm{C,th}$ / $\mathrm{mm^2\ K\ W^{-1}}$
1.01	4.37	−4.45	3.98	9.12	1.33	5.21

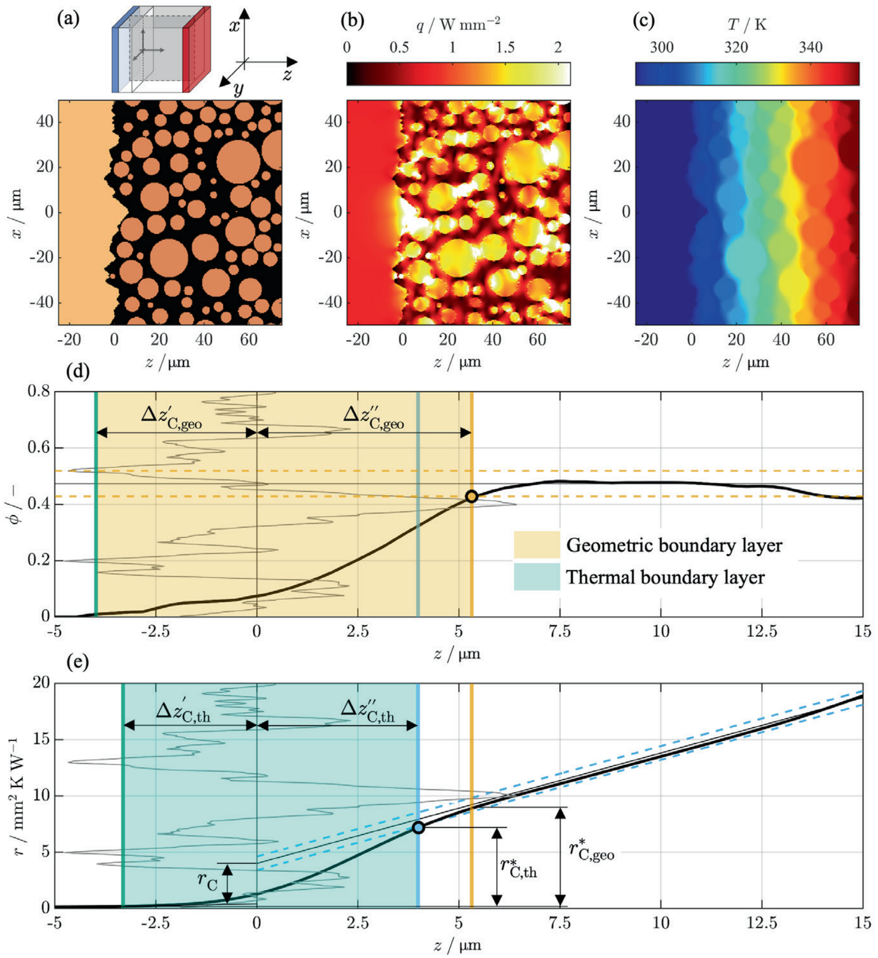

Figure 6.10. Evaluation of the boundary layer at an FPS transition with rough substrate surface. Exemplary calculation results. Central cross-sections of geometry (a), steady-state heat flux field (b), steady-state temperature field (c), average filler volume fraction curve (d), and cumulative specific thermal resistance curve across the FPS transition (e). Polymer: $\lambda_{\mathrm{C}} = 0.25$ W m^{-1} K^{-1} (e.g., epoxy). Filler: Spheres with log-normal size distribution with $\log(\sigma) = 0.2$, $D_{50} = 10$ µm, $\phi_{\max} = 0.55$, $\phi = 0.48$, $\lambda_{\mathrm{D}} = 35$ W m^{-1} K^{-1} (e.g., alumina). Substrate: Artificial random rough surface with $S_{\mathrm{q}} = 2.0$ µm, see **Figure 6.1**, $\lambda_{\mathrm{S}} = 130$ W m^{-1} K^{-1} (e.g., aluminum alloy). Full surface wetting. Results, see **Table 6.2**.

The thickness of the boundary layers below the reference level is referred to as $\Delta z'_{\mathrm{C}}$ and above as $\Delta z''_{\mathrm{C}}$, see parts (d) and (e) of **Figure 6.10**. The lower limits are also evaluated geometrically and thermally, based on the modeled $\phi(z)$ curve and the calculated $r(z)$

curve. The lower limit of the geometric boundary layer is identified using the threshold $\phi(z) > 0$. For the lower limit of the thermal boundary layer, there is a threshold applied of 5% deviation from the expected linear resistance increase in the substrate. This threshold was defined to correspond to twice the residual error in the substrate layers, enabling a reliable and reproducible evaluation. **Table 6.2** summarizes the results evaluated in this manner for the example provided in **Figure 6.10**.

From the simulations, $\Delta z'_{\mathrm{C,geo}} = 3.98\ \mu\mathrm{m}\ \pm 13\ \%$ and $\Delta z''_{\mathrm{C,geo}} = 5.31\ \mu\mathrm{m}\ \pm 5\ \%$, as well as $\Delta z'_{\mathrm{C,th}} = 3.31\ \mu\mathrm{m}\ \pm 5\ \%$ and $\Delta z''_{\mathrm{C,th}} = 3.99\ \mu\mathrm{m} \pm 6\ \%$ are determined as the boundary layer thicknesses. The specified error intervals represent 1σ uncertainties, derived from ten repeated simulations with randomly generated filler packings. The corresponding thermal contact resistances are $r^*_{\mathrm{C,geo}} = 8.71\ \mathrm{mm}^2\ \mathrm{K}\ \mathrm{W}^{-1}\ \pm 5\ \%$ and $r^*_{\mathrm{C,th}} = 6.99\ \mathrm{mm}^2\ \mathrm{K}\ \mathrm{W}^{-1}\ \pm 10\ \%$. They are of similar magnitude as those determined with an ideally flat substrate. However, the boundary layers are considerably thicker in case of a rough surface. A projection onto $z = 0$ leads to $r_{\mathrm{C}} = 3.82\ \mathrm{mm}^2\ \mathrm{K}\ \mathrm{W}^{-1} \pm 8\ \%$ which is 13 $\%$ less compared to a smooth surface. The corresponding equivalent thermal height of the simulated FPS transition is $z_{\mathrm{th}} = -3.93\ \mu\mathrm{m}\ \pm 8\ \%$. The equivalent thermal height of a substrate to unfilled polymer interface, where the polymer has the same thermal conductivity as the filled polymer $\lambda_{\mathrm{eff}} = 1.02$ W m^{-1} K^{-1}, is $z_{\mathrm{th,hom}} = 1.58\ \mu\mathrm{m}$. This characterizes the exclusive effect of the rough substrate surface. As discussed in chapter 6.2, the pure effect of surface roughness is positive for heat conduction across the interface. The thermal contact resistances are negative, and the equivalent thermal heights are positive. The comparison of the calculated equivalent thermal height of the FPS transition z_{th} with the reference value $z_{\mathrm{th,hom}}$ results in the pure impact of the heterogeneous particle packing with wall effect. The joint specification of the two equivalent thermal heights allows for separate analysis of the contributions of the rough substrate surface and the particle packing based on simulations. As before, the variance observed across multiple simulations of this representative setup is used to estimate the 1σ margin for subsequent simulations (rough substrate surfaces in section 6.4.3).

Table 6.2. Results of microscale simulations, corresponding to **Figure 6.10**.

Bulk	Projection		Geometric boundary layer		Thermal boundary layer	
λ_{eff} / W m^{-1} K^{-1}	r_{C} / $\mathrm{mm}^2\ \mathrm{K}\ \mathrm{W}^{-1}$	$\left\lvert \begin{matrix} z_{\mathrm{th,hom}} \\ z_{\mathrm{th}} \end{matrix} \right.$ / µm	$\left\lvert \begin{matrix} \Delta z'_{\mathrm{C,geo}} \\ \Delta z''_{\mathrm{C,geo}} \end{matrix} \right.$ / µm	$r^*_{\mathrm{C,geo}}$ / $\mathrm{mm}^2\ \mathrm{K}\ \mathrm{W}^{-1}$	$\left\lvert \begin{matrix} \Delta z'_{\mathrm{C,th}} \\ \Delta z''_{\mathrm{C,th}} \end{matrix} \right.$ / µm	$r^*_{\mathrm{C,th}}$ / $\mathrm{mm}^2\ \mathrm{K}\ \mathrm{W}^{-1}$
1.02	3.82	$\left\lvert \begin{matrix} 1.58 \\ -3.93 \end{matrix} \right.$	$\left\lvert \begin{matrix} 3.98 \\ 5.31 \end{matrix} \right.$	8.71	$\left\lvert \begin{matrix} 3.31 \\ 3.99 \end{matrix} \right.$	6.99

6.4 EFFECTS OF THE MICROSCALE PACKING AND SUBSTRATE STRUCTURE

Following the introductory sections of this chapter, the subsequent sections focus on investigating the microstructural effects on the boundary layers and thermal contact resistances at FPS transitions. The geometric microstructure of FPS transitions is influenced by a variety of material parameters and manufacturing conditions, making it complex and difficult to predict. The actual 3D microstructure at the FPS transitions, in particular the local particle arrangements and the particle-substrate-distances (PSD), was not experimentally accessible within the scope of this work. Only rough insights into the particle packing close to the substrate could be derived from cross-sectional images.

Therefore, it is not the aim of the following studies to quantitatively predict the thermal contact resistance for real material combinations. Instead, the focus is on gaining a qualitative understanding of the key relationships using simplified microstructural assumptions and model systems. This approach enables a systematic exploration of the underlying mechanisms, considering the limitations of experimental accessibility and modeling capability. As already in the chapters 4 and 5, stochastic variations in the simulations are minimized by systematically varying only one parameter at a time.

In all simulation studies, the same parameter combination for the thermal conductivities of the polymer $\lambda_\mathrm{C} = 0.25\ \mathrm{W\ m^{-1}\ K^{-1}}$ (e.g., epoxy), the substrate $\lambda_\mathrm{S} = 130\ \mathrm{W\ m^{-1}\ K^{-1}}$ (e.g., aluminum alloy), and the filler $\lambda_\mathrm{D} = 35\ \mathrm{W\ m^{-1}\ K^{-1}}$ (e.g., alumina) is used. While this limits the transferability of the results, it allows for a focused investigation of microstructural effects. The influence of the thermal conductivities of the components is examined separately in chapter 6.5.

Sections 6.4.1 and 6.4.2 focus on filler packing effects in combination with an ideally smooth substrate. This is followed in section 6.4.3 by investigations with rough substrate surfaces. Finally, local variations are considered in section 6.4.4.

6.4.1 PARTICLE SIZE, PARTICLE SIZE DISTRIBUTION, AND FILLER VOLUME FRACTION

Even if ideally smooth substrates have no practical relevance, they are a suitable reference for the systematic exploration of packing effects in the filled polymer. Neglecting rough surfaces, the FPS microscale simulations are arbitrarily scalable. Boundary layer thickness and thermal contact resistances scale directly with the particle size, see **Figure 6.11**. Shown here are cross-sections through the microstructure of an FPS transition with increasing particle size from (a) to (c). Also illustrated schematically is the local cumulative thermal resistance curve $r(z)$ across the FPS transition. As particle size increases, the characteristic length scale of the microstructure increases, leading to a thicker geometric boundary layer. This directly affects the formation of the thermal boundary layer.

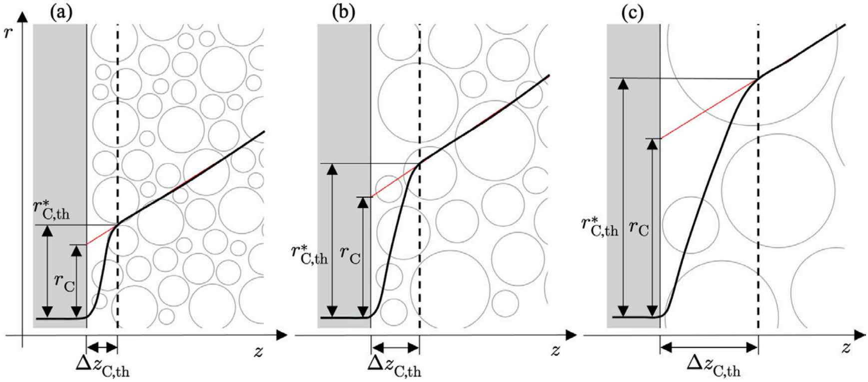

Figure 6.11. Schematic representation of the phenomena at an FPS transition with increasing particle size.

Gray marked zone: Substrate. Red line: Extrapolation of the thermal resistance curve in the bulk area to $z = 0$.

Since thermal resistances are also directly proportional to the respective layer thickness, both the boundary layer thickness and the specific thermal contact resistance r_{C} increase linearly with particle size. This purely theoretical consideration can also be verified experimentally to a good approximation using micro thermography. **Figure 6.12** shows the projected thermal contact resistances evaluated in a micro thermography study with three different spherical alumina fillers with significantly different volumetric median diameters. In addition to the actual micro thermography results, the thermographed sections through the multi-layered samples and a laser microscope image of the individual fillers are shown. The substrate with the lowest roughness height SUB-R0 is selected. The fillers used are Alox-S-08 with $D_{50} = 7.9\ \mu\mathrm{m}$, Alox-S-22 with $D_{50} = 22.2\ \mu\mathrm{m}$, and Alox-S-63 with $D_{50} = 63.4\ \mu\mathrm{m}$. Epoxy E01 is used as the polymeric matrix. The study shows a clear dependence of thermal contact resistance on particle size. Although the limited number of data points and experimental uncertainties do not allow a definitive assessment or confirmation of linearity, the results nevertheless support the underlying analytical hypothesis.

In the experiments, all fillers exhibit similar, but not identical particle size distributions (see **Table 3.2**, page 41), and the selected substrate deviates from ideal smoothness (see **Table 3.3**, page 48). In addition, stochastic variations during sample preparation and measurement lead to further uncertainties. These factors have a combined effect on the analyses and may contribute to deviations from the expected ideal linear trend.

Besides the absolute size of the filler particles, additionally of interest is their size distribution. In section 4.2.2, the impact of particle size distribution on the effective thermal conductivity of a filled polymer was investigated and shown to have a significant impact.

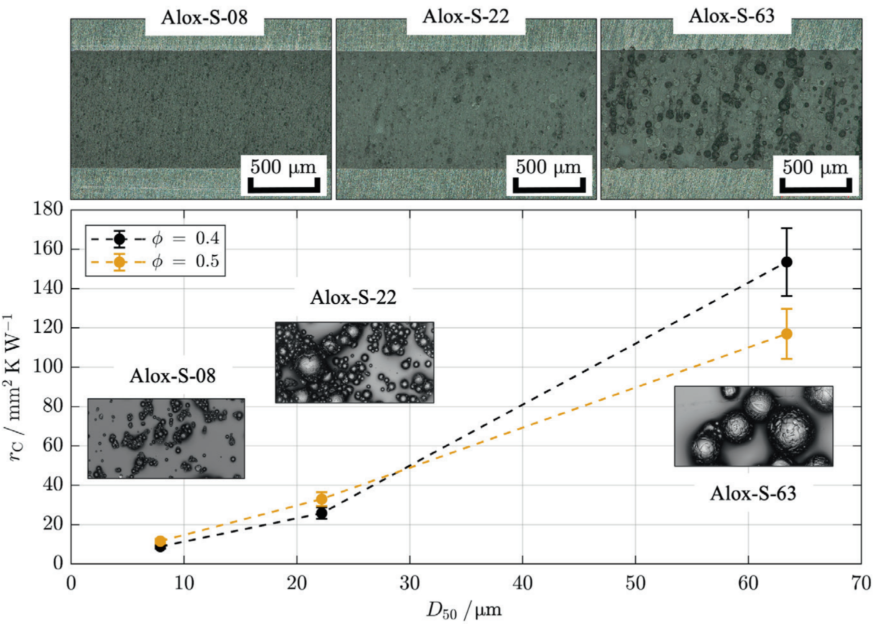

Figure 6.12. Specific thermal contact resistance as a function of the volumetric mean particle diameter. Presentation of the micro thermography results, micrographs of the samples at $\phi = 0.4$ taken with a digital light microscope VHX with a dual-light high-magnification zoom lens VH-Z250R from Keyence, and laser microscope images of the fillers, extracted from **Figure 3.1**. Polymer: Epoxy E01. Fillers: Alox-S-08, Alox-S-22, Alox-S-63, $\phi = 0.4$ and $\phi = 0.5$. Substrate: SUB-R0. Error bars show the systematic uncertainties of the measurement. Connecting lines are only shown for better visualization and interpretation. Based on [0].

An experimental study is not feasible, since no fillers with a systematically variable width of the particle size distribution are available that have otherwise identical property profiles. To isolate and analyze the effect of particle size distribution under controlled and simplified conditions, a numerical simulation study is performed.

To suppress the impact of particle-substrate distances (PSDs), ϕ_{max} configurations are modeled and calculated. All particles are in contact with each other and with the substrate. This is an unrealistic configuration for practical applications but enables a controlled, qualitative investigation without the interference of random packing variations or irregular PSDs, which would otherwise complicate the analyses. **Figure 6.13** shows the results of this simulative study where an ideally smooth substrate is modeled in contact with a filled polymer with ideally spherical particles in a log-normal size distribution, considering a variable width of the particle size distribution.

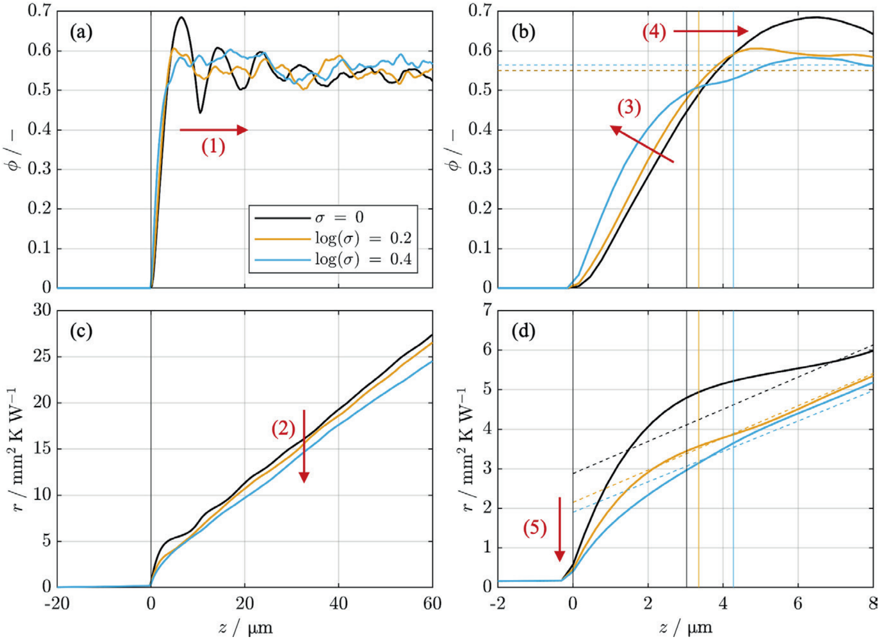

Figure 6.13. Filler volume fraction and cumulative specific thermal resistance curve across an FPS transition with different widths of the particle size distributions.

Curve of filler volume fraction along the z axis of the modeled filler packing in (a) and (b). Calculated cumulative specific thermal resistance in (c) and (d). Overall representations in (a) and (c). Magnified view of boundary layer in (b) and (d). Polymer: $\lambda_C = 0.25$ W m^{-1} K^{-1} (e.g., epoxy). Filler: Spheres with log-normal size distribution, $D_{50} = 10$ µm, $\phi = \phi_{\max} \approx 0.55$, $\lambda_D = 35$ W m^{-1} K^{-1} (e.g., alumina). Substrate: $\lambda_S = 130$ W m^{-1} K^{-1} (e.g., aluminum alloy). Full surface wetting. Results, see appendix D.3, **Table D.1**.

The thermal conductivities of the materials are kept constant at $\lambda_C = 0.25$ W m^{-1} K^{-1} (e.g., epoxy), $\lambda_D = 35$ W m^{-1} K^{-1} (e.g., alumina), and $\lambda_S = 130$ W m^{-1} K^{-1} (e.g., aluminum alloy). All packings are modeled with a similar density (RLP), so that the filler volume fractions and effective thermal conductivities in the bulk region are similar despite different particle size distributions. Parts (a) and (c) show $\phi(z)$ and $r(z)$ curves in the entire RVE, and parts (b) and (d) show magnifications of the FPS transition. The formation of the geometric boundary layers and thermal contact resistances can be seen better in these magnified views. In addition to the $\phi(z)$ and $r(z)$ curves, parts (b) and (d) show the upper ends of the geometric boundary layers (colored vertical lines) and the regression lines of the bulk area (dashed colored lines). **Figure 6.14** supports the analysis by comparing the evaluated projected specific contact resistances r_C as well as the thicknesses $\Delta z_{C,\text{geo}}$ and specific thermal resistances $r^*_{\mathrm{C,geo}}$ of the geometric boundary layers. All quantitative results of the study are provided in appendix D.3, **Table D.1**.

Part (a) of **Figure 6.13** shows a characteristically different course of the $\phi(z)$ curves near the substrate surface. While at $\sigma = 0$, thus with equally sized spheres, an oscillation in the filler volume fraction occurs, which only disappears after approx. $5 \times D_{50}$, see annotation arrow (1), the curves at $\log(\sigma) = 0.2$ and $\log(\sigma) = 0.4$ only show stochastic variations. The packing at $\sigma = 0$ tends to form layers and thus a micro-order near the surface, while the size distribution with $\log(\sigma) > 0$ leads to better intermixing and randomness. The rate at which the present oscillations decay past the surface is a measure of the distance after which the particle packing can form a pattern undisturbed by the surface.

Part (c) of **Figure 6.13** shows that the effective thermal conductivity in the bulk of the filled polymer is very similar in all three configurations. The slopes of the $r(z)$ curves are almost identical. The thermal resistance decreases systematically with increasing width of the particle size distribution, suggesting lower thermal contact resistances, see annotation arrow (2) and part (a) of **Figure 6.14**. When the width of the particle size distribution increases, the filler volume fraction directly at the substrate surface can increase, as the smaller particles can fill the gaps on the surface more effectively, see annotation arrow (3). However, a fully developed, undisturbed filler packing can only form at a certain distance from the substrate, as larger particles within the distribution only integrate into the packing structure at greater depths, see annotation arrow (4). As a result, the thickness of the geometric boundary layer increases with increasing width of the particle size distribution, see part (b) of **Figure 6.14**.

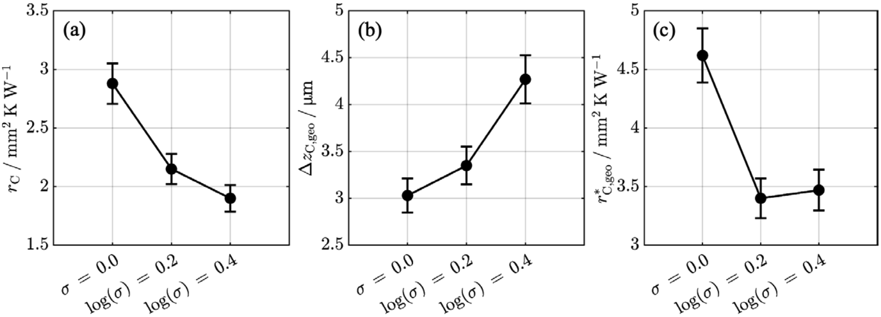

Figure 6.14. Specific thermal contact resistance of an FPS transition and geometric boundary layer thickness with different widths of the particle size distributions.

Results of the study shown in **Figure 6.13**. Projected thermal contact resistance r_{C} in (a). Thickness $\Delta z_{\mathrm{C,geo}}$ and specific thermal resistance $r^*_{\mathrm{C,geo}}$ of geometric boundary layer in (b) and (c). Error bars represent the 1σ margin, estimated from repeated simulations, as described in chapter 6.3.

The earlier rise in filler volume fraction leads to a more gradual increase in thermal resistance within the boundary layer, see annotation arrow (5) in **Figure 6.13** and part (c) of **Figure 6.14**. What the study in **Figure 6.13** shows, is a purely geometric packing effect. When using spheres of the same size, a layer formation directly at the substrate surface is likely. The introduction of a size distribution provides smaller particles that can effectively fill the gaps between the first particle layer and the wall. The smaller the available particles, the faster the filler volume fraction can increase directly at the surface. However, the simultaneously occurring larger particles can only appear with increasing distance from the surface and shift the end of the geometric boundary layer further into the bulk region.

This effect is expected to be even more pronounced in multi-scale filled polymers, where the particle size distribution is significantly broader. Due to the scale-related limitations discussed in chapter 5.1.1, a detailed microscale simulation is not feasible. Instead, the influence of the broader size distribution can be estimated using a simplified analytical model. The model assumes that any continuous particle size distribution can be decomposed into infinitesimally small size classes $\mathrm{d}D$, with the particles in each class packing like equally sized particles. By integrating the packing effects over all size classes, the overall filler volume fraction curve $\phi(z)$ can be approximated. Let $\phi_0(D, z)$ denote the numerically calculated curve of filler volume fraction along the z axis for equally sized spheres of diameter D, and let $\mathrm{d}Q_3(D)/\mathrm{d}D$ represent the differential particle size distribution of any filler. Then the total volume fraction curve is given by

$$\phi(z) = \int_0^{\infty} \frac{\mathrm{d}Q_3(D)}{\mathrm{d}D} \cdot \phi_0(D, z)\,\mathrm{d}D \ . \tag{6.7}$$

This expression approximates the filler volume fraction curve $\phi(z)$ for an arbitrary particle size distribution under a constant PPD configuration. In the further discussion, simplified $\phi_{\max}$ configurations are examined. **Figure 6.15** shows the $\Phi(z) = \phi(z)/\phi_{\max}$ curves approximated by **Eq. (6.7)** for individual fillers and a multi-scale filler blend with different particle size distributions. In part (a) the differential distributions of the fillers and the filler blend are provided in scaled representation for improved visualization. Part (b) shows the $\Phi(z)$ curves calculated by superimposing the packing fractions of each included individual size fraction using **Eq. (6.7)**.

The results are shown for three ideally log-normal size distributed single-scale fillers with $\log(\sigma) = 0.2$, $\log(\sigma) = 0.4$, and $\log(\sigma) = 0.6$. Additionally included is the ternary blend previously shown in **Figure 5.1**, page 141, consisting of Alox-S-63, Alox-S-08, and Alox-S-01 in a volumetric ratio of 40: 20: 10.

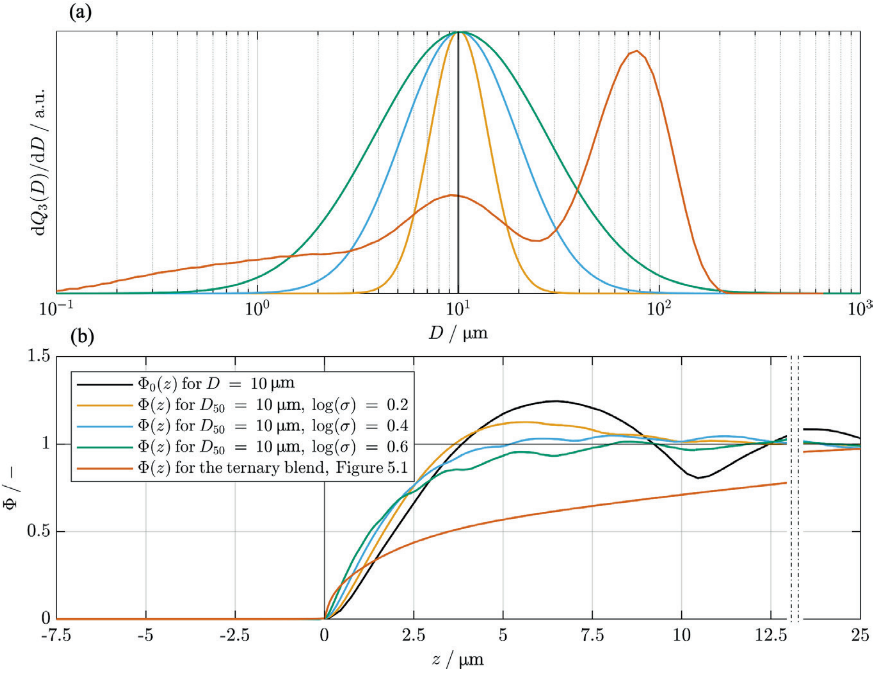

Figure 6.15. Analytically approximated $\Phi(z)$ curves for differently size distributed fillers. Differential particle size distributions of three single-scale fillers and one ternary filler blend in (a). Approximated $\Phi(z)$ curves using **Eq. (6.7)** in (b). Ternary filler blend consisting of spherical alumina fillers Alox-S-63, Alox-S-08, and Alox-S-01 in a volumetric ratio of 40: 20: 10, see **Figure 5.1**, page 141.

The results for the single-scale fillers nicely reflect the results of the numerical simulation in **Figure 6.13**, confirming the validity of the analytical model. The wider the size distribution, the earlier the increase in filler concentration begins past the substrate surface, while the bulk level is reached later. Thus, the thickness of the geometric boundary layer increases. Using a typical ternary filler blend with the largest proportion of coarse-grained filler and the smallest proportion of the finest filler amplifies this effect significantly. Directly on the surface, the smallest particles can rapidly increase filler concentration. Considerably greater distances from the surface are required for the largest particles to also appear in the packing pattern. In the example shown, the bulk filler concentration is not reached until approximately 25 µm from the substrate surface. The analysis assumes that the filler blend is homogeneously distributed and there is no local shift in the particle size distribution. Under this assumption, the common filler blends described in section 5.1.1 are disadvantageous, as they lead to extremely thick boundary layers. A further discussion of the problems that arise with very thick boundary layers is presented in chapter 6.6.

The previous analyses have been limited to $\phi_{\max}$ configurations; however, the thermal contact resistances at arbitrary filler volume fractions $\phi < \phi_{\max}$ are also of interest. The effect of filler volume fraction must be discussed together with the effect of the particle-substrate distance, which makes the analysis considerably more difficult. A simulative study can isolate the effects of the filler volume fraction, see **Figure 6.16**, when the simplifying assumptions are added that the particles are distributed ideally homogeneously in the available volume and the particle-particle distances (PPD) and particle-substrate distances (PSD) are identical and proportional to the particle size. FPS transitions are modeled and calculated for an ideally smooth substrate with $\lambda_S = 130$ W m^{-1} K^{-1}, a polymer with $\lambda_C = 0.25$ W m^{-1} K^{-1}, and an ideally spherical filler with $\lambda_D = 35$ W m^{-1} K^{-1} and a log-normal size distribution with $\log(\sigma) = 0.2$.

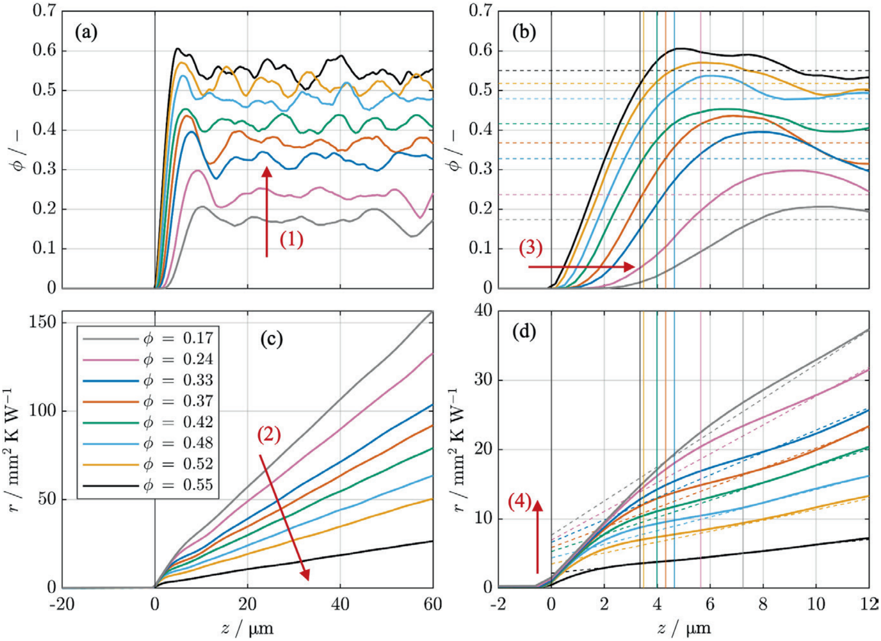

Figure 6.16. Filler volume fraction and cumulative specific thermal resistance curve across an FPS transition with different filler concentrations.

Curve of filler volume fraction along the z axis of the modeled filler packing in (a) and (b). Calculated cumulative specific thermal resistance in (c) and (d). Overall representations in (a) and (c). Magnified view of the boundary layer in (b) and (d). Polymer: $\lambda_C = 0.25$ W m^{-1} K^{-1} (e.g., epoxy). Filler: Spheres with log-normal size distribution with $\log(\sigma) = 0.2$, $D_{50} = 10$ µm, $\phi_{\max} = 0.55$, $\lambda_D = 35$ W m^{-1} K^{-1} (e.g., alumina). Substrate: $\lambda_S = 130$ W m^{-1} K^{-1} (e.g., aluminum alloy). Full surface wetting. Results, see appendix D.3, **Table D.2**.

An RLP with $\phi_{\max} = 0.55$ and seven configurations with $\phi < \phi_{\max}$ are modeled. Parts (a) and (c) show $\phi(z)$ and $r(z)$ curves in the entire RVE, and parts (b) and (d) show a close-up of the FPS transition. The quantitative results of the study are provided in appendix D.3, **Table D.2**. In part (a) of **Figure 6.16**, the increasing filler volume fraction of the individual configurations is recognizable, see annotation arrow (1). Part (b) shows the lower slope of the $r(z)$ curve, and thus the resulting higher thermal conductivity with increasing filler volume fraction, see annotation arrow (2). The described modeling strategy which has increasing PSDs when the PPDs increase, leads to a later increase of the filler concentration past the substrate surface with lower filler volume fractions, see annotation arrow (3). This results in thicker geometric boundary layers (colored vertical lines). As a result, the thermal contact resistances increase systematically with decreasing filler volume fraction, see annotation arrow (4). This applies to both the projected contact resistances and the resistances of the contact layers.

Figure 6.17 supports the analysis by comparing the evaluated projected specific contact resistances r_{C} and equivalent thermal heights z_{th}, as well as the thicknesses $\Delta z_{\mathrm{C,geo}}$ and specific thermal resistances $r^*_{\mathrm{C,geo}}$ of the geometric boundary layers. Part (a) shows that the projected (positive) thermal contact resistances decrease systematically and significantly with increasing filler volume fraction. Part (b) presents the corresponding negative equivalent thermal heights, which, contrary to intuitive expectations, increase in magnitude as r_{C} decreases. This is due to the concentration-dependent effective thermal conductivity of the filled polymer in the bulk region, which affects the slope of the extrapolation, see **Eq. (6.6)**, page 179. The extrapolated thermal contact resistances, as used in other works (e.g., [159,161,213]), depend not only on the FPS transition but also on the thermal conductivity of the bulk material. Consequently, they can only describe the increase in thermal resistance relative to a homogeneous material layer exhibiting bulk behavior.

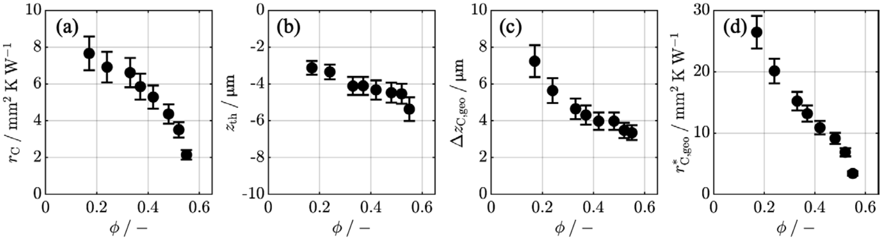

Figure 6.17. Specific thermal contact resistance, equivalent thermal height, and geometric boundary layer thickness with different filler concentrations.

Results of the study shown in **Figure 6.16**. Projected thermal contact resistance r_{C} in (a). Equivalent thermal height z_{th} in (b). Thickness $\Delta z_{\mathrm{C,geo}}$ and specific thermal resistance $r^*_{\mathrm{C,geo}}$ of geometric boundary layer in (c) and (d). Error bars represent the 2σ margin, estimated from repeated simulations, as described in chapter 6.3.

The isolated boundary layer effects are characterized by their thickness $\Delta z_{\mathrm{C,geo}}$ (see part (c) of **Figure 6.17**) and thermal resistance $r^*_{\mathrm{C,geo}}$ (see part (d)), both of which systematically decrease with increasing filler volume fraction for the selected PSD configuration. This simple analysis highlights the limitations of using extrapolated contact resistances and supports the approach developed in chapter 6.3, which proposes a separate evaluation of thickness and resistance of the boundary layers.

6.4.2 BOUNDARY LAYER PACKING STRUCTURE

The previous considerations naturally lead to a discussion of the geometric conditions in the boundary layer. The effect of the first particle layer above the substrate surface appears to play a critical role at $\phi < \phi_{\mathrm{max}}$. **Figure 6.18** shows micrographs of four micro thermography samples with SUB-R0 and the filler Alox-S-63 with ascending filler volume fraction from (a) to (d). In (d) at $\phi = 0.6$, i.e., close to the maximum packing density, the first particles are very close to the substrate surface. The thin polymer layer between particles and substrate is difficult to detect. In the limiting case of maximum packing density, assuming direct particle-substrate contact is justified for the samples studied. At lower filler volume fractions in (a) and (c), no particle-substrate contacts can be seen in the captured section. The distances increase with decreasing volume fraction. However, two-dimensional analysis does not allow a systematic quantification of the distances. Accurate characterization would require non-destructive 3D methods such as micro-CT. The particle packing close to the substrate can be influenced by external processing conditions and internal interaction forces. External factors include the method of sample preparation, such as injection or compression between substrates, which can influence particle orientation and local particle density.

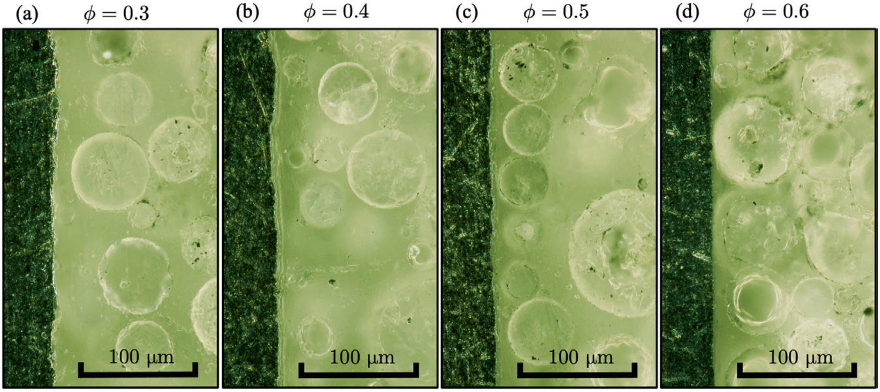

Figure 6.18. Micrographs of FPS transition in multi-layered samples.
Substrate: SUB-R0. Filler: Alox-S-63. Polymer: Epoxy E01. Images taken with a digital light microscope VHX with a dual-light high-magnification zoom lens VH-Z250R from Keyence.

Internal influences include forces between the particles, interactions between particles and substrate, as well as hydrodynamic effects in the liquid polymer phase. Due to the large number of influencing variables, a general experimental investigation is challenging. Instead, several representative PSD configurations are analyzed numerically to capture general trends qualitatively. **Figure 6.19** shows the investigated PSD configurations, all modeled relative to the particle diameter. The PPD increases with decreasing filler volume fraction, and two smaller particles are always positioned closer to each other in absolute terms than two larger ones. Five PSD configurations are considered:

(a) Equilibrium state: PSD $=$ PPD, used in all previous models;
(b) Direct contact: PSD $= 0$;
(c) Random: $0 \leq$ PSD $\leq$ PPD, individually for each particle;
(d) Constant: PSD $= x$;
(e) Offset: PSD $=$ PPD $+ x$.

The parameter x represents a diameter fraction for modeling of the substrate distance. As **Figure 6.18** shows, this diameter fraction tends to be $0 < x < 1$ in the physical samples but can also be > 1 at very low filler volume fractions, see part (a) of **Figure 6.18**.

Figure 6.20 shows the results of a simulative study considering the different PSD configurations, maintaining the previously used combination of $\lambda_{\mathrm{S}} = 130$ W m^{-1} K^{-1}, $\lambda_{\mathrm{D}} = 35$ W m^{-1} K^{-1} and $\lambda_{\mathrm{C}} = 0.25$ W m^{-1} K^{-1}. The filler has ideally spherical particles with $D_{50} = 10$ µm and $\log(\sigma) = 0.2$. Different filler loading levels $0.3 \leq \Phi \leq 1$ are set by varying the PPD, with a maximum packing density of $\phi_{\max} = 0.55$ in the bulk region. Part (a) shows the specific thermal contact resistances of the individual configurations projected onto $z = 0$. Shown in (b) and (c) are the specific thermal resistances of the geometrically evaluated boundary layers and the corresponding boundary layer thicknesses.

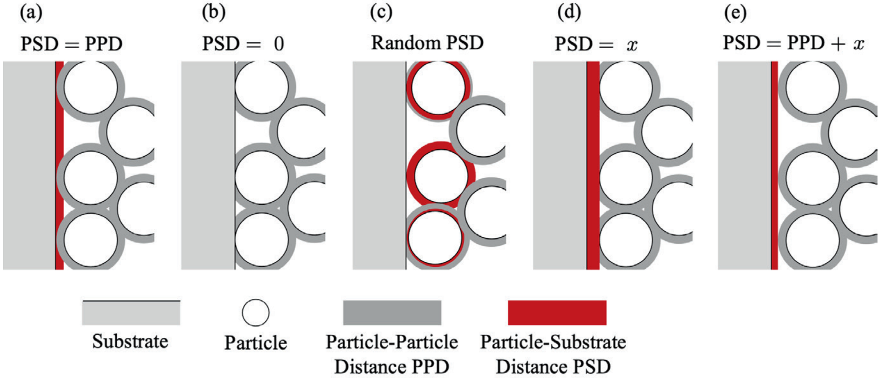

Figure 6.19. Schematic representation of different PSD configurations.

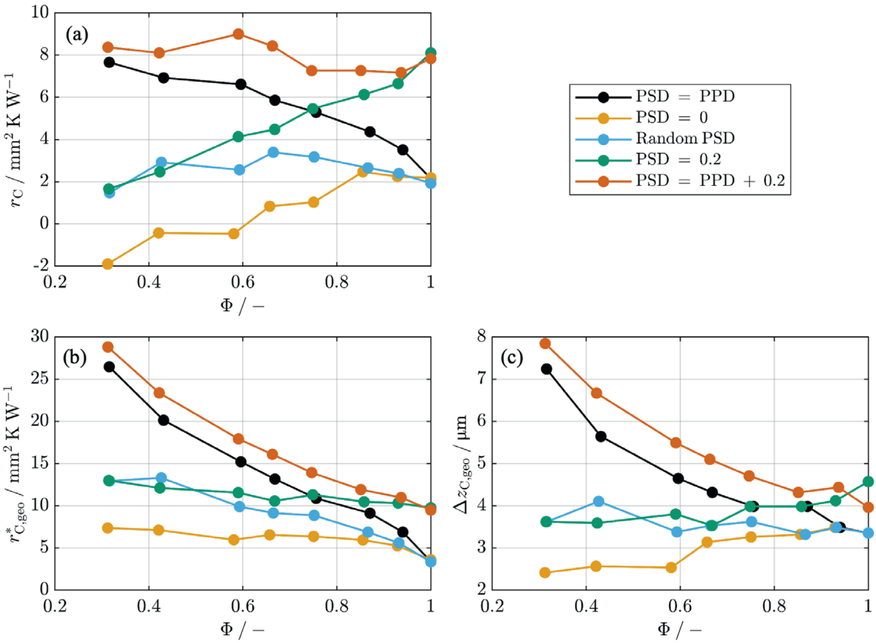

Figure 6.20. Specific thermal contact resistance and boundary layer thickness as a function of filler loading level, considering different PSD configurations.

Connecting lines are only shown for a better allocation of the data points. Polymer: $\lambda_C = 0.25$ W m^{-1} K^{-1} (e.g., epoxy). Filler: Spheres with log-normal size distribution with $\log(\sigma) = 0.2$, $D_{50} = 10$ µm, $\phi_{max} = 0.55$, $\lambda_D = 35$ W m^{-1} K^{-1} (e.g., alumina). Substrate: $\lambda_S = 130$ W m^{-1} K^{-1} (e.g., aluminum alloy). Full surface wetting. Error bars are omitted for clearer visualization. The 1σ margin of the simulations is $\pm$ 6 % for r_C, $\pm$ 5 % for $r^*_{C,geo}$, and $\pm$ 6 % for $\Delta z_{C,geo}$, estimated as described in chapter 6.3.

The value of $x = 0.2$ set in configuration (d) and (e) is chosen arbitrarily, serving only as an example. The results show that thermal contact resistances and boundary layer thicknesses are highly sensitive to the modeled PSD configuration, especially at low filler volume fractions.

The lower limiting case with the lowest possible contact resistances and thinnest possible boundary layers is achieved with PSD = 0. The highest contact resistances and thickest boundary layers are determined with PSD = PPD + x.

With the standard configuration PSD = PPD, r_C, $r^*_{C,geo}$, and $\Delta z_{C,geo}$ all drop simultaneously with increasing Φ. For PSD = 0 and PSD = 0.2 however, there is a strong increase in the projected thermal contact resistances r_C. The boundary layer thicknesses $\Delta z_{C,geo}$

increase slightly and the specific thermal resistances of the boundary layer $r^*_{\mathrm{C,geo}}$ drop approx. $-56\ \%$ from $\Phi = 0.3$ to $\Phi = 1$ for the PSD $= 0$ configuration.

For many practical applications, the extreme configuration with PSD $= 0$ can be excluded for $\Phi < 1$. The combination of the standard particle size in the micrometer range with the polymer's viscosity of a few hundred mPas (see **Table 3.1**) opposes this configuration with an ideal deposition of particles on the substrate surface. A noticeable additional polymer layer, as seen with the PSD $=$ PPD $+\,x$ configuration, could only occur in special cases due to the processing. All other configurations are conceivable and thus cause considerable uncertainty in the prediction of thermal contact resistances at FPS transitions.

This can also be confirmed by an experimental study. **Figure 6.21** shows the thermal contact resistances determined with micro thermography on multi-layered samples with SUB-R0 and the three spherical alumina fillers already presented in **Figure 6.12**, page 188. These three fillers show completely different trends with increasing filler volume fraction.

While the finest filler (Alox-S-08) shows increasing contact resistances with filler volume fraction, the coarsest (Alox-S-63) shows a decrease, and the medium filler (Alox-S-22) yields inconsistent results. For all filler volume fractions except $\phi = 0.6$, the expected trend is shown with the highest thermal contact resistances for the coarsest filler and the lowest for the finest particles. The thermal contact resistances at $\phi = 0.6$ and thus just below the maximum packing density are very similar, confirming the simulative results from **Figure 6.20**.

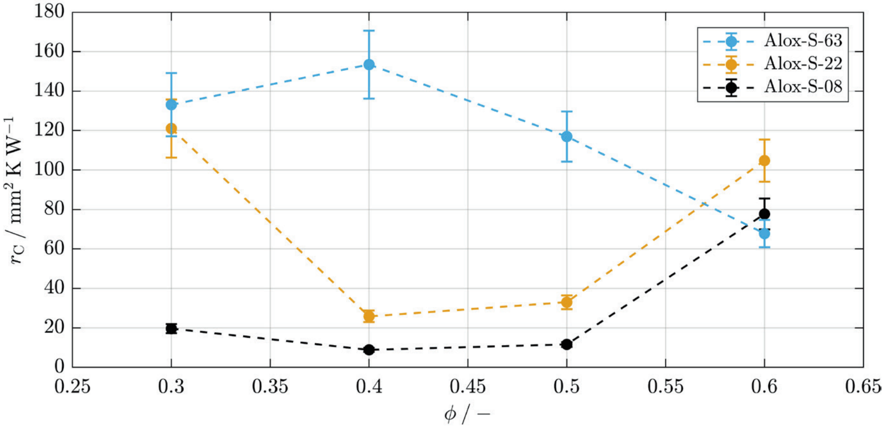

Figure 6.21. Specific thermal contact resistance as a function of filler volume fraction.

Measured using the micro thermography method, described in chapter 3.3. Connecting lines are only shown for better visualization and interpretation. Polymer: Epoxy E01. Fillers: Alox-S-08, Alox-S-22, Alox-S-63, Substrate: SUB-R0. Error bars show the systematic uncertainties of the measurement. Based on [0].

The decreasing contact resistance with Alox-S-63 indicates a uniform particle distribution (PSD $=$ PPD or PSD $=$ PPD $+ x$), whereas local particle-substrate contacts are likely with Alox-S-08 and -22. An analysis of micrographs of the thermographed samples can partially confirm this assumption. **Figure 6.22** shows sections of the micrographs at $\phi = 0.40$ with SUB-R0. Representative local sections were selected. With the coarsest filler Alox-S-63, see part (c), remaining polymer can be seen between the substrate surface and the first particle layer. In contrast, sample (b) with Alox-S-22 displays clear direct particle-substrate contact, helping explain the lower measured resistance at $\phi = 0.40$, see **Figure 6.21**. For the sample with Alox-S-08 (a), the packing structure in the boundary layer is no longer resolvable and recognizable. However, the irregular structure directly on the substrate surface in the micrograph also suggests that there are particles directly on the substrate surface.

Overall, the study shows that the dependence of thermal contact resistance on the filler concentration varies greatly between the fillers investigated. This is at least partly due to the different particle arrangements close to the substrate. However, due to limitations in controlling or fully characterizing the PSD configuration in 3D, no general conclusions can be drawn. Therefore, the preceding simulation study is particularly valuable as it examines PSD configurations in the limiting case, compares trends and provides important insights into the potential effects of particle arrangement in the boundary layers. The analysis of $\phi_{\max}$ configurations continues to be a suitable procedure to suppress the effect of the PSD configuration in further studies.

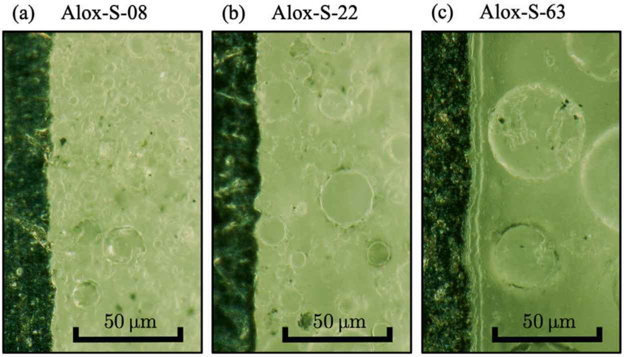

Figure 6.22. Micrographs of FPS transition in multi-layered samples.
Substrate: SUB-R0. Fillers: Alox-S-08, Alox-S-22, Alox-S-63, $\phi = 0.40$. Polymer: Epoxy E01. Images were taken with a digital light microscope VHX with a dual-light high-magnification zoom lens VH-Z250R from Keyence.

6.4.3 ROUGHNESS CHARACTERISTICS OF THE SUBSTRATE

After numerous investigations into FPS transitions with ideally smooth substrate surfaces, the effects of a rough substrate surface and the roughness characteristics will be discussed in this section. As already described in section 6.1.1, all simulations are carried out with the same surface structure to suppress stochastic variations within simulations. By spatially scaling the surface shown in **Figure 6.1**, page 167, both the roughness depth and lateral fineness can be systematically varied. The first central parameter investigated is the root mean square roughness, which is varied in the range $0.0\ \mu\mathrm{m} \leq S_\mathrm{q} \leq 5.0\ \mu\mathrm{m}$ in a simulative study to evaluate its influence on the thermal resistances at the FPS transition.

The established combination of an aluminum substrate with $\lambda_\mathrm{S} = 130\ \mathrm{W\ m^{-1}\ K^{-1}}$ and an ideally spherical alumina filler with $\lambda_\mathrm{D} = 35\ \mathrm{W\ m^{-1}\ K^{-1}}$, $D_{50} = 10\ \mu\mathrm{m}$, and $\log(\sigma) = 0.2$ is used. $\lambda_\mathrm{C} = 0.25\ \mathrm{W\ m^{-1}\ K^{-1}}$ is set for the polymer.

Figure 6.23 shows the central cross-sections through the modeled RVEs with increasing root mean square roughness. It can be seen with the selected geometrical parameters, that the particles can get into the surface valleys between the asperities. There is no pronounced polymer accumulation in the valleys. This only works as long as the lateral structure of the surface is coarse enough for the particles to find sufficient space between the asperities, in this case with $S_\mathrm{al} = 5.43\ \mu\mathrm{m}$. The detailed effects of the lateral structure are investigated in the further course of this section. **Figure 6.24** presents the calculated $\phi(z)$ and $r(z)$ curves based on the RVEs shown in **Figure 6.23**. Parts (a) and (c) of **Figure 6.24** show the entire RVE, and parts (b) and (d) show a magnified view of the FPS transition. **Figure 6.25** supports the analysis by comparing the projected specific contact resistances r_C as well as the thicknesses $\Delta z_\mathrm{C,geo} = \Delta z'_\mathrm{C,geo} + \Delta z''_\mathrm{C,geo}$ and specific thermal resistances $r^*_\mathrm{C,geo}$ of the geometric boundary layers. All quantitative results of the study are provided in appendix D.3, **Table D.3**.

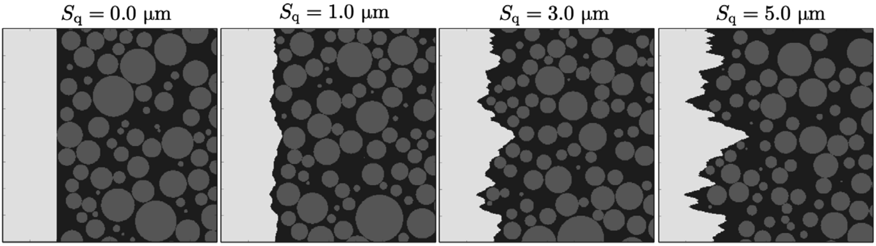

Figure 6.23. Modeled FPS transitions with varying roughness depth of substrate surfaces. Central cross-sections of RVEs. Random loose packing of spherical particles with log-normal size distribution with $\log(\sigma) = 0.2$ and $D_{50} = 10\ \mu\mathrm{m}$. Substrate: Artificial random rough surface from **Figure 6.1**, scaled.

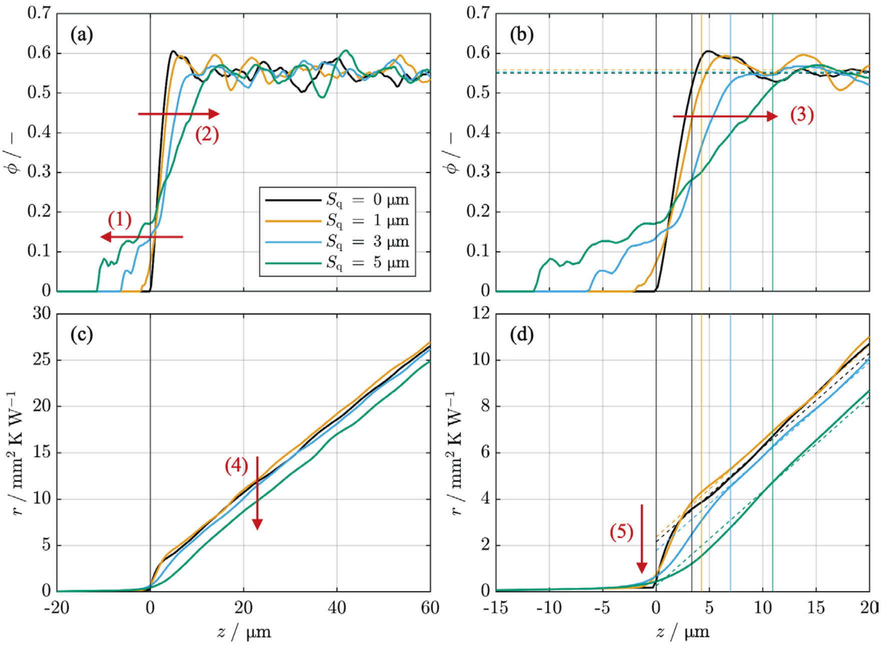

Figure 6.24. Filler volume fraction and cumulative specific thermal resistance curve across an FPS transition with varying surface root mean square roughness.

Curve of filler volume fraction along the z axis of the modeled filler packing in (a) and (b). Calculated cumulative specific thermal resistance in (c) and (d). Overall representations in (a) and (c). Magnified view of the boundary layer in (b) and (d). Polymer: $\lambda_C = 0.25$ W m^{-1} K^{-1} (e.g., epoxy). Filler: Spheres with log-normal size distribution with $\log(\sigma) = 0.2$, $D_{50} = 10$ µm, $\phi = \phi_{max} \approx 0.55$, $\lambda_D = 35$ W m^{-1} K^{-1} (e.g., alumina). Substrate: Artificial random rough surface, see **Figure 6.1**, scaled, $\lambda_S = 130$ W m^{-1} K^{-1} (e.g., aluminum alloy). Full surface wetting. Results, see appendix D.3, **Table D.3**.

As seen in part (a) of **Figure 6.24**, an increasing root mean square roughness has a similar effect on the local filler volume fraction as an increasing width of the particle size distribution. The deeper the valleys of the surface roughness, the lower the first particles can arrange themselves, see annotation arrow (1). Therefore, the local filler volume fraction increases earlier. At the same time, longer surface asperities ensure that complete packing formation is only possible at a greater distance from $z = 0$, see annotation arrow (2). This also results in a thicker geometric boundary layer, as indicated by annotation arrow (3) in part (b). The effective thermal conductivity, and thus the slope of the $r(z)$ curve in the bulk region is the same for all investigated configurations, see part (c) of **Figure 6.24**. However, the absolute height of the thermal resistance curve decreases with increasing root mean square roughness, see annotation arrow (3).

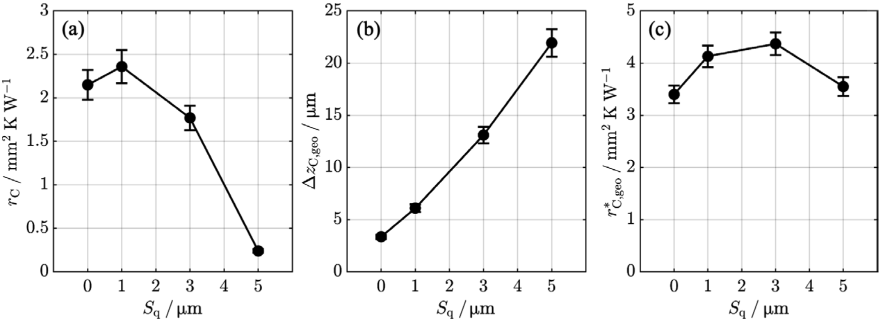

Figure 6.25. Specific thermal contact resistance of an FPS transition and geometric boundary layer thickness with varying surface root mean square roughness.

Results of the study shown in **Figure 6.24**. Projected thermal contact resistance r_C in (a). Thickness $\Delta z_\mathrm{C,geo} = \Delta z'_\mathrm{C,geo} + \Delta z''_\mathrm{C,geo}$ and specific thermal resistance $r^*_\mathrm{C,geo}$ of geometric boundary layer in (b) and (c). Error bars represent the 1σ margin, estimated from repeated simulations, as described in chapter 6.3.

In contrast to the thicknesses, the resistances of the boundary layers are only insignificantly dependent on the root mean square roughness of the substrate. The thermal contact resistances projected onto $z = 0$ drop, see annotation arrow (5) in of **Figure 6.24** and part (a) of **Figure 6.25**. The transition from substrate to filled polymer is wider but has a lower thermal resistance as there is spatial overlap between the substrate and particle zones with high thermal conductivity. It is particularly interesting to consider the geometric boundary layer. This layer grows significantly with increasing roughness depth, but its thermal resistance is less affected, see parts (b) and (c) of **Figure 6.25**. The impact on applications with thin filled polymer layers is discussed in chapter 6.6.

The simplified, simulative study has shown that the roughness depth can have a noticeable effect on the particle arrangement close to the substrate and thus on the geometric boundary layer. This in turn affects the thermal boundary layer and the resulting thermal contact resistances. It can be assumed that the described thermal effects at an FPS transition shift for other ratios of particle size to surface roughness or when a surface skewness is introduced but remain qualitatively the same.

A further experimental study on the influence of surface roughness can confirm the results obtained by simulation. The aluminum substrates introduced in section 3.1.3 were used for this purpose, with a root mean square roughness in the range $1.8\ \mu\mathrm{m} \leq S_\mathrm{q} \leq 4.5\ \mu\mathrm{m}$. The samples were prepared with Epoxy E01, mixed with the two spherical alumina fillers Alox-S-22 and Alox-S-63 at $\phi = 0.4$. **Figure 6.26** shows the values measured for the specific thermal contact resistances (a) and the thicknesses of the thermal boundary layers (b) as a function of the root mean square roughness.

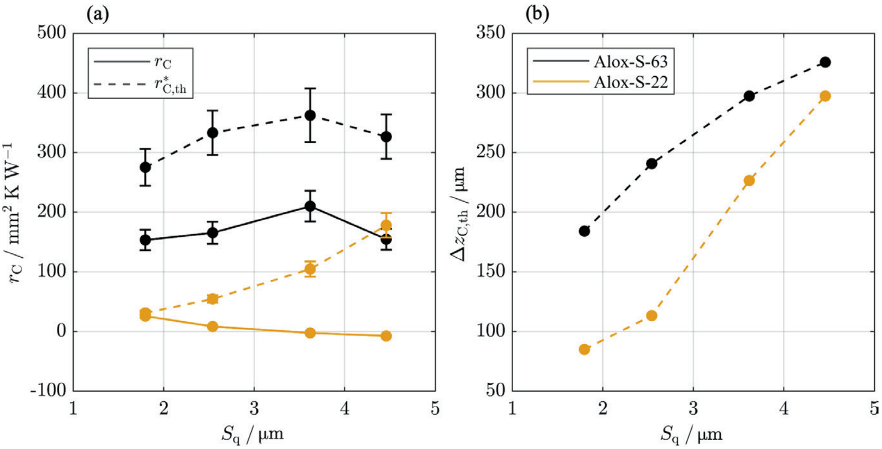

Figure 6.26. Specific thermal contact resistance and thermal boundary layer thickness as a function of the substrate's root mean square roughness.

Measured using the micro thermography method, described in chapter 3.3. Connecting lines are only shown for better visualization and interpretation. Polymer: Epoxy E01. Fillers: Alox-S-22, Alox-S-63, Substrates: SUB-R0, SUB-R1, SUB-R3, SUB-R4. Error bars show the systematic uncertainties of the measurement.

The black data points and lines indicate the results with Alox-S-63 and the orange data points and lines show the results with Alox-S-22. Solid lines show thermal contact resistances projected onto $z = 0$. Dashed lines refer to the evaluated thermal boundary layers.

Despite the uncertainty associated with the image blurriness in micro thermography when identifying boundary layers, the results are in good qualitative agreement with the simulative findings. A clear increase in the boundary layer thickness and its thermal resistance can be seen with Alox-S-22. The projected thermal contact resistances decrease slightly and even reach a negative level. Considering part (d) of **Figure 6.24**, evidently negative thermal contact resistances are quite likely with sufficient roughness depth. However, this is dependent on the ratio of particle size to surface roughness, as well as the filler volume fraction and the PSD configuration, so it cannot be generalized. With Alox-S-63, significantly higher thermal contact resistances and thicker boundary layers are observed due to the particles that are approximately three times larger. The difference between the thermal resistance of the boundary layer and the projected value is not as clear as with Alox-S-22, which is due to the significant increase in the ratio of particle size to roughness depth.

With the ratios of particle size to surface roughness shown in **Figure 6.23**, the particles can get into the surface valleys between the asperities. However, as the lateral surface structure becomes finer, it is likely that beyond a certain threshold, particles can no longer penetrate these valleys, which leads to other geometric effects within the boundary layers. These effects are investigated in a further simplified simulation study. The root mean square roughness is fixed at $\mathrm{S_q} = 2.0\ \mu\mathrm{m}$ and the lateral structure is modified by scaling the surface in the x and y directions. The resulting autocorrelation length of the surface is evaluated, while retaining all other model parameters identical to those in the previous study.

Figure 6.27 shows central cross-sections through the modeled RVEs with decreasing autocorrelation length S_{al} of the substrate surfaces. The largest autocorrelation length considered is $S_{\mathrm{al}} = 12.27\ \mu\mathrm{m}$, which is slightly above the median particle size of $D_{50} = 10\ \mu\mathrm{m}$. Even the larger particles can enter the surface valleys. This ability decreases with decreasing autocorrelation length. The smallest autocorrelation length considered is $S_{\mathrm{al}} = 1.93\ \mu\mathrm{m}$, well below the median particle size of $D_{50} = 10\ \mu\mathrm{m}$. The threshold at which the majority of the particles can no longer enter the surface valleys is between $S_{\mathrm{al}} = 5.43\ \mu\mathrm{m}$ and $S_{\mathrm{al}} = 2.60\ \mu\mathrm{m}$. **Figure 6.28** presents the $\phi(z)$ and $r(z)$ curves calculated based on the RVEs illustrated in **Figure 6.27**. Parts (a) and (c) again show the entire RVE and parts (b) and (d) show a close-up of the FPS transition. **Figure 6.29** supports the analysis by comparing the evaluated projected specific contact resistances r_{C} as well as the thicknesses $\Delta z_{\mathrm{C,geo}} = \Delta z'_{\mathrm{C,geo}} + \Delta z''_{\mathrm{C,geo}}$ and specific thermal resistances $r^*_{\mathrm{C,geo}}$ of the geometric boundary layers. All quantitative results of the study are provided in appendix D.3, **Table D.4**.

The previously qualitatively predicted effect, that the particles are unable to enter deeply into the surface valleys as the lateral structure becomes finer, is evident in parts (a) and (b) of **Figure 6.28**. The increase in the filler volume fraction shifts further and further away from $z = 0$ with decreasing autocorrelation length, see annotation arrow (1). This leads to thicker geometric boundary layers, see annotation arrow (2) in **Figure 6.28** and part (b) of **Figure 6.29**. An interesting observation that can be made with the $r(z)$ curves in part (c) of **Figure 6.28** is the almost perfect alignment of the curves for $S_{\mathrm{al}} = 12.27\ \mu\mathrm{m}$ and $S_{\mathrm{al}} = 5.43\ \mu\mathrm{m}$, except for stochastic variations. For the smaller autocorrelation lengths, the thermal resistance curve shifts upwards, see annotation arrow (3).

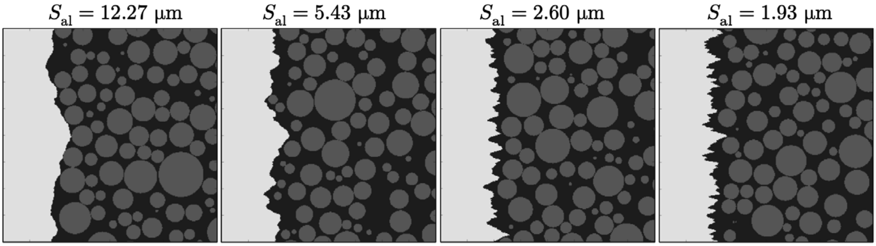

Figure 6.27. Modeled FPS transitions with varying lateral surface structure.
Central cross-sections of RVEs. Random loose packing of spherical particles with log-normal size distribution with $\log(\sigma) = 0.2$ and $D_{50} = 10\ \mu\mathrm{m}$. Substrate: Artificial random rough surface from **Figure 6.1**, scaled to $\mathrm{S_q} = 2.0\ \mu\mathrm{m}$.

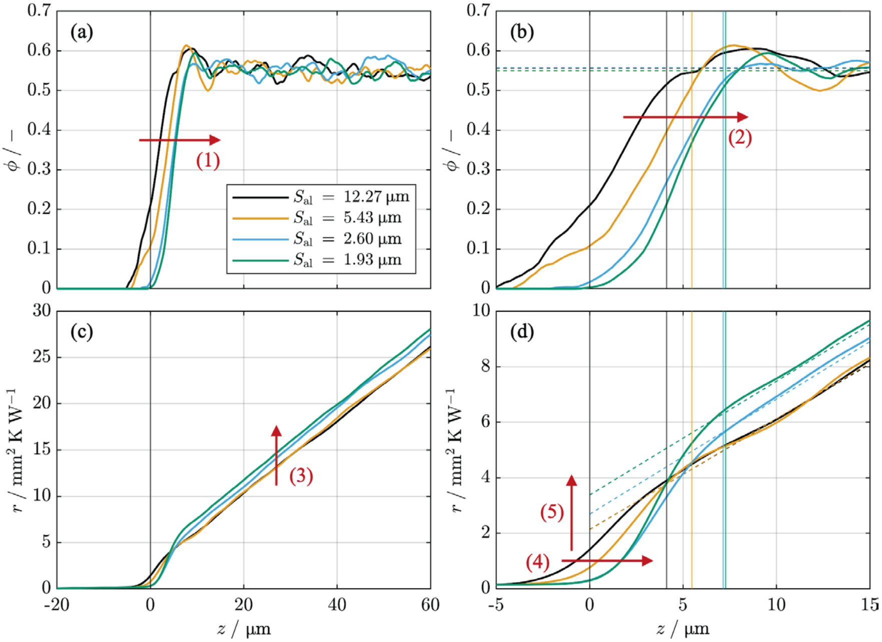

Figure 6.28. Filler volume fraction and cumulative specific thermal resistance curve across an FPS transition with varying surface autocorrelation length.

Curve of filler volume fraction along the z axis of the modeled filler packing in (a) and (b). Calculated cumulative specific thermal resistance in (c) and (d). Overall representations in (a) and (c). Magnified view of the boundary layer in (b) and (d). Polymer: $\lambda_C = 0.25$ W m^{-1} K^{-1} (e.g., epoxy). Filler: Spheres with log-normal size distribution with $\log(\sigma) = 0.2$, $D_{50} = 10$ µm, $\phi = \phi_{max} \approx 0.55$, $\lambda_D = 35$ W m^{-1} K^{-1} (e.g., alumina). Substrate: Artificial random rough surface, see **Figure 6.1**, scaled to $S_q = 2.0$ µm, $\lambda_S = 130$ W m^{-1} K^{-1} (e.g., aluminum alloy). Results, see appendix D.3, **Table D.4**.

The projected thermal contact resistances increase, see part (a) of **Figure 6.29**. This effect is caused by the geometric and thermal effects in the boundary layer, see part (d) of **Figure 6.28**. A decreasing autocorrelation length of the surface leads to better heat conduction in the substrate layers and thus to the right shift of the $r(z)$ curve in the boundary layer, see annotation arrow (4). However, the later the filler packing forms, the steeper the increase in resistance and thus the higher the thermal contact resistance, see annotation arrow (5) in **Figure 6.28** and parts (a) and (c) of **Figure 6.29**. The threshold which was found purely geometrically in **Figure 6.27** is identifiable from a thermal point of view. Due to the lateral fineness of the surface, there is a significant increase in thermal contact resistance as the particles can no longer enter the valleys. Before that, the effects in the boundary layer shift, while the macroscopically perceptible thermal resistances remain the same, see part (a) of **Figure 6.29**.

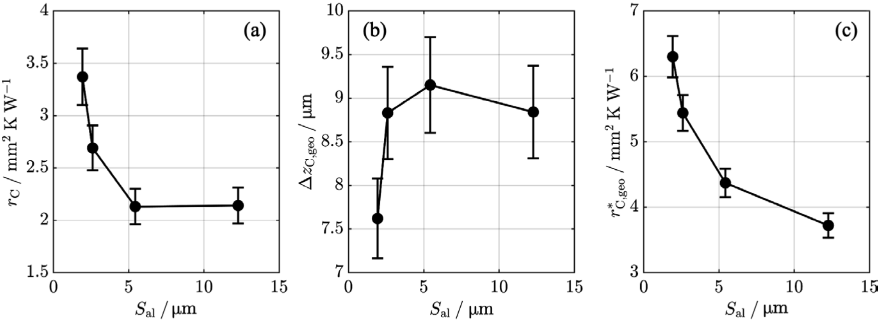

Figure 6.29. Specific thermal contact resistance of an FPS transition and geometric boundary layer thickness with varying surface autocorrelation length.

Results of the study shown in **Figure 6.28**. Projected thermal contact resistance r_C in (a). Thickness $\Delta z_\mathrm{C,geo} = \Delta z'_\mathrm{C,geo} + \Delta z''_\mathrm{C,geo}$ and specific thermal resistance $r^*_\mathrm{C,geo}$ of geometric boundary layer in (b) and (c). Error bars represent the 1σ margin, estimated from repeated simulations, as described in chapter 6.3.

This study also simplifies the geometric conditions at an FPS transition, so the results are not completely generalizable. The observation that oversized particles, which cannot penetrate surface valleys, result in thicker boundary layers is applicable to a wide range of material systems. However, the specific thermal effects must be assessed individually.

Another qualitative simulation study can examine the superimposed effect of substrate roughness depth and particle size distribution. While otherwise similar to the study already presented in **Figure 6.13**, page 189, this study uses the artificial random rough surface from **Figure 6.1**, page 167, instead of an ideally flat substrate. **Figure 6.30** shows the $\phi(z)$ and $r(z)$ curves calculated for FPS transitions with a rough substrate surface and filler packings with varying width of the particle size distribution. The surface is scaled to $S_\mathrm{q} = 2.0\ \mu\mathrm{m}$, with an autocorrelation length of $S_\mathrm{al} = 5.43\ \mu\mathrm{m}$. All other model parameters are identical with the previous study. Steady-state heat conduction is calculated with $\lambda_\mathrm{S} = 130$ W m^{-1} K^{-1}, $\lambda_\mathrm{C} = 0.25$ W m^{-1} K^{-1}, and $\lambda_\mathrm{D} = 35$ W m^{-1} K^{-1}. The average particle size is $D_{50} = 10\ \mu\mathrm{m}$. Log-normal size distributions of the ideally spherical particles are considered with $\sigma = 0$, $\log(\sigma) = 0.2$, and $\log(\sigma) = 0.4$. Again, parts (a) and (c) show the entire RVE and parts (b) and (d) show a magnified view of the FPS transition.

Figure 6.31 supports the analysis by comparing the evaluated projected specific contact resistances r_C as well as the thicknesses $\Delta z_\mathrm{C,geo} = \Delta z'_\mathrm{C,geo} + \Delta z''_\mathrm{C,geo}$ and specific thermal resistances $r^*_\mathrm{C,geo}$ of the geometric boundary layers. All quantitative results of the study are provided in appendix D.3, **Table D.5**.

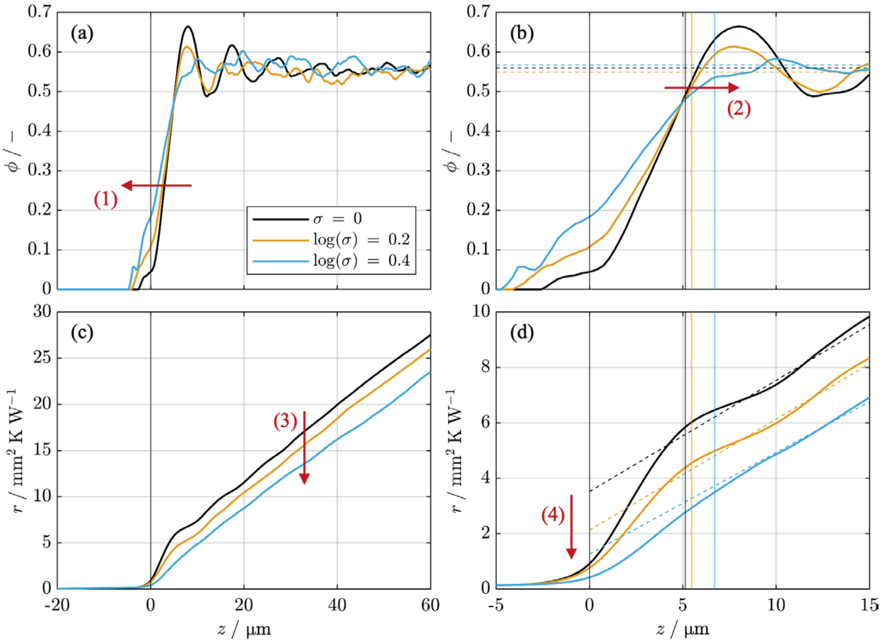

Figure 6.30. Filler volume fraction and cumulative specific thermal resistance curve across an FPS transition with different widths of the particle size distributions.

Curve of filler volume fraction along the z axis of the modeled filler packing in (a) and (b). Calculated cumulative specific thermal resistance in (c) and (d). Overall representations in (a) and (c). Magnified view of the boundary layer in (b) and (d). Polymer: $\lambda_C = 0.25$ W m^{-1} K^{-1} (e.g., epoxy). Filler: Spheres with log-normal size distribution, $D_{50} = 10$ µm, $\phi = \phi_{\max} \approx 0.55$, $\lambda_D = 35$ W m^{-1} K^{-1} (e.g., alumina). Substrate: Artificial random rough surface with $S_q = 2.0$ µm, see **Figure 6.1**, $\lambda_S = 130$ W m^{-1} K^{-1} (e.g., aluminum alloy). Full surface wetting. Results, see appendix D.3, **Table D.5**.

Seen in part (a) of **Figure 6.30** is an earlier increase in the volume fraction with increasing width of the particle size distribution, see annotation arrow (1), as already observed in **Figure 6.13**, page 189. At the same time, the end of the geometric boundary layer shifts to the right, see annotation arrow (2) in part (b) of **Figure 6.30** and part (b) of **Figure 6.31**. In comparison with **Figure 6.13**, page 189, it is visible that the rough surface leads to better intermixing of the near-surface particle layers and thus to a less pronounced oscillation of the volume fraction, especially for $\sigma = 0$. With increasing width of the particle size distribution, the thermal contact resistances at the FPS transitions decrease, see part (c) of **Figure 6.30** and part (a) of **Figure 6.31**. The slope of the $r(z)$ curve in the bulk region is approximately constant. The difference in the position of the curves, see annotation arrow (3), is caused solely by the thermal contact resistance.

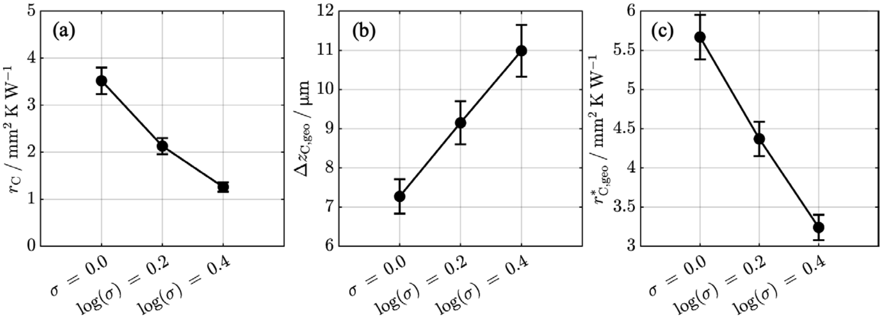

Figure 6.31. Specific thermal contact resistance of an FPS transition and geometric boundary layer thickness with different widths of the particle size distributions.

Results of the study shown in **Figure 6.30**. Projected thermal contact resistance r_C in (a). Thickness $\Delta z_{C,geo} = \Delta z'_{C,geo} + \Delta z''_{C,geo}$ and specific thermal resistance $r^*_{C,geo}$ of geometric boundary layer in (b) and (c). Error bars represent the 1σ margin, estimated from repeated simulations, as described in chapter 6.3.

The resistance contributions of the boundary layers are shown in detail in part (d) of **Figure 6.30**. There is a smaller increase in the resistance curve for wider particle size distribution and consequently lower thermal contact resistances, see annotation arrow (4) in part (d) of **Figure 6.30** and part (c) of **Figure 6.31**. Therefore, the results are similar to those of the previous study with an ideally smooth surface in **Figure 6.13**, page 189, but much more pronounced. The rough surface supports intermixing of the particle packing, reduces the layer formation, and the roughness peaks which protrude far into the filled polymer serve as efficient parallel heat paths. In addition to the surface asperities, the lower increase in resistance of the boundary layer is due to the higher average volume fraction of the filler particles in the boundary layer, see part (b) of **Figure 6.30**.

Taking the equally sized spheres with $\sigma = 0$ as a reference, the specific thermal contact resistance projected onto $z = 0$ drops with increasing width of the particle size distribution. A reduction of $64\ \%$ is calculated for $\log(\sigma) = 0.4$. With an ideally smooth surface, see **Figure 6.14**, page 190, the reduction was only $34\ \%$.

In the simulated cases, the substrate only minimally affects the packing formation for wide particle size distributions. With narrower particle size distributions however, the rough substrate surface negatively impacts the packing formation. The specific thermal resistances of the geometric boundary layers are higher for the equally sized spheres compared to the results with an ideally smooth surface (**Figure 6.14**, page 190), but they also drop more significantly. This is due to the superimposed effects of the rough substrate surface. For the geometric boundary layer, for example, a reduction of $43\ \%$ can be evaluated for $\log(\sigma) = 0.4$. For an ideally smooth surface, it was only $25\ \%$. The boundary layers are systematically thicker in the calculations with a rough substrate surface than with a smooth surface and increase systematically with increasing width of the particle size distribution.

Basically, the study shown in **Figure 6.13** and **Figure 6.14** was better suited to analyze the individual effect of the particle size distribution. The current results reflect overlapping influences of roughness and distribution. From the differences in the results, the individual effect of the rough surface can be derived as a good approximation. For all geometrically similar FPS transitions, it can be generalized that both a rough surface and a broader particle size distribution lead to a broadening of the boundary layers, but concurrently to a reduction in thermal resistance.

6.4.4 LOCAL VARIATIONS

In all previous studies, the thermal contact resistances at FPS transitions were evaluated as area-averaged values. At the same time, it has been shown that the local thermal contact resistances are strongly stochastic, and both the simulations and experiments produce results with noticeable variations. This is because, unlike the studies on thermal conductivity in chapters 4 and 5, the analysis is on a local effect in comparatively thin boundary layers rather than a large-volume phenomenon. This chapter presents a local evaluation of thermal contact resistances and the determination of scattering quantities.

The analysis is carried out on a typical micro thermography study. Measurements were performed on a multi-layered sample, consisting of a filled epoxy layer in between two aluminum substrates SUB-R1. Alox-S-63 is used as filler with $\phi = 0.5$. Measurements were made on all four side surfaces of the sample. Unlike in the previous sections, the thermal images are divided into 20 equally wide intervals along the x axis, and the thermal resistance curves are evaluated separately for each interval. **Figure 6.32** presents the thermal contact resistances projected onto $z = 0$ for all 20 intervals on all four sample surfaces. In addition to the quantitative evaluation of the local thermal contact resistances in part (c), and the distribution graphs of evaluated specific thermal contact resistances in (d), a section of a micrograph of the first surface is shown in part (a), as well as a section of the corresponding thermal image in part (b). A thermal image with a total width of just over 16 mm is evaluated. The thermal contact resistances vary from $r_\mathrm{C} = 91\ \mathrm{mm^2\ K\ W^{-1}}$ to $r_\mathrm{C} = 143\ \mathrm{mm^2\ K\ W^{-1}}$ with a mean value of $115\ \mathrm{mm^2\ K\ W^{-1}}$. The standard deviation of all evaluated intervals on all four surfaces is $16\ \mathrm{mm^2\ K\ W^{-1}}$, which is just below $14\ \%$. The results of the individual surfaces are:

- Surface 1: $r_\mathrm{C} = (119 \pm 12)\ \mathrm{mm^2\ K\ W^{-1}}$,
- Surface 2: $r_\mathrm{C} = (113 \pm 8)\ \mathrm{mm^2\ K\ W^{-1}}$,
- Surface 3: $r_\mathrm{C} = (115 \pm 9)\ \mathrm{mm^2\ K\ W^{-1}}$,
- Surface 4: $r_\mathrm{C} = (116 \pm 8)\ \mathrm{mm^2\ K\ W^{-1}}$.

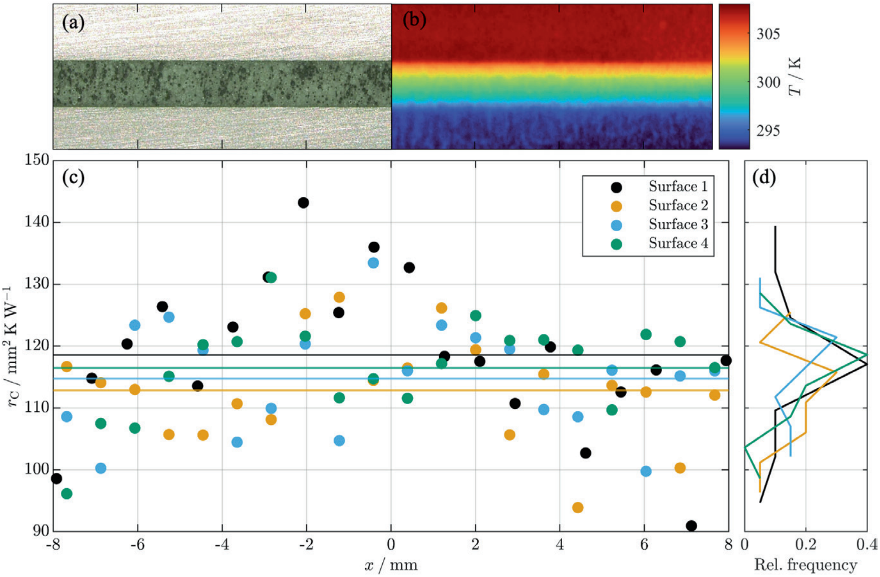

Figure 6.32. Local thermal contact resistances of a multi-layered sample.

Section of a micrograph of multi-layered sample, taken with a digital light microscope VHX with a dual-light high-magnification zoom lens VH-Z250R from Keyence in (a). Section of steady-state temperature field on sample surface 1, captured with the micro thermography setup described in chapter 3.3 in (b). Comparison of local thermal contact resistances, measured with micro thermography on four sample surfaces in (c). Solid lines represent the average value of the respective samples surface. Distribution functions of evaluated contact resistances in (d). Polymer: Epoxy E01. Filler: Alox-S-63, $\phi = 0.5$, $D_{50} = 63.4$ µm.

The good agreement between the mean values of all four sample surfaces verifies the reproducibility of the measurements with globally homogeneous samples. However, the extreme variations between the intervals show that the thermal contact resistances are a strongly stochastically affected phenomenon, confirming the previous findings of the high dependency on the formation of the local microstructure. Random particle arrangements and rough surfaces lead to random particle-substrate contacts or proximities which can significantly reduce local thermal resistances. As a result, averaging over larger areas remains a practical and meaningful approach. Accurately predicting thermal contact resistance in small-scale samples is challenging. This also calls into question how well simplified model systems can represent the complexity of real-world applications. The investigations in the previous sections have shown general trends and qualitative relationships but were based on highly simplified models and material combinations. An exact quantification of the thermal contact resistances is only possible if the material structures within the boundary layers of real applications are known, spatially uniform, and reproducible.

6.5 EFFECTS OF THE COMPONENTS THERMAL CONDUCTIVITIES

This chapter presents the results of a further purely simulative study on the impact of the thermal conductivities of substrate, polymer, and filler on thermal contact resistances at FPS transitions. Effects of the microstructure are intentionally excluded here by using a consistent microstructural model across all simulations. A representative microstructure was modeled with an artificial random rough surface with $S_\mathrm{q} = 2.0\ \mathrm{\mu m}$, $S_\mathrm{al} = 5.43\ \mathrm{\mu m}$, and a filler packing with ideally spherical particles with $D_{50} = 10\ \mathrm{\mu m}$ and $\log(\sigma) = 0.2$. For this, calculations were made with different thermal conductivity combinations of the components. The ϕ_max configuration was considered with $\mathrm{PSD} = \mathrm{PPD} = 0$. In appendix D.4, **Table D.6**, the quantitative results are given as the effective thermal conductivity λ_eff of the filled polymer, as well as the specific thermal contact resistances r_C projected onto $z = 0$, and the specific thermal resistances of the geometric boundary layer $r^*_\mathrm{C,geo}$.

Figure 6.33 shows the $\phi(z)$ curve of the modeled filler packing in parts (a) and (b), as well as the calculated $r(z)$ curves for all investigated thermal conductivity combinations in part (c). **Figure 6.34** supports the analysis by illustrating how the projected specific contact resistances r_C and the specific thermal resistances $r^*_\mathrm{C,geo}$ of the geometric boundary layers vary with the thermal conductivities of the individual components. The calculated contact resistances are given relative to an initial value r_0, obtained using $\lambda_\mathrm{C} = 0.3\ \mathrm{W\ m^{-1}\ K^{-1}}$, $\lambda_\mathrm{D} = 50\ \mathrm{W\ m^{-1}\ K^{-1}}$, and $\lambda_\mathrm{S} = 100\ \mathrm{W\ m^{-1}\ K^{-1}}$. These values reflect a combination of materials that is typical in technical applications. Part (c) of **Figure 6.33** illustrates the calculated $r(z)$ curves in a set of plots with different combinations of thermal conductivities for the substrate, the polymer, and the filler in the range of $-5\ \mathrm{\mu m} \le z \le +20\ \mathrm{\mu m}$. Substrate thermal conductivities of $10\ \mathrm{W\ m^{-1}\ K^{-1}} \le \lambda_\mathrm{S} \le 200\ \mathrm{W\ m^{-1}\ K^{-1}}$ are considered in ascending order from top to bottom. From left to right, ascending polymer thermal conductivities are examined in the range $0.10\ \mathrm{W\ m^{-1}\ K^{-1}} \le \lambda_\mathrm{C} \le 0.50\ \mathrm{W\ m^{-1}\ K^{-1}}$. Filler thermal conductivities are considered in the range $10\ \mathrm{W\ m^{-1}\ K^{-1}} \le \lambda_\mathrm{D} \le 150\ \mathrm{W\ m^{-1}\ K^{-1}}$ and are visualized by the colored curves.

Due to the constant microstructure in all cases, the geometric conditions and thus the geometric boundary layer are constant, see vertical dashed lines in parts (b) and (c). As expected, the $r(z)$ curves look qualitatively similar in all cases, see **Figure 6.33** part (c).

However, the thermal resistance contributions from the substrate, boundary layer, and bulk decrease systematically as the thermal conductivities of the individual components increase. This trend is also illustrated in **Figure 6.34**. All thermal resistance values decline with increasing thermal conductivity of the components.

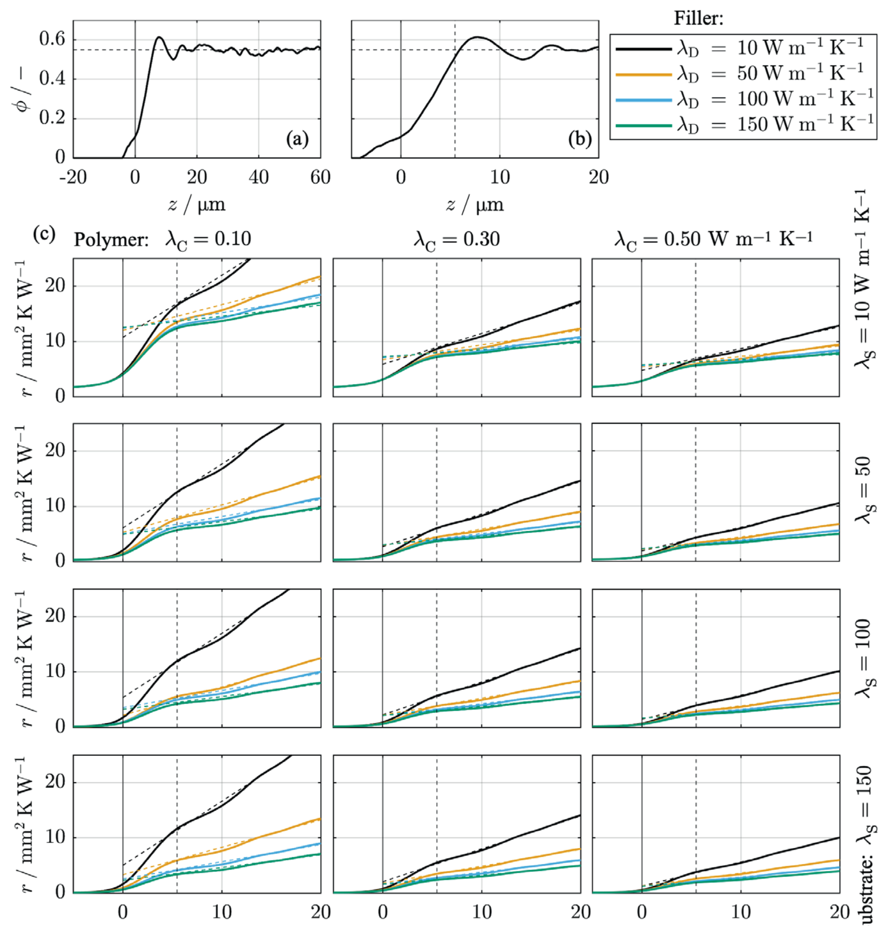

Figure 6.33. Filler volume fraction and cumulative specific thermal resistance curve across an FPS transition with different components' thermal conductivities.

Curve of filler volume fraction along the z axis of the modeled filler packing in (a) and (b). Calculated cumulative specific thermal resistance for different thermal conductivity combinations in (c). Filler: Spheres with log-normal size distribution with $\log(\sigma) = 0.2$, $D_{50} = 10$ µm, $\phi = \phi_{\max} \approx 0.55$. Substrate: Artificial random rough surface with $S_q = 2.0$ µm, see **Figure 6.1**. Full surface wetting. Results, see appendix D.4, **Table D.6**.

An exception is observed in the behavior of r_C in part (a), which shows a non-intuitive response to changes in polymer thermal conductivity λ_C. This is due to the overlapping influences of the thermal conductivities of all three components.

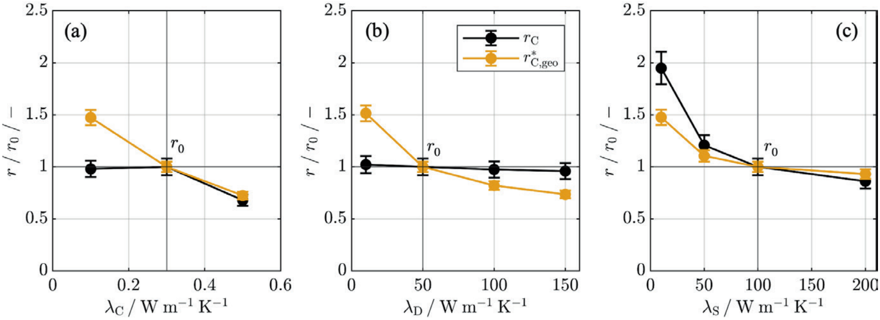

Figure 6.34. Normalized specific thermal contact resistance of an FPS transition with different components' thermal conductivities.

Results of the study shown in **Figure 6.33**. All results are given relative to the reference value r_0, obtained from an initial calculation using $\lambda_C = 0.3$ W m^{-1} K^{-1}, $\lambda_D = 50$ W m^{-1} K^{-1}, and $\lambda_S = 100$ W m^{-1} K^{-1}. Variation of the polymer's thermal conductivity λ_C in (a). Variation of the filler's thermal conductivity λ_D in (b). Variation of the substrate's thermal conductivity λ_S in (c). Error bars represent the 1σ margin, estimated from repeated simulations, as described in chapter 6.3.

The projected thermal contact resistance r_C only reflects the additional resistance introduced by the contact, based on an assumption of uniform bulk thermal conductivity. At very low polymer thermal conductivity, the effective thermal conductivity of the filled polymer is also low, reducing the relative impact of contact resistance compared to cases with higher polymer thermal conductivity. Overall, the results indicate that the polymer exhibits the greatest potential for reducing thermal contact resistance within the parameter space investigated. Starting from the intermediate parameter set ($\lambda_C = 0.3$ W m^{-1} K^{-1}, $\lambda_D = 50$ W m^{-1} K^{-1}, $\lambda_S = 100$ W m^{-1} K^{-1}), increasing λ_C to 0.5 W m^{-1} K^{-1} reduces $r^*_{C,geo}$ by 28 %. Increasing λ_D to 150 W m^{-1} K^{-1} results in a 27 % reduction and increasing λ_S to 200 W m^{-1} K^{-1} results in a 16 % reduction. This again emphasizes the fact that the contact resistances are primarily caused by reduced filler volume fractions and thus polymer accumulations in the boundary layers. The impact of polymer thermal conductivity is correspondingly high.

If the analysis is started from a scenario with a very highly thermally conductive substrate (e.g., $\lambda_S = 200$ W m^{-1} K^{-1}), the impact of the filler's thermal conductivity becomes dominant. At $\lambda_C = 0.1$ W m^{-1} K^{-1}, $r^*_{C,geo}$ drops by 72 % when the filler's thermal conductivity is increased from 10 W m^{-1} K^{-1} to 150 W m^{-1} K^{-1}. The effect is due to both substrate and filler. If both have a very high thermal conductivity, they can form very highly conductive local heat paths, which overshadow the effect of the polymer. However, if the substrate or filler thermal conductivity is < 100 W m^{-1} K^{-1}, the most dominant parameter is the polymer's thermal conductivity.

6.6 THIN LAYER PHENOMENA

This final chapter deals with the effect of FPS transitions on heat conduction across very thin filled polymer layers. Particularly thin filled polymer layers are commonly used in applications such as insulated metal substrates (IMS) or thermal greases in electronics [8,9,11,13,14]. The term "thin" must be understood in relation to the size of the utilized filler particles. In this context, layers are considered "thin" if they allow only a few particle layers (≤ 10) to form between the two solid surfaces to be contacted. As previous studies have shown, thermal contact resistance at FPS transitions is not an isolated phenomenon only occurring at the contact surface. Noticeable boundary layers are formed in which the thermal resistance increases strongly. As the filled polymer layer becomes thinner, the influence of the boundary layers increases. Micro thermography can be used to show that in extreme cases, the boundary layers of the FPS transitions occupy almost the entire filled polymer layer, thus preventing an undisturbed bulk zone from forming in between. **Figure 6.35** shows a typical micrograph (a) of a multi-layered sample with a thin filled polymer layer, and the specific thermal resistance curve measured across this sample (b). The coarse-grained Alox-S-63 is chosen for better resolution of the phenomenon. The filled polymer layer is applied with a thickness of $596\ \mu\mathrm{m}$ between two aluminum substrates SUB-R0. The measured total specific thermal resistance of the multi-layered sample is approximately $500\ \mathrm{mm}^2\ \mathrm{K}\ \mathrm{W}^{-1}$. The two surface levels are marked with $z_{\mathrm{C},1}$ and $z_{\mathrm{C},2}$. For better visualization, only a portion of the actual measured sample thickness is shown. Most of the actual substrate area is removed. The two regression lines with the slopes $(\mathrm{d}r/\mathrm{d}z)_{\mathrm{S1}} = (\mathrm{d}r/\mathrm{d}z)_{\mathrm{S2}} = \lambda_{\mathrm{S}}^{-1}$ are drawn to approximate the resistance progression in the substrates.

The two boundary layers take up a large part of the entire filled polymer layer, and only in the very center there is an approximately linear section that can theoretically be identified as bulk. The image blurriness is undoubtedly an important factor in micro thermography, causing high uncertainties in the boundary layer identification. However, as long as the $r(z)$ curve is approximately linear within the bulk region, an evaluation of the bulk thermal conductivity would still be possible. Analysis of the example in **Figure 6.35** yields a bulk thermal conductivity of $\lambda_{\mathrm{eff}} = (\mathrm{d}r/\mathrm{d}z)_{\mathrm{bulk}}^{-1} = 2.04\ \mathrm{W}\ \mathrm{m}^{-1}\ \mathrm{K}^{-1}$. This value is unrealistically high when compared with the result from **Figure 3.15**, page 69. In that example, the same filler was used at the same filler volume fraction but in a layer with roughly twice the thickness. The thermal conductivity was measured at only $\lambda_{\mathrm{eff}} = 1.66\ \mathrm{W}\ \mathrm{m}^{-1}\ \mathrm{K}^{-1}$. When analyzing the corresponding micrograph in part (a), it is evident that the identified bulk region contains just three to four particle layers. The comparison between **Figure 6.35** and **Figure 3.15**, page 69, illustrates that this thin filled polymer layer does not exhibit macroscopically averageable behavior. In the present example, the two boundary layers effectively merge, leaving no measurable bulk region between them. This is an important finding that is only possible through the microscopic resolution of the thermal resistance. The analysis of such layers with macroscopic methods and zero gap extrapolation would be associated with considerable errors. Filled polymer layers with such a size ratio of particles to layer thickness can only be measured as a whole and described with an apparent thermal conductivity, see **Figure 2.3**, page 18.

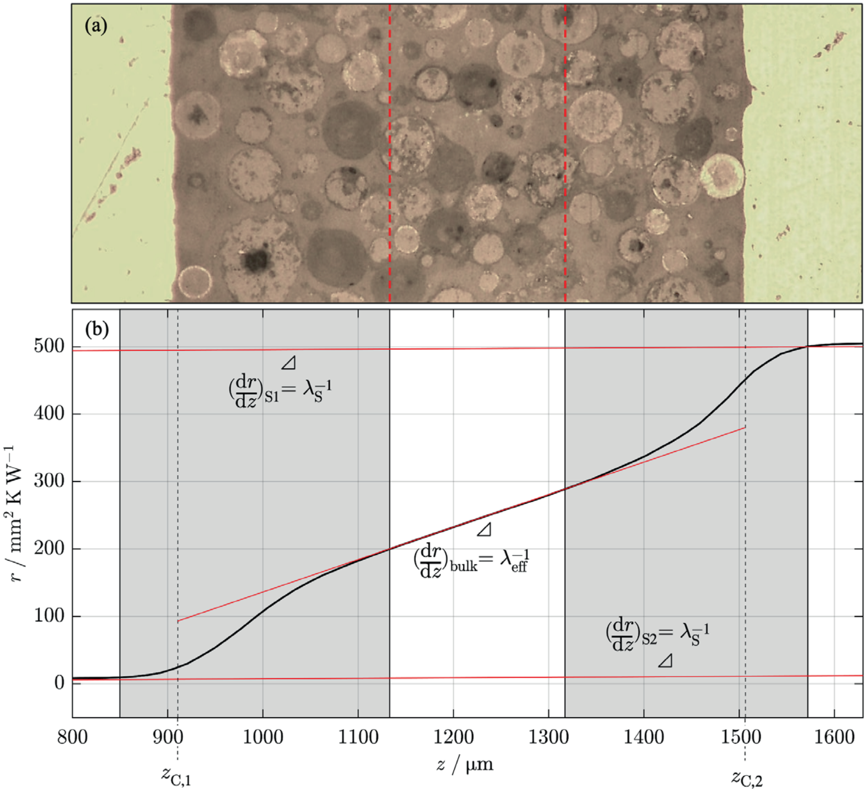

Figure 6.35. Exemplary micro thermography result of a thin-layer sample. Cumulative thermal resistance curve across a multi-layered sample with two aluminum substrates and a thin filled polymer layer. Polymer: Epoxy E01. Filler: Alox-S-63, $\phi = 0.5$, $D_{50} = 63.4\ \mu\mathrm{m}$. Substrate: SUB-R0. Based on [0].

6.7 CHAPTER SUMMARY AND CONCLUSION

This chapter presented experimental and simulative studies on the occurrence of thermal contact resistance at filled polymer to substrate (FPS) transitions, along with a discussion of the results. The focus was on the description of geometric effects at the FPS transition. The disturbance of the particle packing by an adjacent substrate leads to reduced filler volume fractions at the interface, resulting in increased thermal resistances. Chapter 6.1

describes the modification of the microscale simulation approach presented initially in chapter 4.1 to describe heat conduction across FPS transitions. The substrate surface and adjacent filler packing are resolved in geometric detail. In contrast to the previous chapters, the focus of this chapter is not on a macroscopically averaged quantity but on the detailed local processes at the interface. New definitions and evaluation strategies were introduced in chapter 6.2 and chapter 6.3 for the precise description and analysis of these local interfacial phenomena. Chapter 6.4 described experimental and simulative studies on the microstructure effects on heat conduction across FPS transitions. Finally, chapter 6.5 dealt with the impact of the thermal conductivities of the components, and chapter 6.6 with the difficulties encountered in practical applications when describing heat conduction across very thin filled polymer layers.

The studies show that thermal contact resistances are highly stochastic, so that large areas are required for averaging to obtain representative results. Both simulations and measurements on different samples yield considerable variations. Local particle-substrate contacts and particle accumulations in the boundary layers affect the thermal contact resistances considerably. The effective thermal conductivity in a filled polymer is also strongly affected by stochastics. However, the effect is significantly lower since it is always determined as a large-volume mean value and not limited to comparatively thin layers.

Accurately predicting and precisely describing the microstructure and particle packing in the boundary layers remains a significant and largely unresolved challenge. Micrographs only provide a rough indication of the formation of particle-substrate contacts. Large uncertainties remain in the geometric modeling of the boundary layers. The presented micro thermography experiments have qualitatively confirmed the simulative predictions but remain subject to the same limitations and further uncertainties due to image blurriness. It is assumed that the microstructure formation in the boundary layers is significantly dependent on the manufacturing process, therefore it is only reproducible to a limited extent on a laboratory scale. To suppress this effect, numerous simulative studies were carried out with ϕ_{max} configurations, in which all particles are in ideal contact with the substrate. Although this limits the transferability and generalizability of the results, it enabled an isolated investigation of the influence of surface structure and particle size distribution.

For the parameter combinations studied, it can generally be concluded that surfaces with greater roughness depths or particle packings with a wider particle size distribution lead to a broadening of the boundary layers, but also reduce the thermal contact resistances. They prevent the excessive formation of a micro-order directly on the substrate surface, which is correlated to the strong reduction in filler volume fraction in the boundary layer. In many material combinations, the polymer is also a bottleneck in the FPS transition. The most significant reduction in thermal contact resistance can be achieved by increasing its thermal conductivity.

7 SUMMARY AND CONCLUSION

Within the scope of this work, experimental and simulative techniques were used to investigate the microstructural and thermal influences on heat conduction in filled polymers and across FPS transitions. The focus was on the effective thermal conductivity of single-scale filled polymers and multi-scale filled polymers, as well as the thermal contact resistances and boundary layer thicknesses at FPS transitions. The steady-state cylinder method according to ASTM D5470-17 [184] was used for macroscopic measurement of effective thermal conductivities. A new method based on micro thermography was developed and successfully applied for the microscopic resolution of thermal resistances across FPS transitions [0]. This method provided new awareness of thermal contact resistances between substrate surfaces and filled polymers that were previously inaccessible by measurement.

Simulation methods were developed and used to reduce experimental effort as well as to carry out studies on length scales that were not experimentally accessible. The effective thermal conductivity of single-scale filled polymers and the heat conduction across FPS transitions could be simulated in full geometric detail, accounting for particle shapes, particle size distributions, and substrate structures. The suitability of the simulation approach for the description of heat conduction in filled polymers was confirmed by satisfactory validation of the results. For the significantly more complex microstructure of multi-scale filled polymers, a multi-step homogenization approach was developed. This enabled a detailed description of all individual size fractions with stepwise superimposition of their impact on the effective thermal conductivity. Good validation results were also achieved with this simulation technique.

In addition to the effects of the thermal conductivities of the polymer, filler, and substrate, the investigation also assessed the impacts of thermal interfacial resistances and numerous microstructural parameters. These parameters include particle size distribution, particle shape, maximum packing density, particle orientation, agglomeration, and sedimentation. Numerous empirical theories were derived from the results and confirmed with experimental findings. Overall, these built a comprehensive picture of heat conduction in filled polymeric materials.

In experimental studies, the investigation started with single-scale filled polymers based on silicone rubber or epoxy with $\lambda_{\mathrm{C}} = (0.22 \ldots 0.28)\ \mathrm{W\ m^{-1}\ K^{-1}}$, modified with different fillers. The filler volume fractions were between $\phi = 0.2$ and $\phi = 0.6$, and the measured effective thermal conductivities were $\lambda_{\mathrm{eff}} = (0.37 \ldots 2.1)\ \mathrm{W\ m^{-1}\ K^{-1}}$. The experimental results and simulations allow the following conclusions to be drawn on the effective thermal conductivity of single-scale filled polymers:

- If a polymer is modified with a highly thermally conductive granular filler, the effective thermal conductivity increases superlinearly with filler volume fraction. A pronounced percolation threshold is not detectable.
- The effective thermal conductivity scales linearly with the polymer's thermal conductivity when the TC ratio and filler content are kept constant.
- The higher the thermal conductivity of the filler, the higher the effective thermal conductivity of the composite, with saturation occurring at a TC ratio of $\kappa \approx 100$, as the remaining polymer layers between the particles limit further increase.
- A higher maximum packing density of the filler requires a higher filler volume fraction to develop highly thermally conductive paths.
- The lower the sphericity of the filler particles, the lower the maximum packing density and filler volume fraction required for a desired effective thermal conductivity.
- A wider size distribution of the particles leads to a higher max. packing density and higher filler volume fraction required for a desired effective thermal conductivity.
- An inhomogeneous particle distribution results in only a minor increase in thermal conductivity compared to a homogeneous packing structure.
- Highly inhomogeneous filler distribution caused by agglomeration or sedimentation leads to a significant increase in effective thermal conductivity, as the influence of locally highly conductive paths and clusters dominates.
- The alignment of non-spherical, elongated particles along the heat flow direction increases the effective thermal conductivity, however the optimum is not $100\ \%$ alignment but a slightly random inclination of all particles.

Further experimental studies investigated multi-scale filled polymers based on epoxy with $\lambda_\mathrm{C} = 0.25\ \mathrm{W\ m^{-1}\ K^{-1}}$ and modified with different binary, ternary, and quaternary filler blends. The filler volume fractions were between $\phi = 0.4$ and $\phi = 0.77$. The measured effective thermal conductivities were $\lambda_\mathrm{eff} = (0.46 \dots 6.1)\ \mathrm{W\ m^{-1}\ K^{-1}}$. For multi-scale filled polymers, the conclusions that may be drawn are:

- If fillers from different size classes are combined and used with low to medium filler loading levels, the microstructure can be simplified as consisting of distinct fraction domains.
- Each individual fraction domain behaves like a single-scale filled polymer.
- Interfacial transitions zones (ITZs) form at the domain interfaces, which slightly reduce the effective thermal conductivity of the composite.
- In multi-scale filled polymers, the saturation limit is shifted for the coarser-grained fractions and more conductive fillers can perform up to their higher capabilities.
- When combining fillers of different maximum packing densities, the highest effective thermal conductivity is achieved by using the filler with the lowest maximum packing density in the fine-grained fraction.

For the experimental investigation into heat conduction processes across FPS transitions, multi-layered samples were prepared from aluminum substrates with different surface structures and filled epoxy composites. Spherical alumina fillers with $D_{50} = (7.9 \ldots 63.4)\ \mu\mathrm{m}$ in filler volume fractions of $\phi = 0.3 \ldots 0.6$ were used. The measurement results and observations from additional simulations allow the following conclusions to be drawn for thermal contact resistances at FPS transitions:

- If a filler packing at an FPS transition is geometrically disturbed by a substrate surface, a wall effect occurs. This causes the formation of particle layers and reduced filler volume fraction close to the substrate surface.
- The resulting boundary layer has reduced thermal conductivity and thus increased thermal resistance, which can be interpreted as the thermal contact resistance of the FPS transition.
- Greater roughness heights or wider particle size distributions cause wider boundary layers while reducing the local slope of the thermal resistance curve $r(z)$.
- The particle arrangement near the substrate is crucial, as local particle-substrate contacts create thermally conductive paths, reducing thermal contact resistances.
- The random formation of such local particle-substrate contacts leads to enormous local variations in thermal contact resistance. Only averaging over large areas can provide representative information.
- For heat transfer, the polymer in the boundary layer represents the bottleneck. By increasing its thermal conductivity, the thermal contact resistances can be reduced most significantly.
- If filled polymers are used in thin layers (approx. $9 \times D_{50}$ in the example investigated), two wide FPS transitions result, which prevent the formation of an undisturbed bulk in between. Experimentally separating thermal conductivity and thermal contact resistance has not been possible.

The results are considered broadly valid, supported by numerous validation studies across a range of material combinations. However, their generalizability is constrained by the limited number of materials and combinations investigated. In particular, the limited selection of polymers, whose specific effects were only briefly examined, may restrict the applicability of the findings. The polymer matrices used in the experiments have different property profiles, which influence the interactions with the fillers differently. In addition, the studies were limited to ideal conditions at room temperature and did not consider potential material damage, such as the detachment of particles or the formation of cracks in the matrix, which could be caused by unequal expansion coefficients between the filler and the polymer at higher temperatures.

OUTLOOK

The findings and conclusions of this work contribute significantly to advancing the understanding of heat transport processes in filled polymers, and thus toward more efficient product development in a continuously growing industry. The derived relationships and fundamental principles provide a valuable basis for developing new highly thermally conductive polymer composites. The simulation approaches developed within this work can be applied to material development and substantially reduce the amount of required experimental work. Many insights, especially regarding the geometric microstructure of the materials, can also be applied to areas outside of filled polymers, such as to metal-matrix composites. In the future, machine learning can help to conduct multi-parameter studies and analyze the results more efficiently. While traditional approaches, like those used in this work, are limited in scope, machine learning techniques can process larger datasets more quickly, identify patterns, and help to interpret them. Further systematic investigations are necessary for particular components including the agglomeration effect in single scale filled polymers and the geometric particle arrangement in the boundary layers of FPS transitions. Both aspects require detailed, three-dimensional, imaging analysis of packing effects using, for example, micro-CT. In the context of this work, these effects were not experimentally accessible, limiting the study to simulations with hypothetical structural parameters. Future work can expand on these findings by exploring particle formation in boundary layers, then advancing to multi-scale filled polymers at FPS transitions and examining various particle shapes. The effect of multi-scale filler blends on boundary layers formation was only superficially analyzed from a geometrical perspective. Further investigation into these processes is essential since the usage of these multi-scale filled polymers is unavoidable in many applications. The experimental studies in this work were limited to filled silicone and epoxy polymers in cured condition, though it is possible that other unexplored effects may occur in the uncured condition or when using other fillers. The use of other wetting and dispersing agents may yield different effects than those observed in this study. Generally, surfactants influence the particle-polymer interface by lowering surface tension, which can reduce agglomeration and change the composite structure. As the studies have demonstrated, this composite structure significantly affects both the effective thermal conductivity and thermal resistance at FPS transitions. While the basic geometric microstructural effects are mainly transferable to other material combinations, the specific outcomes for material combinations with different chemical and physical interactions will require further extensive studies. Completely different results are expected at FPS transitions when using thermal pads that are applied between two substrates in the already cured state. The most important factor might be how well the surface asperities penetrate the soft polymer matrix and contact the particles during joining.

REFERENCES

PUBLISHED WORK OF THE AUTHOR

[0] O. Roser, A. Griesinger, O. Marti, Investigations on thermal contact resistance between filled polymer composites and solids using micro thermography, Meas. Sci. Technol. 34 (2023) 125401. https://doi.org/10.1088/1361-6501/acec8f.

© 2023 The Author(s). Published by IOP Publishing Ltd.

Content reused in accordance with the Creative Commons Attribution 4.0 International (CC BY 4.0) license. https://creativecommons.org/licenses/by/4.0/

Several of the modeling and calculation algorithms developed in this project are published as MATLAB® code in

O. Roser, Supplementary MATLAB Code for doctoral thesis Heat Conduction in Filled Polymers - Experimental and Simulative Investigations on Microscopic Heat Transport and Particle-Level Phenomena, (2024). https://doi.org/10.18725/OPARU-54388.

GENERAL REFERENCES

[1] C. Breitkopf, Theoretical Characterization of Thermal Conductivities for Polymers - A Review, Thermo 4 (2024) 31–47. https://doi.org/10.3390/thermo4010004.

[2] H. Chen, V.V. Ginzburg, J. Yang, Y. Yang, W. Liu, Y. Huang, L. Du, B. Chen, Thermal conductivity of polymer-based composites: Fundamentals and applications, Progress in Polymer Science 59 (2016) 41–85. https://doi.org/10.1016/j.progpolymsci.2016.03.001.

[3] C. Huang, X. Qian, R. Yang, Thermal conductivity of polymers and polymer nanocomposites, Materials Science and Engineering: R: Reports 132 (2018) 1–22. https://doi.org/-10.1016/j.mser.2018.06.002.

[4] J. Wang, L. Hu, W. Li, Y. Ouyang, L. Bai, Development and Perspectives of Thermal Conductive Polymer Composites, Nanomaterials 12 (2022) 3574. https://doi.org/10.3390/nano-12203574.

[5] Y. Xu, X. Wang, Q. Hao, A mini review on thermally conductive polymers and polymer-based composites, Composites Communications 24 (2021) 100617. https://doi.org/10.-1016/j.coco.2020.100617.

[6] X. Yang, C. Liang, T. Ma, Y. Guo, J. Kong, J. Gu, M. Chen, J. Zhu, A review on thermally conductive polymeric composites: classification, measurement, model and equations, mechanism and fabrication methods, Adv Compos Hybrid Mater 1 (2018) 207–230. https://-doi.org/10.1007/s42114-018-0031-8.

[7] R. Mahajan, Thermal Interface Materials: A Brief Review of Design Characteristics and Materials, (2004). https://www.electronics-cooling.com/2004/02/thermal-interface-materials-a-brief-review-of-design-characteristics-and-materials/ (accessed May 26, 2024).

[8] F. Sarvar, D. Whalley, P. Conway, Thermal Interface Materials - A Review of the State of the Art, in: 2006 1st Electronic Systemintegration Technology Conference, IEEE, Dresden, Germany, 2006: pp. 1292–1302. https://doi.org/10.1109/ESTC.2006.280178.

[9] W. Xing, Y. Xu, C. Song, T. Deng, Recent Advances in Thermal Interface Materials for Thermal Management of High-Power Electronics, Nanomaterials 12 (2022) 3365. https://doi.org/10.3390/nano12193365.

[10] A. Sahu, D.S. Mondloe, S. Upadhyay, A review on thermal properties of epoxy composites as thermal interface material, International Research Journal of Engineering and Technology (IRJET) Vol 4, Issue 6 (2017). https://api.semanticscholar.org/CorpusID:212580034 (accessed May 26, 2024).

[11] J. Broughton, V. Smet, R.R. Tummala, Y.K. Joshi, Review of Thermal Packaging Technologies for Automotive Power Electronics for Traction Purposes, Journal of Electronic Packaging 140 (2018) 040801. https://doi.org/10.1115/1.4040828.

[12] J. Shen, Y. Feng, Recent Advances in Encapsulation Materials for Light Emitting Diodes: a Review, Silicon 15 (2023) 2163–2172. https://doi.org/10.1007/s12633-022-02171-y.

[13] E. Juntunen, A. Sitomaniemi, O. Tapaninen, R. Persons, M. Challingsworth, V. Heikkinen, Thermal Performance Comparison of Thick-Film Insulated Aluminum Substrates With Metal Core PCBs for High-Power LED Modules, IEEE Trans. Compon., Packag. Manufact. Technol. 2 (2012) 1957–1964. https://doi.org/10.1109/TCPMT.2012.2206390.

[14] S. Klarmann, B. Manesh, T. Hoenle, Y. Vagapov, Analysis of insulated-metal-substrates structures in the context of heat dissipation enhancement, in: 2017 Internet Technologies and Applications (ITA), IEEE, Wrexham, 2017: pp. 161–164. https://doi.org/10.1109/-ITECHA.2017.8101929.

[15] M. Hamidnia, Y. Luo, X.D. Wang, Application of micro/nano technology for thermal management of high power LED packaging – A review, Applied Thermal Engineering 145 (2018) 637–651. https://doi.org/10.1016/j.applthermaleng.2018.09.078.

[16] D. Borba Marchetto, D. Carneiro Moreira, G. Ribatski, A review on polymer heat sinks for electronic cooling applications, in: 17th Brazilian Congress of Thermal Sciences and Engineering, ABCM, 2018. https://doi.org/10.26678/ABCM.ENCIT2018.CIT18-0394.

[17] K. Timbs, M. Khatamifar, E. Antunes, W. Lin, Experimental study on the heat dissipation performance of straight and oblique fin heat sinks made of thermal conductive composite polymers, Thermal Science and Engineering Progress 22 (2021) 100848. https://-doi.org/10.1016/j.tsep.2021.100848.

[18] S. Bagatella, A. Cereti, F. Manarini, M. Cavallaro, R. Suriano, M. Levi, Thermally Conductive and Electrically Insulating Polymer-Based Composites Heat Sinks Fabricated by Fusion Deposition Modeling, Polymers 16 (2024) 432. https://doi.org/10.3390/polym-16030432.

[19] Md.A. Alim, M.Z. Abdullah, M.S.A. Aziz, R. Kamarudin, P. Gunnasegaran, Recent Advances on Thermally Conductive Adhesive in Electronic Packaging: A Review, Polymers 13 (2021) 3337. https://doi.org/10.3390/polym13193337.

[20] Fact.MR, Thermal Interface Material Market Study by Pads, Foam, Encapsulants/Gel for Automotive and Aerospace & Defence from 2024 to 2034, (2024). https://www.-factmr.com/report/879/thermal-interface-materials-market (accessed March 11, 2024).

[21] Precedence Research Pvt. Ltd., Thermal Interface Materials Market (By Product: Elastomeric Pads, Tapes & Films, Greases & Adhesives, Metal Based, Phase Change Materials, and Others; By Application: Computer, Telecom, Medical Devices, Consumer Durables, Industry Machinery, Automotive Electronics, and Others) - Global Market Size, Trends Analysis, Segment Forecasts, Regional Outlook 2024 - 2033, (2024). https://www.precedenceresearch.com/thermal-interface-materials-market (accessed March 11, 2024).

[22] Grand View Research, Inc., Thermal Interface Materials Market Size, Share & Trends Analysis Report By Product (Tapes & Films, Adhesives), By Application (Telecom, Computer), By Region, And Segment Forecasts, 2023 - 2030, (2023). https://www.grandviewresearch.com/industry-analysis/thermal-interface-materials-market (accessed March 11, 2024).

[23] IDTechEx, Thermal Interface Materials: Technologies, Markets, and Forecasts 2023-2033, (2023). https://www.idtechex.com/en/research-report/thermal-interface-materials-technologies-markets-and-forecasts-2023-2033/926 (accessed March 11, 2024).

[24] Straits Research, Potting Compound Market Size, Share & Trends Analysis Report By Resin Type (Epoxy, Polyurethane, Silicone, Polyester, Polyamide, Polyolefin, Acrylics), By Curing Technology (UV Curing, Thermal Curing, Room Temperature Curing), By Application (Electrical, Electronics), By End User (Electronics, Aerospace, Automotive, Industrial, Energy & Power), By function (Corrosion resistance, Insulation) and By Region(North America, Europe, APAC, Middle East and Africa, LATAM) Forecasts, 2023-2031, (2023). https://straitsresearch.com/report/potting-compound-market (accessed March 11, 2024).

[25] Data Bridge Market Research Private Ltd., Global Potting and Encapsulating Compounds Market – Industry Trends and Forecast to 2030, (2023). https://www.databridgemarketresearch.com/reports/global-potting-and-encapsulating-compounds-market (accessed March 11, 2024).

[26] Business Research Insights, Insulated Metal Substrate (IMS) Market Size, Share, Growth, And Industry Analysis, By Type (Below 2, Between 2 and 3, Above 3), By Application (LED Lighting, Automotive Electronics, Power Electronics), Regional Insights and Forecast to 2031, (2023). https://www.businessresearchinsights.com/market-reports/insulated-metal-substrate-ims-market-108764 (accessed March 11, 2024).

[27] Zion Market Research, Insulated Metal Substrates Market By Type (Copper-Based, Steel-Based, And Aluminum-Based), By Application (LED Lighting, LCD Display Backlighting, LED Display, Power Electronics, Automotive Electronics, Switches & Semiconductor Relays, And Others), And By Region - Global And Regional Industry Overview, Market Intelligence, Comprehensive Analysis, Historical Data, And Forecasts 2023 – 2030, (2023). https://www.zionmarketresearch.com/report/insulated-metal-substrates-market (accessed March 11, 2024).

[28] Fortune Business Insights Pvt. Ltd., Thermal Conductive Polymer Material Market Size, Share & Share & COVID-19 Impact Analysis, By Type (Polyamide, Polybutylene Terephthalate, Polycarbonate, Polyphenylene Sulfide, Polyetherimide, and Others), By Application (Electrical & Electronics, Industrial, Automotive, Healthcare, Aerospace, and Others), and Regional Forecast, 2023-2030, (2023). https://www.fortunebusinessinsights.com/thermal-conductive-polymer-materials-market-103721 (accessed March 15, 2024).

[29] N. Burger, A. Laachachi, M. Ferriol, M. Lutz, V. Toniazzo, D. Ruch, Review of thermal conductivity in composites: Mechanisms, parameters and theory, Progress in Polymer Science 61 (2016) 1–28. https://doi.org/10.1016/j.progpolymsci.2016.05.001.

[30] H.S. Kim, J. Jang, H. Lee, S.Y. Kim, S.H. Kim, J. Kim, Y.C. Jung, B.J. Yang, Thermal Management in Polymer Composites: A Review of Physical and Structural Parameters, Adv. Eng. Mater. 20 (2018) 1800204. https://doi.org/10.1002/adem.201800204.

[31] J.B.J. Fourier, Théorie analytique de la chaleur, Gauthier-Villars, 1822.

[32] H.S. Carslaw, J.C. Jaeger, Conduction of heat in solids, 2nd ed, Clarendon press, Oxford, 1990.

[33] X. Zhang, P. Zhang, C. Xiao, Y. Wang, X. Ding, X. Liu, X. Tian, Physical Basis of Thermal Conduction, in: X. Tian (Ed.), Thermal Management Materials for Electronic Packaging: Preparation, Characterization, and Devices, Wiley-VCH, Weinheim, 2024.

[34] P.A. Tipler, G. Mosca, Physik: für Wissenschaftler und Ingenieure, Springer, Berlin, Heidelberg, 2015. https://doi.org/10.1007/978-3-642-54166-7.

[35] G. Czycholl, Theoretische Festkörperphysik Band 1, Springer, Berlin, Heidelberg, 2016. https://doi.org/10.1007/978-3-662-47141-8.

[36] D. Meschede, Gerthsen Physik, Springer, Berlin, Heidelberg, 2015. https://doi.org/-10.1007/978-3-662-45977-5.

[37] C. Kittel, S. Hunklinger, Einführung in die Festkörperphysik, 15., unveränderte Auflage, Oldenbourg Verlag, München, 2013.

[38] R. Berman, Thermal conduction in solids, Repr, Clarendon Pr, Oxford, 1978.

[39] R.P. Tye, ed., Thermal conductivity, Academic P, London, New York, 1969.

[40] T.M. Tritt, ed., Thermal Conductivity, Springer US, 2004. https://doi.org/10.1007/b136496.

[41] P. Brüesch, Phonons: Theory and Experiments III: Phenomena Related to Phonons, Springer Berlin Heidelberg, Berlin, Heidelberg, 1987. https://doi.org/10.1007/978-3-642-52271-0.

[42] Y.S. Touloukian, R.W. Powell, C.Y. Ho, P.G. Klemens, Thermophysical properties of matter - the TPRC data series. Volume 2. Thermal conductivity - nonmetallic solids. (Reannouncement). Data book, (1971).

[43] J.M. Ziman, Electrons and phonons: the theory of transport phenomena in solids, Reprinted, Clarendon Press, Oxford, 2007.

[44] G.E. Childs, L.J. Ericks, R.L. Powell, Thermal Conductivity of Solids At Room Temperature and Below: A Review and Compilation of the Literature, (1973). https://doi.org/-10.6028/NBS.MONO.131.

[45] I.A.I. Frenkel, Wave Mechanics: Elementary Theory, International Series of Monographs on Physics; Ed. by R.H. Fowler and P. Kapitza (1932).

[46] P.G. Klemens, Heat conduction in solids by phonons, Thermochimica Acta 218 (1993) 247–255. https://doi.org/10.1016/0040-6031(93)80426-B.

[47] Y.K. Koh, Thermal Conductivity and Phonon Transport, in: Bhushan, B. (Eds) Encyclopedia of Nanotechnology, Springer Netherlands, Dordrecht, 2012: pp. 2704–2711. https://-doi.org/10.1007/978-90-481-9751-4_277.

[48] M. Planck, P.J.W. Debye, W. Nernst, M. Smoluchowski, A. Sommerfeld, H.A. Lorentz, Vorträge über die kinetische Theorie der Materie und der Elektrizität: Gehalten in Göttingen auf Einladung der Kommission der Wolfskehlstiftung, B.G. Teubner, 1914.

[49] P. Debye, Zur Theorie der spezifischen Wärmen, Annalen Der Physik 344 (1912) 789–839. https://doi.org/10.1002/andp.19123441404.

[50] R. Peierls, Zur kinetischen Theorie der Wärmeleitung in Kristallen, Ann. Phys. 395 (1929) 1055–1101. https://doi.org/10.1002/andp.19293950803.

[51] P.G. Klemens, The thermal conductivity of dielectric solids at low temperatures (Theoretical), Proc. R. Soc. Lond. A 208 (1951) 108–133. https://doi.org/10.1098/rspa.1951.0147.

[52] P.G. Klemens, Thermal Conductivity of Solids at Low Temperatures, in: S. Flügge (Ed.), Low Temperature Physics I / Kältephysik I, Springer, Berlin, Heidelberg, 1956: pp. 198–281. https://doi.org/10.1007/978-3-662-39773-2_4.

[53] Y.S. Touloukian, R.W. Powell, C.Y. Ho, P.G. Klemens, Thermophysical properties of matter - the TPRC data series. Volume 1. Thermal conductivity - metallic elements and alloys. (Reannouncement). Data book, (1970).

[54] X. Wei, Z. Wang, Z. Tian, T. Luo, Thermal Transport in Polymers: A Review, Journal of Heat Transfer 143 (2021) 072101. https://doi.org/10.1115/1.4050557.

[55] J.E. Mark, Physical properties of polymers handbook, 2nd ed, Springer, New York, 2007.

[56] N. Mehra, L. Mu, T. Ji, X. Yang, J. Kong, J. Gu, J. Zhu, Thermal transport in polymeric materials and across composite interfaces, Applied Materials Today 12 (2018) 92–130. https://doi.org/10.1016/j.apmt.2018.04.004.

[57] B. Zhang, P. Mao, Y. Liang, Y. He, W. Liu, Z. Liu, Modulating Thermal Transport in Polymers and Interfaces: Theories, Simulations, and Experiments, ES Energy Environ. (2019). https://doi.org/10.30919/esee8c306.

[58] V. Sciamanna, B. Nait-Ali, M. Gonon, Mechanical properties and thermal conductivity of porous alumina ceramics obtained from particle stabilized foams, Ceramics International 41 (2015) 2599–2606. https://doi.org/10.1016/j.ceramint.2014.10.011.

[59] A.S. Wagh, Porosity dependence of thermal conductivity of ceramics and sedimentary rocks, Journal of Materials Science 28 (1993) 3715–3721. https://doi.org/10.1007/-BF00353169.

[60] S. Wada, T. Wasanapiarnpong, S. Jinawath, Thermal Conductivity of Al2O3 Ceramics: The Inconsistency between Measured Value and Calculated Value Based on Analytical Models for a Composite, J. Sci. Res.Chula. Univ. Vol. 30, No. 1 (2005). https://www.thaiscience.info/journals/Article/CJSR/10324250.pdf (accessed December 6, 2020).

[61] Z. Živcová, E. Gregorová, W. Pabst, D.S. Smith, A. Michot, C. Poulier, Thermal conductivity of porous alumina ceramics prepared using starch as a pore-forming agent, Journal of the European Ceramic Society 29 (2009) 347–353. https://doi.org/10.1016/j.jeurceramsoc.2008.06.018.

[62] J.K. Carson, S.J. Lovatt, D.J. Tanner, A.C. Cleland, Thermal conductivity bounds for isotropic, porous materials, International Journal of Heat and Mass Transfer 48 (2005) 2150–2158. https://doi.org/10.1016/j.ijheatmasstransfer.2004.12.032.

[63] C.T. Hsu, P. Cheng, K.W. Wong, A Lumped-Parameter Model for Stagnant Thermal Conductivity of Spatially Periodic Porous Media, Journal of Heat Transfer 117 (1995) 264–269. https://doi.org/10.1115/1.2822515.

[64] I. Sumirat, Y. Ando, S. Shimamura, Theoretical consideration of the effect of porosity on thermal conductivity of porous materials, J Porous Mater 13 (2006) 439–443. https://-doi.org/10.1007/s10934-006-8043-0.

[65] Y.-L. Shen, M.G. Abdo, I.J. Van Rooyen, Numerical Study of Effective Thermal Conductivity for Periodic Closed-Cell Porous Media, Transp Porous Med 143 (2022) 245–269. https://doi.org/10.1007/s11242-022-01768-6.

[66] D.S. Smith, A. Alzina, J. Bourret, B. Nait-Ali, F. Pennec, N. Tessier-Doyen, K. Otsu, H. Matsubara, P. Elser, U.T. Gonzenbach, Thermal conductivity of porous materials, J. Mater. Res. 28 (2013) 2260–2272. https://doi.org/10.1557/jmr.2013.179.

[67] P.L. Kapitza, The study of heat transfer in helium II, in: Helium 4, Elsevier, 1971: pp. 114–153. https://doi.org/10.1016/B978-0-08-015816-7.50014-6.

[68] A. Giri, P.E. Hopkins, A Review of Experimental and Computational Advances in Thermal Boundary Conductance and Nanoscale Thermal Transport across Solid Interfaces, Adv Funct Materials 30 (2020) 1903857. https://doi.org/10.1002/adfm.201903857.

[69] E.T. Swartz, R.O. Pohl, Thermal boundary resistance, Rev. Mod. Phys. 61 (1989) 605–668. https://doi.org/10.1103/RevModPhys.61.605.

[70] I. Khalitnikov, Heat exchange between a solid body and helium-I, Zh Eksp Teor Fiz 22 (1952) 687–704.

[71] W.A. Little, The transport of heat between dissimilar solids at low temperatures, Can. J. Phys. 37 (1959) 334–349. https://doi.org/10.1139/p59-037.

[72] V.I. Khvesyuk, B. Liu, A.A. Barinov, Development of acoustic and diffuse mismatch models for predicting the Kapitza resistance, J. Phys.: Conf. Ser. 1382 (2019) 012155. https://doi.org/10.1088/1742-6596/1382/1/012155.

[73] E.T. Swartz, R.O. Pohl, Thermal resistance at interfaces, Appl. Phys. Lett. 51 (1987) 2200–2202. https://doi.org/10.1063/1.98939.

[74] C.V. Madhusudana, Thermal Contact Conductance, Springer International Publishing, Cham, 2014. https://doi.org/10.1007/978-3-319-01276-6.

[75] P. Reddy, K. Castelino, A. Majumdar, Diffuse mismatch model of thermal boundary conductance using exact phonon dispersion, Applied Physics Letters 87 (2005) 211908. https://doi.org/10.1063/1.2133890.

[76] R. Prasher, Acoustic mismatch model for thermal contact resistance of van der Waals contacts, Appl. Phys. Lett. 94 (2009) 041905. https://doi.org/10.1063/1.3075065.

[77] M.M. Yovanovich, E.E. Marotta, Thermal Spreading and Contact Resistances, in: A. Bejan, A.D. Kraus (Eds.), Heat Transfer Handbook, J. Wiley, New York, 2003.

[78] M.M. Yovanovich, Four decades of research on thermal contact, gap, and joint resistance in microelectronics, IEEE Trans. Comp. Packag. Technol. 28 (2005) 182–206. https://doi.org/10.1109/TCAPT.2005.848483.

[79] X. Li, R. Luo, W. Zhang, H. Liao, Method for measuring thermal contact resistance of graphite thin film materials, Measurement 93 (2016) 202–207. https://doi.org/10.1016/j.measurement.2016.07.015.

[80] C.V. Madhusudana, Accuracy in thermal contact conductance experiments - the effect of heat losses to the surroundings, International Communications in Heat and Mass Transfer 27 (2000) 877–891. https://doi.org/10.1016/S0735-1933(00)00168-8.

[81] A.E. Stark, Thermal Contact Resistance Measurement and Related Uncertainties, (2020). https://doi.org/10.25777/MKTZ-ZF27.

[82] M.H. Shojaefard, K. Goudarzi, The Numerical Estimation of Thermal Contact Resistance in Contacting Surfaces, American J. of Applied Sciences 5 (2008) 1566–1571. https://doi.org/10.3844/ajassp.2008.1566.1571.

[83] M. Zou, B. Yu, J. Cai, P. Xu, Fractal Model for Thermal Contact Conductance, Journal of Heat Transfer 130 (2008) 101301. https://doi.org/10.1115/1.2953304.

[84] M. Bahrami, J.R. Culham, M.M. Yovanovich, Modeling Thermal Contact Resistance: A Scale Analysis Approach, Journal of Heat Transfer 126 (2004) 896–905. https://doi.org/10.1115/1.1795238.

[85] X. Zhang, P.Z. Cong, M. Fujii, A Study on Thermal Contact Resistance at the Interface of Two Solids, Int J Thermophys 27 (2006) 880–895. https://doi.org/10.1007/s10765-006-0064-z.

[86] P. Zhang, Y. Xuan, Q. Li, A high-precision instrumentation of measuring thermal contact resistance using reversible heat flux, Experimental Thermal and Fluid Science 54 (2014) 204–211. https://doi.org/10.1016/j.expthermflusci.2013.12.012.

[87] Y.-J. Dai, J.-J. Gou, X.-J. Ren, F. Bai, W.-Z. Fang, W.-Q. Tao, A test-validated prediction model of thermal contact resistance for Ti-6Al-4V alloy, Applied Energy 228 (2018) 1601–1617. https://doi.org/10.1016/j.apenergy.2018.06.134.

[88] C. Fieberg, R. Kneer, Determination of thermal contact resistance from transient temperature measurements, International Journal of Heat and Mass Transfer 51 (2008) 1017–1023. https://doi.org/10.1016/j.ijheatmasstransfer.2007.05.004.

[89] E.M. Burghold, Y. Frekers, R. Kneer, Determination of time-dependent thermal contact conductance through IR-thermography, International Journal of Thermal Sciences 98 (2015) 148–155. https://doi.org/10.1016/j.ijthermalsci.2015.07.009.

[90] P. Zhang, T. Cui, Q. Li, Effect of surface roughness on thermal contact resistance of aluminium alloy, Applied Thermal Engineering 121 (2017) 992–998. https://doi.org/10.1016/j.applthermaleng.2017.04.142.

[91] J. Emily Cousineau, K. Bennion, V. Chieduko, R. Lall, A. Gilbert, Experimental Characterization and Modeling of Thermal Contact Resistance of Electric Machine Stator-to-Cooling Jacket Interface Under Interference Fit Loading, Journal of Thermal Science and Engineering Applications 10 (2018) 041016. https://doi.org/10.1115/1.4039459.

[92] D. Bi, H. Chen, T. Ye, Influences of temperature and contact pressure on thermal contact resistance at interfaces at cryogenic temperatures, Cryogenics 52 (2012) 403–409. https://doi.org/10.1016/j.cryogenics.2012.03.006.

[93] V.V. Rao, K. Bapurao, J. Nagaraju, M.V.K. Murthy, Instrumentation to measure thermal contact resistance, Meas. Sci. Technol. 15 (2004) 275–278. https://doi.org/10.1088/0957-0233/15/1/040.

[94] T. Ishizaki, T. Igami, H. Nagano, Measurement of local thermal contact resistance with a periodic heating method using microscale lock-in thermography, Review of Scientific Instruments 91 (2020) 064901. https://doi.org/10.1063/5.0002937.

[95] T. Ishizaki, A. Ueno, H. Nagano, Measurement of Line Distribution of Thermal Contact Resistance Using Microscopic Lock-In Thermography, in: The 16th International Workshop on Advanced Infrared Technology & Applications, MDPI, 2021: p. 18. https://-doi.org/10.3390/engproc2021008018.

[96] E.E. Marotta, L.S. Fletcher, Thermal contact conductance of selected polymeric materials, Journal of Thermophysics and Heat Transfer 10 (1996) 334–342. https://doi.org/10.2514/-3.792.

[97] Y. Mo, S. Segawa, Thermal contact resistance measurements, J Enh Heat Transf 19 (2012) 561–569. https://doi.org/10.1615/JEnhHeatTransf.2012006005.

[98] Y. Chen, S. Feng, Y. Zhang, X. He, K. Bai, X. Li, Effect of Surface Roughness on Thermal Contact Resistance of Fixed Interface in Thermal Measurement of Electron Device, in: 2020 3rd International Conference on Electron Device and Mechanical Engineering (ICEDME), IEEE, Suzhou, China, 2020: pp. 43–47. https://doi.org/10.1109/ICEDME50972.2020.-00017.

[99] M. Thompson, A multi-scale iterative approach for finite element modeling of thermal contact resistance, PhD Thesis, Massachusetts Institute of Technology, Dept. of Mechanical Engineering, 2007. http://hdl.handle.net/1721.1/42069 (accessed May 26, 2024).

[100] Y. Wei, CFD modeling of thermal contact resistance between solid contacting surfaces, Energy Sources, Part A: Recovery, Utilization, and Environmental Effects 40 (2018) 3009–3018. https://doi.org/10.1080/15567036.2018.1515278.

[101] N.N. Verma, S. Mazumder, Extraction of thermal contact conductance of metal–metal contacts from scale-resolved direct numerical simulation, International Journal of Heat and Mass Transfer 94 (2016) 164–173. https://doi.org/10.1016/j.ijheatmasstransfer.2015.-11.026.

[102] T. Cui, Q. Li, Y. Xuan, P. Zhang, Multiscale simulation of thermal contact resistance in electronic packaging, International Journal of Thermal Sciences 83 (2014) 16–24. https://doi.org/10.1016/j.ijthermalsci.2014.04.006.

[103] D. Liu, J. Zhang, Numerical simulation of high-temperature thermal contact resistance and its reduction mechanism, PLoS ONE 13 (2018) e0194483. https://doi.org/10.1371/journal.pone.0194483.

[104] X.-J. Ren, Y.-J. Dai, J.-J. Gou, W.-Q. Tao, Numerical study on thermal contact resistance of 8-harness satin woven pierced composite, International Journal of Thermal Sciences 159 (2021) 106584. https://doi.org/10.1016/j.ijthermalsci.2020.106584.

[105] J.-J. Gou, X.-J. Ren, Y.-J. Dai, S. Li, W.-Q. Tao, Study of thermal contact resistance of rough surfaces based on the practical topography, Computers & Fluids 164 (2018) 2–11. https://doi.org/10.1016/j.compfluid.2016.09.018.

[106] M.G. Cooper, B.B. Mikic, M.M. Yovanovich, Thermal contact conductance, International Journal of Heat and Mass Transfer 12 (1969) 279–300. https://doi.org/10.1016/0017-9310(69)90011-8.

[107] M. Yovanovich, J. Devaal, A. Hegazy, Astatistical model to predict thermal gap conductance between conforming rough surfaces, in: 3rd Joint Thermophysics, Fluids, Plasma and Heat Transfer Conference, American Institute of Aeronautics and Astronautics, St. Louis, MO, U.S.A., 1982. https://doi.org/10.2514/6.1982-888.

[108] M. Grujicic, C.L. Zhao, E.C. Dusel, The effect of thermal contact resistance on heat management in the electronic packaging, Applied Surface Science 246 (2005) 290–302. https://doi.org/10.1016/j.apsusc.2004.11.030.

[109] K. Fujiwara, M. Shibahara, Thermal transport mechanism at a solid-liquid interface based on the heat flux detected at a subatomic spatial resolution, Phys. Rev. E 105 (2022) 034803. https://doi.org/10.1103/PhysRevE.105.034803.

[110] J. Li, Q. Zhu, J. Sun, Study on thermal contact resistance at liquid–solid interface based on fractal theory, AIP Advances 11 (2021) 125308. https://doi.org/10.1063/5.0076323.

[111] C. Yuan, B. Duan, L. Li, B. Shang, X. Luo, An improved model for predicting thermal contact resistance at liquid–solid interface, International Journal of Heat and Mass Transfer 80 (2015) 398–406. https://doi.org/10.1016/j.ijheatmasstransfer.2014.09.048.

[112] S.C. Somé, D. Delaunay, V. Gaudefroy, Comparison and validation of thermal contact resistance models at solid–liquid interface taking into account the wettability parameters, Applied Thermal Engineering 61 (2013) 531–540. https://doi.org/10.1016/j.applthermaleng.-2013.08.032.

[113] A. Hamasaiid, M.S. Dargusch, T. Loulou, G. Dour, A predictive model for the thermal contact resistance at liquid–solid interfaces: Analytical developments and validation, International Journal of Thermal Sciences 50 (2011) 1445–1459. https://doi.org/10.1016/j.ijthermalsci.2011.02.016.

[114] R.C. Progelhof, J.L. Throne, R.R. Ruetsch, Methods for predicting the thermal conductivity of composite systems: A review, Polym. Eng. Sci. 16 (1976) 615–625. https://doi.org/-10.1002/pen.760160905.

[115] Y. Agari, T. Uno, Estimation on thermal conductivities of filled polymers, J. Appl. Polym. Sci. 32 (1986) 5705–5712. https://doi.org/10.1002/app.1986.070320702.

[116] K. von Lichtenecker, Der elektrische Leitungswiderstand künstlicher und natürlicher Aggregate, Physikalische Zeitschrift 25 (1924) 169–181.

[117] VDI e. V., ed., VDI-Wärmeatlas, Springer, Berlin, Heidelberg, 2013. https://doi.org/-10.1007/978-3-642-19981-3.

[118] P. Vinod, B.M.A. Desai, R. Sarathi, S. Kornhuber, Investigation on the thermal properties, space charge and charge trap characteristics of silicone rubber nano–micro composites, Electr Eng 103 (2021) 1779–1790. https://doi.org/10.1007/s00202-020-01195-0.

[119] S.M. Kong, M. Mariatti, J.J.C. Busfield, Effects of types of fillers and filler loading on the properties of silicone rubber composites, Journal of Reinforced Plastics and Composites 30 (2011) 1087–1096. https://doi.org/10.1177/0731684411416267.

[120] Q. Mu, S. Feng, G. Diao, Thermal conductivity of silicone rubber filled with ZnO, Polym. Compos. 28 (2007) 125–130. https://doi.org/10.1002/pc.20276.

[121] W. Zhou, C. Wang, Q. An, H. Ou, Thermal Properties of Heat Conductive Silicone Rubber Filled with Hybrid Fillers, Journal of Composite Materials 42 (2008) 173–187. https://doi.org/10.1177/0021998307086184.

[122] B.Z. Gao, J.Z. Xu, J.J. Peng, F.Y. Kang, H.D. Du, J. Li, S.W. Chiang, C.J. Xu, N. Hu, X.S. Ning, Experimental and theoretical studies of effective thermal conductivity of composites made of silicone rubber and Al2O3 particles, Thermochimica Acta 614 (2015) 1–8. https://doi.org/10.1016/j.tca.2015.06.005.

[123] S.S. Samsudin, M.S.A. Majid, M.J.M. Ridzuan, A.F. Osman, Thermal polymer composites of hybrid fillers, IOP Conf. Ser.: Mater. Sci. Eng. 670 (2019) 012037. https://doi.org/10.1088/1757-899X/670/1/012037.

[124] R. Nayak, D.P. Tarkes, A. Satapathy, A computational and experimental investigation on thermal conductivity of particle reinforced epoxy composites, Computational Materials Science 48 (2010) 576–581. https://doi.org/10.1016/j.commatsci.2010.02.025.

[125] W.M. Haynes, CRC Handbook of Chemistry and Physics, 95th Edition, 95th ed, CRC Press, Hoboken, 2014.

[126] Y. Zhao, Z. Zhai, D. Drummer, Thermal Conductivity of Aluminosilicate- and Aluminum Oxide-Filled Thermosets for Injection Molding: Effect of Filler Content, Filler Size and Filler Geometry, Polymers 10 (2018) 457. https://doi.org/10.3390/polym10040457.

[127] J.P. Meyer, P.N. Nwosu, M. Sharifpur, T. Ntumba, Parametric Analysis of Effective Viscosity Models for Nanofluids, in: Volume 7: Fluids and Heat Transfer, Parts A, B, C, and D, American Society of Mechanical Engineers, Houston, Texas, USA, 2012: pp. 1149–1157. https://doi.org/10.1115/IMECE2012-93200.

[128] S. Grunder, N. Hillesheim, A. Lutz, F. Ardizzone, Thermal interface materials, US20220251331A1, 2022. https://patentimages.storage.googleapis.com/7a/79/0c/daab55ca2a9f7b/US20220251331A1.pdf (accessed May 26, 2024).

[129] G. Czel, A. Sycheva, D. Janovszky, Effect of different fillers on thermal conductivity, tribological properties of Polyamide 6, Sci Rep 13 (2023) 845. https://doi.org/10.1038/s41598-023-27740-y.

[130] Y. Liu, J. Li, A protocol to further improve the thermal conductivity of silicone-matrix thermal interface material with nano-fillers, Thermochimica Acta 708 (2022) 179136. https://doi.org/10.1016/j.tca.2021.179136.

[131] H.S. Tekce, D. Kumlutas, I.H. Tavman, Effect of Particle Shape on Thermal Conductivity of Copper Reinforced Polymer Composites, Journal of Reinforced Plastics and Composites 26 (2007) 113–121. https://doi.org/10.1177/0731684407072522.

[132] W.-Y. Zhou, S.-H. Qi, H.-Z. Zhao, N.-L. Liu, Thermally conductive silicone rubber reinforced with boron nitride particle, Polym. Compos. 28 (2007) 23–28. https://doi.org/10.1002/pc.20296.

[133] K. Gharagozloo-Hubmann, A. Boden, G.J.F. Czempiel, I. Firkowska, S. Reich, Filler geometry and interface resistance of carbon nanofibres: Key parameters in thermally conductive polymer composites, Appl. Phys. Lett. 102 (2013) 213103. https://doi.org/10.1063/1.4807420.

[134] K. Pietrak, T.S. Wisniewski, A review of models for effective thermal conductivity of composite materials, Journal of Power Technologies (2015) 14–24.

[135] W. Tian, L. Qi, X. Chao, J. Liang, M.W. Fu, Numerical evaluation on the effective thermal conductivity of the composites with discontinuous inclusions: Periodic boundary condition and its numerical algorithm, International Journal of Heat and Mass Transfer 134 (2019) 735–751. https://doi.org/10.1016/j.ijheatmasstransfer.2019.01.072.

[136] N.K. Sharma, Finite element modelling and simulations on effective thermal conductivity of particulate composites, J Therm Anal Calorim 147 (2022) 3441–3452. https://doi.org/-10.1007/s10973-021-10756-9.

[137] A. Devpura, P.E. Phelan, R.S. Prasher, Percolation theory applied to the analysis of thermal interface materials in flip-chip technology, in: ITHERM 2000. The Seventh Intersociety Conference on Thermal and Thermomechanical Phenomena in Electronic Systems (Cat. No.00CH37069), IEEE, Las Vegas, NV, USA, 2000: pp. 21–28. https://doi.org/10.1109/-ITHERM.2000.866803.

[138] A. Chatterjee, R. Verma, H.P. Umashankar, S. Kasthurirengan, N.C. Shivaprakash, U. Behera, Heat conduction model based on percolation theory for thermal conductivity of composites with high volume fraction of filler in base matrix, International Journal of Thermal Sciences 136 (2019) 389–395. https://doi.org/10.1016/j.ijthermalsci.2018.09.015.

[139] S. Zhai, P. Zhang, Y. Xian, J. Zeng, B. Shi, Effective thermal conductivity of polymer composites: Theoretical models and simulation models, International Journal of Heat and Mass Transfer 117 (2018) 358–374. https://doi.org/10.1016/j.ijheatmasstransfer.2017.09.067.

[140] J.C. Maxwell, A Treatise on Electricity and Magnetism, 1st ed., Clarendon Press, Oxford, 1873.

[141] Lord Rayleigh, On the influence of obstacles arranged in rectangular order upon the properties of a medium, The London, Edinburgh, and Dublin Philosophical Magazine and Journal of Science 34 (1892) 481–502. https://doi.org/10.1080/14786449208620364.

[142] D.A.G. Bruggeman, Berechnung verschiedener physikalischer Konstanten von heterogenen Substanzen. I. Dielektrizitätskonstanten und Leitfähigkeiten der Mischkörper aus isotropen Substanzen, Ann. Phys. 416 (1935) 636–664. https://doi.org/10.1002/andp.19354160705.

[143] S.C. Cheng, R.I. Vachon, The prediction of the thermal conductivity of two and three phase solid heterogeneous mixtures, International Journal of Heat and Mass Transfer 12 (1969) 249–264. https://doi.org/10.1016/0017-9310(69)90009-X.

[144] G.T.-N. Tsao, Thermal Conductivity of Two-Phase Materials, Ind. Eng. Chem. 53 (1961) 395–397. https://doi.org/10.1021/ie50617a031.

[145] T.B. Lewis, L.E. Nielsen, Dynamic mechanical properties of particulate-filled composites, J. Appl. Polym. Sci. 14 (1970) 1449–1471. https://doi.org/10.1002/app.1970.070140604.

[146] L.E. Nielsen, Generalized Equation for the Elastic Moduli of Composite Materials, Journal of Applied Physics 41 (1970) 4626–4627. https://doi.org/10.1063/1.1658506.

[147] L.E. Nielsen, Thermal conductivity of particulate-filled polymers, J. Appl. Polym. Sci. 17 (1973) 3819–3820. https://doi.org/10.1002/app.1973.070171224.

[148] L.E. Nielsen, The Thermal and Electrical Conductivity of Two-Phase Systems, Ind. Eng. Chem. Fund. 13 (1974) 17–20. https://doi.org/10.1021/i160049a004.

[149] N.A. Mohd Radzuan, A.B. Sulong, J. Sahari, A review of electrical conductivity models for conductive polymer composite, International Journal of Hydrogen Energy 42 (2017) 9262–9273. https://doi.org/10.1016/j.ijhydene.2016.03.045.

[150] A.C. Anderson, R.B. Rauch, Low-Temperature Thermal Conductivity of a Suspension of Copper Particles, Journal of Applied Physics 41 (1970) 3648–3651. https://doi.org/-10.1063/1.1659486.

[151] K.W. Garrett, H.M. Rosenberg, The thermal conductivity of epoxy-resin / powder composite materials, Journal of Physics D: Applied Physics 7 (1974) 1247–1258. https://doi.org/-10.1088/0022-3727/7/9/311.

[152] C. Schmidt, Influence of the Kapitza resistance on the thermal conductivity of filled epoxies, Cryogenics 15 (1975) 17–20. https://doi.org/10.1016/0011-2275(75)90162-9.

[153] A. Devpura, P.E. Phelan, R.S. Prasher, Size effects on the thermal conductivity of polymers laden with highly conductive filler particles, Microscale Thermophysical Engineering 5 (2001) 177–189. https://doi.org/10.1080/108939501753222869.

[154] W. Jiajun, Y. Xiao-Su, Effects of interfacial thermal barrier resistance and particle shape and size on the thermal conductivity of AlN/PI composites, Composites Science and Technology 64 (2004) 1623–1628. https://doi.org/10.1016/j.compscitech.2003.11.007.

[155] D.P.H. Hasselman, L.F. Johnson, Effective Thermal Conductivity of Composites with Interfacial Thermal Barrier Resistance, Journal of Composite Materials 21 (1987) 508–515. https://doi.org/10.1177/002199838702100602.

[156] A.G. Every, Y. Tzou, D.P.H. Hasselman, R. Raj, The effect of particle size on the thermal conductivity of ZnS/diamond composites, Acta Metallurgica et Materialia 40 (1992) 123–129. https://doi.org/10.1016/0956-7151(92)90205-S.

[157] S. Holotescu, F.D. Stoian, Evaluation of the effective thermal conductivity of composite polymers by considering the filler size distribution law, J. Zhejiang Univ. Sci. A 10 (2009) 704–709. https://doi.org/10.1631/jzus.A0820733.

[158] A.D. Drozdov, J. deClaville Christiansen, Thermal conductivity of highly filled polymer nanocomposites, Composites Science and Technology 182 (2019) 107717. https://doi.org/-10.1016/j.compscitech.2019.107717.

[159] R.S. Prasher, J.C. Matayabas, Thermal Contact Resistance of Cured Gel Polymeric Thermal Interface Material, IEEE Trans. Comp. Packag. Technol. 27 (2004) 702–709. https://-doi.org/10.1109/TCAPT.2004.838883.

[160] S. Narumanchi, M. Mihalic, K. Kelly, G. Eesley, Thermal interface materials for power electronics applications, in: 2008 11th Intersociety Conference on Thermal and Thermomechanical Phenomena in Electronic Systems, IEEE, Orlando, FL, USA, 2008: pp. 395–404. https://doi.org/10.1109/ITHERM.2008.4544297.

[161] R. Schacht, D. May, B. Wunderle, O. Wittler, A. Gollhardt, B. Michel, H. Reichl, Characterization of Thermal Interface Materials, in: 2006 1st Electronic Systemintegration Technology Conference, IEEE, Dresden, Germany, 2006: pp. 1367–1373. https://doi.org/-10.1109/ESTC.2006.280189.

[162] T. Kowalik, M. Rütters, R. Stadler, A. Kuhn, R. Szilluweit, Wärmeleitpasten für Elektrofahrzeuge: Leitfähigkeit, Dichte, Viskosität und Kosten, Adhaes Kleb Dicht 65 (2021) 30–37. https://doi.org/10.1007/s35145-021-0513-7.

[163] M. Frauenhofer, M. Gormanns, M. Simon, M. Rütters, H. Fricke, Optimierte Wärmeableitung aus Energiespeichern für Serien-Elektrofahrzeuge, Adhaes Kleb Dicht 64 (2020) 38–43. https://doi.org/10.1007/s35145-020-0122-x.

[164] O. Skrabala, C. Bonten, Enhanced thermal conductivity in plate-shaped polymer parts, in: PROCEEDINGS OF PPS-29: The 29th International Conference of the Polymer Processing Society - Conference Papers, Nuremberg, Germany, 2014: pp. 424–427. https://doi.org/-10.1063/1.4873813.

[165] B.L. Zhu, J. Wang, H. Zheng, J. Ma, J. Wu, Z.H. Gan, J. Liu, Thermal conductivity and dielectric properties of immiscible LDPE/epoxy blend filled with hybrid filler consisting of HGM and nitride particle, Journal of Alloys and Compounds 701 (2017) 499–507. https://doi.org/10.1016/j.jallcom.2017.01.182.

[166] Z. Tian, J. Sun, S. Wang, X. Zeng, S. Zhou, S. Bai, N. Zhao, C.-P. Wong, A thermal interface material based on foam-templated three-dimensional hierarchical porous boron nitride, J. Mater. Chem. A 6 (2018) 17540–17547. https://doi.org/10.1039/C8TA05638B.

[167] W. Zhou, S. Qi, C. Tu, H. Zhao, C. Wang, J. Kou, Effect of the particle size of Al2O3 on the properties of filled heat-conductive silicone rubber, J. Appl. Polym. Sci. 104 (2007) 1312–1318. https://doi.org/10.1002/app.25789.

[168] R. Kochetov, T. Andritsch, P.H.F. Morshuis, J.J. Smit, Thermal and electrical behaviour of epoxy-based microcomposites filled with Al2O3 and SiO2 particles, in: 2010 IEEE International Symposium on Electrical Insulation, IEEE, San Diego, CA, USA, 2010: pp. 1–5. https://doi.org/10.1109/ELINSL.2010.5549745.

[169] L.C. Sim, S.R. Ramanan, H. Ismail, K.N. Seetharamu, T.J. Goh, Thermal characterization of Al2O3 and ZnO reinforced silicone rubber as thermal pads for heat dissipation purposes, Thermochimica Acta 430 (2005) 155–165. https://doi.org/10.1016/j.tca.2004.12.024.

[170] G.-W. Lee, M. Park, J. Kim, J.I. Lee, H.G. Yoon, Enhanced thermal conductivity of polymer composites filled with hybrid filler, Composites Part A: Applied Science and Manufacturing 37 (2006) 727–734. https://doi.org/10.1016/j.compositesa.2005.07.006.

[171] M. Harada, N. Hamaura, M. Ochi, Y. Agari, Thermal conductivity of liquid crystalline epoxy/BN filler composites having ordered network structure, Composites Part B: Engineering 55 (2013) 306–313. https://doi.org/10.1016/j.compositesb.2013.06.031.

[172] D.S. Muratov, D.V. Kuznetsov, I.A. Il'inykh, I.N. Burmistrov, I.N. Mazov, Thermal conductivity of polypropylene composites filled with silane-modified hexagonal BN, Composites Science and Technology 111 (2015) 40–43. https://doi.org/10.1016/j.compscitech.-2015.03.003.

[173] C.P. Wong, R.S. Bollampally, Thermal Conductivity, Elastic Modulus, and Coefficient of Thermal Expansion of Polymer Composites Filled with Ceramic Particles for Electronic Packaging, Journal of Applied Polymer Science 74 (1999) 3396–3403.

[174] B. Weidenfeller, M. Höfer, F.R. Schilling, Thermal conductivity, thermal diffusivity, and specific heat capacity of particle filled polypropylene, Composites Part A: Applied Science and Manufacturing 35 (2004) 423–429. https://doi.org/10.1016/j.compositesa.2003.11.005.

[175] M.W. Akhtar, Y.S. Lee, D.J. Yoo, J.S. Kim, Alumina-graphene hybrid filled epoxy composite: Quantitative validation and enhanced thermal conductivity, Composites Part B: Engineering 131 (2017) 184–195. https://doi.org/10.1016/j.compositesb.2017.07.067.

[176] S.Y. Pak, H.M. Kim, S.Y. Kim, J.R. Youn, Synergistic improvement of thermal conductivity of thermoplastic composites with mixed boron nitride and multi-walled carbon nanotube fillers, Carbon 50 (2012) 4830–4838. https://doi.org/10.1016/j.carbon.2012.06.009.

[177] H. Li, W. Zheng, Enhanced thermal conductivity of epoxy/alumina composite through multiscale-disperse packing, Journal of Composite Materials 55 (2021) 17–25. https://doi.org/-10.1177/0021998320942575.

[178] Q.-K. Feng, C. Liu, D.-L. Zhang, Y.-H. Song, K. Sun, H.-P. Xu, Z.-M. Dang, Particle packing theory guided multiscale alumina filled epoxy resin with excellent thermal and dielectric performances, Journal of Materiomics 8 (2022) 1058–1066. https://doi.org/10.1016/-j.jmat.2022.02.008.

[179] K.C. Yung, H. Liem, Enhanced thermal conductivity of boron nitride epoxy-matrix composite through multi-modal particle size mixing, J of Applied Polymer Sci 106 (2007) 3587–3591. https://doi.org/10.1002/app.27027.

[180] J.-P. Hong, S.-W. Yoon, T. Hwang, J.-S. Oh, S.-C. Hong, Y. Lee, J.-D. Nam, High thermal conductivity epoxy composites with bimodal distribution of aluminum nitride and boron nitride fillers, Thermochimica Acta 537 (2012) 70–75. https://doi.org/10.1016/j.tca.-2012.03.002.

[181] S. Choi, J. Kim, Thermal conductivity of epoxy composites with a binary-particle system of aluminum oxide and aluminum nitride fillers, Composites Part B: Engineering 51 (2013) 140–147. https://doi.org/10.1016/j.compositesb.2013.03.002.

[182] L. Mao, J. Han, D. Zhao, N. Song, L. Shi, J. Wang, Particle Packing Theory Guided Thermal Conductive Polymer Preparation and Related Properties, ACS Appl. Mater. Interfaces 10 (2018) 33556–33563. https://doi.org/10.1021/acsami.8b10983.

[183] Y. Su, Q. Ma, T. Liang, Y. Yao, Z. Jiao, M. Han, Y. Pang, L. Ren, X. Zeng, J. Xu, R. Sun, Optimization of Effective Thermal Conductivity of Thermal Interface Materials Based on the Genetic Algorithm-Driven Random Thermal Network Model, ACS Appl. Mater. Interfaces 13 (2021) 45050–45058. https://doi.org/10.1021/acsami.1c11963.

[184] D09 Committee, ASTM D5470-17: Test Method for Thermal Transmission Properties of Thermally Conductive Electrical Insulation Materials, (2017). https://doi.org/10.1520/-D5470-17.

[185] Sika Advanced Resins, Produktdatenblatt - SikaBiresin® TD150 – TD165, (2021). https://deu.sika.com/content/dam/dms/deaddconst01/d/SikaBiresin%20TD150-TD165_de.pdf (accessed July 8, 2023).

[186] Wacker Chemie AG, Technical data sheet - ELASTOSIL® RT 604 A/B, 2023. https://www.wacker.com/h/en-de/medias/ELASTOSIL-RT-625-AB-en-2022.02.23.pdf (accessed April 11, 2024).

[187] Wacker Chemie AG, Technical data sheet - ELASTOSIL® RT 620 A/B, 2022. https://www.wacker.com/h/en-de/medias/ELASTOSIL-RT-620-AB-en-2022.06.28.pdf (accessed April 11, 2024).

[188] Wacker Chemie AG, Technical data sheet - ELASTOSIL® RT 625 A/B, 2022. https://www.wacker.com/h/en-de/medias/ELASTOSIL-RT-625-AB-en-2022.02.23.pdf (accessed April 11, 2024).

[189] HP-Textiles GmbH, Technical data sheet - HP-PK22 - Thickener and Thixotroping Agent, 2018. https://www.hp-textiles.com/TDS/EN/Fillers_Additive/Thixotropypowder/HP-PK-22.pdf (accessed April 11, 2024).

[190] BYK-Chemie GmbH, Data Sheet - BYK-W 996, 2017. https://www.byk.com/en/products/additives-by-name/byk-w-996 (accessed January 4, 2024).

[191] T. Matsuyama, H. Yamamoto, Particle Shape and Laser Diffraction: A Discussion of the Particle Shape Problem, Journal of Dispersion Science and Technology 25 (2005) 409–416. https://doi.org/10.1081/DIS-200025692.

[192] B. Stoib, S. Filser, J. Stötzel, A. Greppmair, N. Petermann, H. Wiggers, G. Schierning, M. Stutzmann, M.S. Brandt, Spatially resolved determination of thermal conductivity by Raman spectroscopy, Semicond. Sci. Technol. 29 (2014) 124005. https://doi.org/-10.1088/0268-1242/29/12/124005.

[193] A. Özden, E. Zuñiga-Puelles, J. Kortus, R. Gumeniuk, C. Himcinschi, Thermal conductivity and phonon anharmonicity of chemical vapor transport grown and mineral–FeS_2 single crystals: An optothermal Raman study, J Raman Spectroscopy 54 (2023) 84–92. https://doi.org/10.1002/jrs.6456.

[194] A.S. Agazhanov, D.A. Samoshkin, Y.M. Kozlovskii, S.V. Stankus, Experimental study of the thermophysical properties for aluminum-magnesium alloy AMg3, J. Phys.: Conf. Ser. 2057 (2021) 012101. https://doi.org/10.1088/1742-6596/2057/1/012101.

[195] DIN EN ISO 25178-2:2023-09, Geometrische Produktspezifikation (GPS) - Oberflächenbeschaffenheit: Flächenhaft - Teil 2: Begriffe und Kenngrößen für die Oberflächenbeschaffenheit (ISO 25178-2:2021); Deutsche Fassung EN_ISO_25178-2:2022, (2023). https://doi.org/10.31030/3294021.

[196] B.N.J. Persson, O. Albohr, U. Tartaglino, A.I. Volokitin, E. Tosatti, On the nature of surface roughness with application to contact mechanics, sealing, rubber friction and adhesion, J. Phys.: Condens. Matter 17 (2005) R1–R62. https://doi.org/10.1088/0953-8984/17/1/R01.

[197] DIN EN ISO 25178-3:2012-11, Geometrische Produktspezifikation (GPS) - Oberflächenbeschaffenheit: Flächenhaft - Teil 3: Spezifikationsoperatoren (ISO 25178-3:2012); Deutsche Fassung EN ISO 25178-3:2012, (2023). https://doi.org/10.31030/1876351.

[198] N. Yüksel, The Review of Some Commonly Used Methods and Techniques to Measure the Thermal Conductivity of Insulation Materials, in: A. Almusaed, A. Almssad (Eds.), Insulation Materials in Context of Sustainability, InTech, 2016. https://doi.org/10.5772/64157.

[199] H. Wang, W. Chu, G. Chen, A Brief Review on Measuring Methods of Thermal Conductivity of Organic and Hybrid Thermoelectric Materials, Adv Elect Materials 5 (2019) 1900167. https://doi.org/10.1002/aelm.201900167.

[200] A. Palacios, L. Cong, M.E. Navarro, Y. Ding, C. Barreneche, Thermal conductivity measurement techniques for characterizing thermal energy storage materials – A review, Renewable and Sustainable Energy Reviews 108 (2019) 32–52. https://doi.org/10.1016/-j.rser.2019.03.020.

[201] D.G. Cahill, R.O. Pohl, Thermal conductivity of amorphous solids above the plateau, Phys. Rev. B 35 (1987) 4067–4073. https://doi.org/10.1103/PhysRevB.35.4067.

[202] D.G. Cahill, Thermal conductivity measurement from 30 to 750 K: the 3ω method, Review of Scientific Instruments 61 (1990) 802–808. https://doi.org/10.1063/1.1141498.

[203] C08 Committee, ASTM C1113/C1113M-09: Test Method for Thermal Conductivity of Refractories by Hot Wire (Platinum Resistance Thermometer Technique), (2019). https://doi.org/10.1520/C1113_C1113M-09R19.

[204] DIN EN ISO 22007-2:2022-09, Kunststoffe - Bestimmung der Wärmeleitfähigkeit und der Temperaturleitfähigkeit - Teil 2: Transientes ebenes Wärmequellenverfahren (Hot-Disc-Verfahren) (ISO 22007-2:2022); Deutsche Fassung EN ISO 22007-2:2022, (2022). https://doi.org/10.31030/3340784.

[205] DIN EN 993-15:2005-07, Prüfverfahren für dichte geformte feuerfeste Erzeugnisse - Teil 15: Bestimmung der Wärmeleitfähigkeit nach dem Heißdraht- (Parallel-) Verfahren; Deutsche Fassung EN 993-15:2005, (2005). https://doi.org/10.31030/9602422.

[206] W.J. Parker, R.J. Jenkins, C.P. Butler, G.L. Abbott, Flash Method of Determining Thermal Diffusivity, Heat Capacity, and Thermal Conductivity, Journal of Applied Physics 32 (1961) 1679–1684. https://doi.org/10.1063/1.1728417.

[207] E37 Committee, ASTM E1461-13: Test Method for Thermal Diffusivity by the Flash Method, (2022). https://doi.org/10.1520/E1461-13R22.

[208] DIN EN ISO 22007-4:2024-04, Kunststoffe - Bestimmung der Wärmeleitfähigkeit und der Temperaturleitfähigkeit - Teil 4: Lichtblitzverfahren (ISO 22007-4:2024); Deutsche Fassung EN ISO 22007-4:2024, (2024). https://doi.org/10.31030/3522582.

[209] A. Griesinger, Wärmemanagement in der Elektronik: Theorie und Praxis, Springer Berlin Heidelberg, Berlin, Heidelberg, 2019. https://doi.org/10.1007/978-3-662-58682-2.

[210] R. Kempers, P. Kolodner, A. Lyons, A.J. Robinson, A high-precision apparatus for the characterization of thermal interface materials, Review of Scientific Instruments 80 (2009) 095111. https://doi.org/10.1063/1.3193715.

[211] M. Abo Ras, Neuartige Charakterisierungsmethoden für moderne Thermische Interface-Materialien einschließlich deren Struktur-Eigenschafts-Korrelation, Fakultät für Elektrotechnik und Informationstechnik der Technischen Universität Chemnitz, 2020. https://nbn-resolving.org/urn:nbn:de:bsz:ch1-qucosa2-706186 (accessed November 21, 2020).

[212] Y. Xian, P. Zhang, S. Zhai, P. Yuan, D. Yang, Experimental characterization methods for thermal contact resistance: A review, Applied Thermal Engineering 130 (2018) 1530–1548. https://doi.org/10.1016/j.applthermaleng.2017.10.163.

[213] P. Teertstra, Thermal Conductivity and Contact Resistance Measurements for Adhesives, in: ASME 2007 InterPACK Conference, Volume 1, ASMEDC, Vancouver, British Columbia, Canada, 2007: pp. 381–388. https://doi.org/10.1115/IPACK2007-33026.

[214] A.N. Smith, N.R. Jankowski, L.M. Boteler, Measurement of High-Performance Thermal Interfaces Using a Reduced Scale Steady-State Tester and Infrared Microscopy, Journal of Heat Transfer 138 (2016) 041301. https://doi.org/10.1115/1.4032172.

[215] R.J. Warzoha, B.F. Donovan, High resolution steady-state measurements of thermal contact resistance across thermal interface material junctions, Rev. Sci. Instrum. 88 (2017) 094901. https://doi.org/10.1063/1.5001835.

[216] J. Wu, R. Morrell, L. Chapman, J. Clark, P. Quested, Characterisation of thermal conductivity reference material using the NPL axial heat flow apparatus, High Temperatures - High Pressures 47 (2018) 511–524.

[217] M.J. Assael, K. Gialou, K. Kakosimos, I. Metaxa, Thermal Conductivity of Reference Solid Materials, International Journal of Thermophysics 25 (2004) 397–408. https://doi.org/-10.1023/B:IJOT.0000028477.74595.d5.

[218] B.F. Blackwell, W. Gill, K.J. Dowding, T.E. Voth, Determiniation of Thermal Conductivity of 304 Stainless Steel Using Parameter Estimation Techniques, (2000). https://www.osti.gov/biblio/760791 (accessed May 26, 2024).

[219] R.S. Graves, T.G. Kollie, D.L. McElroy, K.E. Gilchrist, The thermal conductivity of AISI 304L stainless steel, Int J Thermophys 12 (1991) 409–415. https://doi.org/10.1007/-BF00500761.

[220] R.H. Bogaard, Thermal Conductivity of Selected Stainless Steels, in: T. Ashworth, D.R. Smith (Eds.), Thermal Conductivity 18, Springer US, Boston, MA, 1985: pp. 175–185. https://doi.org/10.1007/978-1-4684-4916-7_20.

[221] P. Chowdhury, K. Sikka, A. De Silva, I. Seshadri, On Thermal Interface Materials With Polydisperse Fillers: Packing Algorithm and Effective Properties, in: ASME 2018 International Technical Conference and Exhibition on Packaging and Integration of Electronic and Photonic Microsystems, American Society of Mechanical Engineers, San Francisco, California, USA, 2018: p. V001T01A007. https://doi.org/10.1115/IPACK2018-8337.

[222] G.K. Batchelor, R.W. O´Brien, Thermal or electrical conduction through a granular material, Proc. R. Soc. Lond. A 355 (1977) 313–333. https://doi.org/10.1098/rspa.1977.0100.

[223] S. Kanuparthi, G. Subbarayan, T. Siegmund, B. Sammakia, An Efficient Network Model for Determining the Effective Thermal Conductivity of Particulate Thermal Interface Materials, IEEE Trans. Comp. Packag. Technol. 31 (2008) 611–621. https://doi.org/-10.1109/TCAPT.2008.2001839.

[224] T.S. Yun, T.M. Evans, Three-dimensional random network model for thermal conductivity in particulate materials, Computers and Geotechnics 37 (2010) 991–998. https://doi.org/-10.1016/j.compgeo.2010.08.007.

[225] C. Yue, Y. Zhang, Z. Hu, J. Liu, Z. Cheng, Modeling of the effective thermal conductivity of composite materials with FEM based on resistor networks approach, Microsyst Technol 16 (2010) 633–639. https://doi.org/10.1007/s00542-009-0984-1.

[226] B. Dan, B.G. Sammakia, G. Subbarayan, S. Kanuparthi, An Improved Efficient Network Model for Determining the Effective Thermal Conductivity of Particulate Thermal Interface Materials, Journal of Electronic Packaging 135 (2013) 031003. https://doi.org/10.1115/-1.4024392.

[227] L.C. Davis, B.E. Artz, Thermal conductivity of metal-matrix composites, Journal of Applied Physics 77 (1995) 4954–4960. https://doi.org/10.1063/1.359302.

[228] C.F. Matt, M.E. Cruz, Effective Thermal Conductivity of Composite Materials with 3-D Microstructures and Interfacial Thermal Resistance, Numerical Heat Transfer, Part A: Applications 53 (2007) 577–604. https://doi.org/10.1080/10407780701678380.

[229] H. Jopek, T. Strek, Optimization of the Effective Thermal Conductivity of a Composite, in: A. Ahsan (Ed.), Convection and Conduction Heat Transfer, InTech, 2011. https://doi.org/10.5772/24531.

[230] B. Mortazavi, T. Rabczuk, Multiscale modeling of heat conduction in graphene laminates, Carbon 85 (2015) 1–7. https://doi.org/10.1016/j.carbon.2014.12.046.

[231] Z. Tong, M. Liu, H. Bao, A numerical investigation on the heat conduction in high filler loading particulate composites, International Journal of Heat and Mass Transfer 100 (2016) 355–361. https://doi.org/10.1016/j.ijheatmasstransfer.2016.04.092.

[232] L. Qian, X. Pang, J. Zhou, J. Yang, S. Lin, D. Hui, Theoretical model and finite element simulation on the effective thermal conductivity of particulate composite materials, Composites Part B: Engineering 116 (2017) 291–297. https://doi.org/10.1016/j.compositesb.2016.10.067.

[233] M. Hu, Z. Yang, Perspective on multi-scale simulation of thermal transport in solids and interfaces, Phys. Chem. Chem. Phys. 23 (2021) 1785–1801. https://doi.org/10.1039/D0CP03372C.

[234] D. Schillinger, M. Ruess, The Finite Cell Method: A Review in the Context of Higher-Order Structural Analysis of CAD and Image-Based Geometric Models, Arch Computat Methods Eng 22 (2015) 391–455. https://doi.org/10.1007/s11831-014-9115-y.

[235] S.A. Langer, E.R. Fuller, W.C. Carter, OOF: an image-based finite-element analysis of material microstructures, Comput. Sci. Eng. 3 (2001) 15–23. https://doi.org/10.1109/5992.919261.

[236] N.K. Sharma, R.K. Misra, S. Sharma, Thermal expansion behavior of Ni–Al2O3 composites with particulate and interpenetrating phase structures: An analysis using finite element method, Computational Materials Science 90 (2014) 130–136. https://doi.org/10.1016/j.commatsci.2014.04.008.

[237] N.K. Sharma, R.K. Misra, S. Sharma, Experimental characterization and numerical modeling of thermo-mechanical properties of Al-B4C composites, Ceramics International 43 (2017) 513–522. https://doi.org/10.1016/j.ceramint.2016.09.187.

[238] W.S. Jodrey, E.M. Tory, Computer simulation of close random packing of equal spheres, Phys. Rev. A 32 (1985) 2347–2351. https://doi.org/10.1103/PhysRevA.32.2347.

[239] A. Yang, C.T. Miller, L.D. Turcoliver, Simulation of correlated and uncorrelated packing of random size spheres, Phys. Rev. E 53 (1996) 1516–1524. https://doi.org/10.1103/PhysRevE.53.1516.

[240] D. He, N.N. Ekere, Computer Simulation of Powder Compaction of Spherical Particles, Journal of Materials Science Letters 17 (1998) 1723–1725. https://doi.org/10.1023/A:1006623201757.

[241] D. He, N.N. Ekere, L. Cai, Computer simulation of random packing of unequal particles, Phys. Rev. E 60 (1999) 7098–7104. https://doi.org/10.1103/PhysRevE.60.7098.

[242] L.D. Norman, Computer Simulation of Particulate Systems, U.S. Dept. of the Interior, Bureau of Mines, 1971. https://digital.library.unt.edu/ark:/67531/metadc12803/m2/1/high_res_d/Bulletin0658.pdf (accessed May 26, 2024).

[243] D.J. Adams, A.J. Matheson, Computation of Dense Random Packings of Hard Spheres, The Journal of Chemical Physics 56 (1972) 1989–1994. https://doi.org/10.1063/1.1677488.

[244] E. Santiso, E.A. Müller, Dense packing of binary and polydisperse hard spheres, Molecular Physics 100 (2002) 2461–2469. https://doi.org/10.1080/00268970210125313.

[245] M.J. Powell, Computer-simulated random packing of spheres, Powder Technology 25 (1980) 45–52. https://doi.org/10.1016/0032-5910(80)87007-0.

[246] G.Q. Lu, L.B. Ti, K. Ishizaki, A New Algorithm for Simulating the Random Packing of Monosized Powder in CIP Processes, Materials and Manufacturing Processes 9 (1994) 601–621. https://doi.org/10.1080/10426919408934934.

[247] Y.T. Feng, K. Han, D.R.J. Owen, Filling domains with disks: an advancing front approach, Int. J. Numer. Meth. Engng. 56 (2003) 699–713. https://doi.org/10.1002/nme.583.

[248] R. Al-Raoush, M. Alsaleh, Simulation of random packing of polydisperse particles, Powder Technology 176 (2007) 47–55. https://doi.org/10.1016/j.powtec.2007.02.007.

[249] A.J. Matheson, Computation of a random packing of hard spheres, J. Phys. C: Solid State Phys. 7 (1974) 2569–2576. https://doi.org/10.1088/0022-3719/7/15/007.

[250] K. Bagi, An algorithm to generate random dense arrangements for discrete element simulations of granular assemblies, Granular Matter 7 (2005) 31–43. https://doi.org/10.1007/-s10035-004-0187-5.

[251] J. Liu, S. Li, Y. Chen, A fast and practical method to pack spheres for mesh generation, Acta Mech Sin 24 (2008) 439–447. https://doi.org/10.1007/s10409-008-0165-y.

[252] W.M. Visscher, M. Bolsterli, Random Packing of Equal and Unequal Spheres in Two and Three Dimensions, Nature 239 (1972) 504–507. https://doi.org/10.1038/239504a0.

[253] M.J. Jiang, J.M. Konrad, S. Leroueil, An efficient technique for generating homogeneous specimens for DEM studies, Computers and Geotechnics 30 (2003) 579–597. https://doi.org/10.1016/S0266-352X(03)00064-8.

[254] K. Han, Y.T. Feng, D.R.J. Owen, Sphere packing with a geometric based compression algorithm, Powder Technology 155 (2005) 33–41. https://doi.org/10.1016/j.powtec.2005. -04.055.

[255] L.N. Smith, P.S. Midha, A computer model for relating powder density to composition, employing simulations of dense random packings of monosized and bimodal spherical particles, Journal of Materials Processing Technology 72 (1997) 277–282. https://doi.org/-10.1016/S0924-0136(97)00181-7.

[256] S. Torquato, T.M. Truskett, P.G. Debenedetti, Is Random Close Packing of Spheres Well Defined?, Phys. Rev. Lett. 84 (2000) 2064–2067. https://doi.org/10.1103/PhysRevLett.-84.2064.

[257] G.D. Scott, Packing of Spheres: Packing of Equal Spheres, Nature 188 (1960) 908–909. https://doi.org/10.1038/188908a0.

[258] G.D. Scott, D.M. Kilgour, The density of random close packing of spheres, J. Phys. D: Appl. Phys. 2 (1969) 863–866. https://doi.org/10.1088/0022-3727/2/6/311.

[259] A.S. Clarke, J.D. Wiley, Numerical simulation of the dense random packing of a binary mixture of hard spheres: Amorphous metals, Phys. Rev. B 35 (1987) 7350–7356. https://doi.org/10.1103/PhysRevB.35.7350.

[260] J.D. Bernal, J. Mason, Packing of Spheres: Co-ordination of Randomly Packed Spheres, Nature 188 (1960) 910–911. https://doi.org/10.1038/188910a0.

[261] E.M. Tory, N.A. Cochrane, S.R. Waddell, Anisotropy in Simulated Random Packing of Equal Spheres, Nature 220 (1968) 1023–1024. https://doi.org/10.1038/2201023a0.

[262] K.D.L. Kristiansen, A. Wouterse, A. Philipse, Simulation of random packing of binary sphere mixtures by mechanical contraction, Physica A: Statistical Mechanics and Its Applications 358 (2005) 249–262. https://doi.org/10.1016/j.physa.2005.03.057.

[263] X.Z. An, R.Y. Yang, K.J. Dong, R.P. Zou, A.B. Yu, Micromechanical Simulation and Analysis of One-Dimensional Vibratory Sphere Packing, Phys. Rev. Lett. 95 (2005) 205502. https://doi.org/10.1103/PhysRevLett.95.205502.

[264] J. Zhao, S. Li, P. Lu, L. Meng, T. Li, H. Zhu, Shape influences on the packing density of frustums, Powder Technology 214 (2011) 500–505. https://doi.org/10.1016/j.powtec.-2011.09.013.

[265] X. Jia, R.A. Williams, A packing algorithm for particles of arbitrary shapes, Powder Technology 120 (2001) 175–186. https://doi.org/10.1016/S0032-5910(01)00268-6.

[266] M. Gan, N. Gopinathan, X. Jia, R.A. Williams, Predicting Packing Characteristics of Particles of Arbitrary Shapes, KONA 22 (2004) 82–93. https://doi.org/10.14356/kona.2004012.

[267] S. Li, J. Zhao, P. Lu, Y. Xie, Maximum packing densities of basic 3D objects, Chin. Sci. Bull. 55 (2010) 114–119. https://doi.org/10.1007/s11434-009-0650-0.

[268] M. Taiebat, P. Mutabaruka, R. Pellenq, F. Radjai, Effect of particle size distribution on 3D packings of spherical particles, EPJ Web Conf. 140 (2017) 02030. https://doi.org/-10.1051/epjconf/201714002030.

[269] H. Wadell, Volume, Shape, and Roundness of Quartz Particles, The Journal of Geology 43 (1935) 250–280. https://doi.org/10.1086/624298.

[270] W. Fei, G.A. Narsilio, M.M. Disfani, Impact of three-dimensional sphericity and roundness on heat transfer in granular materials, Powder Technology 355 (2019) 770–781. https://doi.org/10.1016/j.powtec.2019.07.094.

[271] B. Zhou, J. Wang, H. Wang, Three-dimensional sphericity, roundness and fractal dimension of sand particles, Géotechnique 68 (2018) 18–30. https://doi.org/10.1680/jgeot.16.P.207.

[272] B. Zhao, J. Wang, 3D quantitative shape analysis on form, roundness, and compactness with µCT, Powder Technology 291 (2016) 262–275. https://doi.org/10.1016/j.powtec.2015.-12.029.

[273] Z. Nie, Z. Liang, X. Wang, A three-dimensional particle roundness evaluation method, Granular Matter 20 (2018) 32. https://doi.org/10.1007/s10035-018-0802-5.

[274] D.J.M. Hodgson, M. Hermes, E. Blanco, W.C.K. Poon, Granulation and suspension rheology: A unified treatment, Journal of Rheology 66 (2022) 853–858. https://doi.org/-10.1122/8.0000515.

[275] W. Evans, R. Prasher, J. Fish, P. Meakin, P. Phelan, P. Keblinski, Effect of aggregation and interfacial thermal resistance on thermal conductivity of nanocomposites and colloidal nanofluids, International Journal of Heat and Mass Transfer 51 (2008) 1431–1438. https://doi.org/10.1016/j.ijheatmasstransfer.2007.10.017.

[276] R. Prasher, W. Evans, P. Meakin, J. Fish, P. Phelan, P. Keblinski, Effect of aggregation on thermal conduction in colloidal nanofluids, Applied Physics Letters 89 (2006) 143119. https://doi.org/10.1063/1.2360229.

[277] W. Yang, Y. Chen, Y. Zhang, Y. Fu, K. Zheng, K. Wang, Y. Ma, Thermal Conductance of Epoxy/Alumina Interfaces, J. Phys.: Conf. Ser. 2133 (2021) 012002. https://doi.org/10.1088/1742-6596/2133/1/012002.

[278] C. Schmidt, Thermal boundary (Kapitza) resistance at niobium-epoxy interfaces in the superconducting and normal states, Phys. Rev. B 15 (1977) 4187–4192. https://doi.org/-10.1103/PhysRevB.15.4187.

[279] G. Schmidt, Thermal boundary resistance at interfaces between two dielectrics, Physics Letters A 50 (1974) 241–242. https://doi.org/10.1016/0375-9601(74)90733-6.

[280] K.W. Desmond, E.R. Weeks, Influence of particle size distribution on random close packing of spheres, Phys. Rev. E 90 (2014) 022204. https://doi.org/10.1103/PhysRevE.90.022204.

[281] H.Y. Sohn, C. Moreland, The effect of particle size distribution on packing density, Can. J. Chem. Eng. 46 (1968) 162–167. https://doi.org/10.1002/cjce.5450460305.

[282] S.V. Anishchik, N.N. Medvedev, Three-Dimensional Apollonian Packing as a Model for Dense Granular Systems, Phys. Rev. Lett. 75 (1995) 4314–4317. https://doi.org/-10.1103/PhysRevLett.75.4314.

[283] S.M.K. Rassouly, The packing density of `perfect' binary mixtures, Powder Technology 103 (1999) 145–150. https://doi.org/10.1016/S0032-5910(98)00223-X.

[284] G. Roquier, A Theoretical Packing Density Model (TPDM) for ordered and disordered packings, Powder Technology 344 (2019) 343–362. https://doi.org/10.1016/j.powtec.-2018.12.033.

[285] R.D. Sudduth, Practical Limits for Two Fundamental Approaches to Designing Particle Size Distributions to Address a Specific Physical Property like Viscosity, Polymers 13 (2021) 3047. https://doi.org/10.3390/polym13183047.

[286] Y. Yuan, L. Liu, Y. Zhuang, W. Jin, S. Li, Coupling effects of particle size and shape on improving the density of disordered polydisperse packings, Phys. Rev. E 98 (2018) 042903. https://doi.org/10.1103/PhysRevE.98.042903.

[287] T. Stovall, F. De Larrard, M. Buil, Linear packing density model of grain mixtures, Powder Technology 48 (1986) 1–12. https://doi.org/10.1016/0032-5910(86)80058-4.

[288] R.S. Farr, R.D. Groot, Close packing density of polydisperse hard spheres, The Journal of Chemical Physics 131 (2009) 244104. https://doi.org/10.1063/1.3276799.

[289] W. Du, M. Li, Z. Pei, C. Ma, Performances of three models in predicting packing densities and optimal mixing fractions of mixtures of micropowders with different sizes, Powder Technology 397 (2022) 117095. https://doi.org/10.1016/j.powtec.2021.117095.

[290] Z. Chen, Y. Zhao, A quasi-physical method for random packing of spherical particles, Powder Technology 412 (2022) 118002. https://doi.org/10.1016/j.powtec.2022.118002.

[291] M.M. Rueda, M.-C. Auscher, R. Fulchiron, T. Périé, G. Martin, P. Sonntag, P. Cassagnau, Rheology and applications of highly filled polymers: A review of current understanding, Progress in Polymer Science 66 (2017) 22–53. https://doi.org/10.1016/j.progpolymsci.2016.12.007.

[292] P. Chowdhury, K. Sikka, A. Grill, D.P. Parekh, Optimal Filler Sizes for Thermal Interface Materials, in: 2019 18th IEEE Intersociety Conference on Thermal and Thermomechanical Phenomena in Electronic Systems (ITherm), IEEE, Las Vegas, NV, USA, 2019: pp. 52–57. https://doi.org/10.1109/ITHERM.2019.8757459.

[293] I.L. Ngo, V.A. Truong, An investigation on effective thermal conductivity of hybrid-filler polymer composites under effects of random particle distribution, particle size and thermal contact resistance, International Journal of Heat and Mass Transfer 144 (2019) 118605. https://doi.org/10.1016/j.ijheatmasstransfer.2019.118605.

[294] M.-C. Lu, A synergistic model for thermal conductivity with hybrid fillers in polymeric matrix composites, in: 2016 32nd Thermal Measurement, Modeling & Management Symposium (SEMI-THERM), IEEE, San Jose, CA, USA, 2016: pp. 151–156. https://doi.org/-10.1109/SEMI-THERM.2016.7458459.

[295] C.-Y. Zhu, G.-L. Yu, X. Ren, B. Huang, L. Gong, Modelling of the effective thermal conductivity of composites reinforced with fibers and particles by two-step homogenization method, Composites Science and Technology 230 (2022) 109766. https://doi.org/10.1016/j.compscitech.2022.109766.

[296] I. Mehdipour, K.H. Khayat, Understanding the role of particle packing characteristics in rheo-physical properties of cementitious suspensions: A literature review, Construction and Building Materials 161 (2018) 340–353. https://doi.org/10.1016/j.conbuildmat.2017.11.147.

[297] M. Santhanam, S.V. Kumar, Particle packing theories and their application in concrete mixture proportioning: A review, The Indian Concrete Journal 77 (2003) 1324–1331.

[298] Ł. Mrozik, Shaping the structure of low water-binder ratio cement pastes, in: 23rd International Conference Engineering Mechanics, Svratka, Czech Republic, 15 – 18 May 2017, 2017. https://www.engmech.cz/improc/2017/0674.pdf (accessed May 26, 2024).

[299] M.N. Mangulkar, S.S. Jamkar, Review of Particle Packing Theories Used For Concrete Mix Proportioning, International Journal Of Scientific & Engineering Research Volume 4, Issue 5 (2013).

[300] K.L. Scrivener, A.K. Crumbie, P. Laugesen, The Interfacial Transition Zone (ITZ) Between Cement Paste and Aggregate in Concrete, Interface Science 12 (2004) 411–421. https://doi.org/10.1023/B:INTS.0000042339.92990.4c.

[301] P. Stroeven, H. He, Z. Guo, M. Stroeven, Particle packing in a model concrete at different levels of the microstructure: Evidence of an intrinsic patchy nature, Materials Characterization 60 (2009) 1088–1092. https://doi.org/10.1016/j.matchar.2009.02.011.

[302] M.M. Kanafi, Surface generator: artificial randomly rough surfaces, MATLAB Central File Exchange (2016). https://www.mathworks.com/matlabcentral/fileexchange/60817-surface-generator-artificial-randomly-rough-surfaces (accessed May 26, 2024).

[303] S. Song, M.M. Yovanovich, Relative contact pressure - Dependence on surface roughness and Vickers microhardness, Journal of Thermophysics and Heat Transfer 2 (1988) 43–47. https://doi.org/10.2514/3.60.

[304] S. Song, M.M. Yovanovich, F.O. Goodman, Thermal Gap Conductance of Conforming Surfaces in Contact, Journal of Heat Transfer 115 (1993) 533–540. https://doi.org/10.1115/1.2910719.

[305] I. Hughes, T.P.A. Hase, I.G. Hughes, Measurements and their uncertainties: a practical guide to modern error analysis, 1. publ, Oxford Univ. Press, Oxford New York, 2010.

[306] S.P. Venkateshan, Heat Transfer, Springer International Publishing, Cham, 2021. https://doi.org/10.1007/978-3-030-58338-5.

LIST OF FIGURES

LIST OF TABLES

Appendix A SUPPLEMENTARY MODELS TO CHAPTER 1

A.1 Cooper-Mikic-Yovanovich model for solid contribution to contact conductance

This appendix supplements section 2.3.1 with a very popular model for determining the solid contribution to contact conductance h_S, the Cooper-Mikic-Yovanovich (CMY) model [78,106], well summarized in [77].

A dimensionless solid contact conductance for isotropic rough surfaces and for purely plastic deformation of the asperities can be expressed as [77]

$$H_\mathrm{S} \equiv \frac{h_\mathrm{S}\,\sigma_\mathrm{S}}{\lambda_\mathrm{S}\,m} = 1.25\left(\frac{P}{H_\mathrm{p}}\right)^{0.95} \quad . \tag{A.1}$$

This semi-empirical model considers

- the effective solid thermal conductivity $\lambda_\mathrm{S} = \frac{2\,\lambda_1\,\lambda_2}{\lambda_1+\lambda_2}$, with the thermal conductivities $\lambda_{1,2}$ of the two contacting solids,
- the effective rms surface roughness $\sigma_\mathrm{S} = \sqrt{\sigma_{\mathrm{S},1} + \sigma_{\mathrm{S},2}}$, with the rms surface roughnesses $\sigma_{\mathrm{S},1,2}$ of the two contacting solids according to [106],
- the effective absolute mean asperity slope $m = \sqrt{m_1 + m_2}$, with the absolute mean asperity slopes $m_{1,2}$ of the two contacting solids according to [106],
- the mean contact area pressure P, and
- the microhardness of the softer contacting asperities H_p, according to [303].

A.2 Gap conductance model for two conforming rough surfaces

This appendix supplements section 2.3.1 with a statistical model for describing the gas path at a solid-solid contact. It was developed by Yovanovich et al. [107] and is also well summarized in [77].

The gap conductance between two conforming rough surfaces is expressed as [77,107,304]

$$h_\mathrm{G} = \frac{\lambda_\mathrm{G}}{\sigma}\,\frac{1}{\sqrt{2\pi}} \int_0^\infty \frac{\exp(-(Y/\sigma_\mathrm{S} - u_\mathrm{G})^2/2)}{u_\mathrm{G} + M/\sigma_\mathrm{S}}\;\mathrm{d}u_\mathrm{G} \;, \tag{A.2}$$

where λ_G is the thermal conductivity of the gas in the gap. Y denotes the effective gap thickness, M the gas rarefaction parameter, and $u_\mathrm{G} = t_\mathrm{G}/\sigma_\mathrm{S}$ the local dimensionless gap thickness with the absolute local gap thickness t_G. The effective gap thickness is affected by several parameters, such as the microscopic surface structures, the surface pressure, and the hardness of the surfaces. According to [77], it can be expressed in dimensionless form as

$$\frac{Y}{\sigma_\mathrm{S}} = \sqrt{2}\ \mathrm{erfc}^{-1}\left(\frac{2P}{H_\mathrm{p}}\right), \tag{A.3}$$

for a purely plastic deformation of the asperities. The thermal conductivity of gases in narrow gaps is severely limited because the intermolecular collisions are statistically reduced compared to molecule-wall collisions. The effect is similar to that of the rarefaction of gases. The quite complex phenomena in the gaps between two rough solids are therefore described using the theories of heat transfer in rarefied gases, expressed by the gas rarefaction parameter [77]

$$M = \alpha_\mathrm{G}\beta_\mathrm{G} l\ . \tag{A.4}$$

It is dependent upon the thermal gas accommodation coefficient α_G with [77]

$$\alpha_\mathrm{G} = \frac{2-\alpha_\mathrm{G,1}}{\alpha_\mathrm{G,1}} + \frac{2-\alpha_\mathrm{G,2}}{\alpha_\mathrm{G,2}}\ , \tag{A.5}$$

where $\alpha_\mathrm{G,1,2}$ are the thermal gas accommodation coefficients of the two gas-solid combinations, and the gas parameter β_G with [77]

$$\beta_\mathrm{G} = \frac{2\gamma_\mathrm{a}}{(\gamma_\mathrm{a}+1)\mathrm{Pr}}\ , \tag{A.6}$$

where Pr is the Prandtl number of the gas and $\gamma_\mathrm{a} = C_\mathrm{P}/C_\mathrm{V}$ is the adiabatic index, the ratio between the isobaric and isochoric heat capacity of the gas [77]. l describes the molecular mean free path of the gas molecules, which may be dependent on temperature and pressure in the gaps.

A.3 Fractal model for predicting thermal contact resistance at solid-liquid interfaces

This appendix supplements section 2.3.3 with a fractal model for predicting the thermal contact resistance at a solid-liquid interface, developed by Li et al. [110]. Li et al. express the specific solid-liquid contact resistance as

$$r_\mathrm{C} = \frac{1}{2\ \lambda_\mathrm{SL}\ L}\sqrt{\frac{(1-\sqrt{\phi_\mathrm{S}})^3}{\phi_\mathrm{S}}}\ , \tag{A.7}$$

where

- $\lambda_{\mathrm{SL}} = \frac{2\lambda_{\mathrm{S}}\,\lambda_{\mathrm{L}}}{\lambda_{\mathrm{S}}+\lambda_{\mathrm{L}}}$ is the effective thermal conductivity, with the thermal conductivities λ_{S} of the solid, and λ_{L} of the liquid,
- L is the sample length of the considered surface with fractal properties, and
- ϕ_{S} is the solid contact fraction with

$$\phi_{\mathrm{S}} = 1 - \frac{\pi}{4}\frac{D_{\mathrm{F}}}{2-D_{\mathrm{F}}}\frac{l_{\mathrm{p,max}}^2}{L^2}\;. \qquad \textbf{(A.8)}$$

The calculation of the solid contact fraction considers the sample length L, the fractal dimension of contours D_{F}, and the maximum base diameter of cavities on the interface $l_{\mathrm{p,max}}$. The latter is determined as a function of applied pressure, wettability, temperature, and surface fractal parameters. For details on surface characterization and model parameters, the reader is referred to [110].

Appendix B DETAILS ON EVALUATIONS AND UNCERTAINTY ANALYSIS IN CHAPTER 3

B.1 Regression parameters for steady-state cylinder method

This appendix supplements section 3.2.5. When evaluating the thermal conductivity of a sample material from the measured specific thermal resistances r_i of n samples of different thicknesses d_i, a linear regression with

$$r(d)_{\mathrm{fit}} = \alpha_0 + \alpha_1\ d \tag{B.1}$$

is performed. The axis intercept α_0 is calculated using [305]

$$\alpha_0 = \frac{\sum_{i=1}^{n} {d_i}^2 \sum_{i=1}^{n} r_i - \sum_{i=1}^{n} d_i \sum_{i=1}^{n} d_i r_i}{D_{\mathrm{C}}}\ , \tag{B.2}$$

and the slope α_1 is obtained with [305]

$$\alpha_1 = \frac{n \sum_{i=1}^{n} d_i r_i - \sum_{i=1}^{n} r_i \sum_{i=1}^{n} d_i}{D_{\mathrm{C}}}\ , \tag{B.3}$$

where D_{C} is the determinant of coefficients, defined as [305]

$$D_{\mathrm{C}} = n \sum_{i=1}^{n} d_i^2 - \left(\sum_{i=1}^{n} d_i\right)^2\ . \tag{B.4}$$

B.2 Uncertainty estimation for the steady-state cylinder method

This appendix supplements section 3.2.6 by describing the uncertainty estimation and propagation analysis for measurements with the steady-state cylinder method.

To estimate the impact of the systematic uncertainties in the measured thermal resistances on the evaluated thermal conductivity (see section 3.2.5), an uncertainty propagation analysis is required. It involves the individual uncertainty components $\Delta r_{i,\mathrm{SYS}}$ of the measured specific thermal resistance values r_i of n samples of different thicknesses d_i. In the propagation of individual uncertainties to a joint quantity, systematic components are considered in terms of magnitude, as no statistical treatment is possible, and their sign is unknown. However, this is a special case where there are n similar measured values and corresponding uncertainty components. Since all measurements were taken directly sequentially in the same apparatus and under the same boundary conditions, it can be assumed that systematic deviations are similar in all n individual measurements. For this reason, the individual contributions are considered with the correct sign and the systematic uncertainty component of the thermal conductivity is expressed as

$$\Delta\lambda_{\mathrm{SYS}} = \sum_{i=1}^{n} \Delta r_{i,\mathrm{SYS}} \left.\frac{\partial\lambda}{\partial r_i}\right|_{\overline{r_1},\ldots,\overline{r_n}} , \tag{B.5}$$

where $\partial\lambda/\partial r_i$ is the partial derivative of the evaluation function in **Eq. (3.14)** after insertion of **Eq. (B.3)**, with respect to the measured specific thermal resistance of sample i. As this is difficult to determine, the evaluation is carried out numerically.

However, it should be mentioned at this point that the uncertainty component of the thermal conductivity $\Delta\lambda_{\mathrm{SYS}}$ is not the uncertainty of the measurement method. Rather, it is its propagated effect on the thermal conductivity calculated after the measurement. Since $n = 4$ measured values of different thicknesses are always used when evaluating the thermal conductivity, $\Delta\lambda_{\mathrm{SYS}}$ varies from sample to sample, even if the uncertainty $\Delta r_{i,\mathrm{SYS}}$ on which this is based is of a systematic nature.

Besides the systematic uncertainty components, there are also random components that must be considered and discussed. Random deviations occur if the same sample is inserted into the measuring device on several days, under slightly varying ambient conditions, or in a slightly different position. Furthermore, four samples of the same composite are required to calculate the thermal conductivity, as described in section 3.2.5. Differences in the mixing ratio, air inclusions or other preparation-related uncertainties can also lead to random uncertainties. Both aspects are considered and evaluated. While the former uncertainties can only be quantified by multiple measurements, the latter can be recognized from the linear regression and its quality. To quantify the former, ten samples were selected from the entire relevant range of specific thermal resistance and measured 20 times each, on different days, with slightly varying ambient conditions in the aforementioned range. The standard deviations for all samples were evaluated and a value of

$$\Delta r_{\mathrm{RND}} \approx 20\ \mathrm{mm}^2\ \mathrm{K}\ \mathrm{W}^{-1} \tag{B.6}$$

was derived. A further propagation calculation is carried out to quantify the impact of this random uncertainty component on the evaluated thermal conductivity. The Gaussian error propagation law is applied and the random uncertainty component, gained by propagation can be expressed as

$$\Delta\lambda_{\mathrm{RND}}^{\mathrm{prop}} = \sqrt{\sum_{i=1}^{n} \left(\Delta r_{\mathrm{RND}} \left.\frac{\partial\lambda}{\partial r_i}\right|_{\overline{r_1},\ldots,\overline{r_n}} \right)^2} . \tag{B.7}$$

To quantify the uncertainty due to deviating individual samples, the uncertainty of the slope calculation in the function $r(d)_{\mathrm{fit}}$, according to **Eq. (3.13)**, and the resulting uncertainty of thermal conductivity must be determined. The uncertainty of the determined slope in **Eq. (3.13)** can be expressed as [305]

$$\Delta\alpha_1 = \sigma_r \sqrt{\frac{n}{D_\mathrm{C}}}\,, \tag{B.8}$$

where n is the number of individual samples, D_C is the determinant of coefficients, calculated according to **Eq. (B.4)**, and σ_r is the standard deviation, sometimes also referred to as common uncertainty with [305]

$$\sigma_r = \sqrt{\frac{\sum_{i=1}^{n}\big(r_i - (\alpha_0 + \alpha_1 d_i)\big)^2}{n-2}}\,. \tag{B.9}$$

The calculation of the uncertainty of thermal conductivity is carried out with

$$\Delta\lambda_\mathrm{RND}^\mathrm{fit} = \left|\Delta\alpha_1 \frac{\mathrm{d}\lambda}{\mathrm{d}\alpha_1}\right| = \frac{\Delta\alpha_1}{\alpha_1^2}\,. \tag{B.10}$$

If the effect of the variations between the samples is smaller than the effect of the general random uncertainty component Δr_RND, it is already well represented by $\Delta\lambda_\mathrm{RND}^\mathrm{prop}$. The effect of this source of uncertainty may be the dominant one, if the variations between the samples increase, which is often the case for composites with higher filler concentrations. Finally, the random uncertainty components estimated to be higher are selected with

$$\Delta\lambda_\mathrm{RND} = \max(\Delta\lambda_\mathrm{RND}^\mathrm{fit}, \Delta\lambda_\mathrm{RND}^\mathrm{prop}). \tag{B.11}$$

B.3 Uncertainty estimation for micro thermography

This appendix supplements section 3.3.7 by describing the uncertainty estimation and propagation analysis for measurements with the micro thermography method.

The systematic contributions to uncertainty remaining after calibration are:

- an uncertainty in the samples' cross-sectional area determination ΔA,
- an uncertainty in the reference samples' cross-sectional area determ. ΔA_ref, and
- an uncertainty in the reference samples' thermal conductivity $\Delta\lambda_\mathrm{ref}$.

Furthermore, the quasi-systematic uncertainty in the linear regression of the temperature profile $\Delta(\mathrm{d}\bar{T}/\mathrm{d}z)$ during the calibration run can be considered as systematic. This uncertainty is caused by surface non-uniformities of the reference sample, environmental heat losses, local deviations in emissivity, and statistical noise in the temperature measurements of the individual thermal image pixels. Thus, it is partially based on statistical deviations, but it is determined once and systematically affects all subsequent measurements. Beginning with the calibration procedure, the systematic uncertainty of the derived thermal reference resistance according to **Eq. (3.18)**, page 66, can be expressed as

$$\Delta R_0 = \left| \Delta \dot{Q}_{\text{calib}} \left(\frac{\partial R_0}{\partial \dot{Q}_{\text{calib}}} \right) \right| , \tag{B.12}$$

solely considering the contribution of an uncertainty in the calibration heat flow $\Delta \dot{Q}_{\text{calib}}$. Systematic uncertainties in temperature difference measurement $\Delta(T_{\text{TC},1} - T_{\text{TC},2})$ can be neglected as they are compensated for when evaluating the final measurements, as described in section 3.3.4. The uncertainty in the determination of the calibration heat flow can be expressed as

$$\begin{aligned} \Delta \dot{Q}_{\text{calib}} = &\left| \Delta \lambda_{\text{ref}} \left(\frac{\partial \dot{Q}_{\text{calib}}}{\partial \lambda_{\text{ref}}} \right) \right| + \left| \Delta A_{\text{ref}} \left(\frac{\partial \dot{Q}_{\text{calib}}}{\partial A_{\text{ref}}} \right) \right| \\ &+ \left| \Delta(\mathrm{d}\bar{T}/\mathrm{d}z) \left(\frac{\partial \dot{Q}_{\text{calib}}}{\partial(\mathrm{d}\bar{T} \,/\, \mathrm{d}z)} \right) \right| . \end{aligned} \tag{B.13}$$

Uncertainties in the reference samples' thermal conductivity $\Delta\lambda_{\text{ref}}$, errors in the reference samples' cross-sectional area ΔA_{ref}, and the quasi-systematic uncertainty in the linear regression of the temperature profile $\Delta(\mathrm{d}\bar{T}/\mathrm{d}z)$ are considered. $\Delta\lambda_{\text{ref}}/\Delta\lambda = 4.8\ \%$ is taken from **Eq. (3.16)**, page 65. Length and width of the reference sample and all multi-layered samples were measured using a caliper gauge. To determine ΔA_{ref}, an uncertainty of $0.01\ \text{mm}$ for the manual measurements was assumed. The uncertainty in the linear regression of the temperature profile can be obtained with

$$\Delta(\mathrm{d}\bar{T}/\mathrm{d}z) = \sqrt{\frac{n\ \sum_{i=1}^{n} \left(\bar{T}_i - (\bar{T}(0) + (\mathrm{d}\bar{T}/\mathrm{d}z) z_i) \right)^2}{D_{\text{C}}(n-2)}} , \tag{B.14}$$

and

$$D_{\text{C}} = n \sum_{i=1}^{n} z_i^2 - \left(\sum_{i=1}^{n} z_i \right)^2 , \tag{B.15}$$

where n is the number of pixel rows considered for linear regression, $\bar{T}_i$ is the average temperature of pixel row i, z_i is its z coordinate, and $T(0)$ is the temperature at $z = 0$, obtained by linear regression. Finally, the uncertainty of the specific thermal resistance measured by micro thermography can be formulated as

$$\Delta r = \left| \Delta A \left(\frac{\partial r}{\partial A} \right) \right| + \left| \Delta \dot{Q} \left(\frac{\partial r}{\partial \dot{Q}} \right) \right| , \tag{B.16}$$

where ΔA is the uncertainty in the samples' cross-sectional area. Again, an uncertainty of $0.01\ \text{mm}$ is considered for the length and width measurements via caliper gauge. The uncertainty in heat flow determination can be expressed as

$$\Delta \dot{Q} = \left| \Delta (T_{\mathrm{TC},1} - T_{\mathrm{TC},2}) \left(\frac{\partial \dot{Q}}{\partial (T_{\mathrm{TC},1} - T_{\mathrm{TC},2})} \right) \right| + \left| \Delta R_0 \left(\frac{\partial \dot{Q}}{\partial R_0} \right) \right| , \qquad \textbf{(B.17)}$$

where $\Delta(T_{\mathrm{TC},1} - T_{\mathrm{TC},2})$ is an uncertainty in temperature difference measurement with respect to the previously performed calibration measurement. It is mainly determined by the resolution of the entire temperature measurement system and is estimated as $0.05\ \mathrm{K}$.

Appendix C SUPPLEMENTARY DETAILS ON MODELING AND SIMULATION

C.1 Details on RVE size determination

This appendix supplements section 4.1.2 with details on the RVE size determination and exemplary verification data. The modeled RVEs must be sufficiently large to represent the desired particle size distribution and sufficiently large to account for local variations in the microstructure and thus to reduce the variance between repeated simulations.

Before modeling a filler packing, a random sample of typically 100,000 particle sizes is created based on a particle size distribution, discretized into 145 logarithmically spaced intervals. After the packing is modeled, the resulting particle size distribution of the placed particles is evaluated using the same discretization. **Figure C.1** illustrates an exemplary comparison of desired (target) and modeled cumulative particle size distributions of a packing with log-normal size distributed spheres ($\log(\sigma) = 0.2$, $D_{50} = 100\ \mu\text{m}$). In this model, 1,999 particles were positioned within the RVE. The diameters D_{10}, D_{50}, and D_{90} are extracted and compared. Linear interpolation is performed between the evaluated sampling points. An RVE is considered as sufficiently large if all three reference diameters deviate by less than 2 % from the target size distribution. This criterion is met in the example shown in **Figure C.1**.

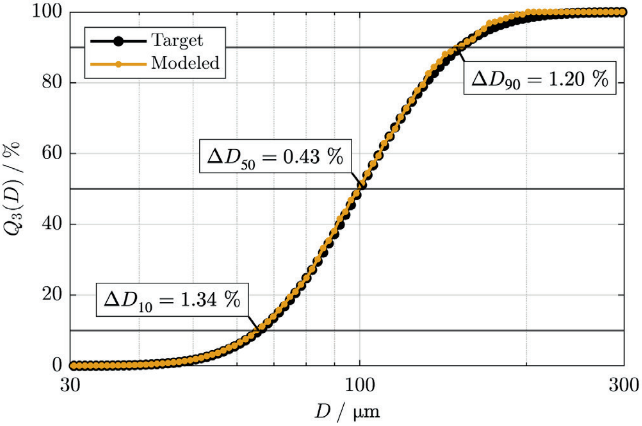

Figure C.1. Exemplary comparison of desired and modeled particle size distribution. Filler: Spheres with log-normal size distribution with $\log(\sigma) = 0.2$, $D_{50} = 100\ \mu\text{m}$, $\phi_{\text{max}} = 0.66$. RVE size: $6 \times D_{50}$.

To assess simulation reproducibility, preliminary studies were conducted in which multiple packings with identical parameters, but different stochastic particle arrangements were modeled and analyzed. **Figure C.2** shows the effective thermal conductivity results from a set of 20 repeated simulations for a packing of log-normal size distributed spheres ($\log(\sigma) = 0.2,\ D_{50} = 100\ \mu\text{m}$) at $\phi \approx 0.6$, $\phi \approx 0.5$, $\phi \approx 0.4$, and $\phi \approx 0.3$. Solid lines represent the mean value, and the shaded bands indicate the $\pm 1\sigma$ margin. The maximum variation is $\pm\ 0.93\ \%$ which remains below the $1\ \%$ threshold considered acceptable. Based on this result, the RVE with a size of $6 \times D_{50}$ can be considered sufficiently large. Based on several such preliminary analyses carried out at the start of the simulation studies, a conservative worst-case uncertainty margin of $\pm 1\ \%$ was defined and subsequently used for all simulation results, see section 4.1.2.

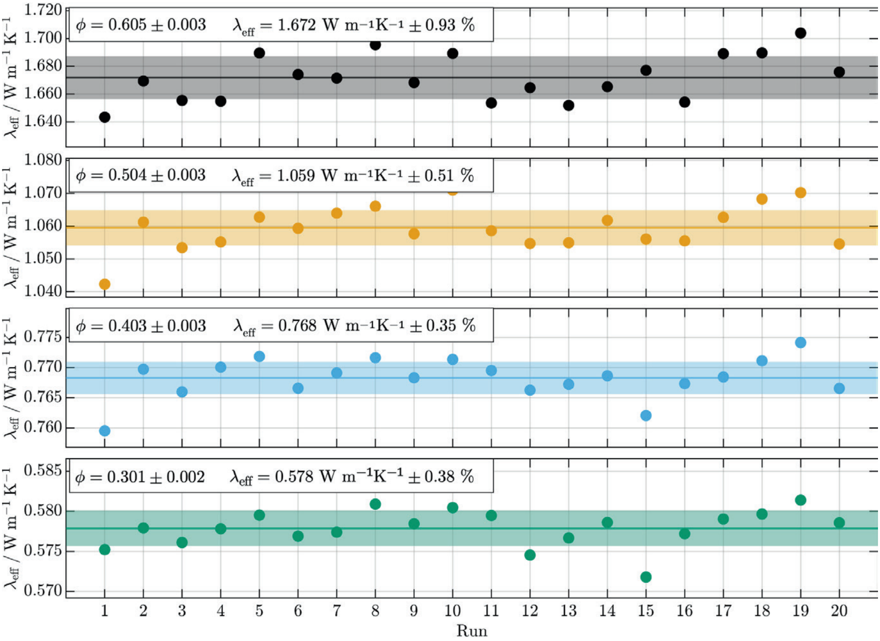

Figure C.2. Exemplary study on reproducibility of microscale simulations.

Calculated effective thermal conductivities for 20 repetitions at $\phi \approx 0.6$, $\phi \approx 0.5$, $\phi \approx 0.4$, and $\phi \approx 0.6$. Labels show the respective mean values and standard deviations. Polymer: $\lambda_C = 0.25$ W m^{-1} K^{-1} (e.g., epoxy). Filler: Spheres with log-normal size distribution with $\log(\sigma) = 0.2,\ D_{50} = 100\ \mu\text{m},\ \phi_{\max} = 0.66,\ \lambda_D = 35$ W m^{-1} K^{-1} (e.g., alumina). Packing structure: RMP ($N = 5{,}000$). RVE size: $6 \times D_{50}$.

C.2 Computational details for steady-state heat conduction through RVEs

This appendix supplements section 4.1.4 with further details on the computational method and the applied iteration scheme. Based on an initial temperature field guess, the basic Jacobi scheme is applied to obtain the steady-state temperature field inside the RVE. The temperatures in each iteration I are calculated with

$$T^{I} = \left(\frac{\Delta T_{-x}^{I-1}}{r_{-x}} + \frac{\Delta T_{+x}^{I-1}}{r_{+x}} + \frac{\Delta T_{-y}^{I-1}}{r_{-y}} + \frac{\Delta T_{+y}^{I-1}}{r_{+y}} + \frac{\Delta T_{-z}^{I-1}}{r_{-z}} + \frac{\Delta T_{+z}^{I-1}}{r_{+z}} \right) r_{\mathrm{eff}} \tag{C.1}$$

for each mesh cell. $\Delta T_{""}^{I-1}$ is the temperature difference between the cell under consideration and the adjacent cell in the indexed direction at the previous iteration $I-1$. r_{eff} denotes the effective specific thermal resistance of the cell under consideration

$$r_{\mathrm{eff}} = \left(\frac{1}{r_{-x}} + \frac{1}{r_{+x}} + \frac{1}{r_{-y}} + \frac{1}{r_{+y}} + \frac{1}{r_{-z}} + \frac{1}{r_{+z}} \right)^{-1} . \tag{C.2}$$

During the iterative calculation, convergence is continuously monitored, and a defined stopping criterion is applied. As the primary target value of the calculations is the effective thermal conductivity of the RVE, this is also used for convergence assessment. The evaluation of the effective thermal conductivity is described in section 4.1.5.

The difference between the computed effective thermal conductivities of the last two iterations $\Delta\lambda_{\mathrm{R}} = |\lambda_{\mathrm{eff}}^{I} - \lambda_{\mathrm{eff}}^{I-1}|$ is monitored and the iterative procedure is stopped, when $\Delta\lambda_{\mathrm{R}} < 10^{-8}\ \mathrm{W\ m^{-1}\ K^{-1}}$ is achieved. This threshold is based on a comprehensive convergence study involving ten different RVEs. For a maximum allowable deviation of $0.01\ \mathrm{W\ m^{-1}\ K^{-1}}$ from the converged value, this criterion ensures sufficient accuracy. The iterative calculations are performed in two sequential steps. First, a calculation in single precision (7 decimal digits) is performed. Once the stopping criterion is reached, the calculations are continued in double precision (14 decimal digits) until the stopping criterion is reached again. This procedure saves an average of 20 $\%$ calculation time compared to a full calculation in double precision. Depending on the complexity of the microstructure and the local gradients, between $2 \cdot 10^5$ and $2 \cdot 10^6$ iterations are necessary. If the calculations are performed on a NVIDIA® A100 80GB PCIe GPU, the average calculation time at maximum mesh size of $n_x = n_y = n_z = 300$ is approx. one hour.

C.3 Derivation of the first ϕ correction for the ITZ extension model

This appendix supplements section 5.1.3 with the mathematical derivation of the first correction of the filler volume fractions in the ITZ extension model. The relative filler volume fractions ϕ_i^{r} must be corrected to $\phi_i^{\mathrm{r}} \rightarrow \hat{\phi}_i^{\mathrm{r}}$, so that they correspond to the filler volume fraction in the bulk areas $\hat{\phi}^{\mathrm{r}}_i = \phi_{\mathrm{bulk},i}$. Therefore, the overall filler volume fraction ϕ^{r}_i is expressed with the particle volumes $V_{\mathrm{D,ITZ},i}$ and $V_{\mathrm{D,bulk},i}$ in the ITZ and in the bulk zone as well as the total volume $V_{\mathrm{tot},i}$ in which the fraction is dispersed

$$\phi^{\mathrm{r}}_i = \frac{V_{\mathrm{D,ITZ},i} + V_{\mathrm{D,bulk},i}}{V_{\mathrm{tot},i}} \,. \tag{C.3}$$

The volume of the particles in the bulk region and the ITZ can be replaced with the respective filler volume fractions $\phi_{\mathrm{ITZ},i}$ and $\phi_{\mathrm{bulk},i}$, as well as the respective volume proportions $V_{\mathrm{ITZ},i}$ and $V_{\mathrm{bulk},i}$, thus you get

$$\phi^{\mathrm{r}}_i = \frac{\phi_{\mathrm{ITZ},i} V_{\mathrm{ITZ},i} + \phi_{\mathrm{bulk},i} V_{\mathrm{bulk},i}}{V_{\mathrm{tot},i}} \,. \tag{C.4}$$

Substituting the bulk volume $V_{\mathrm{bulk},i}$ with $V_{\mathrm{tot},i} - V_{\mathrm{ITZ},i}$ results in

$$\phi^{\mathrm{r}}_i = \phi_{\mathrm{ITZ},i} \left(\frac{V_{\mathrm{ITZ}}}{V_{\mathrm{tot}}}\right)_i + \phi_{\mathrm{bulk},i} \left(1 - \left(\frac{V_{\mathrm{ITZ}}}{V_{\mathrm{tot}}}\right)_i\right) \,. \tag{C.5}$$

After **Eq. (C.5)** is divided by $\phi_{\mathrm{bulk},i}$ and rearranged, the corrected filler volume fraction becomes

$$\hat{\phi}^{\mathrm{r}}_i = \phi_{\mathrm{bulk},i} = \phi^{\mathrm{r}}_i \left[1 + \left(\frac{V_{\mathrm{ITZ}}}{V_{\mathrm{tot}}}\right)_i \left(\left(\frac{\phi_{\mathrm{ITZ}}}{\phi_{\mathrm{bulk}}}\right)_i - 1\right)\right]^{-1} \,. \tag{C.6}$$

This can be calculated, based on the filler volume fraction ratio $\left(\frac{\phi_{\mathrm{ITZ}}}{\phi_{\mathrm{bulk}}}\right)_i = A2_i$ according to **Eq. (5.8)**, page 149, and the proportion of the volume of all ITZs towards particles of larger fractions in the total volume in which fraction i is dispersed $\left(\frac{V_{\mathrm{ITZ}}}{V_{\mathrm{tot}}}\right)_i$. For the sum of all ITZ volumes and the total volume available for fraction i in the global total volume V, there forms the relation:

$$\left(\frac{V_{\mathrm{ITZ}}}{V_{\mathrm{tot}}}\right)_i = \frac{\sum_{k=1}^{i-1} V_{\mathrm{ITZ},k}}{(1 - \phi_{\mathrm{l},i})V} \,. \tag{C.7}$$

The sum of all ITZ volumes can be determined from the spherical shell volumes around all particles of the larger fractions k with the wall thickness $\Delta r_{\mathrm{ITZ},i}$, according to **Eq. (5.7)**, page 149. These depend only on the filler loading level and the median volumetric particle size D_{50}. For the volume of the ITZ towards one particle of fraction k,

$$V_{\mathrm{ITZ},k,\mathrm{p}} = \frac{4}{3}\pi\left((r_{\mathrm{p},k} + \Delta r_{\mathrm{ITZ},i})^3 - r^3_{\mathrm{p},k}\right) \tag{C.8}$$

can be written. For the volume of the ITZ towards all particles of fraction k with its associated filler volume fraction ϕ_k in the total volume V,

$$V_{\mathrm{ITZ},k} = \frac{4}{3}\pi\left((r_{\mathrm{p},k} + \Delta r_{\mathrm{ITZ},i})^3 - r_{\mathrm{p},k}^3\right)\frac{\phi_k V}{\frac{4}{3}\pi r_{\mathrm{p},k}^3} \tag{C.9}$$

results. Insertion in **Eq. (C.7)** and reduction results in

$$\left(\frac{V_{\mathrm{ITZ}}}{V_{\mathrm{tot}}}\right)_i = [(1-\phi_{\mathrm{l},i})V]^{-1}\sum_{k=1}^{i-1}\frac{((r_{\mathrm{p},k} + \Delta r_{\mathrm{ITZ},i})^3 - r_{\mathrm{p},k}^3)\phi_k V}{r_{\mathrm{p},k}^3}\,. \tag{C.10}$$

Eq. (C.10) can be reduced and supplemented with **Eq. (5.5)**, page 144, to

$$\left(\frac{V_{\mathrm{ITZ}}}{V_{\mathrm{tot}}}\right)_i = \frac{\sum_{k=1}^{i-1}\phi_k\left(\left(1+\frac{\Delta r_{\mathrm{ITZ},i}}{r_{\mathrm{p},k}}\right)^3 - 1\right)}{1-\sum_{k=1}^{i-1}\phi_k}\,. \tag{C.11}$$

C.4 Derivation of the second ϕ correction for the ITZ extension model

This appendix supplements section 5.1.3 with the derivation of the second correction of the filler volume fractions in the ITZ extension model. A particle shrinkage $r_{\mathrm{p},i} \rightarrow \hat{r}_{\mathrm{p},i}$ is intended to replicate the additional thermal resistance that the ITZ in the adjacent finer fraction $(i+1)$ would introduce. This is associated with a reduction in the filler volume fraction $\hat{\phi}_i^{\mathrm{r}} \rightarrow \hat{\hat{\phi}}_i^{\mathrm{r}}$. Assuming that the particles have a significantly higher thermal conductivity than the continuous phase, a uniform temperature within the particles and temperature gradients only in the continuous phase can be considered a good approximation. With volumetrically isothermal particles, the expectation is that the heat flows exit and enter the particles perpendicularly to the respective surface. Purely radial heat flows are present on and near the particle surface. Therefore, the heat flow through the ITZ can be described as a purely radial heat flow through an ideally spherical shell. The addition of radial thermal resistance from the spherical shell-shaped ITZ to the resistance of the homogenized continuous phase with $\lambda_{\mathrm{C},i}$ can be expressed as

$$R_i^{\mathrm{ITZ}} = \frac{1}{4\pi}\left(\frac{1}{\lambda_{\mathrm{ITZ},(i+1)}} - \frac{1}{\lambda_{\mathrm{C},i}}\right)\left(\frac{1}{r_{\mathrm{p},i}} - \frac{1}{r_{\mathrm{p},i} + \Delta r_{\mathrm{ITZ},(i+1)}}\right)\,, \tag{C.12}$$

following the derivation of the radial thermal resistance of a spherical shell in [306]. $\lambda_{\mathrm{ITZ},(i+1)}$ represents the reduced effective thermal conductivity of the ITZ, which can be derived from **Eq. (5.9)**, page 149. $r_{\mathrm{p},i}$ is the initial particle radius and $\Delta r_{\mathrm{ITZ},(i+1)}$ is the thickness of the ITZ under consideration, according to **Eq. (5.7)**, page 149. R_i^{ITZ} is now replaced by removing a thin particle shell, thus replacing the particle volume with the less conductive continuous medium, see part (c) of **Figure 5.6**, page 150. The radial thermal resistance R_i^{shrink} caused by this particle shrinkage can be expressed as

$$R_i^{\text{shrink}} = \frac{1}{4\pi}\left(\frac{1}{\lambda_{\mathrm{C},i}} - \frac{1}{\lambda_{\mathrm{D},i}}\right)\left(\frac{1}{\hat{r}_{\mathrm{p},i}} - \frac{1}{r_{\mathrm{p},i}}\right). \tag{C.13}$$

Setting **Eqs. (C.12)** and **(C.13)** equal results in the new, reduced particle radius

$$\hat{r}_{\mathrm{p},i} = \left[\frac{\left(\frac{1}{\lambda_{\mathrm{ITZ},(i+1)}} - \frac{1}{\lambda_{\mathrm{C},i}}\right)\left(\frac{1}{r_{\mathrm{p},i}} - \frac{1}{r_{\mathrm{p},i} + \Delta r_{\mathrm{ITZ},(i+1)}}\right)}{\left(\frac{1}{\lambda_{\mathrm{C},i}} - \frac{1}{\lambda_{\mathrm{D},i}}\right)} + \frac{1}{r_{\mathrm{p},i}}\right]^{-1} . \tag{C.14}$$

The resulting reduction in particle volume causes a reduction of the filler volume fraction in fraction i to

$$\hat{\hat{\phi}}_i^{\mathrm{r}} = \hat{\phi}_i^{\mathrm{r}}\left(\frac{\hat{r}_{\mathrm{p},i}}{r_{\mathrm{p},i}}\right)^3 . \tag{C.15}$$

Appendix D SUPPLEMENTARY RESULTS OF SIMULATIVE STUDIES IN CHAPTER 6

D.1 Heat transfer between unfilled polymers and rough substrate surfaces

This appendix supplements chapter 6.2 with further simulation results on the influence of the surface structure, surface wetting and thermal conductivities of the contact partners on the thermal contact resistances and the equivalent thermal heights of interfaces between unfilled polymers and solid substrates. All subsequent simulative studies are based on the surface structure shown in **Figure 6.1**, page 167. **Figure D.1** presents the results of a study, where the surface structure is scaled to a root mean square roughness of $1.0\ \mu\mathrm{m} \leq S_\mathrm{q} \leq\ 5.0\ \mu\mathrm{m}$ and distorted to a skewness of $-6.8 < S_\mathrm{sk} < 6.4$. An aluminum alloy substrate with $\lambda_\mathrm{S} = 130\ \mathrm{W\ m^{-1}\ K^{-1}}$ in contact with an epoxy polymer with $\lambda_\mathrm{C} = 0.25\ \mathrm{W\ m^{-1}\ K^{-1}}$, considering full surface wetting, is modeled.

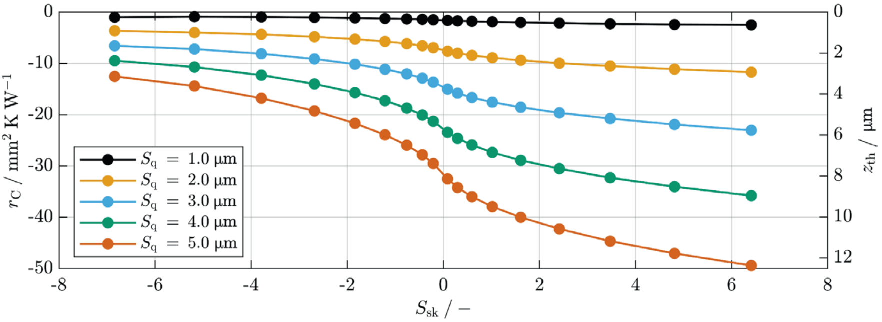

Figure D.1. Specific thermal contact resistance and equivalent thermal height as a function of surface root mean square roughness and skewness.

Polymer: $\lambda_\mathrm{C} = 0.25\ \mathrm{W\ m^{-1}\ K^{-1}}$ Substrate: Artificial rough surface with $S_\mathrm{q} = 2\ \mu\mathrm{m}$, see **Figure 6.1**, $\lambda_\mathrm{S} = 130\ \mathrm{W\ m^{-1}\ K^{-1}}$. Full surface wetting.

In a further simulative study, incomplete wetting of the polymer on the substrate surface is modeled in a geometrically simplified way and the effects on contact resistance and equivalent thermal height are investigated. A new parameter, the wetting density

$$\nu = \frac{A_\mathrm{w}}{A_0} \tag{D.1}$$

is defined as the ratio between the wetted projection area in the z direction A_w, and the nominal interfacial area A_0. Starting with complete wetting, ν is gradually reduced by successive insertion of air voids, beginning at the deepest roughness valleys, see **Figure D.2**. Central cross-sections of the modeled and meshed RVEs are shown in (a). In part (b), the corresponding wetting footprints are shown with a top view of the surface. For the air inclusions, a heat conduction path is calculated with $\lambda_G = 0.026$ W m^{-1} K^{-1}, representing the worst case and neglecting additional heat transport via radiation or convection.

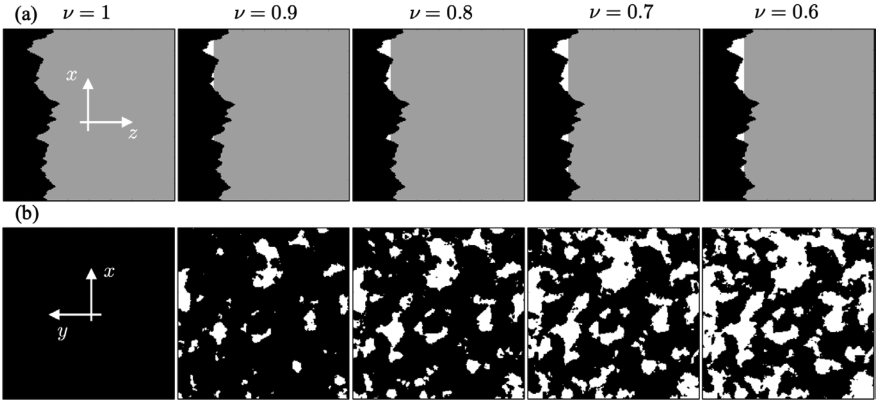

Figure D.2. Stepwise reduction of wetting density.

Central cross-sections of meshed RVE in (a). Illustration of surface wetting at $z = 0$ in (b). Black: substrate; grey: polymer; white: air voids.

Figure D.3 shows the calculated and standardized specific thermal contact resistances for a thermal setup with $\lambda_S = 130$ W m^{-1} K^{-1} and $\lambda_C = 0.25$ W m^{-1} K^{-1} at a constant surface root mean square roughness $S_q = 2.0$ µm.

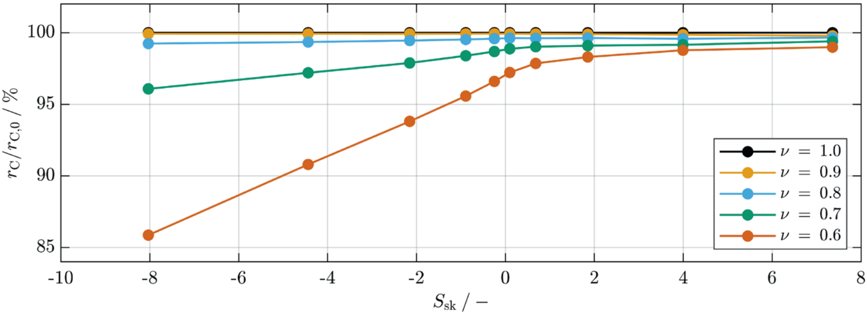

Figure D.3. Change in thermal contact resistance as a function of wetting density considering surface skewness.

Results are given in relation to the specific thermal contact resistance $r_{C,0}$ occuring with complete surface wetting $\nu = 1$. Polymer: $\lambda_C = 0.25$ W m^{-1} K^{-1}. Substrate: Artificial rough surface with $S_q = 2.0$ µm, see **Figure 6.1**, $\lambda_S = 130$ W m^{-1} K^{-1}.

The ratio of the calculated specific thermal contact resistance r_C to $r_{C,0}$ is shown, where $r_{C,0}$ is the previously calculated specific thermal contact resistance with full surface wetting. The calculated contact resistances are negative, as already shown in chapter 6.2, because the surface asperities reaching into the polymer cause a locally reduced thermal resistance in comparison to an ideally smooth transition. The reduced wetting density reduces the magnitude of the effect. Positive skewness, even at an unrealistically low wetting density down to $\nu = 0.6$, leads to $< 3\ \%$ in detectable changes. A more pronounced effect, down to $-14\ \%$, can be seen with negative skewness. However, with such small effects, the highly simplified description of the physically and chemically very complex wetting phenomenon can be accepted. The study has shown that the impact will be negligible in most cases with the same combination of λ_S and λ_C, and that a more detailed study is not required. No further consideration is given in the studies, presented in chapter 6. Finally, **Figure D.4** shows the results of a simulative study in which the thermal conductivities of the contact partners λ_S and λ_C are varied. The geometric parameters are kept constant ($S_\mathrm{q} = 2.0\ \mu\mathrm{m}$, $S_\mathrm{sk} = 0$, $\nu = 1.0$). Analytically, it can be assumed that for $\lambda_\mathrm{S} \gg \lambda_\mathrm{C}$, the thermal transition becomes a purely geometric phenomenon with a constant equivalent thermal height z_th. The specific thermal contact resistance r_C then scales with the reciprocal of the polymer's thermal conductivity λ_C, see **Eq. (6.6)**, page 179.

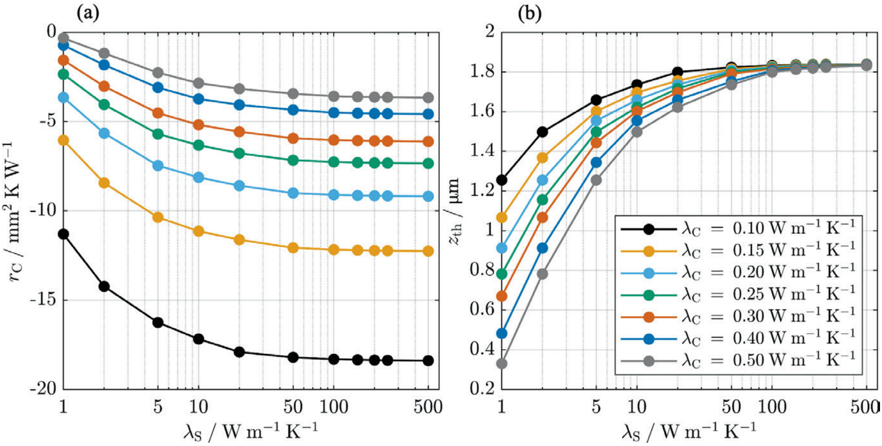

Figure D.4. Specific thermal contact resistance and equivalent thermal height as a function of polymer and substrate thermal conductivities.

Calculated specific thermal contact resistances in (a) and corresponding equivalent thermal heights in (b). Substrate: Artificial random rough surface with $S_\mathrm{q} = 2.0\ \mu\mathrm{m}$, see **Figure 6.1**, $S_\mathrm{sk} = 0$. Full surface wetting.

D.2 Comparison of micro thermography and FPS transition simulation

This appendix supplements chapter 6.1 with an exemplary comparison between a microstructure simulation and a micro thermography measurement of an FPS transition. Comparing complete thermal resistance curves from simulation and experiment is significantly more challenging than just comparing effective thermal conductivity values, as in chapters 5 and 6. Since the local microstructure of a sample was not experimentally accessible within this work and could not be predicted theoretically, modeling requires broad assumptions and empirical adjustments to align simulation with measurement. This process is demonstrated below using a sample with particularly large particles, chosen for pronounced effects and better experimental resolution. The comparison is based the first of the two FPS transitions used as an introductory example for micro thermography in **Figure 3.15**, page 69:

- Substrate: SUB-R2[18]
- Polymer: Epoxy E01
- Filler: Alox-S-63, $\phi = 0.5$

The course of the $r(z)$ curve in the boundary layer depends largely on the packing structure and the PSD configuration. Several packing configurations were tested, and their specific resistance curves compared with the micro thermography result, see **Figure D.5**.

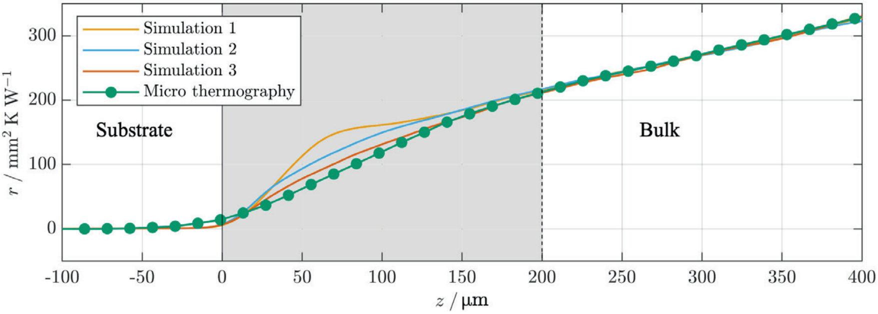

Figure D.5. Comparison of simulated and measured thermal resistance curve across an FPS transition. Experiment: Polymer: Epoxy E01. Filler: Alox-S-63, $\phi = 0.5$, $D_{50} = 63.4$ µm. Substrate: SUB-R2. Simulation: Polymer: $\lambda_C = 0.25$ W m^{-1} K^{-1} (e.g., epoxy). Filler: Spheres with log-normal size distribution with $\log(\sigma) = 0.4$, $D_{50} = 10$ µm (scaled to 63.4 µm), $\phi_{\max} = 0.55$, $\phi = 0.5$, $\lambda_D = 35$ W m^{-1} K^{-1} (e.g., alumina). Substrate: Digitized SUB-R2, $\lambda_S = 130$ W m^{-1} K^{-1} (e.g., aluminum alloy). Full surface wetting.

---

[18] AlMg3 alloy; sandblasted surface, details see **Figure 3.2**, page 45.

In simulation 1, with $\mathrm{PSD} = \mathrm{PPD} + 0.125$, the total thermal resistance matched well but the boundary layer thickness was underestimated. Better agreement with the experiment was achieved in simulations 2 and 3, where equal PSD and PPD values were assumed, decaying exponentially with substrate distance:

$$\mathrm{PPD}(z) = \mathrm{PPD}_{\mathrm{bulk}} + (\mathrm{PPD}_0 - \mathrm{PPD}_{\mathrm{bulk}}) \cdot \exp(-a \cdot z) \ . \tag{D.2}$$

This relationship was derived empirically with the following parameters based on the individual particle sizes D_i:

- $\mathrm{PPD}_{\mathrm{bulk}} = 0.04 \cdot D_i$
- $\mathrm{PPD}_0 = 0.7 \cdot D_i$ (Simulation 2)
- $\mathrm{PPD}_0 = 0.5 \cdot D_i$ (Simulation 3)
- $a = 0.12\ \mu\mathrm{m}^{-1}$ (Simulation 2)
- $a = 0.08\ \mu\mathrm{m}^{-1}$ (Simulation 3)

All shown simulation results are based on theoretically modeled close-to-substrate packing configurations that cannot be verified individually. The best agreement with experimental results is achieved in simulation 3. At the same time, it can’t be ruled out that persistent blurriness of the thermal images in the experiment leads to falsely wider boundary layers.

Nevertheless, simulation and experiment can be brought into good agreement, which confirms the fundamental suitability of the methods for the studies on the effects of microscopic surface and packing effects carried out within this work.

D.3 Tabular results of the simulative studies in chapter 6.4

This appendix supplements chapter 6.4 by providing tabulated results from simulation studies on the influence of the microscale packing and substrate structure on boundary layer formation and the resulting thermal contact resistances of FPS transitions.

Table D.1. Results of simulations, corresponding to **Figure 6.13**.

Size distr.	**Projection**		**Geometric boundary layer**		**Thermal boundary layer**	
$\log(\sigma)$ / –	r_{C} / $\mathrm{mm}^2\ \mathrm{K}\ \mathrm{W}^{-1}$	z_{th} / µm	$\Delta z_{\mathrm{C,geo}}$ / µm	$r^*_{\mathrm{C,geo}}$ / $\mathrm{mm}^2\ \mathrm{K}\ \mathrm{W}^{-1}$	$\Delta z_{\mathrm{C,th}}$ / µm	$r^*_{\mathrm{C,th}}$ / $\mathrm{mm}^2\ \mathrm{K}\ \mathrm{W}^{-1}$
0.0	2.88	−7.19	3.03	4.62	1.21	2.93
0.2	2.15	−5.37	3.35	3.40	1.52	2.36
0.4	1.90	−4.74	4.27	3.47	3.05	2.80

Table D.2. Results of simulations, corresponding to **Figure 6.16**.

Filler vol. fract.	**Projection**		**Geometric boundary layer**		**Thermal boundary layer**	
ϕ /	r_C /	z_th /	$\Delta z_\mathrm{C,geo}$ /	$r^*_\mathrm{C,geo}$ /	$\Delta z_\mathrm{C,th}$ /	$r^*_\mathrm{C,th}$ /
–	$\mathrm{mm^2\ K\ W^{-1}}$	µm	µm	$\mathrm{mm^2\ K\ W^{-1}}$	µm	$\mathrm{mm^2\ K\ W^{-1}}$
0.17	7.66	−3.12	7.24	26.46	3.62	15.44
0.24	6.92	−3.34	5.64	20.13	2.56	11.10
0.33	6.62	−4.11	4.65	15.21	2.11	8.94
0.37	5.86	−4.10	4.31	13.16	1.96	8.13
0.42	5.29	−4.32	3.98	10.87	1.81	7.10
0.48	4.37	−4.47	3.98	9.12	1.33	5.22
0.52	3.51	−4.53	3.48	6.87	0.95	3.52
0.55	2.15	−5.37	3.35	3.40	1.52	2.37

Table D.3. Results of simulations, corresponding to **Figure 6.24**.

Surface	**Projection**		**Geometric boundary layer**		**Thermal boundary layer**	
$\left\vert\begin{array}{l}\mathrm{S_q}\\ S_\mathrm{a}\end{array}\right.$ /	r_C /	$\left\vert\begin{array}{l}z_\mathrm{th,hom}\\ z_\mathrm{th}\end{array}\right.$ /	$\left\vert\begin{array}{l}\Delta z'_\mathrm{C,geo}\\ \Delta z''_\mathrm{C,geo}\end{array}\right.$ /	$r^*_\mathrm{C,geo}$ /	$\left\vert\begin{array}{l}\Delta z'_\mathrm{C,th}\\ \Delta z''_\mathrm{C,th}\end{array}\right.$ /	$r^*_\mathrm{C,th}$ /
µm	$\mathrm{mm^2\ K\ W^{-1}}$	µm	µm	$\mathrm{mm^2\ K\ W^{-1}}$	µm	$\mathrm{mm^2\ K\ W^{-1}}$
$\left\vert\begin{array}{l}0.0\\ 0.0\end{array}\right.$	2.15	$\left\vert\begin{array}{l}0.00\\ -5.48\end{array}\right.$	$\left\vert\begin{array}{l}0.00\\ 3.35\end{array}\right.$	3.40	$\left\vert\begin{array}{l}0.00\\ 1.52\end{array}\right.$	2.36
$\left\vert\begin{array}{l}1.0\\ 0.8\end{array}\right.$	2.36	$\left\vert\begin{array}{l}0.41\\ -6.02\end{array}\right.$	$\left\vert\begin{array}{l}1.84\\ 4.26\end{array}\right.$	4.13	$\left\vert\begin{array}{l}1.53\\ 2.43\end{array}\right.$	3.04
$\left\vert\begin{array}{l}3.0\\ 2.4\end{array}\right.$	1.77	$\left\vert\begin{array}{l}3.29\\ -4.51\end{array}\right.$	$\left\vert\begin{array}{l}6.12\\ 6.98\end{array}\right.$	4.37	$\left\vert\begin{array}{l}4.60\\ 5.76\end{array}\right.$	3.78
$\left\vert\begin{array}{l}5.0\\ 3.9\end{array}\right.$	0.24	$\left\vert\begin{array}{l}6.91\\ -0.61\end{array}\right.$	$\left\vert\begin{array}{l}11.02\\ 10.92\end{array}\right.$	3.55	$\left\vert\begin{array}{l}4.92\\ 9.70\end{array}\right.$	3.96

Table D.4. Results of simulations, corresponding to **Figure 6.28**.

Surface	**Projection**		**Geometric boundary layer**		**Thermal boundary layer**	
$\vert S_\mathrm{q}$ $\vert S_\mathrm{al}$ / µm	r_C / $\mathrm{mm^2\ K\ W^{-1}}$	$\vert z_\mathrm{th,hom}$ $\vert z_\mathrm{th}$ / µm	$\vert \Delta z'_\mathrm{C,geo}$ $\vert \Delta z''_\mathrm{C,geo}$ / µm	$r^*_\mathrm{C,geo}$ / $\mathrm{mm^2\ K\ W^{-1}}$	$\vert \Delta z'_\mathrm{C,th}$ $\vert \Delta z''_\mathrm{C,th}$ / µm	$r^*_\mathrm{C,th}$ / $\mathrm{mm^2\ K\ W^{-1}}$
2.00 12.27	2.14	1.05 −5.45	4.72 4.12	3.72	4.41 2.29	2.78
2.00 5.43	2.13	1.64 −5.43	3.68 5.47	4.37	3.37 3.64	3.28
2.00 2.60	2.69	2.31 −6.86	1.68 7.15	5.44	1.08 6.24	4.92
2.00 1.93	3.37	2.63 −8.59	0.33 7.29	6.30	1.25 6.68	5.96

Table D.5. Results of simulations, corresponding to **Figure 6.30**.

Size distr.	**Projection**		**Geometric boundary layer**		**Thermal boundary layer**	
$\log(\sigma)$ / –	r_C / $\mathrm{mm^2\ K\ W^{-1}}$	$\vert z_\mathrm{th,hom}$ $\vert z_\mathrm{th}$ / µm	$\vert \Delta z'_\mathrm{C,geo}$ $\vert \Delta z''_\mathrm{C,geo}$ / µm	$r^*_\mathrm{C,geo}$ / $\mathrm{mm^2\ K\ W^{-1}}$	$\vert \Delta z'_\mathrm{C,th}$ $\vert \Delta z''_\mathrm{C,th}$ / µm	$r^*_\mathrm{C,th}$ / $\mathrm{mm^2\ K\ W^{-1}}$
0.0	3.52	1.64 −8.97	2.14 5.13	5.67	3.35 3.62	4.50
0.2	2.13	1.64 −5.43	3.68 5.47	4.37	3.37 3.64	3.28
0.4	1.26	1.64 −3.21	4.29 6.70	3.24	2.46 7.92	3.85

D.4 Tabular results of the simulative studies in chapter 6.5

This appendix supplements chapter 6.5 by providing tabulated results from the simulation study investigating the influence of the thermal conductivities of the polymer, filler, and substrate on the thermal contact resistance of an FPS transition. As the microstructure remains constant throughout the study, the geometric conditions and thus the geometric boundary layer remain unchanged, with $\Delta z'_\mathrm{C,geo} = 3.68$ µm and $\Delta z''_\mathrm{C,geo} = 5.47$ µm.

Table D.6. Results of simulations, corresponding to **Figure 6.33**.

		Polymer λ_{C} / $\mathrm{W\ m^{-1}\ K^{-1}}$		
	Filler	0.10	0.30	0.50
	λ_{D} / $\mathrm{W\ m^{-1}\ K^{-1}}$	λ_{eff} / $\mathrm{W\ m^{-1}\ K^{-1}}$	λ_{eff} / $\mathrm{W\ m^{-1}\ K^{-1}}$	λ_{eff} / $\mathrm{W\ m^{-1}\ K^{-1}}$
	10	0.86	1.67	2.29
	50	1.97	3.23	4.28
	100	3.08	4.63	5.88
Substrate	150	4.08	5.85	7.26
λ_{S} / $\mathrm{W\ m^{-1}\ K^{-1}}$	λ_{D} / $\mathrm{W\ m^{-1}\ K^{-1}}$	$\left\lvert\begin{matrix} r_{\mathrm{C}} \\ r^*_{\mathrm{C,geo}} \end{matrix}\right.$ / $\mathrm{mm^2\ K\ W^{-1}}$	$\left\lvert\begin{matrix} r_{\mathrm{C}} \\ r^*_{\mathrm{C,geo}} \end{matrix}\right.$ / $\mathrm{mm^2\ K\ W^{-1}}$	$\left\lvert\begin{matrix} r_{\mathrm{C}} \\ r^*_{\mathrm{C,geo}} \end{matrix}\right.$ / $\mathrm{mm^2\ K\ W^{-1}}$
10	10	7.76 14.26	2.91 6.38	1.80 4.48
	50	9.03 11.22	3.76 5.34	2.41 3.75
	100	9.41 10.44	4.09 5.05	2.65 3.55
	150	9.56 10.15	4.25 4.92	2.78 3.45
50	10	5.51 12.50	2.12 5.62	1.27 3.83
	50	4.73 7.42	2.33 4.00	1.55 2.85
	100	4.49 6.00	2.43 3.48	1.67 2.55
	150	4.36 5.37	2.47 3.23	1.73 2.39
100	10	5.09 11.75	1.97 5.48	1.17 3.73
	50	1.89 5.33	1.93 3.62	1.31 2.62
	100	3.27 4.75	1.88 2.97	1.33 2.23
	150	2.95 4.00	1.85 2.66	1.35 2.04
200	10	4.86 11.54	1.89 5.40	1.12 3.68
	50	3.16 5.78	1.66 3.37	1.14 2.46
	100	2.38 4.00	1.51 2.63	1.09 2.01
	150	2.14 3.27	1.42 2.27	1.06 1.78